

Copyright Warning & Restrictions

The copyright law of the United States (Title 17, United States Code) governs the making of photocopies or other reproductions of copyrighted material.

Under certain conditions specified in the law, libraries and archives are authorized to furnish a photocopy or other reproduction. One of these specified conditions is that the photocopy or reproduction is not to be “used for any purpose other than private study, scholarship, or research.” If a user makes a request for, or later uses, a photocopy or reproduction for purposes in excess of “fair use” that user may be liable for copyright infringement,

This institution reserves the right to refuse to accept a copying order if, in its judgment, fulfillment of the order would involve violation of copyright law.

Please Note: The author retains the copyright while the New Jersey Institute of Technology reserves the right to distribute this thesis or dissertation

Printing note: If you do not wish to print this page, then select “Pages from: first page # to: last page #” on the print dialog screen

The Van Houten library has removed some of the personal information and all signatures from the approval page and biographical sketches of theses and dissertations in order to protect the identity of NJIT graduates and faculty.

ABSTRACT

ENHANCEMENT OF FLUIDIZATION AND FILTRATION USING NANOPARTICLE AGGLOMERATES AND AEROGELS

**by
Jose A. Quevedo**

Previous works have classified the fluidization behavior of nanoparticles as Agglomerate Particulate Fluidization (APF) and Agglomerate Bubbling Fluidization (ABF). These fluidization behaviors are quite different in regard to the fluidized bed expansion, the presence of bubbles and the smoothness of the bed surface, with APF nanopowders showing a much more homogeneous fluidization and a much better dispersion than ABF nanopowders which are generally very difficult to fluidize and show vigorous bubbling. In the present work, the fluidization of APF as well as ABF nanopowders is studied in depth, both conventionally, and in the presence of external assistance; several related topics are discussed such as the presence of pressure fluctuations, electrostatic charge effects, magnetic, vibration and centrifugal (in a rotating fluidized bed) assisted fluidization, jet assisted fluidization and mass transport rates during humidification and drying of hydrophilic fluidized nanopowders. The research on jet assisted fluidization of nanopowders coupled with the reduction of electrostatic charges is one of the most important contributions of the present work. For APF nanopowders, fluidized bed heights of about an order of magnitude larger than the initial bed height are obtained, and for ABF nanopowders, the fluidization behavior is transformed into APF.

In a different but related topic, liquid-solid inverse fluidization of silica aerogel granules-Nanogel[®]-has been studied for the removal of oil from wastewater. The granules are several hundred microns or larger in size, but they have a nano-porous structure that

provides large surface area and low density. The hydrodynamic characteristics of the granules during inverse fluidization and their oil removal efficiency and capacity are described.

The third topic of study was the filtration of submicron particles by customized granular media made of either agglomerates of nanoparticles, aerogel granules or carbon black granules challenged against submicron aerosol particles and oil droplets. Both packed and fluidized customized filters were studied. It is shown that a granular bed filter of porous granules can have a collection efficiency equivalent to HEPA filters but with a larger capacity. Also, the customized filters show larger collection efficiency for the removal of oil droplets when compared against HEPA filters.

**ENHANCEMENT OF FLUIDIZATION AND FILTRATION USING
NANOPARTICLE AGGLOMERATES AND AEROGELS**

by
Jose A. Quevedo

**A Dissertation
Submitted to the Faculty of
New Jersey Institute of Technology
in Partial Fulfillment of the Requirements for the Degree of
Doctor of Philosophy in Chemical Engineering**

Otto H. York Department of Chemical Engineering

January 2007


Copyright © 2007 by Jose A. Quevedo


ALL RIGHTS RESERVED


APPROVAL PAGE


**ENHANCEMENT OF FLUIDIZATION AND FILTRATION USING
NANOPARTICLE AGGLOMERATES AND AEROGELS**

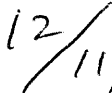
Jose A. Quevedo

 _____ *12/11/06*
Date
Dr. Robert D'Jeffer, Dissertation Advisor
Distinguished Professor of Chemical Engineering (Emeritus), NJIT
Distinguished Research Professor, NJCEP

 _____ *12/11/06*
Date
Dr. Rajesh N. Dave, Dissertation Co-Advisor
Distinguished Professor of Chemical Engineering, NJIT

 _____ *12/11/06*
Date
Dr. Piero M. Armenante, Committee Member
Distinguished Professor of Chemical Engineering, NJIT

 _____ *12/11/2006*
Date
Dr. Chien-Yueh Huang, Committee Member
Assistant Professor of Chemical Engineering, NJIT

 _____ *12/11/06*
Date
Dr. Chao Zhu, Committee Member
Associate Professor of Mechanical Engineering, NJIT

BIOGRAPHICAL SKETCH

Author: Jose A. Quevedo
Degree: Doctor of Philosophy
Date: January 2007

Undergraduate and Graduate Education:

- Doctor of Philosophy in Chemical Engineering
New Jersey Institute of Technology, Newark, NJ, 2007
- Master of Science in Chemical Engineering,
New Jersey Institute of Technology, Newark, NJ, 2004
- Engineer Degree in Chemical Engineering,
National University of Engineering, Lima, Peru, 2002
- Bachelor of Science in Chemical Engineering,
National University of Engineering, Lima, Peru, 1998

Major: Chemical Engineering

Publications:

- J. Quevedo, H. Nakamura, R. Dave, R. Pfeffer, S. Watano, "Fluidization of Nanoagglomerates in a Rotating Fluidized Bed," *AIChE Journal*, July 2006; Vol. 52 (7): 2401-2412.
- Q. Yu, J. Quevedo, R. Pfeffer, R. Dave, C. Zhu, "Enhanced Fluidization of Nanoparticles in an Oscillating Magnetic Field," *AIChE Journal*, July 2005; Vol. 51 (7): 1971-1979.
- J. Quevedo, J. Flesch, R. Pfeffer, R. Dave, "Evaluation of Assisting Methods on Fluidization of Hydrophilic Nanoagglomerates by Monitoring Moisture in the Gas Phase," submitted.
- J. Quevedo, G. Patel, R. Pfeffer, "Removal of Oil from Water by Inverse Fluidization of Aerogels," in preparation.

- J. Quevedo, G. Patel, R. Pfeffer, R. Dave, "Filtration of Submicron Particles by Using Agglomerates of Nanoparticles as Filter Media," in preparation.
- J. Quevedo, A. Omosibi, R. Pfeffer, "Gas-Solid Fluidization of Agglomerates of Nanoparticles: Characterization and Conversion from ABF to APF Behavior by Using Jets," in preparation.
- J. Quevedo, G. Patel, R. Pfeffer, "Residence Time Distribution Study of Packed and Fluidized Bed of Agglomerates of Nanoparticles," in preparation.

Presentations:

- J. Quevedo, H. Nakamura, Y. Shen, R. Dave, R. Pfeffer, S. Watano, "Fluidization of Nanoparticles in a Rotating Fluidized Bed," AIChE Annual Meeting, paper 411f, Cincinnati, OH, November, 2005.
- J. Quevedo, D. Lepek, Q. Yun, R. Dave, R. Pfeffer, S. Dukhin, "Filtration of Submicron Particles by Agglomerates of Nanoparticles," AIChE Annual Meeting, paper 443c, Cincinnati, OH, November 2005.
- J. Quevedo, R. Pfeffer, J. Flesch, R. Dave, "Evaluation of the Impact of Assistance on Fluidization of Nanoparticle Agglomerates by Monitoring Moisture in the Gas Phase," Fifth World Congress on Particle Technology, AIChE Spring Meeting, paper 248d, Orlando, FL, April 2006.
- J. Quevedo, R. Pfeffer, "Fluidization and Filtration using Agglomerates of Nanoparticles and Nanostructured Materials," Schering-Plough Science & Innovation Symposium, Morristown, NJ, June 2006.
- J. Quevedo, G. Patel, R. Dave, R. Pfeffer, "Filtration of Submicron Particles by Agglomerates of Nanoparticles," AIChE Annual Meeting, paper 87b, San Francisco, CA, November 2006.
- J. Quevedo, G. Patel, R. Dave, R. Pfeffer, "Residence Time Distribution Studies in a Fluidized Bed of Fumed Silica Nanopowder," AIChE Annual Meeting, paper 33f, San Francisco, CA, November 2006.

This Dissertation is dedicated to:

*my family,
my future children, as their challenge,
but especially to the people that encouraged me with their
example (some with us, some in God's presence).*

*Row, row, row your boat,
Gently down the stream.
Merrily, merrily, merrily, merrily,
Life is but a dream.
(Sung in, Star Trek: The Final Frontier, 1989)*

ACKNOWLEDGMENT

I would like to express my deepest appreciation to all who have helped me during my journey through the doctoral studies. I am very thankful to the committee members, Dr. Robert Pfeffer, Dr. Rajesh Dave, Dr. Piero Armenante, Dr. Chao Zhu, and Dr. Chien-Yueh Huang. I really appreciate their time, advice and patience throughout this process.

I would like to express my highest appreciation to Dr. Robert Pfeffer, who introduced me to the area of particle technology and provided me with a research assistantship through his National Science Foundation awards NIRT # 0210400 and NER # 0507936. His guidance and support, both mentally and financially, were critical towards the completion of my research and this dissertation. I feel short of words to express my full appreciation towards his persona.

I would also like to acknowledge the financial support from Degussa Corporation and in particular to Prof. Dr. Herbert Riemenschneider for his support and faith in our research team. Thanks also to Jürgen Flesch and Jonah Klein for their collaboration.

I acknowledge the support from Cabot Corporation for the research related to filtration. Thanks to Dr. Vivian Zhang, Dr. Nirmalya Maity and Dr. Bart Kalkstein.

I would like to thank my family: Erica, David, Evelyn, Jorge, Aneta, Adriana, Mark, Leonarda, Tim, Victoria and Jessica. I am indebted to them because I placed my research ahead of them and I am very sorry for not having been with them in times when I should have.

Finally, I would like to thank the assistance of Gaurav Patel and Ayokunle Omoobi whom helped me in the execution of some of the experiments.

TABLE OF CONTENTS

Chapter	Page
1 INTRODUCTION ..	1
2 ENHANCEMENT OF GAS-SOLID FLUIDIZATION OF AGGLOMERATES OF FUMED METAL OXIDE NANOPARTICLES.....	7
2.1 Overview.....	7
2.2 Introduction.....	8
2.2.1 Fluidization of Fumed Silica Nanopowders	9
2.2.2 Removing Electrostatic Charge Effects	13
2.2.3 Enhancement by Micro-Jet	13
2.2.4 In-situ Measurement of Fluidized Agglomerates	15
2.2.5 Modeling of Agglomerate Sizes	16
2.2.6 About This Work on Fluidization of Agglomerates of Nanoparticles	17
2.3 Experimental Methods	19
2.3.1 Experiments Related to the Reduction of Electrostatic Charge.....	23
2.3.2 Experiments Focusing on the Effects of a Jet Applied to a Fluidization Column Internal and in the Absence of a Gas Distributor Plate.....	24
2.3.3 Experiments Focusing on the Characterization of the Agglomerate Size in a Fluidized Bed	26
2.4 Results and Discussion	28
2.4.1 Effect of Electrostatic Charge on the Fluidization of Agglomerates of Nanoparticles.....	28
2.4.2 Hydrodynamic Characteristics of Conventional and Jet Assisted Fluidization of APF Nanopowders Aerosil® R974 and Aerosil® 200.....	30
2.4.3 Hydrodynamic Characteristics of Conventional and Jet Assisted Fluidization of ABF Nano-Powders Aerosil® 90, Aeroxide® Alu C and Aeroxide® TiO ₂ P25	36

TABLE OF CONTENTS
(Continued)

Chapter	Page
2.4.4 Impact of the Nozzle Size on the Jet Assisted Fluidization Performance.....	40
2.4.5 Effect of the Direction of the Nozzle on Jet Assisted Fluidization of Nano-Powders	46
2.4.6 Favored Performance of Internals Installed in the Fluidization Column by Jet Assistance	48
2.4.7 Scale-Up of the Jet Assisted Fluidization	51
2.4.8 Fluidization of Nanopowders When Having Primary Flow Entering From the Side at the Bottom of the Fluidization Column.....	55
2.4.9 In-Situ Measurement of Agglomerates of Nanoparticles in Conventional and Jet Assisted Fluidized Beds	58
2.4.10 Estimating the Agglomerate Size by Using the Richardson-Zaki Criterion	64
2.4.11 Estimating the Agglomerate Size, Density and Terminal Velocity by Using the Richardson-Zaki Criterion Coupled with Fractal Dimension of the Agglomerate.....	77
2.4.12 Fluctuations in Pressure Drop Measurements during Fluidization of Nanopowders.....	82
2.5 Conclusions.....	87
3 EVALUATION OF ASSISTING METHODS ON FLUIDIZATION OF HYDROPHILIC NANOAGGLOMERATES BY MONITORING MOISTURE IN THE GAS PHASE	91
3.1 Overview.....	91
3.2 Introduction.....	92
3.3 Experimental Methods.....	96
3.3.1 Isotherm Experiments by Monitoring Moisture in the Gas Phase.....	100
3.3.2 Isotherm Experiments by Monitoring Moisture in the Solid Phase...	102

TABLE OF CONTENTS
(Continued)

Chapter	Page
3.3.3 Monitoring of the Moisture in the Gas Phase during Drying	102
3.3.4 Short Time Experiments	103
3.3.5 Experiments for Studying the Residence Time Distribution (RTD) of Gas Molecules in Packed and Fluidized Beds of Porous Hydrophobic Agglomerates of Nanoparticles	104
3.4 Results and Discussion	107
3.4.1 Adsorption Isotherms by Monitoring the Gas Phase	110
3.4.2 Adsorption Isotherms by the Gravimetric Method	113
3.4.3 Short Time Experiments	114
3.4.4 Comparison of Conventional and Assisted Fluidization by Monitoring Moisture in the Gas-Phase during Drying	116
3.4.5 Fluidization Characteristics of the Nanopowders Studied.....	121
3.4.6 Residence Time Distribution (RTD) of Packed and Fluidized Beds of Hydrophobic Agglomerates of Aerosil R974.....	125
3.5 Modeling.....	137
3.6 Conclusions.....	144
4 FLUIDIZATION OF NANOAGGLOMERATES IN A ROTATING FLUIDIZED BED: THE INFLUENCE OF TANGENTIAL GAS MOTION	147
4.1 Overview.....	147
4.2 Introduction.....	148
4.3 Experimental Method.....	152
4.4 Results and Discussion	155
4.4.1 Flow Regime in the RFB When Fluidizing Agglomerates of Nanoparticles	162
4.4.2 Computational Simulations of an Empty Rotating Cylinder	165

TABLE OF CONTENTS
(Continued)

Chapter	Page
4.4.3 Tangential Momentum Effects	167
4.4.4 Model That Predicts a Higher Bed Pressure Drop	170
4.5 Concluding Remarks	174
5 AGGLOMERATES AND GRANULES OF NANOPARTICLES AS FILTER MEDIA FOR SUBMICRON PARTICLES	177
5.1 Overview	177
5.2 Introduction	178
5.3 Experimental Methods	183
5.3.1 Description of the Experimental Setup	183
5.3.2 Filter Media Preparation	186
5.3.3 Module Preparation	189
5.3.4 Experimental Procedure	193
5.4 Results and Discussion	194
5.4.1 Filtration of Submicron Solid Aerosol Particles	196
5.4.2 Filtration of Submicron Liquid Aerosol Droplets	207
5.4.3 Pressure Drop Across Filter Media and Evaluation of Capacity	216
5.4.4 Fluidized Bed Filter	223
5.4.5 Discussion on the Filtration Mechanisms and Collection Efficiency	229
5.5 Conclusions	239
6 REMOVAL OF OIL FROM WATER BY INVERSE FLUIDIZATION OF AEROGELS	243
6.1 Overview	243
6.2 Introduction	244

TABLE OF CONTENTS
(Continued)

Chapter	Page
6.3 Experimental Methods	250
6.4 Results and Discussion	255
6.4.1 Hydrodynamics of Inverse Fluidized Beds of Aerogel Granules	255
6.4.2 Relationship Between the Drag Force Function and the Bed Void Fraction	263
6.4.3 Calculation of the Minimum Fluidization Velocity.....	266
6.4.4 Removal of Oil From Water by Using an Inverse Fluidized Bed of Aerogel Granules.....	267
6.5 Conclusions.....	280
7 SUMMARY OF CONTRIBUTIONS.....	283
APPENDIX A MATLAB CODE TO MODEL THE CONCENTRATION OF MOISTURE AT THE EXIT OF A FLUIDIZED BED.....	289
APPENDIX B RESIDENCE TIME DISTRIBUTION FUNCTIONS.....	293
APPENDIX C SEM IMAGES OF GRANULAR FILTRATION MEDIA.....	298
REFERENCES	302

LIST OF TABLES

Table	Page
2.1	Nano-powders Used and Their Properties22
2.2	Summary of the Hydrodynamic Characteristics of Conventional and Jet Assisted Fluidized Beds40
2.3	Data Corresponding the Jet Assisted Fluidization Experiments with Different Nozzle Sizes40
2.4	Slopes and Y-intercepts Corresponding to the Richardson-Zaki Plots from Figure 2.45 to Figure 2.47.....72
2.5	Slopes and Y-intercepts Corresponding to the Richardson-Zaki Plots from Figure 2.4877
2.6	Parameters Corresponding to the Fractal Analysis Coupled with the R-Z Model for the Estimation of the Agglomerate Size80
3.1	Data Corresponding to the Adsorption Isotherm of Aerosil [®] 200 by Monitoring Moisture in the Gas Phase112
3.2	Data Corresponding to the Adsorption Isotherm of Aerosil [®] 90 by Monitoring Moisture in the Gas Phase112
3.3	Space-Time for the Different Experiments Related to the RTD Studies.....127
4.1	Estimated Values of the Dimensionless Numbers for Gas Flowing Through the Bed during Fluidization of APF Powders. Average Particle Diameter Assumed to Be 80 μm164
5.1	List of the Particles Used as Filter Media187
5.2	Summary of the Cumulative Collection Efficiencies of the Filters When Challenged Against Solid Aerosols205
5.3	Summary of the Cumulative Collection Efficiencies of the Filters When Challenged Against Liquid Oily-droplets Aerosol215
5.4	Summary of Characteristics of the Packed Beds of the Customized Filters.....231
6.1	Calculation of the Granule Density and the Initial Void Fraction from Experimental Data260

LIST OF TABLES

Table	Page
6.2 Richardson-Zaki Bed Expansion Parameters and Calculation of the Particle Size from Experimental Data.....	263
6.3 Slopes and Intercepts Corresponding to the Plot of the Drag Force vs. Void Fraction	265
6.4 Comparison of the Experimental and Theoretical Minimum Fluidization Velocities	266
6.5 Summary of Results Corresponding to the Oil Removal from Water by Inverse Fluidized Bed of Nanogel [®]	268

LIST OF FIGURES

Figure	Page
2.1	Schematic diagram of the experimental setup. (1) compressed dry N ₂ cylinder, (2) Pressure regulator for low pressure, (3) pressure regulator for high pressure, (4) tank for liquid, (5) micro-nozzle, (6) fluidization column, (7) differential pressure transmitter, (8) pre-filter, (9) HEPA filter, (10) flowmeter and (11) computer.....20
2.2	Detail of the locations of the nozzles inside the fluidization column, the bottom line is the gas distributor plate. (a, b, c) correspond to the 3 inches ID column, and (d) correspond to the 5 inches ID column for scaling up experiments.....23
2.3	Detail of the trays inserted in the fluidization column as internals. (a) wire mesh, hexagonal shape; (b) Orifices internal diameter of 10 mm, (c) diagram showing the location of the grid (at 12 inches from the distributor plate) and the nozzle.25
2.4	Images showing the wire mesh (A), and the location of the nozzle above the mesh (B). The mesh is used as internal to break down bubbles and to slow down the downward flow of nanopowder.....25
2.5	Schematic showing the setup used for the in-situ measurement of agglomerates of nanoparticles in a fluidized bed. (1) compressed dry N ₂ cylinder, (2) pressure regulator for low pressure, (3) pressure regulator for high pressure, (4) tank holding alcohol, (5) sintered metal plate-distributor, (6) micro-nozzle, (7) fluidization column, (8) location of the FBRM probe, (9) location of the PVM probe, 10) filtering mesh, 11) HEPA filter, (12) flowmeter and (13) computer for image and data acquisition.26
2.6	Images showing the tip of the PVM probe, (a) covered with nanopowder due to electrostatic charge, (b) without nanopowder when removing the electrostatic charge from the bed by using alcohol vapor.....27
2.7	Comparison of the non-dimensional fluidized bed pressure drop and bed height during evaluation of the effects of electrostatic charge on fluidization of nano-agglomerates of Aerosil [®] 200.29
2.8	Comparison of the reduced fluidized bed height with respect to gas velocity of conventional and jet assisted fluidization.31
2.9	Non-dimensional pressure drop as function of gas velocity during fluidization of different amounts of Aerosil [®] R974.....32
2.10	Bed expansion during jet processing plotted against time.....33

**LIST OF FIGURES
(Continued)**

Figure	Page
2.11 Comparison of the reduced bed height of fluidized beds of Aerosil [®] 200 and Aerosil [®] R974	34
2.12 Non-dimensional pressure drop as function of gas velocity during fluidization of Aerosil [®] 200	34
2.13 Comparison of the non-dimensional bed height for fluidized beds of “Raw” Aerosil 90, an APF nanopowder (undensified material taken directly from the process) with and without jet assistance.	35
2.14 Non-dimensional pressure drop as a function of gas velocity of conventional and assisted fluidization of “Raw” Aerosil 90 (an APF nanopowder).	35
2.15 Non-dimensional bed expansion as function of gas velocity for conventional fluidization of ABF type nano-powders.....	37
2.16 Non-dimensional bed expansion vs. superficial gas velocity of the micro-jet assisted fluidization of ABF nano-powders.	37
2.17 Non-dimensional pressure drop as function of gas velocity corresponding to the fluidization of Aerosil 90.....	38
2.18 Non-dimensional pressure drop as function of gas velocity corresponding to the fluidization of Aeroxide Alu C.	39
2.19 Non-dimensional pressure drop as function of gas velocity corresponding to the fluidization of Aeroxide TiO ₂ P25.....	39
2.20 Time dependant non-dimensional bed height during jet processing of nanopowders. Gas velocity about 1.6 cm/s.....	42
2.21 Non-dimensional bed height as a function of gas velocity for jet assisted fluidization experiments of Aerosil 90 using different nozzle sizes.....	43
2.22 Theoretical mean axial velocity profile for two different nozzles (127 μm and 508 μm) under the same upstream pressure (120 psig). Axial distance from the nozzle about 80 mm.	45
2.23 Theoretical mean axial velocity profile for two different nozzles (127 μm and 508 μm) under different upstream pressure (120 psig for 127 μm and 20 psig for the 508 μm). Axial distance from the nozzle about 80 mm.	46

LIST OF FIGURES
(Continued)

Figure	Page
2.24 Fluidized bed pressure drop for the fluidization of Aerosil 90 when comparing the effects of nozzle direction.....	47
2.25 Fluidized bed height corresponding to the fluidization of Aerosil 90 comparing the effect of the nozzle direction.....	48
2.26 Non-dimensional bed height of fluidized beds of Aerosil 90 (commercial grade).	49
2.27 Non-dimensional bed height of fluidized beds of Aerosil Raw 90 (process grade).	50
2.28 Images showing the evolution of the bed of powder when a grid is assisted by a jet. Grid is located at 12 inches above the air distributor and jet is 4 inches above it. Primary flow passing through distributor is set constant. (a) only primary flow, no jet, most powder sitting on the grid, (b) jet has been activated and acts on the grid, powder passes through, (c) fluidization starts, (d) section below the grid is filled with fluidized powder that easily passes through the grid, (e) the entire bed of powder is fluidized, a condition promoted by the jet.	51
2.29 Area ratio of different plant scale vs. lab scale columns.	52
2.30 Non-dimensional bed height for fluidization of Aeroxide TiO ₂ P25 in a 5 inches ID column.	53
2.31 Non-dimensional bed height as a function of the gas velocity for fluidization of Aeroxide Raw TiO ₂ P25 (from plant) in a 5 inches ID column.....	54
2.32 Images corresponding to the fluidization of Aeroxide TiO ₂ P25 in a 5 ID column. (a) Initial bed height, (b) maximum bed height while fluidized with jet assistance, (c) close-up of the fluidized bed surface, bed expanded from 5.5 to 25.5 inches and surface of the bed shows no large bubbles.....	55
2.33 Configuration of the fluidizing gas inlet at the bottom of the column.....	56
2.34 Fluidized bed height as a function of the gas velocity for the case when the primary flow is fed sidewise at the bottom of the column. Fluidized powder is Aeroxide Raw TiO ₂ P25. (Mass: 61.5 grams, sieved under 500 μm).	56

**LIST OF FIGURES
(Continued)**

Figure	Page
2.35 (a) & (b) Images showing the bed of powder with a channel due to the sidewise entrance of gas; bed height around 5 inches. (c) Partially fluidized bed of powder when the downward jet is activated; bed height around 13 inches.	57
2.36 Number based agglomerate size distribution of conventionally fluidized Aerosil R974 measured by the FBRM (Lasentec); (a) probe at different positions, (b) different gas velocities through the fluidized bed.....	60
2.37 Comparison of the agglomerate size distribution obtained during conventional and jet assisted fluidization of Aerosil R974 at 3 cm/s. (a) Volume based number size distribution, (b) volume based percentage size distribution, (c) number based number size distribution.	61
2.38 In-situ images of agglomerates of Aerosil R974 in a fluidized bed obtained with the PVM probe, (a) conventional fluidized bed, and (b) jet assisted fluidized bed.....	62
2.39 Comparison of the agglomerate size distributions of a conventional and a jet assisted fluidized bed of Aerosil 90. (a) Number based size distribution, (b) volume based size distribution.	63
2.40 In-situ images of agglomerates of Aerosil 90 in a fluidized bed obtained with the PVM probe, (a) conventional fluidized bed, and (b) jet assisted fluidized bed.....	63
2.41 Comparison of the volume agglomerate size distributions in conventional fluidized beds of Aerosil R974 and Aerosil 90 measured by the FBRM.	64
2.42 Richardson-Zaki plots corresponding to conventional and jet assisted fluidization of different amounts of Aerosil R974.....	73
2.43 Richardson-Zaki plots corresponding to conventional and jet assisted fluidization of other APF nanopowders (Aerosil 200, “Raw” Aerosil 90, and “Raw” Aeroxide TiO ₂ P25). The term “Raw” is used to describe nanopowder obtained directly from the process (undensified).....	73
2.44 Richardson-Zaki plot corresponding to conventional and jet assisted fluidization of ABF nano-powders.	74
2.45 Richardson-Zaki plots corresponding to conventional and jet assisted fluidization of different masses of Aerosil R974 assuming a higher agglomerate density for the jet assisted cases.....	77

LIST OF FIGURES
(Continued)

Figure	Page
2.46 Plot corresponding to the fractal analysis coupled with the Richardson-Zaki models for conventional and micro-jet assisted fluidization of APF nano-powders.....	81
2.47 Plot corresponding to the fractal analysis coupled with the Richardson-Zaki models for conventional and micro-jet assisted fluidization of ABF nano-powders.....	81
2.48 Pressure drop data at two different gas velocities obtained during fluidization of Aerosil R974 under reduced electrostatic charge conditions.....	83
2.49 Average and standard deviations of the pressure drop with respect to superficial gas velocity during conventional fluidization of 20 grams of Aerosil R974.....	84
2.50 Standard deviation of the pressure drop readings as a function of gas velocity during fluidization of Aerosil R974 under different electrostatic charge conditions (ES: Electrostatic).....	85
2.51 Standard deviation of the pressure drop readings as a function of gas velocity during fluidization of Aerosil R974 with different gases and under reduced electrostatic charge conditions (ES: Electrostatic).....	86
2.52 Standard deviation of the pressure drop readings as a function of gas velocity during fluidization of Aerosil R974 with nitrogen under reduced electrostatic charge conditions.....	87
3.1 Schematic of the experimental apparatus for evaluating the drying process in a fluidized bed of nanopowder. (1) Gas cylinder with pressurized N ₂ ; (2) valve; (3) mass flowmeter; (4) humidifier; (5) vibrating device; (6) fluidized bed column; (7) pressure drop display; (8) data acquisition system for humidity sensors; (9) electromagnetic coils; (10) control unit for the vibrator; (11) voltage regulator for the electromagnetic coils.....	97
3.2 Schematic showing the setup used for the Residence Time Distribution studies of packed beds and fluidized beds of hydrophobic agglomerates of nanoparticles. (1) compressed dry N ₂ cylinder, (2) pressure regulator for low pressure, (3) tank holding water, (4) humidity sensors, (5) sintered metal plate-distributor, (6) fluidization column, (7) differential pressure drop transmitter, (8) filtering mesh, (9) HEPA filter, (10) flowmeter (11) absolute humidity sensor (low range), and (12) computer for data acquisition.....	105

**LIST OF FIGURES
(Continued)**

Figure	Page
3.3 Packed beds for the RTD studies; (a) packed bed of glass beads, (b) packed bed of clusters of agglomerates of nanoparticles.....	106
3.4 Absolute humidity as a function of time during humidification and drying of Aerosil [®] 200.	107
3.5 Schematic showing the procedure to find the moisture released by the powder during drying from data collected by the sensor at the top of the column.....	108
3.6 Moisture levels obtained from the sensor at the top of the column showing the humidification and drying runs at different partial pressures for finding the adsorption isotherm of Aerosil [®] 200.....	111
3.7 Moisture levels obtained from the sensor at the top of the column showing the humidification and drying runs at different partial pressures for finding the adsorption isotherm of Aerosil [®] 90.....	111
3.8 Adsorption isotherms of Aerosil [®] 200 and Aerosil [®] 90 found by monitoring the moisture in the gas phase.	113
3.9 Adsorption isotherms of Aerosil [®] 200 and Aerosil [®] 90 at room temperature found by the gravimetric method.....	114
3.10 Data from two short time experiments for assessing the impact of vibration. 40 grams of Aerosil [®] 200 were humidified for about 5 minutes. Gas velocity was 1.5 cm/s and the temperature of the experiment was 128°F.	115
3.11 Short time experiment showing the effect of vibration applied to the fluidized bed of Aerosil [®] 200. Gas velocity was 1.5 cm/s and full fluidization was obtained when vibration was applied; without vibration, channeling occurred.	116
3.12 Comparison of the moisture data obtained from the sensor at the top of the column for conventional and assisted fluidized bed drying of Aerosil [®] 200.	117
3.13 Effect of assistance on fluidized bed drying of Aerosil [®] 200 (not sieved). Mass of powder 40 grams, gas velocity 1.5 cm/s, humidification time 90 minutes, 3 inch column diameter.	118

**LIST OF FIGURES
(Continued)**

Figure	Page
3.14 Accumulated moisture released from Aerosil® 90 (not sieved) showing relatively no effect of vibration as compared to conventional fluidization. Experimental conditions: 200 gr. of Aerosil® 90, gas velocity 1.5 cm/s, 3 inch diameter column.....	119
3.15 Comparison of the moisture data obtained from the sensor at the top of the column for conventional and magnetically assisted fluidized bed drying of Aerosil® 90.....	120
3.16 Accumulated moisture released from Aerosil® 90 (not sieved) comparing magnetically assisted and conventional fluidization. Experimental conditions: 40 grams of Aerosil® 90, gas velocity 1.5 cm/s, humidification time 90 minutes, 2.5 inch diameter column.	121
3.17 Comparison of the fluidized bed pressure drop of Aerosil® 200 for conventional fluidization without reducing electrostatic charge, and for vibrated assisted fluidization with reduced electrostatic charge.....	122
3.18 Comparison of bed expansion of Aerosil® 200 for conventional fluidization without reducing electrostatic charge, and for vibrated assisted fluidization with reduced electrostatic charge.	123
3.19 Comparison of the fluidized bed pressure drop of Aerosil® 90 for conventional and assisted fluidization (magnetically assisted coupled with vibration).....	124
3.20 Comparison of the fluidized bed expansion of Aerosil® 90 for conventional and assisted fluidization (magnetically assisted coupled with vibration).....	124
3.21 Sudden changes in moisture concentration seen at the sensor at the top of the column due to bursting of bubbles.....	125
3.22 Schematic showing the regions object of study inside of the fluidization column.....	126
3.23 Examples of the absolute humidity data given by the sensors during RTD studies, moisture at the bottom of the column or input signal in red and moisture at the outlet of the column or response is given in blue, (a) pulse input, (b) step input.	128

LIST OF FIGURES
(Continued)

Figure	Page
3.24 Responses obtained when applying a step moisture input to a packed bed of agglomerates of Aerosil R974. (a) Cumulative distribution function, $F(t)$; (b) residence time distribution function, $E(t)$	131
3.25 Responses obtained when applying a step moisture input to a fluidized bed of agglomerates of Aerosil R974. (a) Cumulative distribution function, $F(t)$; (b) residence time distribution function, $E(t)$	131
3.26 RTD for a model incorporating diffusion (as a PFR) and a CSTR in series.	132
3.27 Time-delay (τ_D) due to diffusion and mean residence time from the RTD function for the different experiments (P.B., Packed Bed; F.B., Fluidized Bed; P. Processed powder; B., Beads).....	135
3.28 Standard deviation and mean residence time of the RTD functions (CSTR portion) obtained from the experimental data.....	136
3.29 Schematic diagram showing homogeneous fluidization of agglomerates of fumed silica nanoparticles and the variables considered in the modeling of the transport of moisture (Flesch J., Doctoral Dissertation, 2006).	140
3.30 Comparison of experimental and modeling data corresponding to the concentration of moisture in the gas phase with respect to time. Experimental data obtained from monitoring moisture in the gas phase at the exit of a vibrated fluidized bed, (data shown in Figure 3.12).	144
4.1 Schematic of the Rotating Fluidized Bed Unit.	153
4.2 Bed pressure drop of Aerosil [®] R974 vs. air velocity at different centrifugal accelerations ($1 G = 9.8 \text{ m/s}^2$).....	156
4.3 Bed pressure drop against air velocity of Aerosil [®] R972 vs. air velocity at different centrifugal accelerations ($1 G = 9.8 \text{ m/s}^2$).....	156
4.4 Bed pressure drop against air velocity of Aeroxide [®] TiO ₂ P25 vs. air velocity at different centrifugal accelerations ($1 G = 9.8 \text{ m/s}^2$).....	157
4.5 Minimum fluidization velocities of the powders at different rotating speeds (G). The open symbols are U_{mf} data obtained for these powders in a conventional fluidized bed (Zhu et al. ⁴).....	158

LIST OF FIGURES
(Continued)

Figure	Page
4.6 Relative bed height against air velocity of Aerosil® R974 vs. air velocity observed during fluidization at different centrifugal accelerations (1 G = 9.8 m/s ²).....	159
4.7 Relative bed height against air velocity of Aerosil® R972 vs. air velocity observed during fluidization at different centrifugal accelerations (1 G = 9.8 m/s ²).....	159
4.8 Relative bed height of Aeroxide® TiO ₂ P25 vs. air velocity observed during fluidization at different centrifugal accelerations (1 G = 9.8 m/s ²).....	160
4.9 Comparison of the experimental data (dots) of the fluidized bed pressure drop at gas velocities higher than the minimum fluidization velocity against the theoretical estimation using Kao's model; (a) Agglomerates of nanoparticles APF type (Aerosil® R974 and R972) , (b) Agglomerates of nanoparticles ABF type (Aeroxide® TiO ₂ P25).....	161
4.10 Comparison between the modeling of the flow in a RFB: (a) Schematic according to Chen ¹¹ in which a rigid body rotation is assumed for the fluidized bed, valid for modeling micron size and ABF type particles; (b) Schematic when fluidizing APF agglomerates of nanoparticles. Light gray represents the expanded fluidized bed and the blue arrows stand for the flow of air in the RFB.	162
4.11 Contours of velocity magnitude of the air inside the rotating cylinder; velocity mostly tangential. The distributor (dotted circle) rotated at 211 rpm (10 times gravity). These figures show that the tangential velocity in the freeboard changes as a function of the velocity at the inlet of the chamber. (a) inlet velocity of 2 m/s equivalent to a radial velocity at the distributor of 0.095 m/s; (b) inlet velocity of 6 m/s equivalent to a radial velocity at the distributor of 0.286 m/s; (c) inlet velocity of 12 m/s equivalent to a radial velocity at the distributor of 0.573 m/s.	166
4.12 Tangential velocities of the fluid with respect to the rotating frame as function of the radial position in chamber. Solid lines correspond to the results from the numerical simulations from Figure 11 and the dotted line corresponds to Equation 13. The vertical dotted line separates the fluidized bed region from the freeboard.....	167
5.1 Schematic diagram of the experimental setup for the testing of customized filter media against submicron aerosols.....	185

**LIST OF FIGURES
(Continued)**

Figure	Page
5.2 Schematic diagram of the different filter modules. (a) cross sectional view, (b) axial view showing the thickness of the module and the baffles, (c) axial view of a 3 inches thick module, and (d) view of a fluidized bed filter module.....	190
5.3 Particle size distribution (PSD) and cumulative number of particles (blue) corresponding to the solid aerosol from a suspension of polystyrene latex spheres of 0.2 and 0.3 μm in size (peaks).....	196
5.4 Particle size distributions and cumulative plots of the solid aerosol before and after the HEPA filter challenged simultaneously with the customized granular filter.	198
5.5 Cumulative collection efficiency of a brand new HEPA fiber based filter sheet and a used HEPA filter when challenged against solid submicron aerosol at different gas velocities.....	198
5.6 Cumulative collection efficiency of a 2 inches thick packed bed of glass beads (180-220 μm) at different gas velocities.....	199
5.7 Cumulative collection efficiency of a 3 inches thick packed bed of activated carbon particles (250 – 500 μm) with baffles at different gas velocities.	200
5.8 Cumulative collection efficiencies of 3 inches thick packed beds of agglomerates of fumed silica of about 500 to 850 μm in size at different gas velocities. (a) hydrophobic agglomerates of TS-530, and (b) hydrophilic agglomerates of EH-5.....	201
5.9 Cumulative number collection efficiency of a 3 inches thick packed bed of silica shells (250-500 μm) with baffles at different gas velocities.	201
5.10 Cumulative collection efficiency of a 3 inches thick packed bed of granules of carbon black (250 – 500 μm , Black Pearl 460) at different gas velocities.	202
5.11 Cumulative collection efficiency of a 2 inches thick packed bed of granules of carbon black (150 – 250 μm , Regal 660 A69) at different gas velocities.	203
5.12 Particle size distributions and cumulative plots of the solid aerosol before and after the customized granular filter (Regal 660, 150-250 μm , 2inches thick + baffles).	203

**LIST OF FIGURES
(Continued)**

Figure	Page
5.13 Cumulative collection efficiency of a 2 inches thick packed bed of granules of carbon black (150 – 250 μm , Regal 660 A69) with baffles at different gas velocities.	204
5.14 Cumulative collection efficiency of a 3 inches thick packed bed of aerogel granules at different gas velocities. (a) granules of sizes between 150 – 250 μm , (b) granules of sizes between 250 to 500 μm	205
5.15 Cumulative collection efficiencies with respect to gas velocity of the customized filters challenged against solid submicron aerosol.	206
5.16 Droplet size distribution (PSD) and cumulative number of droplets corresponding to liquid aerosol generated from a solution of oil in ethanol.	208
5.17 Cumulative number collection efficiency of HEPA Shop-Vac fiber based filter when challenged against oil submicron size droplets (liquid aerosol).....	209
5.18 Cumulative collection efficiency of 2 inches thick packed beds of glass beads at different gas velocities when challenged against oily submicron aerosol.	210
5.19 Cumulative collection efficiency of 3 inches thick packed beds of fumed silica consolidated agglomerates (500 – 800 μm) at different gas velocities when challenged against oily submicron aerosol.....	211
5.20 Cumulative collection efficiency of packed beds of carbon black granules (Regal 660 A69) at different gas velocities when challenged against oily submicron aerosol.	212
5.21 Cumulative collection efficiency of packed beds of aerogel granules (Nanogel OGD) at different gas velocities when challenged against oily submicron aerosol.	213
5.22 Cumulative collection efficiencies with respect to gas velocity of the customized filters challenged against liquid submicron oil-based aerosol.	215
5.23 Resistance of clean filters tested in the experiments. (Legend: Material, granule size in microns, thickness in inches and with baffles-BAF).	216
5.24 Resistance across HEPA and granular carbon black-based filters as a function of time during filtration of solid submicron particles.	218

LIST OF FIGURES
(Continued)

Figure	Page
5.25 Resistance across HEPA and granular Silica Shells-based filters as a function of time during filtration of solid submicron particles.....	219
5.26 Collection efficiencies of (A) a packed bed filter and (B) a HEPA filter with respect to time during an experiment to compare their removal capacity when challenged against oil-based aerosols. Packed bed filter of Regal 660 granules with sizes between 150 to 250 microns and 2 in thickness with baffles.....	220
5.27 Pressure drop across HEPA and a packed bed of carbon black (Regal 660) with respect to time to compare their capacity for collecting oil-based aerosol.	221
5.28 Collection efficiencies of (A) a packed bed filter and (B) a HEPA filter with respect to time during an experiment to compare their removal capacity when challenged against oil-based aerosols. Packed bed filter of aerogel, Nanogel, granules with sizes between 150 to 250 microns and 1 inch thickness without baffles.....	222
5.29 Pressure drop across HEPA and a packed bed of aerogel granules with respect to time when challenged against oil-based aerosol.	222
5.30 Cumulative number collection efficiency of a fluidized bed of hydrophobic fumed silica (TS-530) when challenged against oil-based aerosol.	223
5.31 Bed expansion of the fluidized bed of Nanogel [®] . (a) Packed bed, no flow passing through the bed; (b-d) flow has been increased but bed not fully fluidized and channels are present; (e) fully fluidized state, a clear horizontal liquid-like interface can be seen.	225
5.32 Fluidization hydrodynamic characteristics of a fluidized bed of 65 μm aerogel granules (Nanogel).	225
5.33 Cumulative number collection efficiency of a fluidized bed of aerogel granules of less than 150 microns. (a) fluidized bed challenged against solid aerosol particles, (b) fluidized bed challenged against oil droplets.	226
5.34 Cumulative number collection efficiency corresponding to a fluidized bed of aerogel granules when challenged against oil-based aerosols at different gas velocities.	227

LIST OF FIGURES
(Continued)

Figure	Page
5.35	Collection efficiencies of a fluidized bed of aerogel granules (A) and a HEPA fiber based filter (B) with respect to time.....228
5.36	Pressure drop or resistance across a HEPA fiber based filter and a fluidized bed of aerogel with respect to time when challenged against the same oil-based aerosol.229
5.37	Reynolds number corresponding to the experimental conditions.....230
5.38	Stokes number (Eq. 5.18) as a function of aerosol particle size and collector size (d_g) for the specified experimental conditions.....234
5.39	Interception based single-sphere collection efficiency corresponding to the specified experimental conditions at 4 cm/s for different collector sizes (d_g) and a packed bed of about 2 inches thick.236
5.40	Mean-square displacement values corresponding to the aerosol particle sizes used in this study. The gas velocity was 4 cm/s and d_g represents the collector size.237
5.41	Diffusion collection efficiency as calculated by Equations 5.9 and 5.29 for aerosols of different sizes as a function of the collector size (gas velocity of 4 cm/s).238
5.42	Theoretically calculated cumulative collection efficiencies corresponding to the size distributions of the PSLS and oil based aerosols used in these experiments. Gas velocity was about 4 cm/s and the thickness of the filter was 2 inches (background: clear = oil, black = PSLS).239
6.1	Classification of oil-water mixtures according to droplet size and corresponding removal methods.245
6.2	Schematic diagram of the inverse fluidization experimental setup.251
6.3	Correlation between the oil concentration in water and COD levels measured by HACH DR/890 Colorimeter.....253
6.4	Pressure drop across the empty column.....254
6.5	Inverse fluidized bed pressure drop vs. superficial fluid velocity of small aerogel granules.256

LIST OF FIGURES
(Continued)

Figure	Page
6.6 Plots showing the inverse fluidized bed pressure drop vs. superficial fluid velocity of large aerogel particles.....	257
6.7 Bed height vs. superficial fluid velocity corresponding to the data on Figure 6.5.....	257
6.8 Bed height vs. superficial fluid velocity corresponding to data on Figure 6.6.....	257
6.9 Relationship between the superficial velocity and the void fraction of inverse fluidized beds of aerogel granules accordingly to the Richardson-Zaki criterion.....	262
6.10 Plot showing the relationship between the drag force function “ <i>f</i> ” and the void fraction “ <i>ε</i> ”.....	265
6.11 Chemical oxygen demand (COD) and inverse fluidized bed expansion (squares) as a function of time of 54 grams of aerogel granules (TLD 302) with sizes between 1.7 to 2.3 mm during removal of oil from water (0.26 g of oil/kg of water and fluid velocity of 0.0305 m/s).....	269
6.12 Chemical oxygen demand (COD) and inverse fluidized bed expansion (squares) as a function of time of 49 grams of aerogel granules (OGD 303) with sizes between 1.7 to 2.3 mm during removal of oil from water (0.39 g of oil/kg of water and fluid velocity of 0.0305 m/s).....	270
6.13 Chemical oxygen demand (COD) and inverse fluidized bed expansion (squares) as a function of time of 56 grams of aerogel granules (OGD 303) with sizes between 0.5 to 0.85 mm during removal of oil from water (0.26 g of oil/kg of water and fluid velocity of 0.0305 m/s).....	270
6.14 (a) Pressure drop across the inversely fluidized beds of aerogel during the removal of oil corresponding to Figures 6.12 to 6.14. Superficial flow velocity was kept constant at 0.0305 m/s. (b) Pressure drop across the column without particles during oil injection.	272
6.15 Chemical oxygen demand (COD) and inverse fluidized bed expansion (squares) as a function of time of aerogel granules (OGD 303) with sizes between 0.5 to 0.85 mm during removal of oil from water, upstream oil concentration is 0.18 g of oil/kg of water and the fluid velocity is 0.0305 m/s. (a) 56 grams, (b) 100 grams.	274

**LIST OF FIGURES
(Continued)**

Figure	Page
6.16 Pressure drop across the inversely fluidized beds of aerogel during the removal of oil corresponding to data shown in Figure 15. Superficial flow velocity was kept constant at 0.0305 m/s.....	275
6.17 Chemical oxygen demand (COD) and inverse fluidized bed expansion (squares) as a function of time of 56 grams of aerogel granules (OGD 303) with sizes between 0.5 to 0.85 mm during removal of oil from water, upstream oil concentration is 0.36 g of oil/kg of water and fluid velocity is 0.0244 m/s (a) OGD 303 granules, (b) TLD 101 granules.	276
6.18 Chemical oxygen demand (COD) and inverse fluidized bed expansion (squares) as a function of time of: 56 grams of aerogel granules (TLD 101) with sizes between 0.5 to 0.85 mm during removal of oil from water: (a) Oil concentration is about 0.45 g of oil/kg of water and 0.0107 m/s fluid velocity, and (b) oil concentration is about 0.48 . g of oil/kg of water and 0.0183 m/s fluid velocity.	278
6.19 Pressure drop across the inversely fluidized beds of aerogel during the removal of oil corresponding to Figure 6.18.	279
6.20 Chemical oxygen demand (COD) and inverse fluidized bed expansion (squares) as a function of time of 108 grams of aerogel granules (TLD 101) with sizes between 0.5 to 0.85 mm during removal of oil from water (0.47 g of oil/kg of water and 0.0102 m/s fluid velocity).	280

LIST OF SYMBOLS

a_{Agg}	surface area of an agglomerate, m^2
A	cross sectional area of the fluidization column, m^2
A_{FB}	cross sectional area of the fluidized bed, m^2
AH	absolute humidity, grams moisture/ grams dry air
\bar{B}_{H_2O}	mass of moisture per mass of powder, kg/kg
C	concentration, g/m^3
C_{dn}	concentration of aerosol downstream, # particles/ cm^3
C_{up}	concentration of aerosol upstream, # particles/ cm^3
C_c	Cunningham correction factor
c_{H_2O}	concentration of moisture, kg of moisture/ m^3 of gas
d_{Agg}	diameter of an agglomerate, m
d_c	channel height, m
D	Brownian diffusivity, m^2/s
D_f	fractal dimension, dimensionless
D_m	binary diffusion coefficient, m^2/s
d_p	diameter of particle, m
DP	dew point temperature, $^{\circ}C$
E	total bed collection efficiency, %

f	drag coefficient, $(3\pi\mu d_p C^{-1})$
\mathbf{f}	vectorial force, N
F	force, N
F_b	buoyancy force, N
F_c	cohesive force, N
F_d	drag force, N
F_g	gravitational force, N
F_{gas}	flow of gas, m^3/s
G	gravitational factor, dimensionless
g	gravitational acceleration, m/s^2 (9.8)
g_c	conversion factor, $1 N.s^2/(kg.m)$
H_{FB}	fluidized bed height, m
H_0	initial bed height at no flow, m
$\underline{i_r}$	unit vector in the radial direction
$\underline{i_\theta}$	unit vector in the angular direction
$\underline{i_k}$	unit vector in the axial direction
k	Boltzmann's constant (1.38×10^{-16} erg K^{-1})
K'_c	modified Henry constant considering the porosity of the agglomerate
L	length relative to the Ro or Ek numbers, m
L_C	length of channel, m
LD	moisture content found by the gravimetric method, %

m	mass of the fluidized granules, kg
M_{H_2O}	mass of water, kg
M_{SiO_2}	mass of fumed silica nanopowder, kg
$\tilde{M}_{1,2}$	molecular mass of component 1 and 2 respectively, kg/kgmol
n_{Agg}	number of agglomerates per volume, $1/m^3$
n	Richardson & Zaki index, dimensionless
N	number of primary particles in an agglomerate
P	pressure, Pa
P_{H_2O}	partial pressure of moisture, Pa
r	radial direction, m
S	stopping distance, m
t	time, s
T	temperature, °C
U	gas velocity, m/s
U_{mf}	minimum fluidization velocity, m/s
U_{mb}	minimum bubbling velocity, m/s
u_r	fluid radial velocity, m/s
u_s	gas velocity of the suspension phase, m/s
U_t	terminal velocity, m/s
\mathbf{v}	fluid velocity vector, m/s
\mathbf{v}_θ	tangential fluid velocity, m/s
\mathbf{v}_r	radial fluid velocity, m/s

V	volume, m^3
V_{FB}	volume of the fluidized bed of agglomerates, m^3
W	weight of the bed of powder, N
$\overline{x^2}$	mean square displacement, m

Greek letters

β_{Agg-s}	mass transport coefficient of moisture, m/s
ε_g	void fraction or interparticle voidage, dimensionless
ε_{Agg}	void fraction in an agglomerate, dimensionless
ε_{FB}	void fraction or interparticle voidage, dimensionless
ε_{mf}	void fraction at minimum fluidization, dimensionless
η	single sphere collection efficiency
λ	mean free path of air molecules, μm
μ	fluid viscosity, (N.s/m ²)
μ_f	fluid viscosity, (N.s/m ²)
μ_g	viscosity of the gas, (N.s/m ²)
ν	kinematic viscosity ($= \mu / \rho$), m ² /s
$\nu_{1,2}$	molecule specific constants
ρ	density, kg/m ³
ρ_a	density of agglomerate, kg/m ³
ρ_b	bulk density of the bed of agglomerates, kg/m ³

ρ_f	gas or fluid density, kg/m ³
ρ_p	particle density, kg/m ³
ρ_s	solid particle density, kg/m ³
Ω	angular speed, rd/s
ϕ	solids volume fraction, dimensionless
Δp	bed pressure drop, Pa
τ	space time, s

Subscripts and superscripts

Agg	agglomerate
b	bed
BL	boundary layer
D	diffusion mechanism
FB	fluidized bed
g	gas
I	inertial impaction
lam	laminar
p	particle
PB	packed bed
R	interception mechanism
S	suspension
t	terminal

turb turbulent

Dimensionless numbers

Ar	Archimedes number
C_D	Drag coefficient
E_k	Ekman number, dimensionless
Kn	Knudsen number
Pe	Peclet number
Re	Reynolds number
Re_p	Reynolds number based on particle diameter
Re_t	Reynolds number based on particle diameter at terminal velocity conditions
Re_Ω	Reynolds number based on angular velocity
Ro	Rossby number
Sc	Schmidt number
Sh	Sherwood number
Stk	Stokes number

CHAPTER 1

INTRODUCTION

This chapter briefly explains the objectives of this study and its layout. This dissertation has focused on three main topics: gas-solid fluidization of agglomerates of nanoparticles, filtration of submicron particles by using agglomerates of nanoparticles as a filter media and liquid-solid inverse fluidization of aerogels to remove oil from wastewater. The materials studied are either agglomerates formed from nanoparticles, also called nanopowders or nanoagglomerates, or powders that are nanostructured granules, such as aerogels.

Fluidization is a unit operation widely used in chemical engineering operations. Several books have been published in efforts to explain the principles and applications of fluidization processes. The basic fluidization concept is to transform fine solids into a fluid-like state by use of the fluid's drag force exerted on the particles (fine solids). Fluidization has proved to be very efficient with regards to mass, heat and momentum transports and chemical reaction between the fluid and the fine solids. Nevertheless, the performance of several fluidization processes is reduced due to different problems that arise mainly due to the characteristics of the particulate material. The increased interest and more frequent use of nanopowders requires a better understanding of the fluidization of these materials and is of importance for industry because of future potential applications involving the handling, dispersion, and processing of nanopowders.

With regard to the filtration of submicron particles and/or nanoparticles, these particles are commonly found in the environment, such as those generated from

combustion processes in power stations, cars, trucks, and jet engines. An economic and efficient means for removing these submicron and nanosize particulates from gas streams are needed for several reasons. It is shown in this dissertation that porous materials, such as agglomerates or nanostructured granules made up of networks of nanoparticles successfully remove submicron particles from a gas stream when customized as granular packed bed filter media. Moreover, the customized filters have larger filtration capacities than HEPA fiber-based filters. Porous materials were selected because of the likelihood of the submicron particles to diffuse into the pores, becoming trapped, and increasing the collection efficiency.

Inverse fluidization of aerogel granules applied to oil removal from water is also introduced. It is well known that contamination of water with, miscible or immiscible, hydrocarbons is a major environmental problem. Oily contaminants can originate from oil spills, in the steel manufacturing and metal working industries, and in municipal wastewater containing vegetable oils and animal fats, among others. Hydrophobic aerogel granules have high oil absorption capacity due to their hydrophobicity and nanoporous structure. In this dissertation, an inverse fluidized bed of aerogel granules has been successfully used for removal of oil from water. The advantages of this method reside in the large oil absorption capacity, the possibility of continuous operation, and the low energy consumption due to the inverse fluidized bed configuration.

This dissertation is divided in seven chapters. Each chapter following this introductory chapter is composed of an overview; an introduction, which presents the relevant literature research; an explanation of the experimental setup and experimental procedure; the results of the experiments and/or theoretical modeling and discussion of

the results, and finally, the conclusions related to the topic of the chapter. Each chapter focuses on a specific project, but is within the overall context of the dissertation, i.e., the understanding and demonstration of the principles and concepts underlying the fluidization of nanopowders and the use of nanopowders for filtration of aerosols and wastewater. The research objectives, the approach and the broader impact of each project, i.e., each chapter, are introduced below.

Chapter 2 is related to gas-solid fluidization of agglomerates of nanoparticles. Although this topic has been studied by previous researchers at NJIT and elsewhere, this chapter presents completely new experimental results for fluidizing many different agglomerates of nanoparticles. The research objectives were to develop a new method for assisting gas-solid fluidization of agglomerates of nanoparticles, especially those particles that are very difficult to fluidize such as titania, to scale-up the assisting method, and to characterize the fluidized agglomerates. In previous research, force fields such as sound waves, vertical vibration, stirring magnetic particles and centrifugal forces have been used with relative success. The approach used to attain the research objectives of this project included the reduction of electrostatic charges in the fluidized beds, the use of jets generated by micro-nozzles, the use of internals such as sieve plates, larger diameter fluidization columns, and the use of instrumentation that allowed for in-situ characterization of the agglomerates.

The broader impact of this project is to use the jet assisting method in an actual production process; therefore, the jet assisting method has been scaled up for the purpose of applying in a production facility of Degussa Corporation who has co-sponsored this project. Furthermore, the in-situ characterization of agglomerates of nanoparticles during

fluidization opens a wide range of further studies related to the dynamics of nanopowders in fluidized beds.

Chapter 3 is also related to the fluidization of nanoagglomerates. The research objectives were to quantitatively measure the impact of previously developed assisting methods in fluidized beds of hydrophilic nanopowders, to characterize qualitatively the surface area of the nanopowders from adsorption isotherms data, and to find the effects of porosity and size of the agglomerates on mass transport rates. The assisting methods used were vertical vibration of the fluidization column, stirring of the region at the bottom of the fluidized bed with magnetic particles under the oscillation of an alternate current magnetic field and their combination. The approach used to reach the research objectives of this project included monitoring the moisture in the gas phase in and out of the fluidized bed, the use of nanopowders showing different fluidizing behavior, and the study of packed beds and conventional and assisted fluidized beds. The broader impact of this project was quantifying the effectiveness of the assisting methods and understanding of the transport processes in a fluidized bed of nanopowder.

Chapter 4 is the last chapter related to gas-solid fluidization of agglomerates of nanoparticles and deals with centrifugal assisted fluidization, or use of a rotating fluidized bed (RFB). The research objectives of this project were to fluidize nanopowders under centrifugal forces, to collect data related to their fluidization characteristics and to gain an understanding of the physics governing the fluidization of these nanopowders in a RFB device. The approach used to reach these objectives involved the fluidization of nanopowders showing different fluidizing behavior, the use of rotating speeds that generated centrifugal forces in the range of 10 to 40 times normal gravity acceleration,

and modeling the rotational gas flow using Fluent[®], a standard computational fluid dynamics computer code. The broader impact of this work resides in the better understanding of a process that has extensive potential applications such as rotating fluidized bed reactors; drying, coating and granulation of fine powders as part of powder processing; and the characterization of different fluidization behaviors under centrifugal forces depending on the type of nanopowder fluidized.

Chapter 5 describes the filtration of submicron aerosols by using granular packed and fluidized beds filters made of granules composed of nanoparticles or that have a nanoporous structure such as aerogels. The research objective of this project was to study the feasibility of using agglomerates of fumed silica nanoparticles, carbon black and aerogel granules as filter media for High Efficiency Particulate Air (HEPA) filters. The approach used to attain the objective was constructing an experimental setup that allowed challenging the filters with submicron solid and liquid aerosols, characterizing the aerosols before and after the filter, customizing granular packed beds by optimizing their thickness and resistance with granules of an optimal size, simultaneously challenging the customized filters and a HEPA fiber-based filter, and characterizing the customized filters by measuring the pressure drop and collection efficiencies with respect to time. The broader impact of this work resides on the potential use of granular bed filters made of porous nano-based materials that could provide collection efficiencies equivalent or better than HEPA filters but with the advantage of increase filtration capacity that translates into a longer lifetime.

Chapter 6 describes the removal of oil from water by using an inverse fluidized bed of hydrophobic aerogel granules. The research objectives were to characterize the

hydrodynamic behavior of aerogel granules in an inverse fluidized state and to reduce the concentration of oil in water from about several thousands of milligrams per liter down to a few parts per million using an inverse fluidized bed of aerogels. The approach taken to achieve the research objectives involved the design and construction of an experimental setup appropriate for inverse fluidization and the measurement of Chemical Oxygen Demand (COD) in the mixture of oil and tap water in and out of the inverse fluidized bed containing different aerogel granules and under different operating conditions. The broader impact of this project resides in its advantages in removing oil from water when compared against other available methods. It is well known that in separation processes involving liquids, most of the energy is spent in pumping the fluid through the separation media, i.e., the filter. The resistance across a fluidized bed is significantly lower when compared to a packed bed containing the same amount of particles. The inverse fluidized bed of aerogel granules provides high oil removal efficiency, high absorption capacity and low energy consumption.

Chapter 7, the last chapter, presents a summary of the contributions of this dissertation. There are also appendixes that contain additional, more detailed, information than that given in the corresponding chapter. A list of references cited is also included at the end of the dissertation.

CHAPTER 2

ENHANCEMENT OF GAS-SOLID FLUIDIZATION OF AGGLOMERATES OF FUMED METAL OXIDE NANOPARTICLES

2.1 Overview

Gas-solid fluidization of agglomerates of nanoparticles has been greatly enhanced by a jet flow coming from a micro-nozzle under reduced electrostatic charge conditions. The enhancement in fluidization can be readily seen by the large increase in bed expansion and the smooth, homogeneous fluidization observed. This assisting method has been successfully applied to APF as well as ABF nanopowders. In particular, hard-to-fluidize ABF nanopowders have been fully fluidized presenting an APF-like behavior. The nanopowders studied are fumed silica Aerosil[®] R974, 200, 90 and Aeroxide[®] TiO₂ P25 and Alu C. The micro-nozzle size ranges from 100 up to 500 microns and the velocity of the jet is of the order of hundreds of meters per second. Several experimental conditions have been studied such as the axial position of the nozzle, direction, upstream pressure, number of nozzles, interaction with a packing structure (internal), as well as scale-up in order to optimize the assisting method for commercial applications.

In addition, the electrostatic charge was significantly reduced by adding a vapor to the fluidizing gas. This allowed reproducible results and promoted proper dispersion of the nanoagglomerates. The removal of electrostatic charge was crucial for getting in-situ images of the agglomerates and their size distribution in the fluidized bed by using Focused Beam Reflectance Method (FBRM) and Particle Vision and Measurement (PVM) from Lasentec. The introduced method has advantages over previous methods to characterize the size of the agglomerates, i.e., by photographing them in the splash zone

above the fluidized bed, since the agglomerates in the splash zone (region above the fluidized bed) may not be representative of the agglomerates in the bed. Experimental data related to the bed expansion is used to find the terminal velocity and to predict the size of the agglomerates by using the well-known Richardson-Zaki method. Agglomerate size predictions from fractal analysis were also compared against the experimental data.

2.2 Introduction

The study of the hydrodynamic behavior of amorphous nano-size particles in gas-solid fluidized beds has been the focus of extensive research in previous years because of the increasing importance of nano-size particles for developing new composite materials and applications. Nanoparticles are well known for their properties that differ quite significantly from those of bulk materials. Gas-solid fluidization is extensively used in industry for dispersing particulates in a gas phase for different purposes such as in reactors, modifying powder properties by coating or granulation, adsorption and desorption, drying and filtration among others. It is believed that nano-size particles will be incorporated as part of large scale industrial processes in the near future, and then large amounts of these nano-size particles would be handled and processed, in many cases using fluidization as unit a operation.

Previous research works with fluidization of nanoparticles show that many nanopowders are difficult to fluidize due to the large cohesive forces among particles given their extensive surface area. Also, it has been shown that the hydrodynamic properties of nanopowders are quite different from any of the powders classified under the Geldart criterion. For example, Group A particles such as FCC do not expand more

than 50% of the initial bed height and small bubbles are precursors of the full fluidized state. For Group B particles, characterized by bubbling, the possibility of break-up of the particles which occurs with agglomerates of nanoparticles is not considered. Group C particles do not fluidize at all, and the gas passes through the bed by channeling and spouting. As will be shown in this work, nanopowders have quite different properties than the powders used in the various experiments that Geldart performed to develop his classification. Among these key differences are: porosity, irregular surface, breakability, reagglomeration, deformation, variable density, and large bed expansion during fluidization.

2.2.1 Fluidization of Fumed Silica Nanopowders

Yao et al.¹ (2002) conducted experiments on the fluidization of fumed silica nanoparticles showing that hydrophobic nanoparticles expanded several times, from 2.5 up to 10 times their initial bed height and that hydrophilic nanoparticles expanded in the range of 1.5 up to 3 times their initial bed height. They did not explain the reason for the difference in bed expansion observed for the different nanopowders used. They also found relatively large minimum fluidization velocities for the hydrophobic nanoparticles. For example, for R812 they give a value of 1 cm/s which is 3 to 4 times the minimum fluidization velocity of FCC micron size particles. They also underestimated the void fraction corresponding to hydrophilic nanopowders. The classification of the fluidization of nanopowders into “agglomerate particulate fluidization” (APF) and “agglomerate bubbling fluidization” (ABF) was introduced; however, the definitions are not clear since they refer to Group C powders as having ABF behavior.

Zhu et al.² (2004) used a force field generated by sound in order to enhance the fluidization of Aerosil R974 fumed silica particles. They obtained a larger bed expansion and also a slight reduction in the minimum fluidization velocity due to the sound whose source, a loudspeaker, was located at the top of the bed. More recently, Guo et al.³ (2006) studied acoustic fluidized beds of two types of nanoparticles, namely 500 nm size TiO₂ and SiO₂ particles; they focused on the effects of the frequency and the intensity of the sound on the minimum fluidization velocity. In addition, Guo et al.⁴ (2006) also fluidized fumed silica nanoparticles under the influence of an acoustic field.

Nam et al.⁵ (2004) applied vibration to the fluidization of Aerosil R974 and found an increase in bed expansion and a reduction in the minimum fluidization velocity. They estimated the fluidizing agglomerate size, density and terminal velocity by using a novel method that combined the fractal structure of the agglomerate and the Richardson-Zaki criterion. However, they only verified the method by applying it to one type of nanopowder, leaving open the possibility that the model would not hold for other nanopowders. Nevertheless, they established that the fluidization of nanopowders can be enhanced by applying an external force.

A recent work on the effects of mechanical and acoustic vibration on the fluidization of fumed silica Aerosil 200 W was done by Levy et al.⁶ (2006). By adding horizontal vibrations, they reduced the minimum fluidization velocity, which was further reduced by adding acoustic vibrations.

Extending the work on fluidization of agglomerates of nanoparticles, Zhu et al. (2005) fluidized conventionally several types of nanopowders, both APF and ABF⁷. They took images of the fluidized agglomerates right at the interface, i.e., in the splash zone,

with a CCD camera to find the agglomerate size. In their analysis, the Richardson-Zaki criterion was applied to estimate the agglomerate size. They also used a correction factor for the drag force based on Happel's formula; the correction factor shows that the drag force in porous agglomerates is lower than in spheres of similar size.

Several studies involving the use of magnetic particles to enhance fluidization have been done for micron size particles. In these studies, the particles to be fluidized were magnetic or a mixture of magnetic and non-magnetic particles. When a magnetic field was applied around the fluidization column the magnetic particles would tend to line-up vertically preventing the growth of bubbles. Following a similar approach, Qun et al.⁸ (2005) used magnetic particles excited by an external oscillating magnetic field to enhance fluidization. However, these magnetic particles were much larger (2-3 mm) than the nanoagglomerates which were fluidized and remained at the bottom of the column, right above the air distributor. The electromagnetic field was provided by coils located outside the column right above the level of the air distributor. In their work, it was shown that fluidization of nanoagglomerates can be enhanced quite significantly by the use of the moving magnetic particles that break clusters of agglomerates and also hinder the formation of bubbles. The enhancement was readily observed by the larger bed expansion obtained with similar amounts of powders when comparing conventional against magnetically assisted fluidization.

Hakim et al.⁹ (2005) studied the fluidization behavior of fumed silica, zirconia and iron oxide nanoparticles at atmospheric and reduced pressures. They studied the effect of cohesive forces, liquid bridging and electrostatic; however, the procedure they used to study the liquid bridging effect is not clear since it seems there was no liquid

phase present on the fluidized agglomerates. Moreover, it will be explained in this work that adding a vapor in concentrations lower than saturation will lead to a reduction of electrostatic forces and better fluidization. To study effects of liquid bridging the fluidizing gas should carry a relative humidity of about 100%.

Agglomerates of carbon nanotubes have been also fluidized in the gas-phase¹⁰. It has been reported that they present agglomerate bubbling fluidization (ABF) behavior in a wide range of gas velocities, but they also present particulate fluidization behavior at gas velocities in the range of 0.017 to 0.038 m/s.

More recently, Wang et al¹¹ (2006) measured more accurately the fluidized agglomerates of fumed silica in the splash zone by using a high resolution CCD camera and a planar laser sheet. They measured an average agglomerate size of about 220 μm for Aerosil R974.

Fumed silica nanoparticles have been also successfully fluidized in a rotating fluidized bed¹². The centrifugal force acting on the agglomerates allowed fluidizing them at higher gas velocities without entrainment or elutriation of particles. A smooth surface and bed expansion were obtained when using APF nanopowders; however, this was not the case with ABF nanopowders which did not expand significantly due to bubbling.

As an example of the potential applications of fluidization for dispersing nanoparticles, Hakim et al.¹³ (2005) fluidized silica nanoparticles under reduced pressure conditions and vibration for coating them using atomic layer deposition (ALD) with alumina. This work indicates the potential application of fumed silica nanoparticles as catalyst support, where the catalyst can be deposited on the surface of the silica nanoparticles.

2.2.2 Removing Electrostatic Charge Effects

This work also deals with suppressing electrostatic charge in fluidized beds of nanopowders. Extensive research on the effect of electrostatic charge in the behavior of fluidized beds has been done by Park et al.¹⁴ (2002) showing that electrostatic charge was dissipated by increasing the relative humidity of the fluidizing air. Mehrani et al.¹⁵ (2005) suggested that most of the electrostatic charges generated in a fluidized bed are due to the entrained particles that leave the bed, which results in build-up of a net charge inside of the fluidized bed. During fluidization of agglomerates of nanoparticles, it has been also reported that the electrostatic forces are important and that the minimum fluidization velocity was reduced when applying an anti-static surfactant⁹ to the wall of the fluidization column.

2.2.3 Enhancement by Micro-Jet

The effects of jets in fluidized beds have been studied since the early 50's and most of the research in this field has been done with jets pointing upwards or horizontally and with nozzle sizes larger than 500 μm . For example, Rowe et al.¹⁶ (1979) had an upward jet at the center of the distributor plate; the size of the nozzle was in the range of 6.4 to 15.9 mm with superficial velocities from 1 to 70 m/s. Because of the large nozzle diameter, the gas entered the fluidized bed as bubbles. Behie et al.¹⁷ (1970) studied the momentum dissipation of jets generated by nozzle diameters that varied from 6.35 mm up to 38 mm in a fluidized bed of 0.28 m diameter. Jet velocities ranged from 15 to 90 m/s. They related the axial momentum of the jet to a modified Froude number. Clift et al.¹⁸ (1976) studied the entrainment of solid particles by gas jets pointing downwards through slotted

nozzles. A very important parameter is the penetration of the jet into the fluidized bed, a topic that has been extensively studied. For example, Zhong et al.¹⁹ (2005) focused on the variables that affect jet penetration length in a spouted fluid bed; they also compiled correlations for the jet penetration from past related works.

From the extensive research on the effects of jets on fluidized beds, it is well known that when properly designed and at high gas velocities, jets enhance fluidization by promoting turbulent mixing and breaking of agglomerates. At high gas velocities, it may happen that the penetration height of an upward jet is larger than the bed height. For this case an alternative is to have the jet pointing downwards. Several studies have focused on the position and numbers of the nozzles generating the jets. Vertical and horizontal single jets have been investigated extensively^{20, 21, 22, 23, 24, 25, 26, 27, 28, 29}. The study using a downward grid jet in a two-dimensional gas fluidized bed of sand particles³⁰ is of particular interest for the present research. It was found that the flow of the jet oscillated from one side to the other due to instabilities. The hydrodynamic behavior of fine powders in jet-fluidized beds has also been studied and modeled³¹.

An important effect produced by the micro-jets used in the present work is related to the grinding of particles. The jet attrition of catalyst particles has been investigated theoretically and experimentally^{32,33}, these studies relate the bed expansion of a fluidized bed to the generation of fines due to attrition by the jet grinding flow.

2.2.4 In-situ Measurement of Fluidized Agglomerates

To understand how agglomerates fluidize is critical due to the diverse fluidization-applications involving nanopowders that are of interest for the industry due to their particular properties that differ from bulk materials. According to the literature, there are no in-situ measurements of nanoparticle agglomerates, nor have they been visualized in the fluidized state. Several research groups have tried to find the size distributions of nanoagglomerates by different methods. These methods have focused on an imaging analysis of photographs of agglomerates in the region right above the fluidized bed, also called the splash¹¹ or disengagement zone⁹. For example, several previous works used a CCD camera coupled with an image processing system to get images of the region right above the interface of a cylindrical fluidized bed which was directly illuminated by using a laser source^{7, 8, 9}. A significant improvement to this method was the use of a squared (rather than round) fluidization column and a lens-arranged laser sheet^{11, 34}.

Other than taking photographs in the splash zone as described above, neither a method for in-situ measurement of nanoagglomerates in a gas-solid fluidized bed, or a characterization of their size distribution has been reported. In the particle sizing market, there are probes that can measure particles on-line in liquid phase suspensions such as the Focused Beam Reflectance Method (FBRM[®]) from Lasentec. This method is based on the measurement of the chord length of the particles which is translated into a population density function. Modeling of the cord length distributions of different particles has been validated³⁵. For example, this method allows for measurement of the agglomerate sizes during gravitational settling of particulate matter in wastewater treatment³⁶. Further studies on in-line monitoring of particle sizes in suspensions show that the position and

orientation of the probe are important in the determination of the particle size distribution³⁷. The FBRM technique has been compared against other particle sizing techniques such as laser diffraction and electrical sensing zone showing good agreement. The squared-weighted chord was closer to the particle distribution given by laser diffraction³⁸.

In addition to measure the chord length of the particles, several research works use a combined technique of measuring and capturing of images of the particles. Particle Vision and Measurement (PVM[®]) from Lasentec is a technique that provides in-process high resolution imaging of particles. For example, among recent work, droplet size distributions in an oil-water dispersion were measured by using in situ video microscopy with the PVM and comparing the results by direct sampling. The use of these techniques for measuring the agglomerate size distribution in a gas fluidized bed of nanoparticles will be described below.

2.2.5 Modeling of Agglomerate Sizes

The traditional Richardson-Zaki method estimates the particle size by finding the terminal velocity from plots of the void fraction, obtained from the fluidized bed expansion, and the superficial gas velocity³⁹. A modified theory, including fractal analysis due to the structure of the agglomerate, has also been suggested and compared with experimental measurements in the splash zone^{40, 5}. Of special interest to this work is the Richardson-Zaki index (or exponent) which has been shown to depend on Reynolds number; however, in some cases, it can fall outside the theoretical range and is apparently larger than expected⁴¹.

Important characteristics of the agglomerates to consider for modeling are the fact that they are highly porous and have a rough surface. These characteristics can change the drag force when compared to a perfect sphere. Several interesting articles focusing on the effects of porosity and aggregation on the drag force are helpful when analyzing the fluidization of nanoagglomerates^{42, 43, 44}.

2.2.6 A New Approach for Enhancing Fluidization of Agglomerates of Nanoparticles

In this work, a new method for enhancing fluidization of agglomerates of nanoparticles is introduced. This method is based on the use of jets generated from micro-nozzles pointing downwards at close distance to the gas distributor plate which can result in bed expansions of up to 50 times the initial bed height for Aerosil R974. It also allows for the conversion of ABF type nanopowders into APF powders such as, for example, Aerosil 90. Aerosil 90 is very difficult to fluidize conventionally, but when it is exposed to the action of a reverse jet, it expands similarly to Aerosil R974, an APF powder. The micro-nozzles, in the range of 127 up to 508 μm , are used to enhance the fluidization of agglomerates of nanoparticles. Upward and downward jets were tested; it was found that downward jets enhance fluidization better when located close to the distributor plate at the bottom of the column. Gas velocities in the jets are of the order of several hundreds of meters per second while the total superficial velocity in the fluidized bed is in the order of a few centimeters per second. As a result of the jets, fluidized bed expansion is increased several times and the quality of fluidization is much better. The onset of bubbling is also delayed due to the better dispersion of the nanopowder in the gas phase.

Also, in the current research work, an organic vapor, ethyl alcohol, has been used to reduce electrostatic charge during fluidization of agglomerates of nanoparticles. Conventional fluidization is greatly improved with the use of the alcohol as an additive in the fluidizing nitrogen gas, allowing for better reproducibility of the experimental results. The vapor has been added by bubbling of the fluidizing gas through the liquid (alcohol); it is important to note that the amount of vapor is much below saturation, i.e., the vapor pressure at the temperature of the experiment.

No previous work has been reported on the use of FBRM and PVM instruments (Mettler Toledo, Lasentec) for the in-situ determination of agglomerates sizes and images in gas-solid fluidized beds of nanopowders. By removing the electrostatic charge, these instruments can be used to characterize agglomerates in-situ. Since the images are obtained by immersing the instruments into the fluidized bed and not in the splash zone, a more representative agglomerate size distribution is obtained.

In addition, the fluidizing agglomerate size is estimated by using the traditional Richardson-Zaki method, coupled with a fractal analysis. A discussion and comparison of the experimental data and the theoretical predictions are given. Also, the standard method by which minimum fluidization is found by when the pressure drop plateaus has been revised, it was found that fluctuations in the pressure drop exist well above the reported minimum fluidization velocities. These fluctuations are reduced by using the assisting methods and the removal of electrostatic charge. The fluctuations on pressure drop may mean that the Blake-Kozeny equation may not apply for a non-fluidized bed of nano-particles; moreover, it is believed that micro-channels exist instead of a fixed packed bed condition at gas velocities lower than the minimum fluidization velocity.

2.3 Experimental Methods

A schematic diagram of the main experimental setup is shown in Figure 2.1. Dry nitrogen was used as fluidizing gas supplied by a compressed cylinder with an initial pressure of around 2500 psig. Two diaphragm pressure regulators were used to give a low pressure line, at about 20 psig and a medium pressure line, at about 120 psig. The low pressure line fed gas to the column through the distributor plate and was called “primary flow.” The medium pressure line supplied gas for the nozzle or nozzles and was called, “secondary flow or injection flow.” Part of the primary flow is bubbled through liquid contained in a tank with the purpose of adding vapor to the dry gas in a controlled manner. The liquid contained in the tank is either water, ethyl alcohol or a mixture. There is a needle valve that controls the primary flow. The secondary flow is controlled by adjusting the pressure with the regulator, no valve is necessary because the nozzle restricts the flow.

The fluidization column is made of cast acrylic plastic and it has an internal diameter of 3 inches with a wall thickness of 0.25 inches. The length of the column can be changed; in some cases, when the bed of powder does not expand significantly, the height of the column is about 5 feet, but when the powder expands several times its initial bed height, the bed height is increased up to 10 feet by adding another tube on top of the main column.

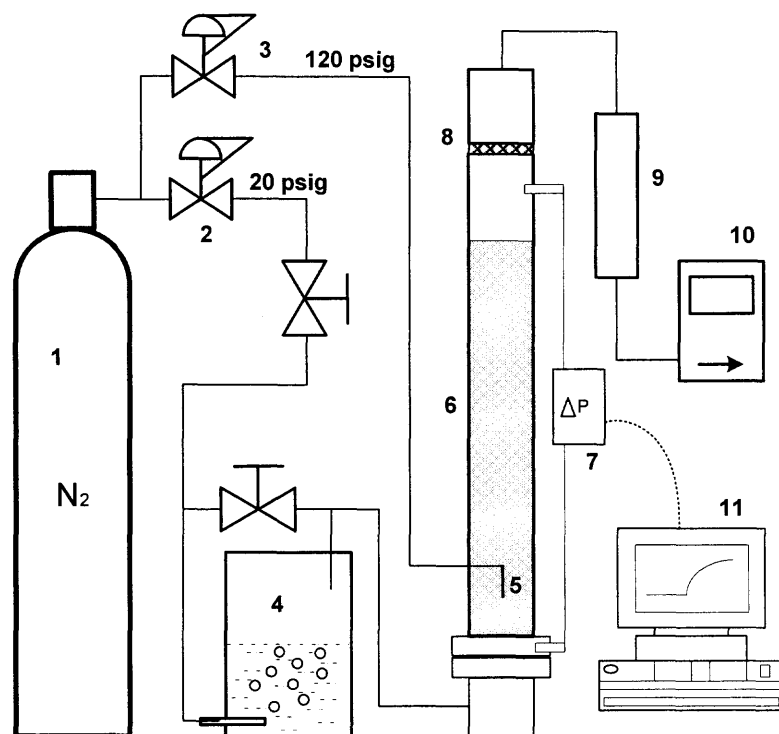


Figure 2.1 Schematic diagram of the experimental setup. (1) compressed dry N₂ cylinder, (2) Pressure regulator for low pressure, (3) pressure regulator for high pressure, (4) tank for liquid, (5) micro-nozzle, (6) fluidization column, (7) differential pressure transmitter, (8) pre-filter, (9) HEPA filter, (10) flowmeter and (11) computer.

Pressure taps are located right above the distributor plate and before the pre-filter. The taps are connected to a highly accurate and sensitive differential pressure transmitter able to measure pressure drops of the order of a few thousands of an inch of water. Several differential pressure transmitters, with ranges from 0 to 0.5, 0 to 1 and 0 to 5 inches of water, were used (Cole-Parmer 68071-04, -06, -10). Pressure transmitters were connected to a digital display panel (Cole-Parmer 93284-02) which was linked to a computer through a RS-232 cable for data recording. MeterView (Cole-Parmer 93284-26) software was used for communication between the computer and the display.

A sintered metal plate located at the bottom of the column uniformly distributes the primary flow. The plate has 20 micron orifices with an open area of about 40 % and a

thickness of a few millimeters (Mott Corporation 1100-10-12-.062-20-A Sheet 316 LSS). At the top of the fluidization column there is a pre-filter that consists of a woven mesh with 20 microns apertures. A HEPA capsule (Pall Corp. PN: 12144) is connected to the top of the fluidization column in order to remove entrained small particles. Two mass flowmeters measure the flow exiting the column at ambient pressure; this means that a pressure correction factor is not needed. The flowmeters have ranges from 0 to 5 and from 0 to 20 liters per minute (Omega: FMA1818 & FMA 1824).

The properties of the nanopowders used in the experiments are listed in Table 2.1. It is important to note that APF and ABF correspond to a classification according to the fluidization behavior¹ of the nanopowders, i.e., agglomerate particulate fluidization (APF) and agglomerate bubbling fluidization (ABF) respectively. The hydrophobicity of the Aerosil R974 is due to a specific surface treatment of Aerosil 200 with DDS (dimethyldichlorosilane). Regarding the source of the nanopowders, there are two types: commercial grade, i.e., powder delivered to customers which is usually compacted, and process grade, where the nanopowder is taken directly from the process. Specific surface areas, as reported by the manufacturer, have been found by using the BET method according to DIN 131 and the tapped density is measured by applying vibration to a standard volume according to ISO787/11. In all the experiments reported in this work, the nanopowders have been sieved for the purpose of removing clusters of agglomerates larger than 850 μm .

Table 2.1 Nanopowders Used and Their Properties

Brand	Type	Property	Fluidization behavior*	Source	Material	Primary particle size, [nm]	Surface area, [m ² /g]	Tap density, [kg/m ³]**
Aerosil	R974	Hydrophobic	APF	comercial	SiO ₂	12	170	50
	200	Hydrophilic	APF	comercial	SiO ₂	12	200	50
	90	Hydrophilic	ABF	comercial	SiO ₂	20	90	80
	90	Hydrophilic	APF	process	SiO ₂	20	90	80
Aeroxide	TiO ₂ P25	Hydrophilic	ABF	comercial	TiO ₂	21	50	130
	TiO ₂ P25	Hydrophilic	ABF	process	TiO ₂	21	50	130
	Alu C	Hydrophilic	ABF	comercial	Al ₂ O ₃	13	100	50

* APF: Agglomerate particulate fluidization, ABF: Agglomerate bubbling fluidization

** Density given by Degussa.

Nozzles of different sizes were used in the experiments. The smaller size was 127 μm and the largest 508 μm (Varian 1/16" x 0.010", 0.020", 0.007", 0.005" ID x 5 cm SS Tube). Depending on the experiment, they were located at different levels of the fluidization column. Usually, the nozzle was pointing downwards and at about 4 inches above the distributor plate. If one nozzle was used, it was located at the center of the column, and when two or more nozzles were used, they were located symmetrically with about a one inch separation between them. The nozzles were welded to copper tubing that connected them to the pressure regulator supplying the "secondary flow" at medium pressure. Figure 2.2 shows some of the different ways the nozzles were located in the fluidization column.

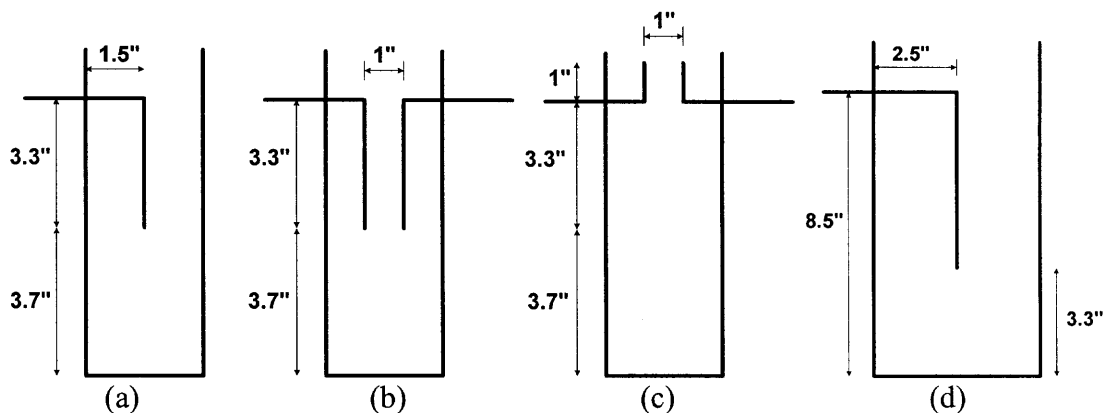


Figure 2.2 Detail of the locations of the nozzles inside the fluidization column, the bottom line is the gas distributor plate. (a, b, c) corresponds to the 3 inches ID column, and (d) corresponds to the 5 inches ID column for scaling up the experiments.

2.3.1 Experiments Related to the Reduction of Electrostatic Charge

In a separate set of experiments, the impact of electrostatic charges on the fluidization of nanopowders was evaluated. The electrostatic charges were generated by a phenomenon similar to triboelectrification due to the different dielectric characteristics of the high surface area particles in combination with their movement during fluidization. In experiments with electrostatic charge, the powder was fluidized with dry nitrogen, i.e., no gas was bubbled through the liquid in the tank; hence, there was some electrostatic charge generated in the fluidized bed. Fluidization data such as the fluidized bed pressure drop and height were recorded. To reduce or eliminate most of the electrostatic charge, a vapor was added by bubbling of the fluidizing gas through water or ethyl alcohol held in a tank. Gas containing the vapor was passed through the bed of powder at low flow and for a long enough time to allow all of the powder to be exposed to the vapor. After 20 to 30 minutes, fluidization was started and data, such as bed height and pressure drop, were recorded and compared to the data obtained using dry nitrogen (no addition of vapor). It is important to note that the humidity level in the fluidizing gas was lower than 50%

relative humidity, and the concentration of alcohol was about 1%. The presence of the electrostatic charges make difficult to achieve repeatability in the fluidization data; for this reason, most of the experiments were done under reduced electrostatic charge conditions, i.e., using alcohol, with the exception of the experiments related to the residence time distribution (RTD) studies and adsorption and desorption of moisture shown in Chapter 3.

2.3.2 Experiments Focusing on the Effects of a Jet in the Presence of a Fluidization Column Internal and in the Absence of a Gas Passing Through the Distributor Plate

In experiments involving the use of a sieve tray or a mesh as an internal in the fluidization column, a nozzle was used pointing downwards towards the grid. The sieve tray was located at about 12 inches above the distributor plate, and the nozzle was located 4 inches above the sieve trays. Nanopowder was fed from the top of the column and at the beginning most of it was held by the sieve tray. Details of the trays used as internals are shown in Figure 2.3. The grid (sieve tray) had orifices of hexagonal shape, the thickness of the wire was of about 1.5 mm and the dimensions of an orifice were 4 mm x 8 mm. A second tray made of perforated acrylic plastic plate was also used is shown in Figure 2.3 (b); the orifices had an internal diameter of about 10 mm. The thickness of the plate was about 5 mm. Figure 2.3 (c) shows the location of the grid and the nozzle with respect to the gas distributor plate at the bottom of the fluidization column. Figure 2.4 (a) and (b) show images of the grid and the location of the nozzle respectively.

In a fluidization column, the gas distributor plate located at the bottom provides uniform flow of gas for properly dispersing the particles. In some industrial applications,

it is not possible to have a distributor installed in the fluidization column; therefore, the fluidizing gas is injected at some point at the bottom of the fluidization column and it is not properly distributed. To demonstrate that jet flows can improve fluidization when there is a poor distribution of the fluidizing gas, flow through the distributor plate was suspended and it was fed to the column through the pressure tap located right above the distributor plate. The nozzle was again located at 4 inches from the distributor plate.

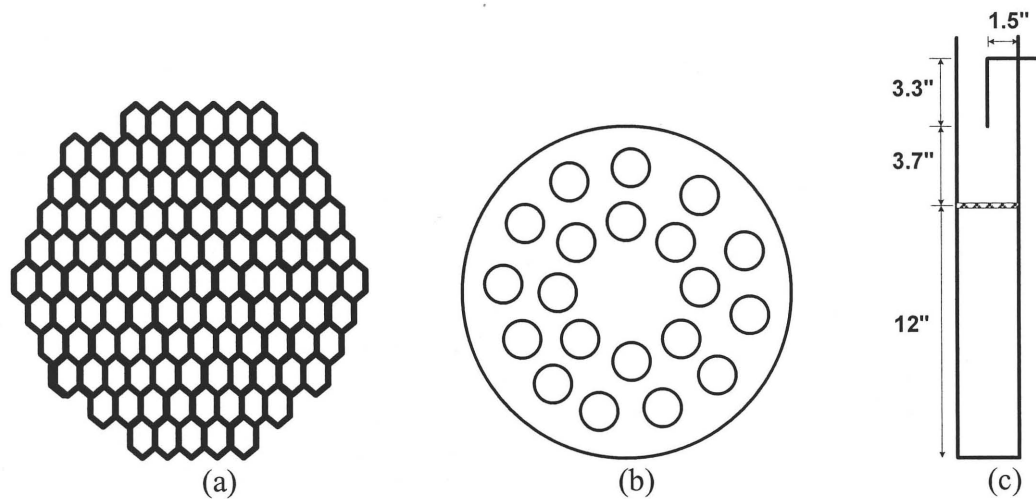


Figure 2.3 Detail of the trays inserted in the fluidization column as internals. (a) grid, hexagonal shape; (b) Orifices internal diameter of 10 mm, (c) diagram showing the location of the grid (at 12 inches from the distributor plate) and the nozzle.

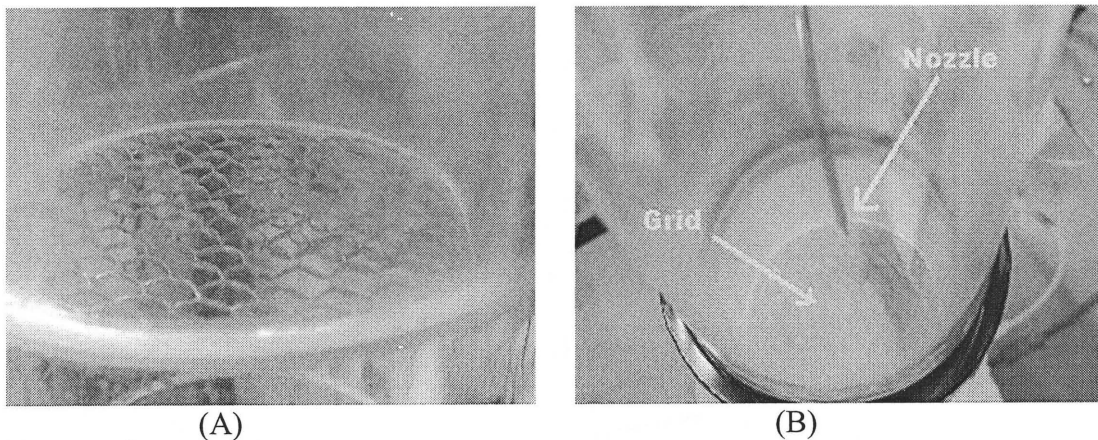


Figure 2.4 Images showing the grid (A), and the location of the nozzle above the mesh (B). The mesh is used as an internal to break down bubbles and to slow down the downward flow of nanopowder.

2.3.3 Experiments Focusing on the Characterization of the Agglomerate Size in a Fluidized Bed

For the in-situ measurement of the agglomerate sizes in a fluidized bed and the capture of agglomerate images, the FBRM and PVM systems from Lasentec were used. A fluidization column made of acrylic plastic with an internal diameter of 3 inches and a length of about 6 feet was specifically modified for the insertion of the probes. Two lateral ports were made in the fluidization column, both having an internal diameter of about 27 mm. The ports were located at about 17 inches and 44 inches above the gas distributor plate as shown in Figure 2.5.

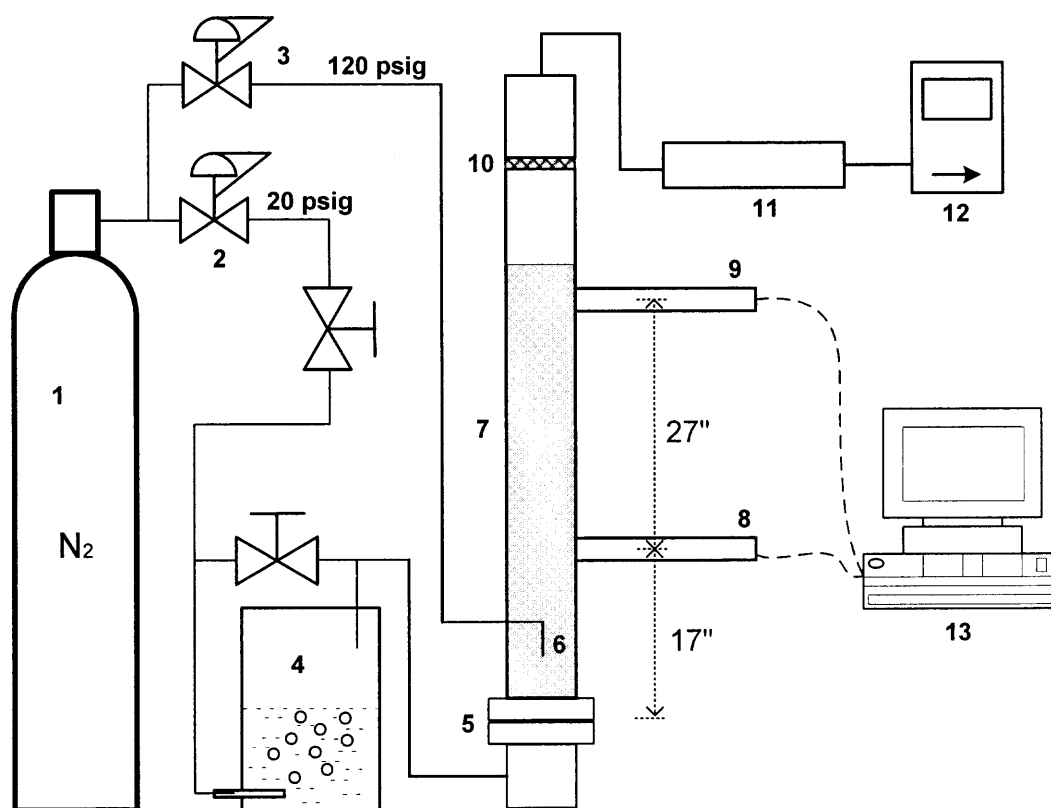


Figure 2.5 Schematic showing the setup used for the in-situ measurement of agglomerates of nanoparticles in a fluidized bed. (1) compressed dry N₂ cylinder, (2) pressure regulator for low pressure, (3) pressure regulator for high pressure, (4) tank holding alcohol, (5) sintered metal plate-distributor, (6) micro-nozzle, (7) fluidization column, (8) location of the FBRM probe, (9) location of the PVM probe, (10) filtering mesh, (11) HEPA filter, (12) flowmeter and (13) computer for image and data acquisition.

The Focused Beam Reflectance Measurement (FBRM) D600L probe has 19 mm in internal diameter and a length of 406 mm, the rotation of its incorporated laser is air driven. The Particle Vision and Measurement (PVM) V700S probe has a diameter of 25 mm and a length of 318 mm, its magnification can be adjusted from 5x to 10x and its field of view is 1.65 x 1.24 mm (640 x 480 pixels, 2.5 $\mu\text{m}/\text{pixel}$). Electrostatic charges were removed from the fluidization experiments as explained in a previous section. Figure 2.6 shows that when the alcohol vapor is used for removing the electrostatic charges, no powder covers the tip of the probe which allows clear images and proper measurement of the agglomerate sizes. Agglomerates of Aerosil R974 and Aerosil 90 in a conventional and jet assisted fluidized bed were in-situ measured with the probes described above. These results were used to compare with the estimations of the model based on the Richardson-Zaki equation that predicts agglomerate sizes.

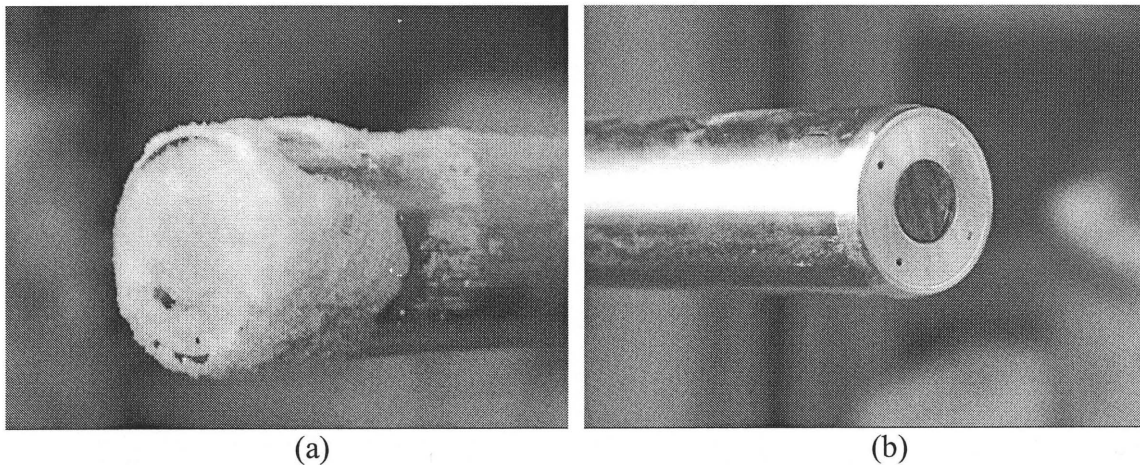


Figure 2.6 Images showing the tip of the PVM probe, (a) covered with nanopowder due to electrostatic charge, (b) without nanopowder when removing the electrostatic charge from the bed by using alcohol vapor.

2.4 Results and Discussion

The use of non-dimensional variables is useful for purposes of comparison between experimental results; hence, a non-dimensional bed height and a non-dimensional pressure drop are used frequently in this section. The non-dimensional bed height is obtained by dividing the actual bed height by the initial bed height of the bed of nanopowder at zero flow conditions, and when the powder has just been loaded into the fluidization column. Similarly, the non-dimensional pressure drops are obtained by dividing the actual pressure drop by the apparent weight of the bed (weight of powder divided by cross-sectional area of the column).

2.4.1 Effect of Electrostatic Charge on the Fluidization of Agglomerates of Nanoparticles

The effects of electrostatic charges in a fluidized bed of agglomerates of nanoparticles are quite significant. These nanopowders have an extremely large surface area which leads to the generation of electrostatic charges much larger than observed for micron size particles. As explained in the experimental methods, the fluidization column was made out of acrylic plastic. When exposed to friction, i.e., when the particles rub against the wall, electrostatic charge is generated by the triboelectric effect; however, it has been also observed that agglomerates of nanoparticles show electrostatic charges even before being placed in the fluidization column, i.e., as received and during sieving. It has also been reported that electrostatic charges in the agglomerates are quite significant during their production process.

Figure 2.7 shows a comparison of the hydrodynamics characteristics, bed expansion and pressure drop, of fluidized beds before and after adding alcohol vapor to

the fluidizing gas to reduce electrostatic charge. In these experiments, about 15.2 grams of Aerosil[®] 200 sieved below 850 microns were fluidized. It can be seen that when the electrostatic charge is not reduced, i.e., the fluidizing gas is nitrogen only, the maximum pressure drop across the fluidized bed is surprisingly only about 0.3 times the apparent weight of the powder. This means that about 70% of the powder is sticking to the wall of the column or on the distributor plate. An immediate consequence of having powder sticking to the wall is a lower bed expansion. However, after passing gas with a small amount of alcohol vapor through the bed of nanopowder for about several minutes and then fluidizing the powder, pressure drop shows that most of the powder is suspended in the gas phase, about 90 %, leading to a larger bed expansion.

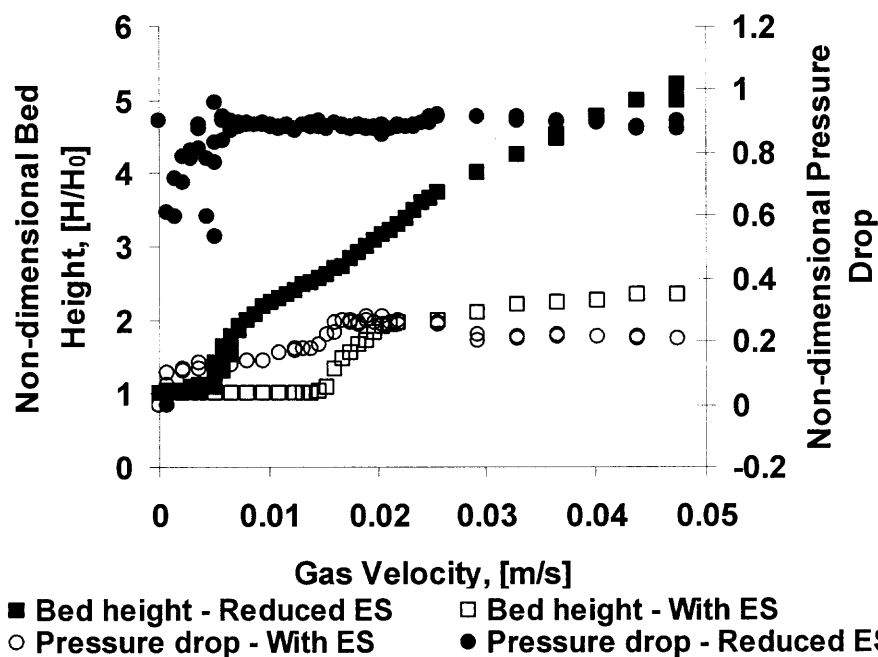


Figure 2.7 Comparison of the non-dimensional fluidized bed pressure drop and bed height during evaluation of the effects of electrostatic charge on fluidization of nanoagglomerates of Aerosil[®] 200.

Even though only data on the fluidization of Aerosil[®] 200 is shown, a similar behavior could be seen for other nanopowders such as Aerosil[®] 90. It also has been observed that the electrostatic charge builds up more in hydrophilic nanopowders making them extremely difficult to fluidize as shown in the fluidization data of Aerosil[®] 200. In order to reduce the impact of electrostatic charge in our results and calculations, all our fluidization experiments have been done with the addition of alcohol vapor unless otherwise specified.

A more clear evidence of the benefits of using alcohol for removal of electrostatic charge can be seen in Figure 2.6, where the nanopowder is sticking to the probe in the presence of electrostatic charges (a) and is not sticking to the probe when the electrostatic charges have been removed (b).

2.4.2 Hydrodynamic Characteristics of Conventional and Jet Assisted Fluidization of APF Nanopowders Aerosil[®] R974 and Aerosil[®] 200

Aerosil[®] R974 has been widely used in fluidization experiments in previous research works^{1, 2, 5, 7, 8, 12}; for that reason, the experimental results obtained with this nanopowder are shown for comparison purposes. Three different masses of Aerosil[®] R974 - 9.5, 13.3 and 20 grams - were fluidized conventionally and with jet assistance. Figure 2.8 shows the non-dimensional bed expansion plotted against gas velocity for the fluidization of the three different amounts of nanopowder. It is important to note that the non-dimensional bed heights are the same regardless of the amount of fluidized powder⁴⁵.

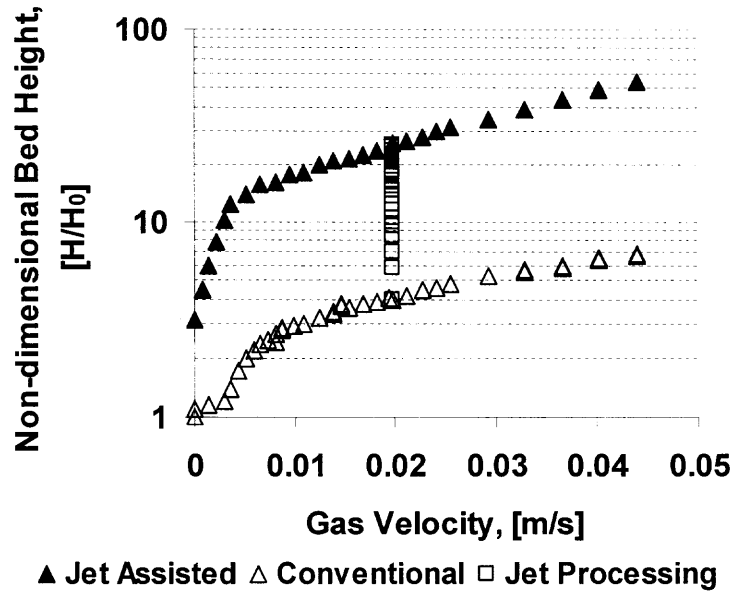


Figure 2.8 Comparison of the reduced fluidized bed height with respect to gas velocity of conventional and jet assisted fluidization.

The increase in bed height during the jet processing at a constant gas velocity (squares) of about 2 cm/s is also shown in Figure 2.8. The resulting expansion of the bed, when using the jet as an assisting method, is quite impressive. For example, during conventional fluidization and at a gas velocity of 4 cm/s, the bed height has expanded six fold; however, when using the jet assistance, the bed height is about fifty times the initial bed height. This huge bed expansion is one of the reasons why the ordinates are plotted in logarithmic scale. Another characteristic observed during the experiments and not clearly seen in the plot is that the conventionally fluidized bed of Aerosil[®] R974 starts to bubble at velocities equal or higher than 3 cm/s. When the jet assistance is used, bubbling is suppressed and is not observed up to 4.5 cm/s.

Figure 2.9 shows the plot of the non-dimensional differential pressure drop across the fluidized bed during conventional and jet assisted fluidization for the three different amounts of Aerosil[®] R974 used. Note that the non-dimensional pressure drops of

conventionally fluidized beds are always below one, indicating that not all the powder is being suspended by the gas; on the other hand, the non-dimensional pressure drops are very close to unity when jet assistance is used indicating that almost the entire mass of powder is suspended by the gas flow. It is well known that a plot of the differential pressure drop against gas velocity is used to find the minimum fluidization velocity (U_{mf}). These are shown in Figure 2.9 by the vertical lines at the points at which the pressure drop plateaus. From Figure 2.9, the U_{mf} corresponding to conventional fluidization is about 0.005 m/s (0.5 cm/s), and it is reduced to 0.0025 m/s (0.25 cm/s) when the jet assistance is used. In addition, at gas superficial velocities higher than 0.03 m/s (3 cm/s), it can be seen that the pressure drop starts to decrease for the jet assisted fluidization case; this may be due to the fact that there is a large bed expansion and more powder is in contact with the wall of the column. At these velocities, entrainment exists but is not large enough to alter the pressure drop by that magnitude.

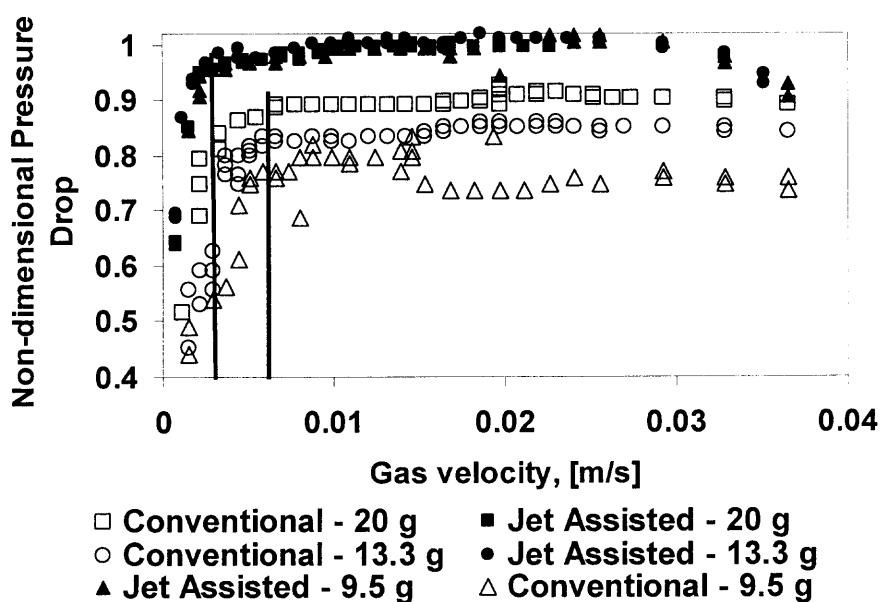


Figure 2.9 Non-dimensional pressure drop as function of gas velocity during fluidization of different amounts of Aerosil® R974

Figure 2.10 shows the changes in non-dimensional bed height with respect to time during jet processing of the different amounts of Aerosil[®] R974. In this plot, the initial bed height used as reference corresponds to the bed height of conventionally fluidized powder at the superficial gas velocity of the jet processing, as given in the legend of the figure. As expected, the time required to process the powder is proportional to the amount of powder and the superficial gas velocity at which the jet processing is done.

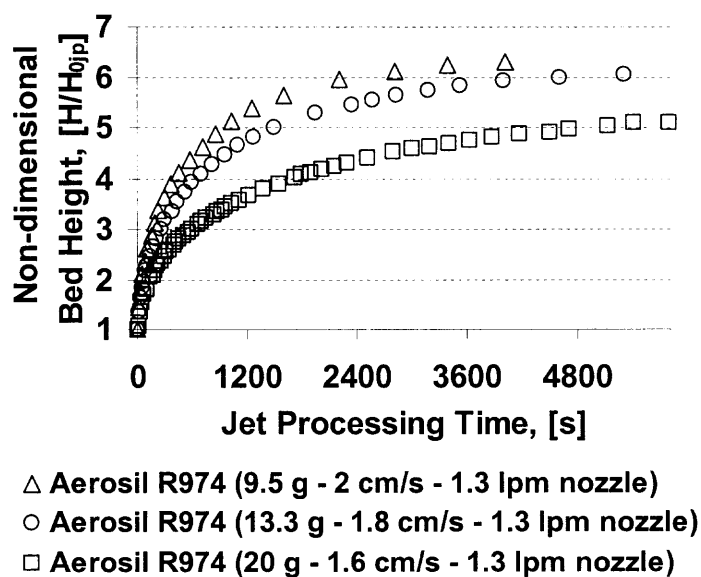


Figure 2.10 Bed expansion during jet processing plotted against time.

Similarly as was done for Aerosil[®] R974, Aerosil[®] 200 was fluidized conventionally and with jet assistance. It is important to note that Aerosil[®] R974 is the hydrophobic version of Aerosil[®] 200; however, as shown in Figure 2.11, Aerosil[®] 200 expands less than Aerosil[®] R974. Nevertheless, there is a large bed expansion due to the jet assistance; for example, at 0.04 m/s (4 cm/s) the fluidized bed height of Aerosil[®] 200 is about 11 times its initial bed height at zero flow. During conventional fluidization, Aerosil[®] 200 only expands up to 4.5 times its initial bed height.

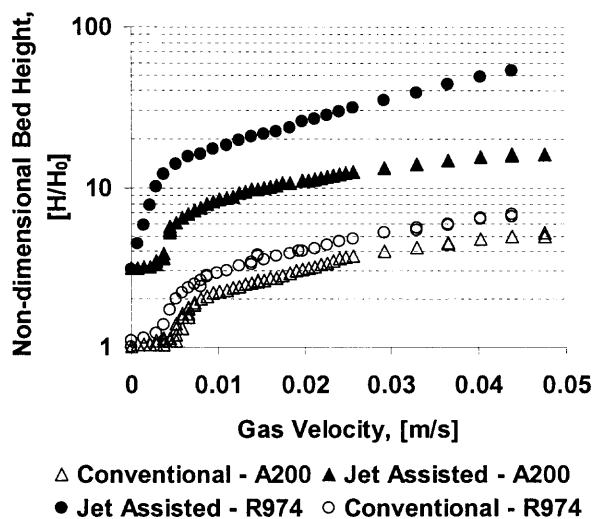


Figure 2.11 Comparison of the reduced bed height of fluidized beds of Aerosil[®] 200 and Aerosil[®] R974

Regarding the pressure drop of the fluidized bed of Aerosil[®] 200, Figure 2.12 shows that when using the jet assistance more powder is suspended by the gas flow. The minimum fluidization velocity for both conventional and jet assisted fluidization is about .0065 m/s (0.65 cm/s); thus, jet assistance does not seem to change significantly the minimum fluidization velocity. Further analysis on the pressure drop readings will be shown below to explain this phenomenon.

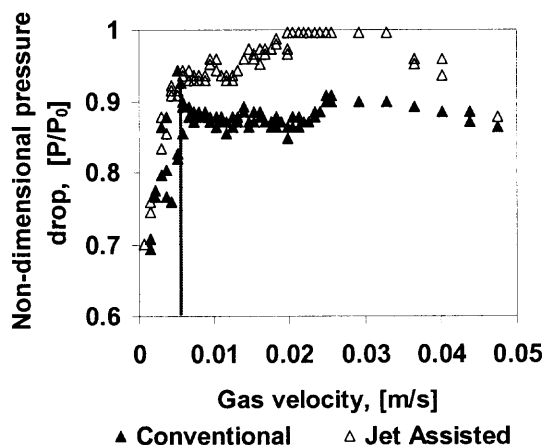


Figure 2.12 Non-dimensional pressure drop as function of gas velocity during fluidization of Aerosil[®] 200

Another type of nanopowder that shows an APF behavior is Aerosil 90 when it is taken directly from the process; this nanopowder is called “Raw” Aerosil 90, and its fluidization characteristics are presented in Figure 2.13 and Figure 2.14, which show bed expansion and pressure drop, respectively.

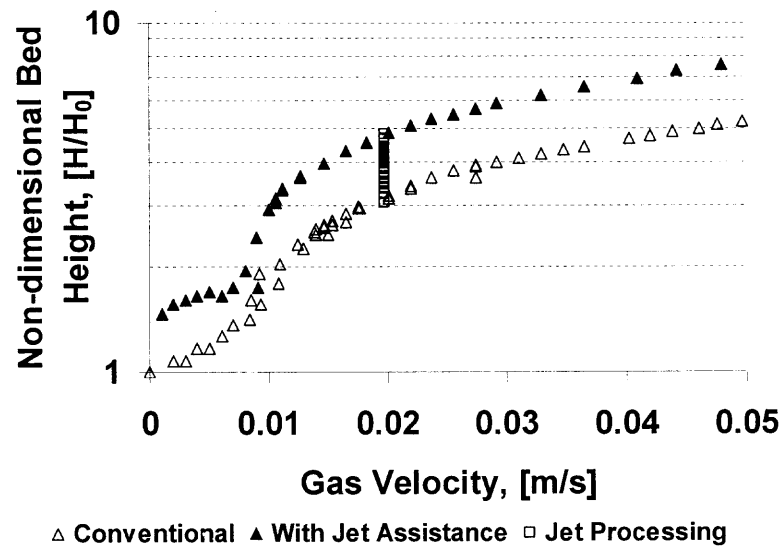


Figure 2.13 Comparison of the non-dimensional bed height for fluidized beds of “Raw” Aerosil 90, an APF nanopowder (material taken directly from the process) with and without jet assistance.

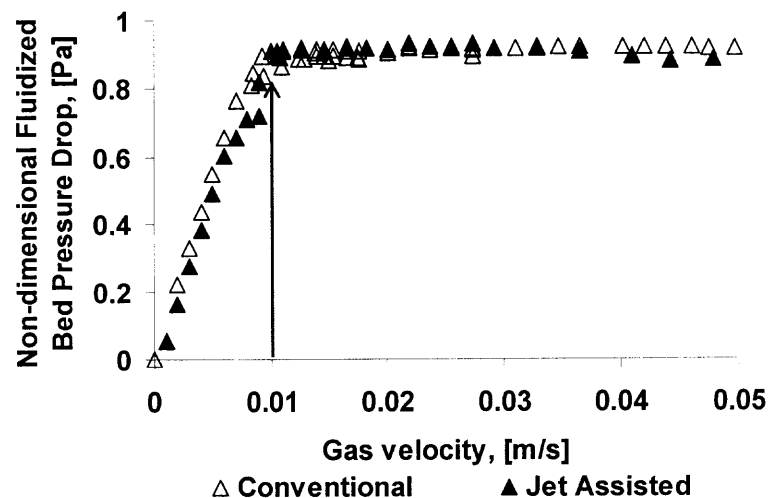


Figure 2.14 Non-dimensional pressure drop as a function of gas velocity of conventional and assisted fluidization of “Raw” Aerosil 90 (an APF nanopowder).

2.4.3 Hydrodynamic Characteristics of Conventional and Jet Assisted Fluidization of ABF Nanopowders Aerosil[®] 90, Aeroxide[®] Alu C and Aeroxide[®] TiO₂ P25

ABF nanopowders are characterized for being very difficult to fluidize, for having a limited bed expansion and for developing bubbles. Figure 2.15 shows the non-dimensional bed expansion corresponding to the conventional fluidization of ABF nanopowders under reduced electrostatic charge conditions. The amounts and types of nanopowders used in these experiments are as follows: 18 grams of Aerosil[®] 90, 22 grams of Aeroxide[®] Alu C and 60 grams of Aeroxide[®] TiO₂ P25. The nanopowders were sieved to get agglomerates under 850 μm (Aeroxide Alu C and Aerosil 90) and 500 μm (Aeroxide TiO₂ P25). When the superficial gas velocity is increased above the minimum bubbling velocity (U_{mb}), the fluidized bed does not expand anymore and the bed height remains constant. Note that Aerosil 90 nanopowder used in our experiments was relatively non-compacted and recently supplied by Degussa Corp. at the time of experiments. Other experiments with Aerosil 90 that was stored for a long period of time resulted in a more difficult fluidization with a bed expansion of no more than 1.5 times the initial bed height⁷.

Figure 2.16 shows the fluidized bed heights as function of superficial gas velocities corresponding to jet assisted fluidization of the three ABF nanopowders. It can be seen that Aerosil 90 and Aeroxide Alu C show a bed expansion that is similar to APF type behavior characterized by an almost linear increase in bed height with gas velocity. Aeroxide TiO₂ P25 expands up to 6.5 times its initial bed height but the bed height remains constant at superficial gas velocities larger than 0.025 m/s (2.5 cm/s) which can be considered to be the minimum bubbling velocity (U_{mb}).

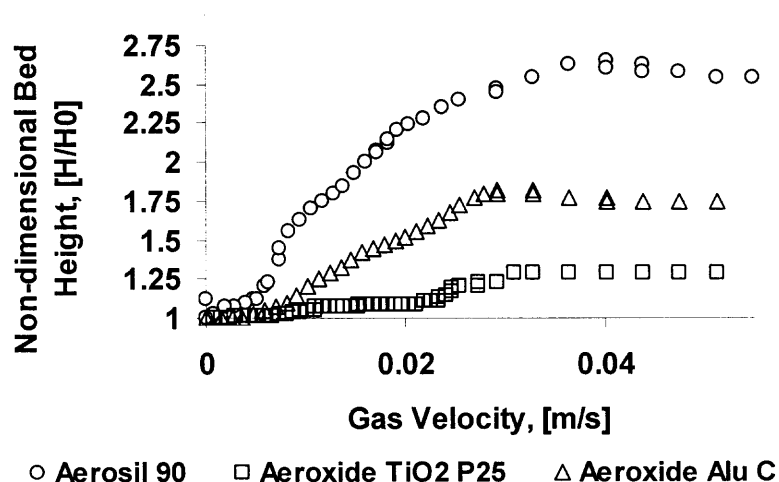


Figure 2.15 Non-dimensional bed expansion as function of gas velocity for conventional fluidization of ABF type nanopowders.

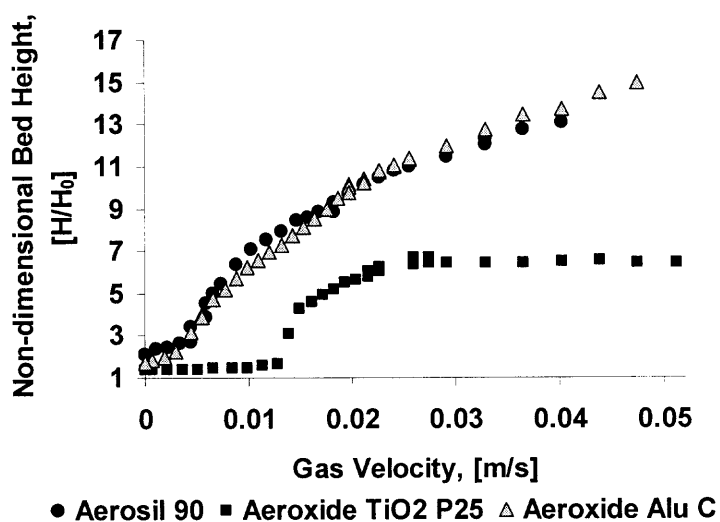


Figure 2.16 Non-dimensional bed expansion vs. superficial gas velocity of the jet assisted fluidization of ABF nanopowders.

The corresponding non-dimensional pressure drops plotted against superficial gas velocities are shown in Figure 2.17, Figure 2.18 and Figure 2.19 for Aerosil 90, Aeroxide AluC and Aeroxide TiO₂ P25, respectively; these plots show that whenever jet assistance is used, more powder is suspended by the gas phase since the pressure drop is close to the apparent weight of the powder, i.e., a non-dimensional pressure drop equal to unity. In

addition, the minimum fluidization velocities are shown by the vertical lines. It is important to note that Aerosil 90 and Aeroxide Alu C agglomerates are less dense than Aeroxide TiO₂ P25. Because of this, the maximum non-dimensional pressure drop is closer to unity for the lighter nanopowders when compared to heavier ones such as Aeroxide TiO₂ P25. Also, if the standard definition of the minimum fluidization velocity is applied, its value is reduced for jet assisted fluidization of lighter agglomerates (A90, Alu C); this does not occur for Aeroxide TiO₂ P25; in fact, the minimum fluidization velocity appears to be higher when jet assistance is used.

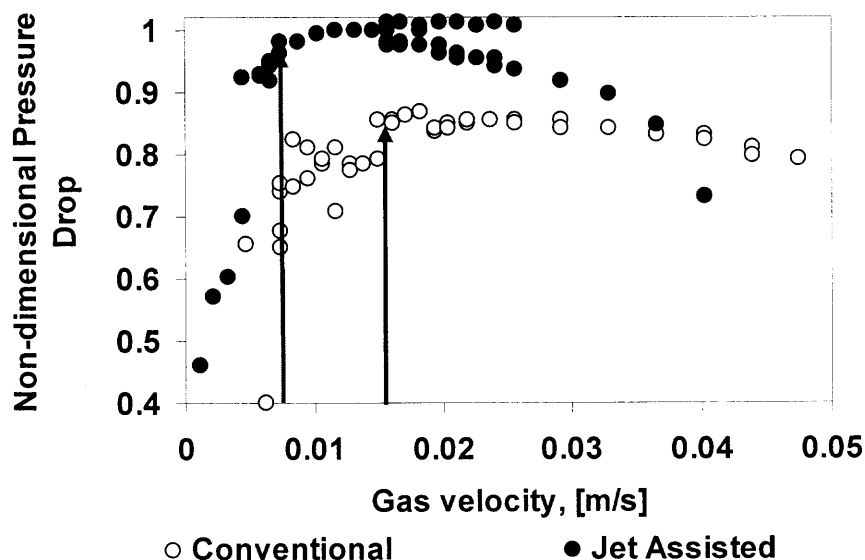


Figure 2.17 Non-dimensional pressure drop as function of gas velocity corresponding to the fluidization of Aerosil 90.

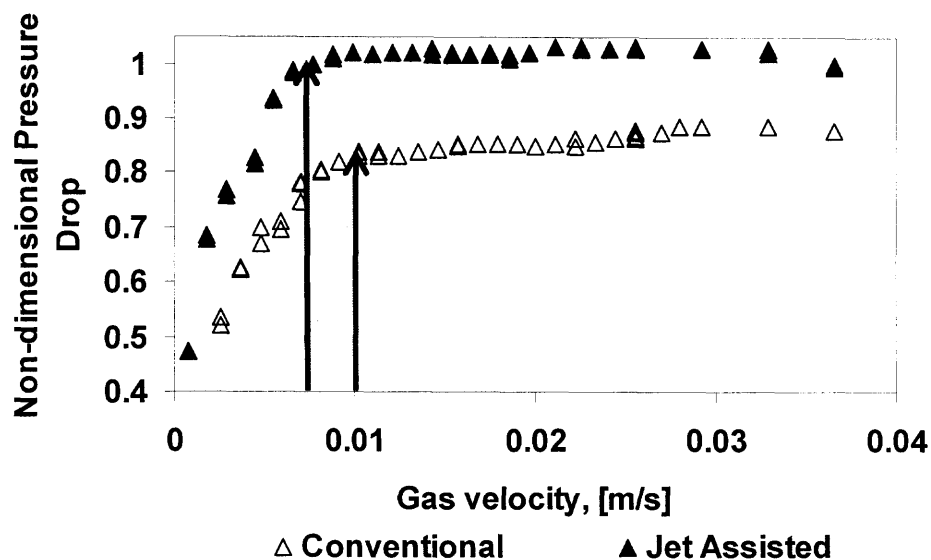


Figure 2.18 Non-dimensional pressure drop as function of gas velocity corresponding to the fluidization of Aeroxide Alu C.

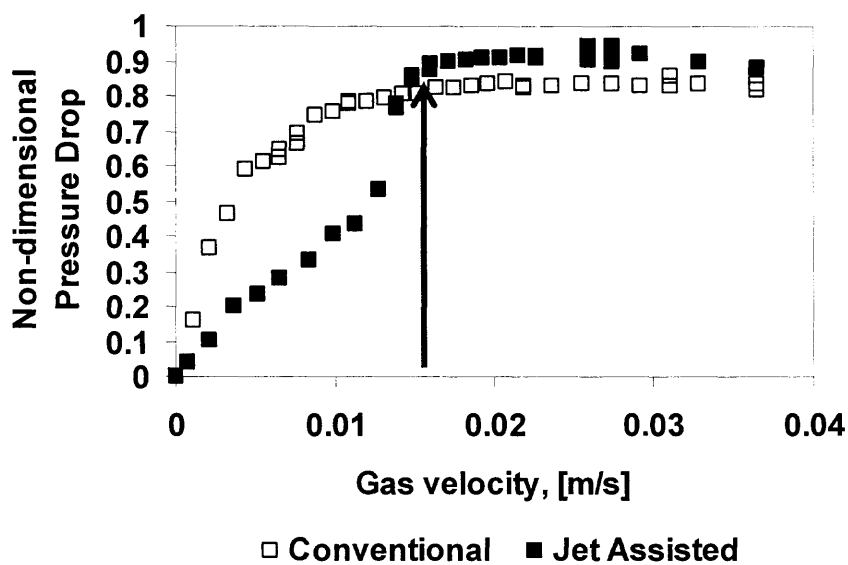


Figure 2.19 Non-dimensional pressure drop as function of gas velocity corresponding to the fluidization of Aeroxide TiO₂ P25.

Table 2.2 summarizes the hydrodynamics characteristics of the fluidization experiments with nanopowders. It can be seen that in most of the cases, the minimum fluidization velocities have been reduced when comparing the conventional against the jet assisted cases; in addition, the fluidized bed heights have increased for all cases.

Table 2.2 Summary of the Hydrodynamic Characteristics of Conventional and Jet Assisted Fluidized Beds

Brand	Type	Mass g	ρ_{b0} kg/m ³	Conventional			Jet Assisted				Height increase %
				Initial bed Height H ₀ , [m]	Bed height @ 3 cm/s H, [m]	Umf cm/s	ρ_{b0} kg/m ³	Initial bed Height H ₀ , [m]	Bed height @ 3 cm/s H, [m]	Umf cm/s	
Aerosil	R974	9.45	40.8	0.051	0.279	0.65	13.2	0.157	1.763	0.35	531
	R974	13.3	38.3	0.076	0.411	0.51	13.4	0.218	2.451	0.25	496
	200	15.7	29.5	0.117	0.470	0.58	9.4	0.366	1.560	0.5	232
	90	18.0	29.9	0.114	0.249	1.5	16.6	0.239	1.283	0.085	415
	Raw 90*	21.2	17.8	0.260	0.889	1.2	16.6	0.279	1.524	1.05	71
Aeroxide	TiO ₂ P25	60	105.5	0.114	0.142	1.5	75.4	0.160	0.737	1.6	418
	Raw TiO ₂ P25*	61.2	81.3	0.165	0.499	2.6	71.7	0.188	0.699	2.5	40
	Alu C	22	46.0	0.107	0.183	1.02	27.6	0.178	1.219	0.77	567

* Means taken directly from process

2.4.4 Impact of the Nozzle Size on the Jet Assisted Fluidization Performance

A set of experiments were done using the same type and amount of nanopowder, Aerosil 90, but using different nozzle sizes for the purpose of finding the optimal nozzle size for the jet processing of nanopowders. For these experiments, about 18 grams of Aerosil 90 sieved under 850 μm were used for each run. The nozzle sizes varied from 508 μm down to 127 μm . The pressure, upstream of the nozzles, was kept at about 120 psig for all the runs unless otherwise specified. Table 2.3 summarizes the experimental conditions for this set of experiments.

Table 2.3 Data for Jet Assisted Fluidization Experiments with Different e Nozzles Sizes

Nozzle	Size μm	Nozzles Number	Mass g	Upstream Pressure psig	Initial Bed Height m	Nozzle Flow lpm	Velocity m/s	Re
Red	127	1	18.18	120	0.107	0.4	526	4512
Black	177.8	1	18.15	120	0.112	1	671	8058
Gray	228.6	1	18.01	120	0.102	1.3	528	8147
Blue	254	1	18.07	120	0.112	1.5	493	8461
Green	508	1	18.23	20-120	0.122	15	1233	42304
Red	127	2	18.01	75	0.114	0.8	526	4512
Red	127	2	18.15	120	0.115	0.8	526	4512

The bed of powder was conventionally fluidized at approximately 1.6 cm/s; then jet assistance was started and the powder was processed for about 30 to 60 minutes until no further bed expansion was observed. Figure 2.20 shows the evolution of the non-dimensional bed heights as function of the jet processing time. The bed heights level off after a certain time indicating that the agglomerates are not undergoing any further changes and that jet processing is close to completion. From the plot, the use of two nozzles of about 127 μm and with an upstream pressure of 120 psig is slightly more effective than the rest of the tested nozzles. Among the single nozzles, a nozzle of about 254 μm performs slightly better (faster) than the others, and a single 127 μm nozzle has the poorest (slowest) performance. This later result is related to the amount of flow passing through the nozzle. Smaller nozzle diameters lead to a smaller flow, since the upstream pressure is kept constant. However, a smaller nozzle generates a jet velocity profile characterized by high shear and turbulence. By using two nozzles of 127 μm , the flow through these two nozzles is equivalent to the flow through a nozzle of 254 μm , however, as shown in Figure 2.20, they process the powder faster due to the larger shear produced by the jet velocity profiles.

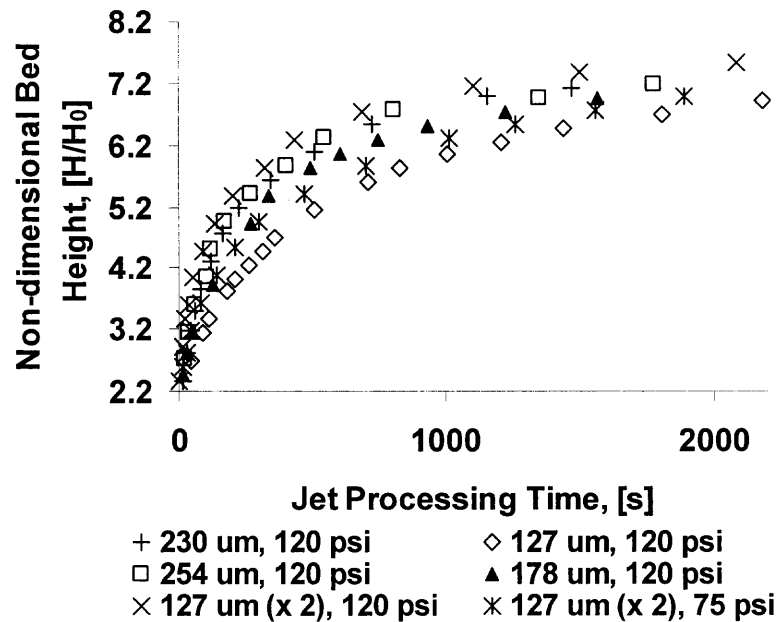


Figure 2.20 Time dependant non-dimensional bed height during jet processing of nanopowders. Gas velocity is about 1.6 cm/s.

Figure 2.21 shows the non-dimensional bed height as function of the superficial gas velocity of jet-processed Aerosil 90 (commercial grade). The figure shows that the size of the nozzle does not have a significant impact on the final bed expansion, but the highest bed heights were obtained with the 254 μm and the 127 μm nozzles. A slightly lower bed expansion was obtained with the 508 μm nozzle. A larger nozzle diameter provides more flow through it, but the shear rate, i.e., the change of the axial velocity as a function of radial position, is lower than for the smaller nozzles. It is believed that a larger shear rate breaks the agglomerates leading to a larger bed expansion and better fluidization quality. Also, it was observed that for the 508 μm size nozzle, there was significant generation of electrostatic charges; this is believed to occur due to the very large gas velocity exiting the nozzle which produces electrostatic charge due to the excessive turbulence generated around the agglomerates.

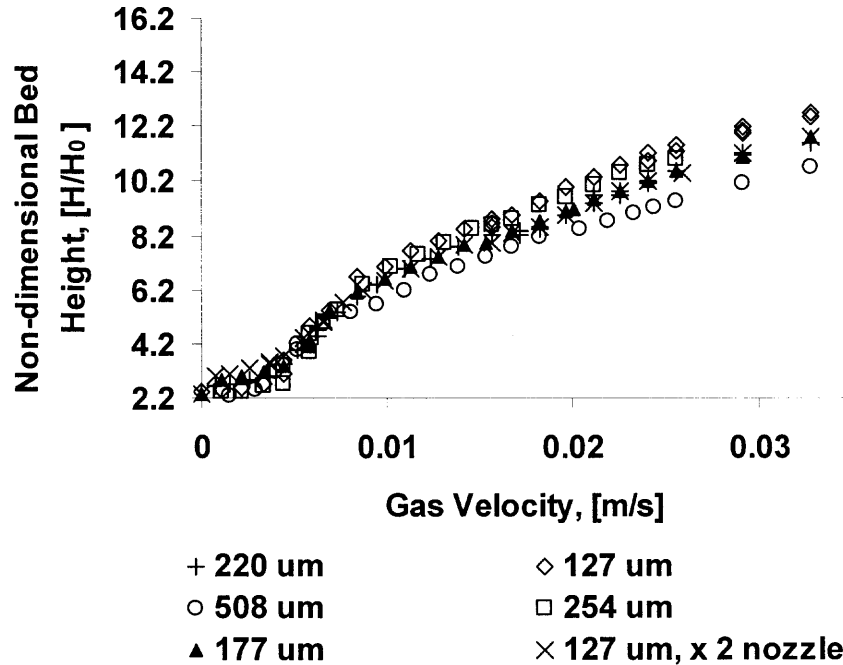


Figure 2.21 Non-dimensional bed height as a function of gas velocity for jet assisted fluidization experiments of Aerosil 90 using different nozzle sizes.

It is of interest to visualize the velocity profile of the jet generated by the flow from the micro-nozzle. For this purpose, the gas phase has been studied without considering the solid phase and by using turbulent jet flow theory available in the literature⁴⁶. The following assumptions were made: the jet is round in shape, the mean velocity profile is self-similar, and there is uniform turbulent viscosity.

The mean axial velocity field $\langle U(x, r, \theta) \rangle$ is dependant on the axial and radial positions but not the angular position due to symmetry. The centerline velocity, in terms of the mean axial velocity, along the jet will be given by

$$U_0(x) \equiv \langle U(x, 0, 0) \rangle \quad (2.1)$$

and the jet's half width $r_{1/2}(x)$ is given by the following equation

$$\langle U(x, r_{1/2}(x), 0) \rangle = \frac{1}{2} U_0(x) \quad (2.2)$$

The axial variation of $U_0(x)$ and $r_{1/2}(x)$ has to be found before proceeding with the estimation of $\langle U(x, r, \theta) \rangle$ in the radial direction. The following equation applies

$$\frac{U_0(x)}{U_j} = \frac{B}{(x - x_0)/d} \quad (2.3)$$

where U_j is the velocity of the fluid at the exit of the nozzle and B is the velocity-decay along the axial direction. Also, considering that the jet spreads linearly, the spreading rate is constant and it is given by,

$$S \equiv \frac{dr_{1/2}(x)}{dx} \quad (2.4)$$

which in the self-similar region empirically translates into:

$$r_{1/2}(x) = S(x - x_0) \quad (2.5)$$

The velocity-decay, B , and the spreading rate, S , are independent of the Reynolds number, and their values can be found in the literature⁴⁶. For the purpose of this work the spreading rate, S , is equal to 0.096, and the velocity-decay, B , is 6.06^{46} .

A cross-stream similarity variable has to be defined in order to correlate the axial and the radial directions, this variable is given by

$$\eta \equiv \frac{r}{(x - x_0)} \quad (2.6)$$

The self-similar mean velocity profile is defined by

$$f(\eta) = \frac{\langle U(x, r, 0) \rangle}{U_0(x)} \quad (2.7)$$

and approximated by the following equation

$$f(\eta) = \frac{\langle U \rangle}{U_0(x)} = \frac{1}{(1 + 45\eta^2)^2} \quad (2.8)$$

Figure 2.22 shows the mean axial velocity profiles of two different jets generated by two nozzle sizes, 127 μm and 508 μm , when the upstream nozzle pressure is 120 psig and at a distance from the nozzle of about 80 mm. The larger nozzle provides higher velocities than the smaller nozzle due to the larger flow passing through it; however, the shear rate produced by the smaller nozzle is larger. In Figure 2.23, the resulting theoretical mean jet velocity profile is given after the pressure upstream of the larger nozzle has been reduced in order to have similar flows passing through both nozzles. It can be seen that the shear rate of the smaller nozzle is larger than the shear rate of the larger nozzle.

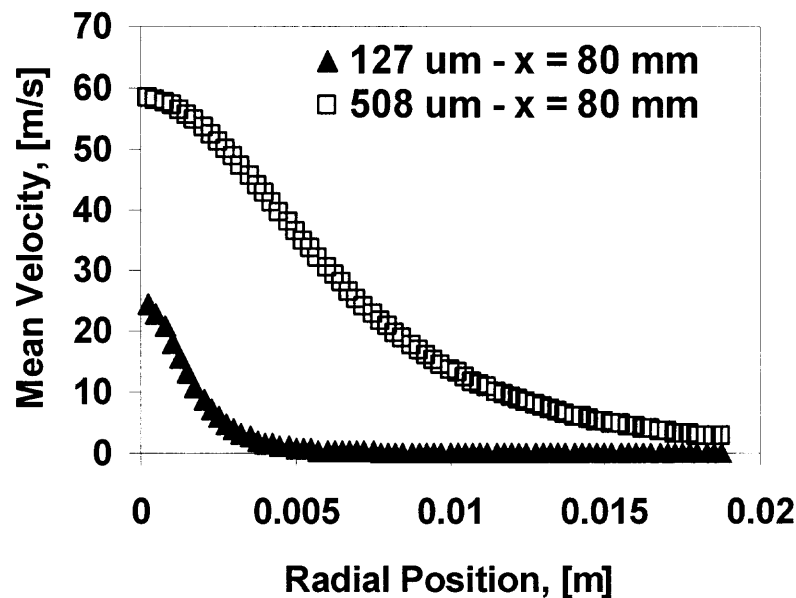


Figure 2.22 Theoretical mean axial velocity profile for two different nozzles (127 μm and 508 μm) under the same upstream pressure (120 psig). Axial distance from the nozzle is about 80 mm.

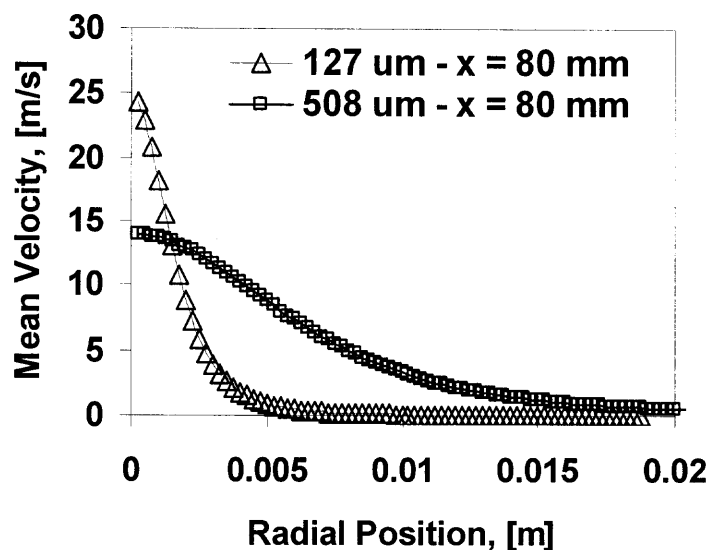


Figure 2.23 Theoretical mean axial velocity profile for two different nozzles (127 μm and 508 μm) under different upstream pressure (120 psig for 127 μm and 20 psig for the 508 μm). Axial distance from the nozzle is about 80 mm.

2.4.5 Effect of the Direction of the Nozzle on Jet Assisted Fluidization of Nanopowders

As explained in the experimental methods section, most of the experiments were done having the nozzle or nozzles pointing downwards and at relatively short distance from the gas distributor plate located at the bottom of the column. However, the effect of having nozzles pointing upwards was also studied. In Figure 2.24, the fluidized bed pressure drops of fluidized beds containing equal amounts of Aerosil 90 are shown as function of the gas superficial velocity. It can be seen that the minimum fluidization velocity (U_{mf}) is only reduced when the nozzle is pointing downwards. If the nozzle points upwards, the minimum fluidization velocity is similar to that obtained using conventional fluidization.

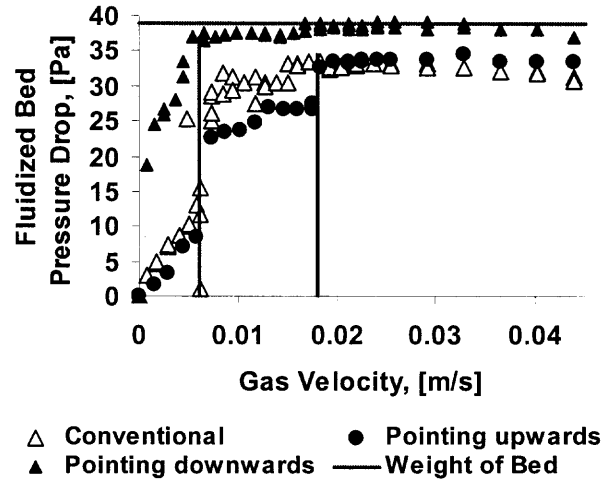


Figure 2.24 Fluidized bed pressure drop for the fluidization of Aerosil 90 when comparing the effects of nozzle direction.

The minimum fluidization velocities (U_{mf}) are given by the vertical blue lines drawn at the corresponding abscissa values. The pressure drop readings to the left of the vertical blue lines are lower than the full fluidized bed pressure drop and fluctuate significantly. The lower pressure drop observed when the nozzle points upwards indicates that the bed is collapsing due to instabilities and non-homogeneity of the gas flow. Figure 2.25 shows the corresponding fluidized bed heights comparing the conventional against the assisted fluidization when the nozzle points in different directions. The maximum bed expansion is obtained with the nozzle pointing downwards - dark triangles. When the jet is pointing upwards, the bed expansion is slightly lower than when the jet is pointing downwards but much higher than during conventional fluidization. It is important to note that only at high gas velocities are the bed heights of the jet assisted fluidized beds similar. Below about 0.02 m/s (2 cm/s) the fluidized bed collapses when the nozzle is pointing upwards. Hence, the gas flow passing through the distributor has to be relatively high for fluidization to occur in the section of the column below the upward nozzle and to transport the nanopowder from the bottom of the column to the jetting region.

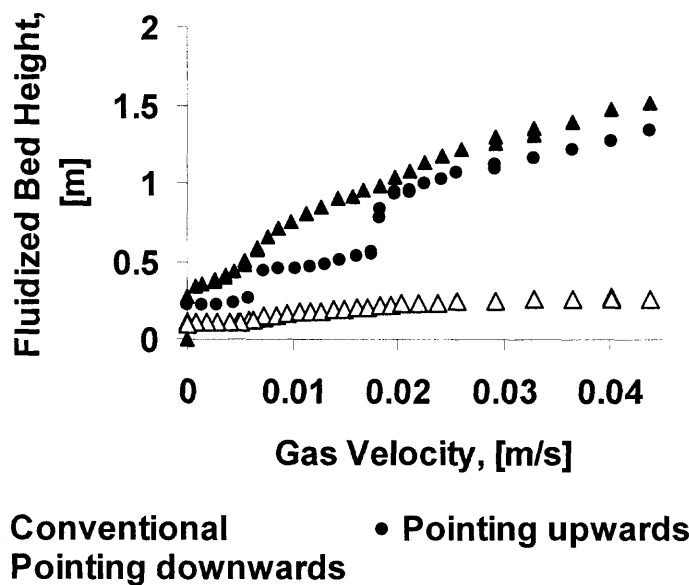


Figure 2.25 Fluidized bed height corresponding to the fluidization of Aerosil 90 comparing the effect of the nozzle direction.

2.4.6 Favored Performance of Internals Installed in the Fluidization Column with Jet Assistance

Several types of internals such as screens or packing materials are currently used to enhance transport in fluidization columns^{47, 48, 49}. Their purpose is to break down bubbles in order to properly disperse the solid particles in the gas phase; however, some problems also arise due to the presence of these internals, such as hindrance of solids motion and segregation of particles. Dead spots and channeling also occur if the powder is not homogeneously distributed in the internal structure.

It is believed that by adding jets pointing towards the structure of the internal, their advantages can be fully exploited since the turbulent jets will minimize the problems that arise due to the presence of the screens or packing materials, i.e., impeded solids motion, segregation and non-homogenous distribution of the air.

To demonstrate the benefits of using jets when applied to internals, a grid was located at around 12 inches from the air distributor plate and a jet pointing downwards was located at about 4 inches above this sieve plate as explained in the experimental methods section. Two series of experiments were carried out with commercial and process (Raw) grades Aerosil 90. As can be seen in Figure 2.26, at superficial gas velocities higher than 0.02 m/s (2 cm/s), the fluidized bed heights are similar when the jet assistance is used regardless of the presence of the mesh (internal); however, when the gas velocities are lower than 0.02 m/s, the bed height is lower when the internal is used. This occurs because the gas velocity is not high enough to aerate the powder in the region above the gas distributor plate and below the grid. It is important to note that at the beginning of the experiment, most of the powder was sitting on the grid and that it could not be fluidized conventionally due to the formation of channels above the grid.

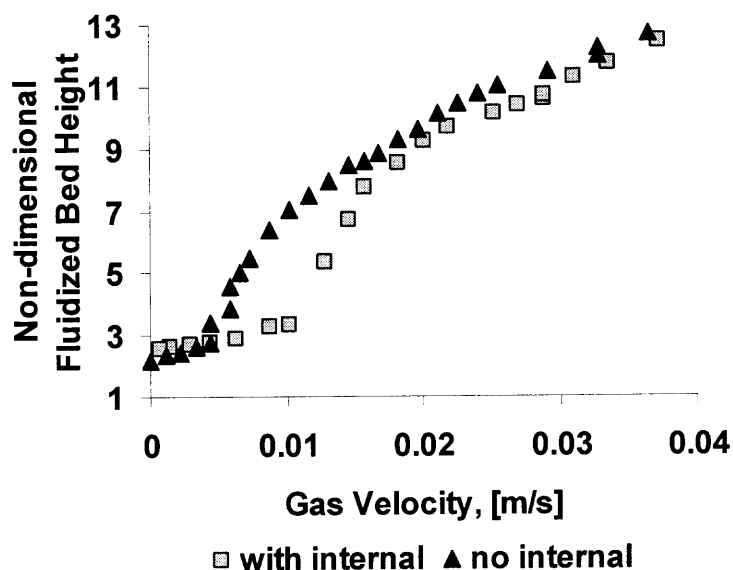


Figure 2.26 Non-dimensional bed height of fluidized beds of Aerosil 90 (commercial grade).

Figure 2.27 shows a comparison of the bed heights when fluidizing Aerosil Raw 90. This powder has an APF behavior and it expands during conventional fluidization. When the powder is fully fluidized it passes easily through the grid, but if the powder is sitting on the grid, as in the beginning of the experiment, it cannot be fluidized conventionally at any gas velocity due to the poor distribution of gas by the grid which leads to the formation of channels. The nanopowder can only be fluidized with the jet acting on the grid (internal). These results demonstrate that the impeded solids motion problem due to packing in a fluidized bed internal can be overcome with the jet or jets.

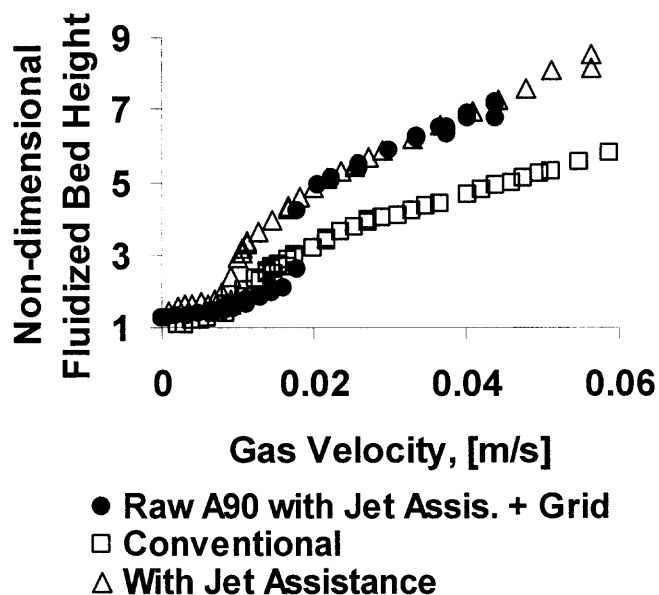


Figure 2.27 Non-dimensional bed height of fluidized beds of Aerosil Raw 90 (process grade).

Figure 2.28 shows images of the evolution of the bed of powder from a packed bed condition to a fully fluidized bed by the action of the jet on the internal (grid). At the beginning, most of the powder was held on the grid as can be seen by the powder suspended in the upper section of the column. The primary flow (the flow passing through the air distributor) was held constant during this experiment. Figure 2.28 (a)

shows the powder above the gas distributor plate begins to fluidize but there is only a channel in the powder held by the grid (region above); in (b), the jet has been activated and pushes the nanopowder through the grid but also aerates part of the powder held by the grid leading to a partially fluidized bed above the grid. In (c) and (d), more powder has passed through the grid and the volume below it is full of aerated powder that rises. Finally, a fully fluidized bed can be seen in (e). These images show that by using jets acting on the grid, which acts as internal packing, the powder can easily flow through the grid solving the problem of having motionless powder.

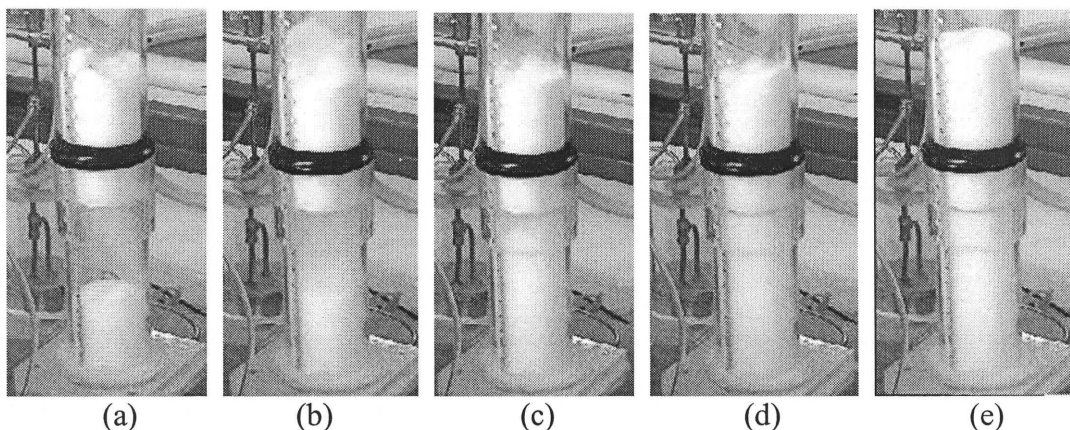


Figure 2.28 Images showing the evolution of the bed of powder when a grid is assisted by a jet. Grid is located at 12 inches above the air distributor and jet is 4 inches above it. Primary flow passing through distributor is set constant. (a) only primary flow, no jet, most powder sitting on the grid, (b) jet has been activated and acts on the grid, powder passes through, (c) fluidization starts, (d) section below the grid is filled with fluidized powder that easily passes through the grid, (e) the entire bed of powder is fluidized, a condition promoted by the jet.

2.4.7 Scale-Up of the Jet Assisted Fluidization

Previous experiments on fluidization of APF and ABF powders were done in a 3 inches internal diameter column. In those experiments it has been shown that jets generated by micro-nozzles successfully enhance fluidization of APF nanopowders and convert ABF

behavior nanopowders into APF-like behavior nanopowders. Proper dispersion of the powder in the gas phase has been successfully achieved by using the jets. However, it is necessary to study how the jet would behave in a larger diameter column. Also, how many jets would be needed to obtain an enhanced fluidization in a pilot or plant scale column? Figure 2.29 shows the ratio of the cross sectional areas of a plant scale and a lab scale columns. As the diameter of the lab scale column decreases and the diameter of the plant scale column increases, the area ratio, or number of lab columns, increases by several orders of magnitude. A rule of thumb would be to select an area ratio within an order of magnitude and less than two orders of magnitude than the plant scale column. Since in our particular example the internal diameter of the pilot plant scale column is about 11 to 15 inches, a reasonable lab scale internal column diameter would be about 4 to 6 inches. Therefore, a 5 inches internal diameter column was selected.

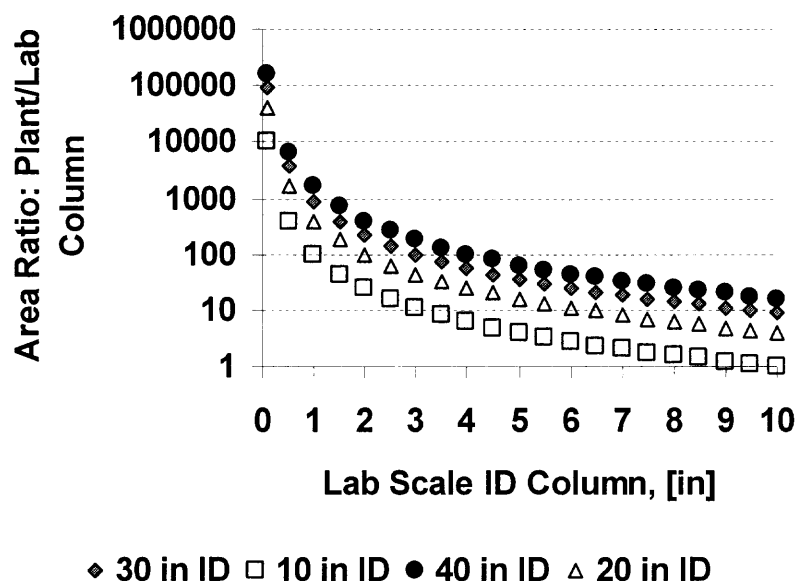


Figure 2.29 Area ratio of different plant scale vs. lab scale columns.

It was of special interest to study the fluidization of Aeroxide TiO₂ P25 because this is one of the most difficult nanopowders to fluidize. As mentioned above, two different types of Aeroxide TiO₂ P25 were tested: commercial and process grades, both grades show an ABF behavior. Figure 2.30 shows a comparison of the non-dimensional fluidized bed heights of conventional and jet assisted fluidized beds of Aeroxide TiO₂ P25 commercial grade. It can be seen that when the fluidization is jet assisted, the bed of nanopowder reaches a maximum bed expansion at about 2.5 cm/s, which is considered to be the minimum fluidization velocity. During conventional fluidization the bed does not expand significantly, but when using jet assistance, the effects of the jet are so dramatic that the ABF behavior with bubbles and almost no bed expansion of the Aeroxide TiO₂ P25 is transformed into a particulate fluidization (APF), bubble free, with large bed expansion.

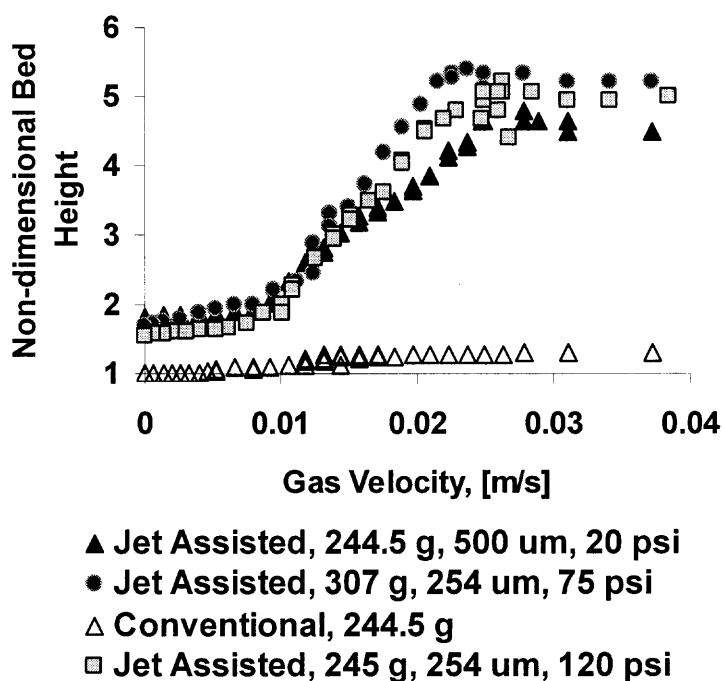


Figure 2.30 Non-dimensional bed height for fluidization of Aeroxide TiO₂ P25 in a 5 inches ID column.

Similarly, when fluidizing Aeroxide Raw TiO₂ P25, a larger bed expansion is obtained as shown in Figure 2.31. Again, the minimum fluidization velocity is about 2.5 cm/s when jet assisted; also, it can be seen that the bed expansion of conventionally fluidized Raw TiO₂ is slightly larger than the commercial grade TiO₂.

Figure 2.32 shows images of Aeroxide TiO₂ P25 in the 5 inches column; (a) shows the initial bed height (5 inches) at zero gas velocity, (b) shows a view of the same amount of nanopowder but fluidized with jet assistance, and (c) shows a close-up of the fluidized bed surface indicating a bed height of about 25.5 inches. The smooth interface verifies transformation into APF behavior, free of bubbles that usually disrupt the surface of the fluidized bed.

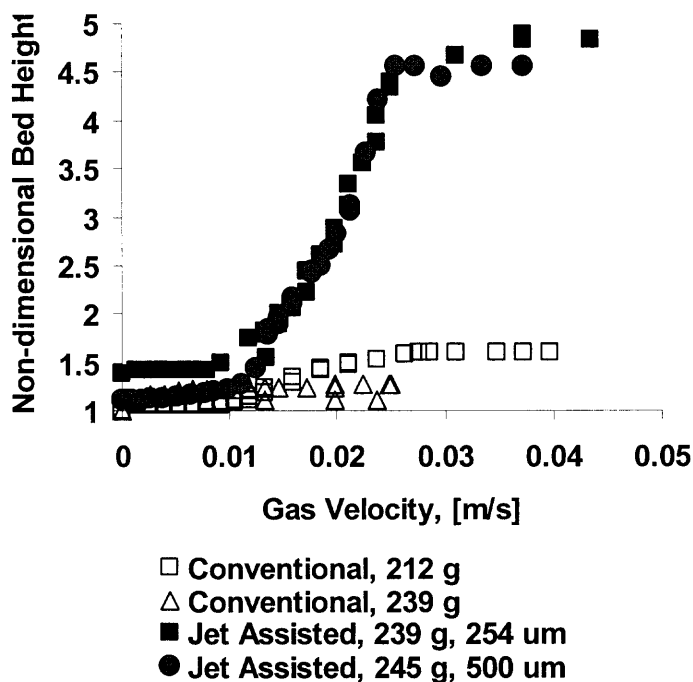


Figure 2.31 Non-dimensional bed height as a function of the gas velocity for fluidization of Aeroxide Raw TiO₂ P25 (from plant) in a 5 inches ID column.

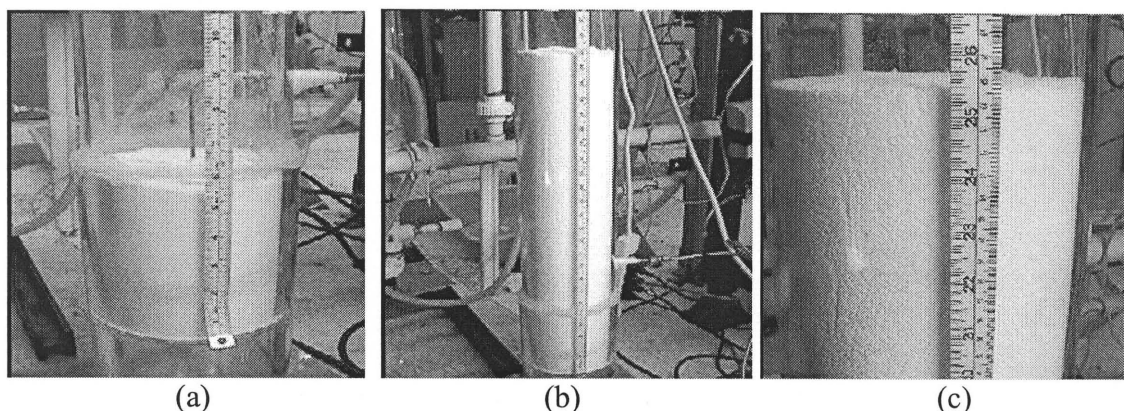


Figure 2.32 Images corresponding to the fluidization of Aerioxide TiO_2 P25 in a 5 ID column. (a) Initial bed height, (b) maximum bed height while fluidized with jet assistance, (c) close-up of the fluidized bed surface, bed expanded from 5.5 to 25.5 inches and the surface of the bed shows no large bubbles.

2.4.8 Fluidization of Nanopowders When Having the Primary Flow Enters From the Side at the Bottom of the Fluidization Column

In many industrial applications it is difficult to have the air properly distributed in the fluidization column. In some cases, the fluidizing gas enters sidewise at the bottom of the column. It is believed that by placing a jet close to the bottom of the fluidization column, the powder can be fluidized successfully. In the following experiments, the fluidizing gas entered the column through the pressure tap located right above the distributor plate as shown in Figure 2.33. In this experiment, no gas flow passed through the distributor plate.

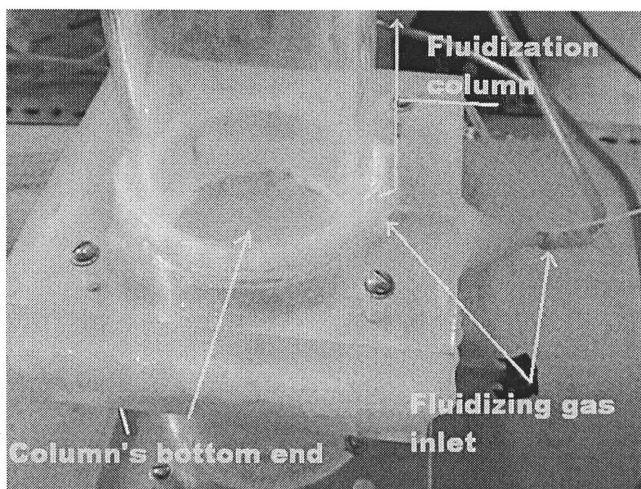


Figure 2.33 Configuration of the fluidizing gas inlet at the bottom of the column.

Figure 2.34 shows the fluidized bed height corresponding to 61.5 grams of Aeroxide Raw TiO_2 P25 under different fluidization conditions. When conventionally fluidized, the bed height is slightly larger than when the flow is entering from the side; this happens because of channeling as shown in Figure 2.35 (a & b).

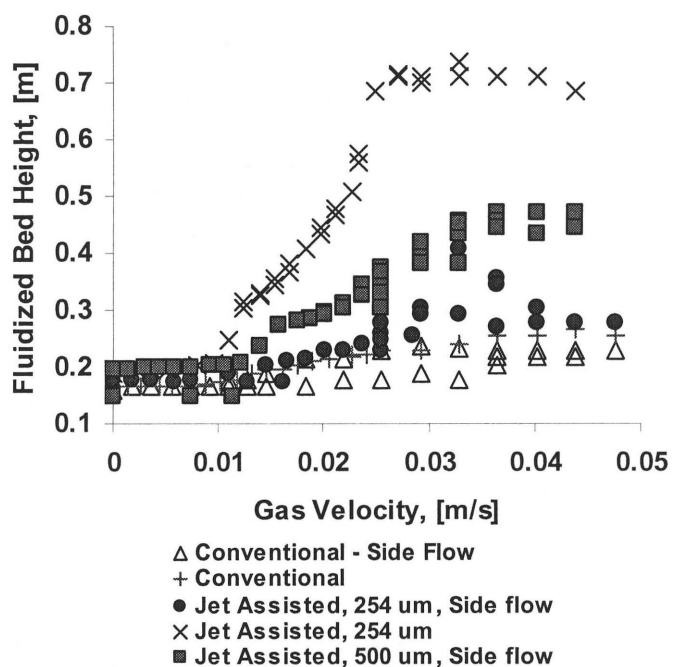


Figure 2.34 Fluidized bed height as a function of the gas velocity for the case when the primary flow is fed sidewise at the bottom of the column. Fluidized powder is Aeroxide Raw TiO_2 P25. (Mass: 61.5 grams, sieved under $500 \mu\text{m}$).

In Figure 2.34, the dots show the bed expansion when the fluidized bed is jet assisted; the size of the nozzle is 254 microns and the primary flow is fed through the pressure tap at the side. It is believed that the velocity of the jet is not large enough to aerate all of the powder sitting at the bottom of the column; that is why the bed height only increases slightly. The squares show the fluidized bed height resulting from using a nozzle of 500 microns, which leads to a larger jet velocity than when using the 254 microns nozzle. The higher gas velocity leads to more powder being aerated and a larger bed expansion; however, when compared against the results obtained when the gas flow passes through the distributor plate (cross signs) with jet assistance, the fluidized bed height is lower indicating that there is still a considerably amount of powder remaining at the bottom of the bed without being aerated.

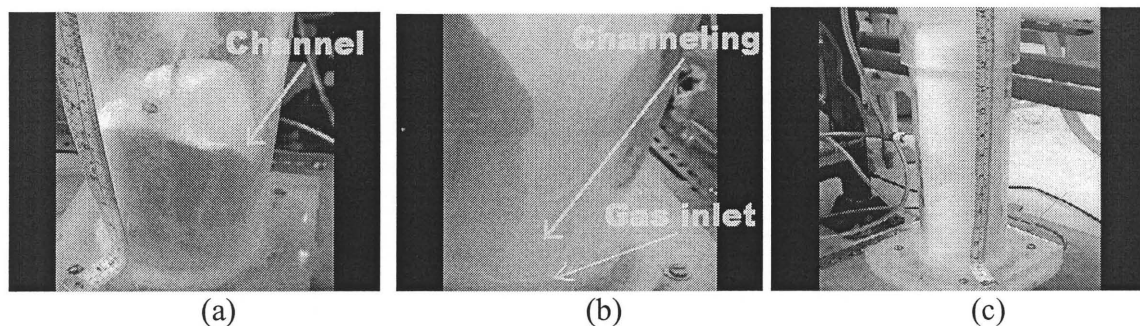


Figure 2.35 (a) & (b) Images showing the bed of powder with a channel due to the sidewise entrance of gas; bed height around 5 inches. (c) Partially fluidized bed of powder when the downward jet is activated; bed height around 13 inches.

Figure 2.35 (a) and (b) show the presence of a large channel right above the entrance of the gas at the bottom of the column and most of the powder remains as a packed bed. Figure 2.35 (c) shows a partially fluidized bed after activation of the jet; the bed height increases from 5 to about 13 inches and also a fluidized bed surface can be

seen when using the jet assistance. This result indicates that a downward jet enhances the distribution of the fluidizing gas at the bottom of the fluidization column when a distributor plate is not available.

2.4.9 In-Situ Measurement of Agglomerates of Nanoparticles in Conventional and Jet Assisted Fluidized Beds

As explained in the introduction, there have been several attempts to characterize agglomerates of nanoparticles in a fluidized bed. An experimental setup was prepared as explained in the experimental methods section, and the corresponding results are given below. Two different probes were used in the measurements and their position was exchanged in order to get images and size distributions of the fluidized agglomerates in two different positions along the fluidized bed. Size distributions are reported as “number based” or “volume based.” A number size distribution reflects the percentage or counts of the particle population in different size categories. A volume size distribution reflects the percentage or counts of the particle volume in different size categories. Also, experiments were done with two different powders, Aerosil R974 (APF) and Aerosil 90 (ABF) under conventional and jet assisted conditions. The use of alcohol for reduction of electrostatic charges was crucial in getting proper measurements and images because it reduced the amount of agglomerates sticking to the surface of the probes.

Figure 2.36 shows two number based agglomerate size distributions of conventionally fluidized Aerosil R974. When number based, the size distribution is given by the number of agglomerates per channel or size range. The plot at the left (a) shows the difference in the size distributions due to the change in the position of the probe. As explained in the experimental section, the two ports were located at 17 and 44 inches

from the distributor plate. When the probe is in the lower position, there is a slightly larger concentration of smaller agglomerates, this shifts the distribution slightly towards the left giving a smaller mean size (180 μm) than when compared to the distribution obtained when the probe was in the upper position (mean size of 198 μm). Having a larger void fraction in the bed (the void fraction increases somewhat with the height of the bed) allows the probe to better detect individual larger agglomerates. Plot (b) shows the difference in the size distributions due to a change in the fluidizing gas velocity. Voids in the fluidized bed are larger at higher gas velocities which again allow for a better identification of individual larger agglomerates. At lower gas velocities the presence of a larger amount of smaller agglomerates in the volume of measurement hinders the counting of large agglomerates. As it can be seen in the figure, the concentration of small agglomerates at high gas velocities is slightly lower than at low gas velocities. This shifts the size distribution towards the right giving a mean size of 182.5 microns. Nevertheless, it can be concluded from Figure 2.36 that the agglomerate size distribution does not change significantly with respect to the point of measurement along the height of the fluidized bed and at different gas velocities.

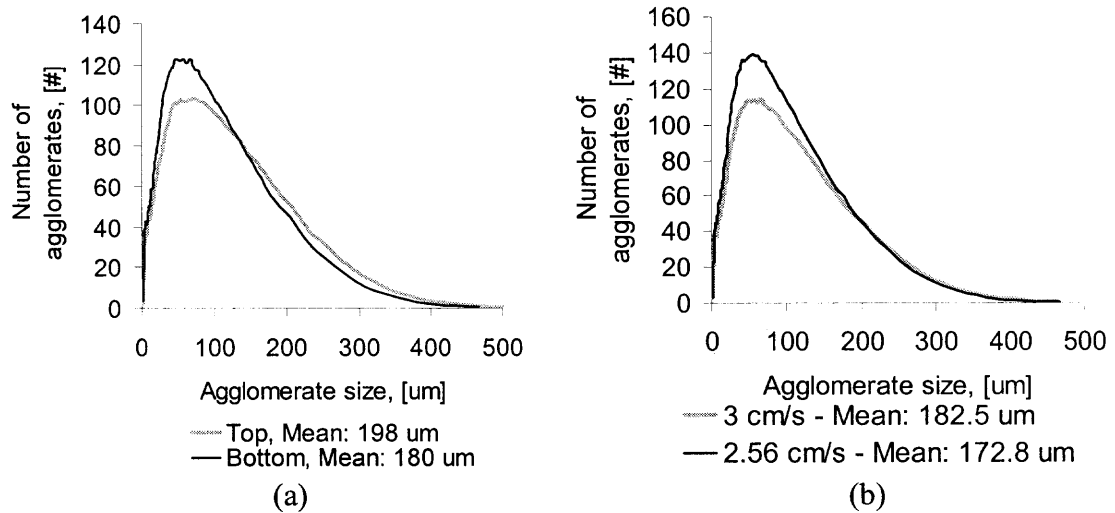


Figure 2.36 Number based agglomerate size distribution of conventionally fluidized Aerosil R974 measured by the FBRM (Lasentec); (a) probe at different positions, (b) different gas velocities through the fluidized bed

Figure 2.37 shows the volume based agglomerate size distributions corresponding to the comparison of measurements from conventional and jet assisted fluidized beds. In plot (a), the number based volume agglomerate size distribution is given and the concentration of agglomerates in the jet assisted fluidization is seen to be significantly lower than for conventional fluidization. When showing the same size distribution, but as a percentage instead of counts, shown in plot (b), a clear reduction in the agglomerate size can be seen as a consequence of the jet assisting method. In plot (c), the number based size distribution shows a reduction on the agglomerate size from 198 μm in the conventional fluidization case to 149 microns for the jet assisted fluidization. From Figure 2.37, it can be conclude that by using the jet assisting method the concentration and the agglomerate size are reduced in the fluidized bed; this indicates a better dispersion of the agglomerates in the gas phase.

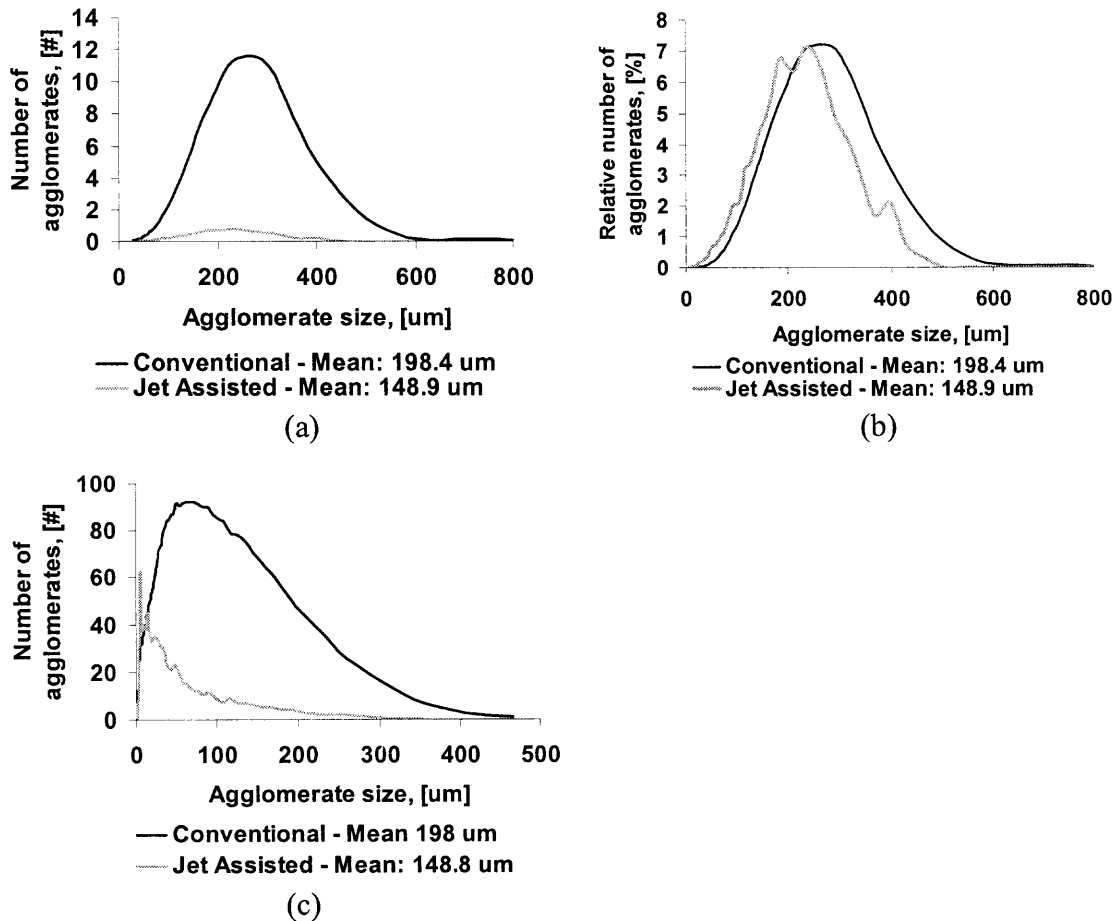


Figure 2.37 Comparison of the agglomerate size distribution obtained during conventional and jet assisted fluidization of Aerosil R974 at 3 cm/s. (a) Volume based number size distribution, (b) volume based percentage size distribution, (c) number based number size distribution.

Figure 2.38 shows images of the agglomerates of Aerosil R974 in the fluidized bed obtained with the PVM probe. The image shown in (a) corresponds to conventional fluidization, and the image shown in (b) corresponds to jet assisted fluidization. Denser and well defined boundaries of the agglomerates can be seen in the conventional fluidization image while there are no clear boundaries and the agglomerates look fluffier in the image corresponding to jet assisted fluidization.

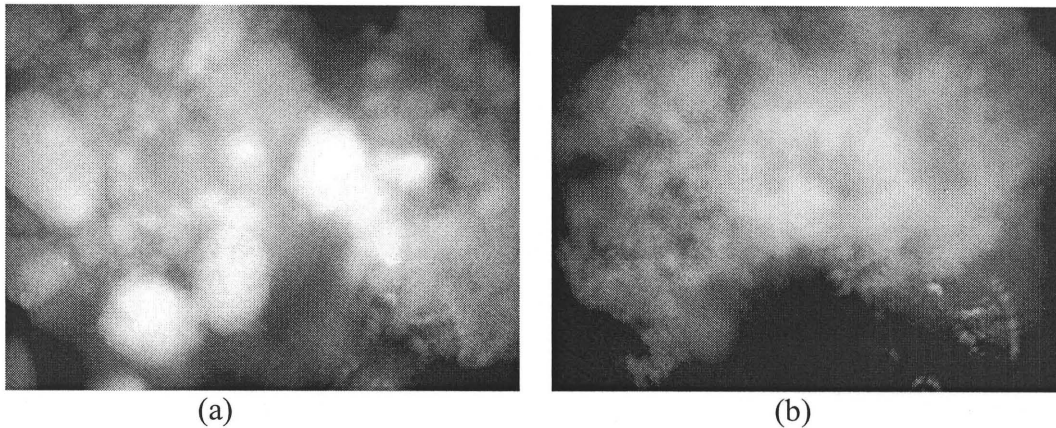


Figure 2.38 In-situ images of agglomerates of Aerosil R974 in a fluidized bed obtained with the PVM probe, (a) conventional fluidized bed, and (b) jet assisted fluidized bed.

In a similar manner, Figure 2.39 shows a comparison of the agglomerate size distribution obtained from a conventional and a jet assisted fluidized beds of Aerosil 90. Plot (a) shows the number based agglomerate size distribution. Note that the number of larger agglomerates is higher than the number of smaller agglomerates for conventional fluidization. After jet processing of the nanopowder, the number of larger agglomerates has been reduced and the resulting mean size of the agglomerates is lower (about 249 microns) than when compared to the conventional fluidization (272 microns). The plot shown in (b) corresponds to the same measurement shown in (a) but in terms of the volume of the agglomerates and the relative concentration in such a way that the shift of the size distribution towards a smaller size is seen more clearly.

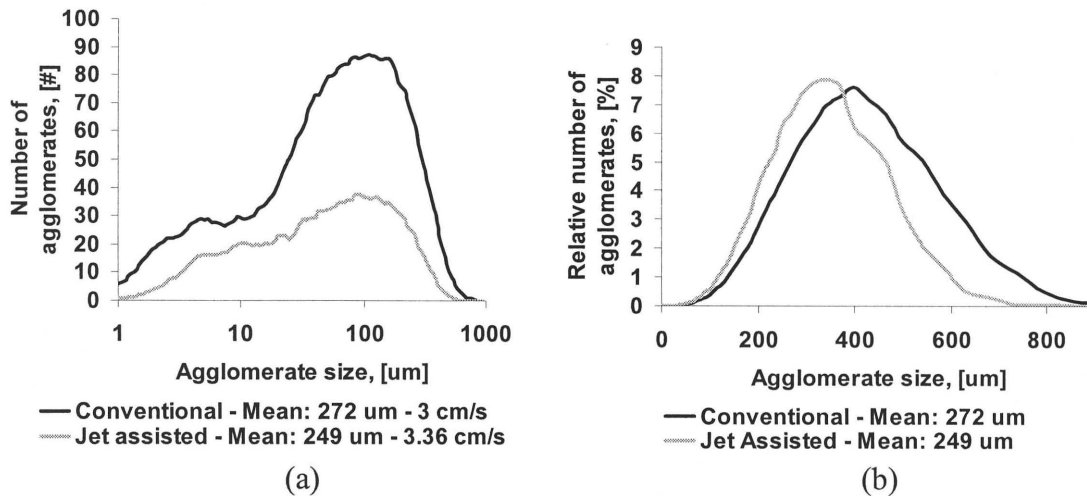


Figure 2.39 Comparison of the agglomerate size distributions of a conventional and a jet assisted fluidized bed of Aerosil 90. (a) Number based size distribution, (b) volume based size distribution.

Images of the fluidized agglomerates of Aerosil 90 were also obtained. These are shown in Figure 2.40, (a) for conventional fluidization and Figure 2.40 (b) after jet processing. Agglomerates obtained during conventionally fluidized bed look denser, larger and well defined while agglomerates after jet processing appear fluffier, smaller and it is difficult to define their boundaries. Jet assistance reduces agglomerate size and density and better disperses nanopowders in the gas phase.

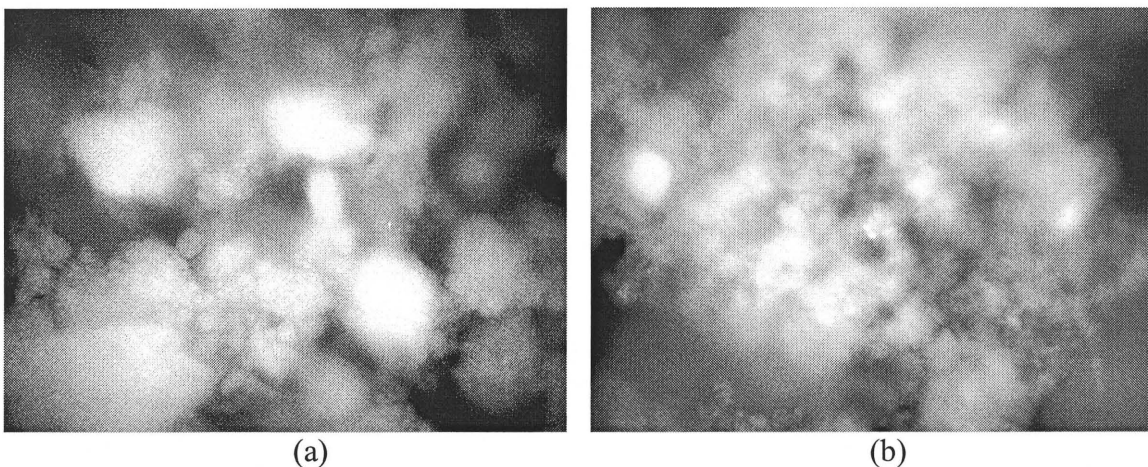


Figure 2.40 In-situ images of agglomerates of Aerosil 90 in a fluidized bed obtained with the PVM probe, (a) conventional fluidized bed, and (b) jet assisted fluidized bed.

A comparison of the agglomerates size distribution during conventional fluidization of Aerosil R974 and Aerosil 90 is shown in Figure 2.41. These results show that the FBRM and PVM probes from Lasentec can properly characterize fluidized agglomerates of nanoparticles under the proper operating conditions.

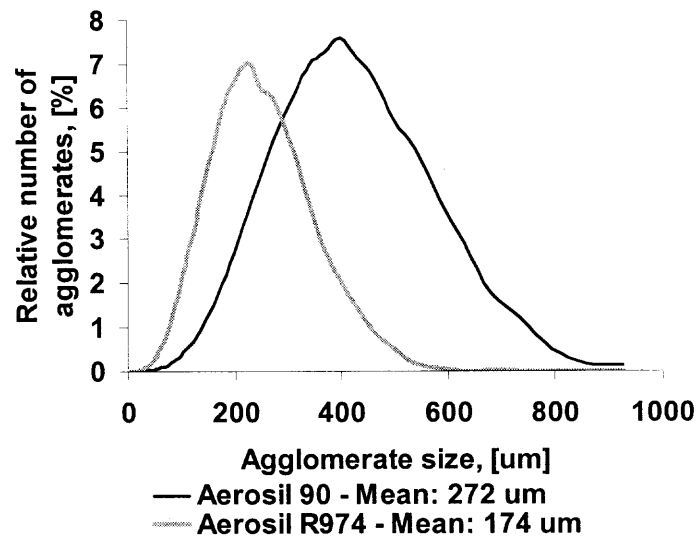


Figure 2.41 Comparison of the volume agglomerate size distributions in conventional fluidized beds of Aerosil R974 and Aerosil 90 measured by the FBRM.

2.4.10 Estimating the Agglomerate Size by Using the Richardson-Zaki Criterion

The Richardson-Zaki (R-Z) criterion has been used by previous investigators to estimate agglomerate sizes since a fluidized bed of APF type agglomerates of nanoparticles shows a homogeneous particulate fluidization behavior very similar to liquid-solid fluidization described by Richardson-Zaki about five decades ago^{5, 7, 12}. However, for conventional fluidization of ABF nanopowders, the relationship between the void fraction and the gas velocity cannot be properly represented by the Richardson-Zaki criterion since the voidage is not homogeneous along the fluidized bed due to the presence of bubbles.

A typical R-Z plot shows the superficial fluid velocity as a function of the fluidized bed void fraction, both on a logarithmic scale. These plots can be represented by the following equation,

$$\ln(U) = n \ln(\varepsilon_{FB}) + \ln(U_i) \quad (2.9)$$

where “ n ” is the well known Richardson-Zaki index which represents the slope of the linear regression of the data, and “ $\ln(U_i)$ ” is the y-intercept corresponding to a void fraction (ε_{FB}) equal to unity, indicating that all the particles have been entrained by the flow due to a fluid velocity close to the terminal velocity of the particles. The terminal velocity in an infinite medium is found by applying a correction factor that takes into account the ratio between the diameters of the particle and the fluidization column,

$$\log U_i = \log U_t - \frac{d_p}{D} \quad (2.10)$$

Hence, the terminal velocity of fluidized agglomerates can be found from the y-intercept value from the R-Z plot. The flow regime around the fluidized agglomerates is laminar which means that the agglomerates are under viscous drag (Stokes regime) assuming that they behave like perfect spheres and neglecting the effects from the surrounding agglomerates. This is inferred from the calculation of the Reynolds number for the agglomerates based on the terminal velocity.

$$\text{Re}_t = \frac{\rho_f U_t d_p}{\mu} \quad (2.11)$$

Calculated values for the Reynolds number are below 10 confirming the laminar flow regime. Also, the agglomerate (particle) Reynolds number can be calculated by using the following equation

$$\text{Re}_p = \frac{\rho_f U_g d_p}{\mu} \quad (2.12)$$

U_g is the actual superficial gas velocity of the fluidizing gas. However, the effective cross sectional area is actually lower due to the presence of the agglomerates; therefore, a higher gas velocity is expected around the swarm of agglomerates and the particle Reynolds number would have to be modified by the void fraction as shown below

$$\text{Re}_p = \frac{\rho_f U_g d_p}{\mu \varepsilon} \quad (2.13)$$

At gas velocities close to the minimum fluidization velocities of the nanopowders, creeping flow is assumed⁷. Therefore, the agglomerate diameter can be estimated with the following equation⁵⁰ assuming Stokes law,

$$d_p = \sqrt{\frac{18U_t \mu}{(\rho_{agg} - \rho_f)g}} \quad (2.14)$$

For Aerosil R974, the fluidizing gas superficial velocity is the range of 0.4 cm/s (U_{mf}) up to 4.5 cm/s. The values for particle Reynolds numbers, as calculated by using Equation 2.12, are in the range of 0.014 up to 0.88. If the void fraction is considered and Equation 2.13 is used then the range is from 0.03 to 1.8. In both calculations, an agglomerate size of 300 μm has been assumed. Therefore, the assumption of Stokes law for the drag force may be valid from these calculations.

Fluidization of agglomerates of nanoparticles is quite different than fluidization of solid micron size particles for which the R-Z procedure was implemented. From Equations 2.9 and 2.14, it can be seen that the two key parameters in the R-Z criterion are

the fluidized bed void fraction (ε_{FB}) and the density of the agglomerate (ρ_{agg}). Both of these parameters cannot be measured directly and have to be estimated. The original equation used by Richardson-Zaki to determine the fluidized bed void fraction is

$$\frac{\Delta P}{H_{FB}} = (\rho_{agg} - \rho_f)(1 - \varepsilon_{FB})g \quad (2.15)$$

However, this equation also depends on the agglomerate density. For solid micron size particles, the agglomerate density remains constant during fluidization, on the contrary, the density of agglomerates of nanoparticles may be different than the original bulk density (before fluidization) and it may even change due to shear or pressure. Nevertheless, to apply the R-Z criterion, it will be assumed that the agglomerate density remains almost constant during conventional fluidization. It will also be assumed that the agglomerate density remains constant during jet assisted fluidization after the powder has been fully processed by the jet; however, its value will be lower than for conventional fluidization. Reduction of the agglomerate density is expected during jet processing because of the much larger bed expansion observed, the reduction in the initial bulk density (after processing but before fluidization) and from the images of the agglomerates.

A good approximation of the agglomerate density for both conventional and jet assisted fluidization can be estimated by using data corresponding to a packed bed of nanopowder at zero flow. The agglomerate density will be close to the bulk density depending on the packing of the agglomerates. The total volume of the packed bed (V_{PB}) will be equal to the volume of the gas (V_g) plus the volume occupied by the agglomerates (V_{agg}). The agglomerates' volume will be equal to the voids in the agglomerates ($V_{g,agg}$) plus the volume occupied by the silica particles (V_{SiO_2}).

$$V_{PB} = V_g + V_{agg} \quad (2.16)$$

and

$$V_{agg} = V_{g,agg} + V_{SiO_2} \quad (2.17)$$

The void fraction in the packed bed is given by

$$\mathcal{E}_{PB} = \frac{V_g + V_{g,agg}}{V_{PB}} \quad (2.18)$$

hence

$$1 - \mathcal{E}_{PB} = \frac{V_{SiO_2}}{V_{PB}} \quad (2.19)$$

Defining the initial void fraction of the packed bed as

$$\mathcal{E}_{e0} = \frac{V_g}{V_{PB}} \quad (2.20)$$

leads to

$$1 - \mathcal{E}_{e0} = \frac{V_{agg}}{V_{PB}} \quad (2.21)$$

where \mathcal{E}_{e0} represents the inter-agglomerate initial void fraction. Similarly, the void fraction inside the agglomerate can be defined as

$$\mathcal{E}_{agg} = \frac{V_{g,agg}}{V_{agg}} \quad (2.22)$$

and subsequently

$$1 - \mathcal{E}_{agg} = \frac{V_{SiO_2}}{V_{agg}} \quad (2.23)$$

where \mathcal{E}_{agg} represents the agglomerate internal void fraction; hence

$$\frac{V_{SiO_2}}{V_{PB}} = \frac{V_{agg}}{V_{PB}} \frac{V_{SiO_2}}{V_{agg}} \quad (2.24)$$

which is equivalent to

$$1 - \varepsilon_{PB} = (1 - \varepsilon_{e0})(1 - \varepsilon_{agg}) \quad (2.25)$$

To find the agglomerate density the initial void fraction has to be assumed, for example, the void fraction corresponding to perfect packing. The total void fraction of the packed bed is given by

$$\varepsilon_{PB} = 1 - \frac{M_{SiO_2}}{\rho_{SiO_2} AH_0} \quad (2.26)$$

Here we have assumed the nanopowder to be silica (SiO_2) and after substituting this equation into Equation 2.25 the following expression is obtained

$$1 - \varepsilon_{agg} = \frac{M_{SiO_2}}{\rho_{SiO_2} AH_0 (1 - \varepsilon_{e0})} = \frac{V_{SiO_2}}{V_{agg}} = \frac{m_{SiO_2} \rho_{agg}}{m_{agg} \rho_{SiO_2}} = \frac{\rho_{agg}}{\rho_{SiO_2}} \quad (2.27)$$

Assuming that the mass of the agglomerate is almost equivalent to the mass of SiO_2 in the agglomerate ($m_{SiO_2} \cong m_{agg}$) then,

$$\rho_{agg} = \frac{M_{SiO_2}}{AH_0 (1 - \varepsilon_{e0})} \quad (2.28)$$

Having estimated the density of the agglomerates by using Equation 2.28, the next step is to estimate the void fraction. In a fluidized bed, the relationship of the volume occupied by the solid silica particles to the volume of the fluidized bed is given by

$$\frac{V_{SiO_2}}{V_{FB}} = \frac{V_{PB}}{V_{FB}} \frac{V_{agg}}{V_{PB}} \frac{V_{SiO_2}}{V_{agg}} \quad (2.29)$$

This equation can be written in terms of the various void fractions as

$$1 - \varepsilon_{tot} = (1 - \varepsilon_{FB})(1 - \varepsilon_{e0})(1 - \varepsilon_{agg}) = \frac{M_{SiO_2}}{\rho_{SiO_2} AH_{FB}} \quad (2.30)$$

from which an expression for the fluidized bed void fraction (ε_{FB}) can be obtained as

$$\varepsilon_{FB} = 1 - \frac{M_{SiO_2}}{\rho_{SiO_2} AH_{FB} (1 - \varepsilon_{e0})(1 - \varepsilon_{agg})} \quad (2.31)$$

An alternative equation to find the inter-agglomerate void fraction was given by Guo et al.⁴

$$\varepsilon_{FB} = 1 - \frac{H_0}{H_{FB}} \quad (2.32)$$

This equation can be derived from Equation 2.15 by making a number of assumptions as described below. The pressure drop in Equation 2.15 is replaced by the weight of the particles divided by the cross sectional area of the column to give

$$\frac{M_{SiO_2} g}{A} \frac{1}{H_{FB}} = (\rho_{agg} - \rho_f)(1 - \varepsilon_{FB}) g \quad (2.33)$$

The first assumption is to neglect the fluid density which is an order of magnitude smaller than the agglomerate density during conventional fluidization

$$\frac{M_{SiO_2} g}{A} \frac{1}{H_{FB}} = \rho_{agg} (1 - \varepsilon_{FB}) g \quad (2.34)$$

It should be noted however, that this assumption weakens when using jet assistance since the agglomerate density is reduced due to the large bed expansion. The agglomerate density can be replaced by Equation 2.28

$$\frac{M_{SiO_2} g}{A} \frac{1}{H_{FB}} = \frac{M_{SiO_2}}{AH_0 (1 - \varepsilon_{e0})} (1 - \varepsilon_{FB}) g \quad (2.35)$$

After simplifying

$$\varepsilon_{FB} = 1 - \frac{H_0}{H_{FB}}(1 - \varepsilon_{e0}) = 1 - \frac{H_0}{H_{FB}} + \frac{H_0}{H_{FB}}\varepsilon_{e0} \quad (2.36)$$

This equation reduces to Equation 2.32 by assuming that the initial external void fraction is very small (approaching to zero) so the third term at the right can be neglected.

Another drawback of using Equation 2.32 for calculating the void fraction is the assumption that the pressured drop equals the apparent weight of powder. As shown in plots related to the hydrodynamic characteristics of the fluidized beds, not all the powder is suspended by the gas phase during conventional fluidization; therefore, the terms corresponding to the mass of the powder in Equation 2.35 are not equal and cannot cancel each other.

In the R-Z plots shown below, Equation 2.28 has been used to find the agglomerate density by using the mass of powder suspended by the gas phase obtained from the experimental pressure drop and by assuming an initial bed voidage (ε_{e0}) of 0.3. The agglomerate density is then used in Equation 2.15 to calculate the inter-agglomerate void fraction (ε_{FB}). The R-Z plots were constructed for the different fluidized nanopowders. Figure 2.42 shows the Richardson-Zaki plots ($\ln(U)$ vs. $\ln(\varepsilon = \varepsilon_{FB})$) corresponding to the conventional and jet assisted fluidization of Aerosil R974. Similarly, Figure 2.43 shows the R-Z plots for other APF nanopowders. Figure 2.44 shows the Richardson-Zaki plots for ABF nanopowders; although the R-Z theory is not applicable for these nanopowders during conventional fluidization because of their non-homogeneous (bubbling) fluidization behavior.

The slopes and y-intercepts of these plots are summarized in Table 2.4. The slopes are used in the R-Z equation to find “ n ”

$$\frac{U}{U_t} = \varepsilon^n \quad (2.37)$$

while the y-intercepts are used to find the terminal velocity (U_t) of the agglomerates. The average agglomerate size can be estimated by using Equation 2.14 which needs the agglomerate density and the terminal velocity as inputs. It has been initially assumed that the agglomerate density decreases as a consequence of the jet-processing which was verified by measuring the bulk density values of the nanopowder after jet processing. The estimated agglomerate sizes are also shown in Table 2.4.

Table 2.4 Slopes and Y-intercepts from the Richardson-Zaki Plots from Figure 2.42 246 and Figure 2.44

Nano-powder	Mass grams	Conventional					Jet Assisted				
		n slope	ln(U _t) y-intercept	ρ_{agg} kg/m ³	U _t m/s	dp um	n slope	ln(U _t) y-intercept	ρ_{agg} kg/m ³	U _t m/s	dp um
Aerosil R974	9.5	6.7	-2.50	40.5	0.082	263	11.1	-2.44	13.9	0.087	474
Aerosil R974	13	6.3	-2.47	40.6	0.085	266	14.5	-2.37	16.7	0.094	447
Aerosil R974	20	8.1	-2.27	37.8	0.105	306	13.7	-2.25	15.4	0.107	496
Aerosil 200	15.7	6.2	-1.93	33.1	0.146	388	9.5	-1.88	14.5	0.154	617
Aerosil 90	18.0	5.8	-1.21	42.1	0.301	492	7.6	-2.34	20.7	0.097	404
Aerosil Raw 90	21.2	7.4	-1.74	20.8	0.177	543	9.5	-1.92	19.4	0.147	515
Aeroxide Alu C	22	2.8	-1.92	52.6	0.147	307	5.9	-3.01	34.5	0.050	221
Aeroxide Raw TiO2 P25	61.2	6.0	1.03	101.6	2.812	960	3.4	-2.66	89.6	0.070	162
Aeroxide TiO2 P25	60	2.2	-1.68	137.0	0.188	213	5.0	-2.78	94.2	0.063	149

The term Raw refers to undensified material obtained from the process.

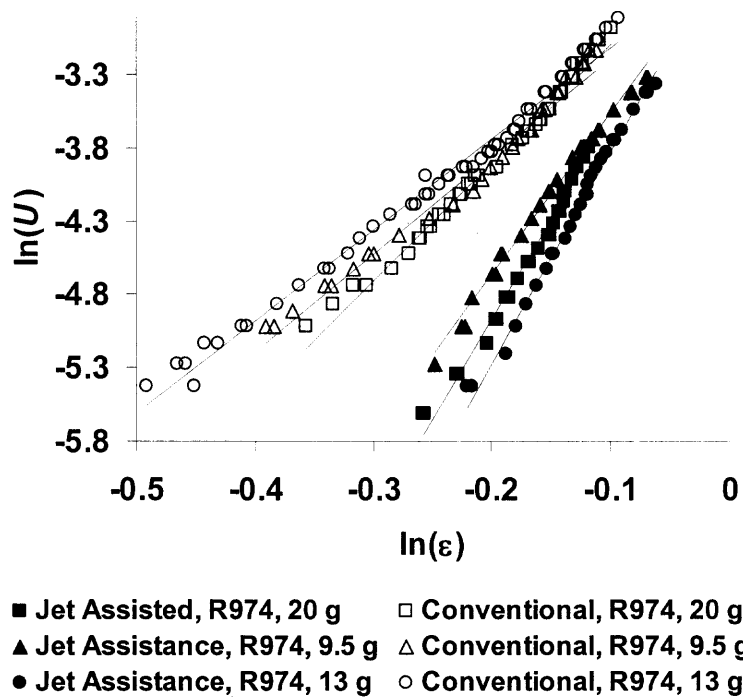


Figure 2.42 Richardson-Zaki plots corresponding to conventional and jet assisted fluidization of different amounts of Aerosil R974.

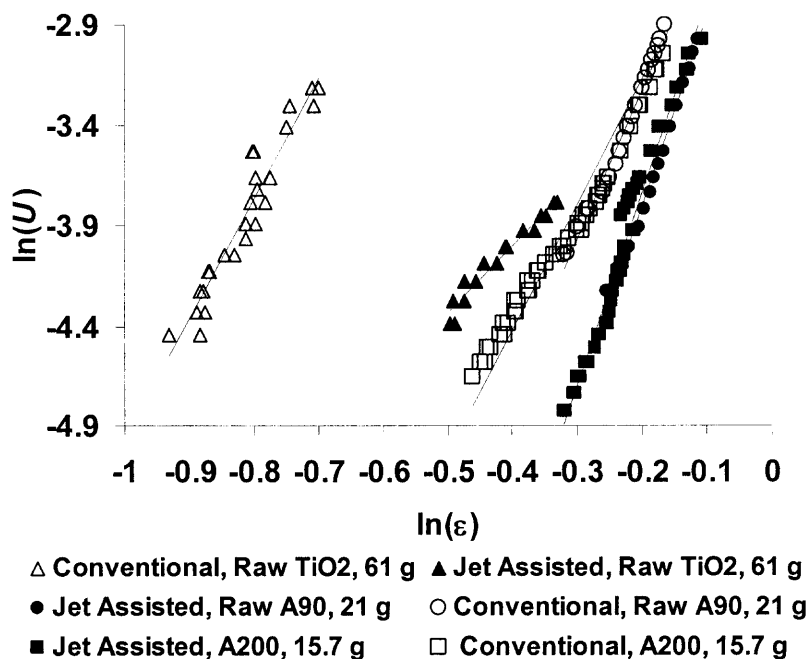


Figure 2.43 Richardson-Zaki plots corresponding to conventional and jet assisted fluidization of other APF nanopowders (Aerosil 200, “Raw” Aerosil 90, and “Raw” Aeroxide TiO₂ P25). The term “Raw” is used to describe nanopowder obtained directly from the process.

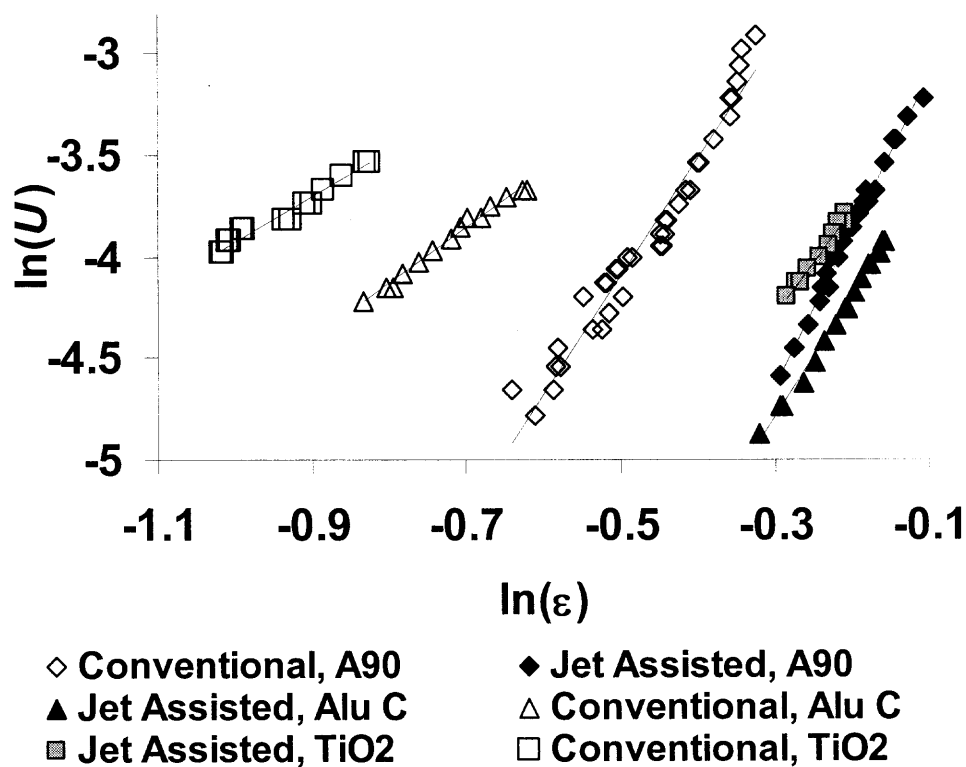


Figure 2.44 Richardson-Zaki plot corresponding to conventional and jet assisted fluidization of ABF nanopowders.

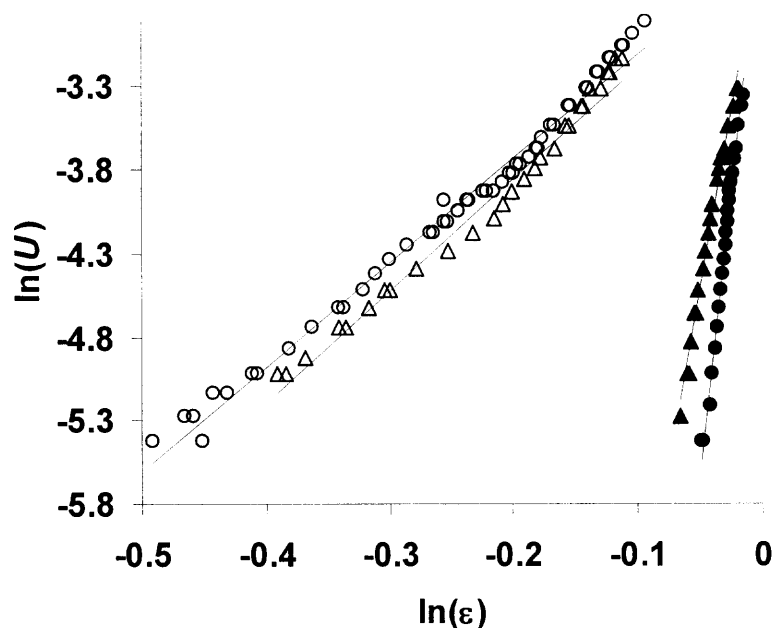
In these figures, the R-Z plots of the jet assisted fluidization have shifted towards the right, indicating an increase in void fraction for equivalent superficial gas velocities. From the data in Table 2.4, it can be seen that the Richardson-Zaki indexes average about 6 for conventional fluidization of APF nanopowders (Aerosil R974, 90, 200, Raw 90 and Raw TiO₂ P25). The R-Z index corresponding to 20 grams of Aerosil R974 is slightly higher (8.1) because the bed height data at high flow rates was not available due to the larger than expected bed expansion. The average R-Z index of the APF nanopowders is close to the typical values of 4.8 to 5.6 commonly used in the literature for low Reynolds number flow (4.65 to 5.3 for $Re < 0.2$)³⁹. The indexes corresponding to ABF nanopowders (Aeroxide Alu C and Aeroxide TiO₂ P25) are much lower; this can be explained by the

fact that the R-Z criterion was not designed for heterogeneous fluidization, i.e., fluidization with bubbles. Furthermore, the R-Z indexes increase for all of the jet assisted fluidization nanopowders. This indicates that the R-Z index may not only be a function of the Reynolds number as originally thought³⁹ when applied to nanopowders, but may also be dependent on the particular fluidization conditions such as the characteristics of the fluidizing powder and the fluidizing gas⁴¹.

The terminal velocities of the agglomerates corresponding to the conventional and assisted fluidization obtained from the R-Z plots do not differ much for the APF type nanoparticles (Aerosil R974 and Aerosil 200) but show significant difference for the ABF type nanoparticles. There is also a significant difference between the calculated agglomerate sizes in a conventional and a jet assisted fluidized bed. Most surprising is the fact that the estimated agglomerate sizes for the assisted fluidization are larger than those estimated for conventional fluidization for APF nanopowders. The difference in the estimated agglomerate sizes is so large that it could not be explained due to a change in the magnitude of the drag coefficient, believed to occur due to the aggregate shape. In these calculations, an extremely low drag coefficient, multiplied by a factor 0.2, had to be used to obtain a smaller agglomerate size. This leaves the agglomerate density as the only variable in Equation 2.14 that could account for such incongruity.

Since a lower than initial agglomerate density has already been assumed in the previous calculations, a higher agglomerate density is assumed for the following calculations related to the fluidization of Aerosil R974. Figure 2.45 shows the R-Z plots of conventional and jet assisted fluidization of Aerosil R974. In this plot, a higher than initial agglomerate density has been assumed for the jet assisted fluidization. The lines

corresponding to the jet assisted data are shifted further towards the right indicating a larger void fraction than when a lower agglomerate density was assumed. Table 2.5 summarizes the data corresponding to Figure 2.45. By increasing the agglomerate density, the estimated agglomerate size is similar or slightly lower than the agglomerate size corresponding to conventional fluidization. However, when analyzing the bulk density of the powder after fluidization (at no flow conditions) it was found that the initial void fraction of the packed bed, as shown in Table 2.5, would have to be quite large which does not seem reasonable. This indicates that assuming a larger agglomerate density may not provide an accurate estimation of the agglomerate sizes. Since, there are no other variables in Equation 2.14 that could further change the estimated agglomerate size; the R-Z method may not be applicable for calculating agglomerate sizes, especially in a jet assisted fluidized bed where the bed expansion is extremely large. Missing parameters in Equation 2.14 that are important for the estimation of agglomerate sizes are the existence of an agglomerate size distribution, the possibility of having agglomerates with different densities and a proper description of the drag coefficient. The standard equations to calculate the drag coefficient may need to be significantly modified to account for the porosity, the irregular surface of the agglomerate and also by the interactions or presence of other agglomerates in the medium.



▲ Jet Assistance, R974, 9.5 g △ Conventional, R974, 9.5 g
● Jet Assistance, R974, 13 g ○ Conventional, R974, 13 g

Figure 2.45 Richardson-Zaki plots corresponding to conventional and jet assisted fluidization of different masses of Aerosil R974 assuming a higher agglomerate density for the jet assisted cases.

Table 2.5 Slopes and Y-intercepts from the Richardson-Zaki Plots in Figure 2.45

Nano-powder	Mass grams	Conventional						Jet Assisted					
		n slope	ln(U _i) y-inter.	ρ_{agg} kg/m ³	ϵ_0	U _t m/s	dp um	n slope	ln(U _i) y-inter.	ρ_{agg} kg/m ³	ϵ_0	U _t m/s	dp um
Aerosil R974	9.5	6.7	-2.50	40.5	0.2	0.082	263	43.0	-2.35	45.3	0.8	0.096	267
Aerosil R974	13	6.3	-2.47	40.6	0.2	0.085	266	68.1	-2.27	66.8	0.8	0.104	229

2.4.11 Estimating the Agglomerate Size, Density and Terminal Velocity by Using the Richardson-Zaki Criterion Coupled with the Fractal Dimension of the Agglomerate

The necessity of assuming a value for the agglomerate density weakens the previous method for the estimation of agglomerate sizes. For that reason, a method based on the fractal analysis has been used in previous works^{5, 51, 52}. This method is based on the assumption that agglomerates of nanoparticles have a hierarchical fractal structure, with

the nanoparticles as the primary particles which form ever larger and more complex nanoagglomerates as the final structure. The theory is based on the number of primary particles (N) and the diffusion limited fractal dimension (D_f). In this theory, it was assumed that the buoyancy force is negligible, the terminal velocity of the primary particles is unaffected by Brownian motion, a drag coefficient corresponding to a perfect hard sphere and a dilute medium that leads to the assumption of a Richardson-Zaki exponent, “ n ”, for example, a value of 5.6⁵² at low particle Reynolds number.

The ratio of the agglomerate density to the primary particle density is given by

$$\frac{\rho_{agg}}{\rho_s} = N^{1-\left(\frac{3}{D_f}\right)} \quad (2.38)$$

Assuming that the settling velocities of the agglomerate and the primary particle are governed by Stokes law, the relationship of the Stokes settling velocity of the agglomerate to the primary particle in terms of N and D_f is given by

$$v_{agg} = v_0 N^{1-\left(\frac{1}{D_f}\right)} \quad (2.39)$$

Considering that under fluidization conditions, the settling velocity is equal to the terminal velocity, the Richardson-Zaki criterion can be applied. This leads to the following equation for the superficial velocity as a function of the terminal velocity of the primary particle, v_0 ; the total solid fraction, ϕ ; the R-Z index, n ; the number of primary particles, N , and the fractal dimension, D_f .

$$U = v_0 N^{1-\left(\frac{1}{D_f}\right)} \left(1 - \phi N^{\left(\frac{3}{D_f}\right)-1} \right)^n \quad (2.40)$$

As indicated in the references⁵, after assuming a value for the R-Z index, n , a plot of the non-dimensional velocity against the solid fraction, $\left(\frac{U}{v_0}\right)^{(1/n)}$ vs. ϕ , of the experimental data should produce a straight line whose y-intercept is “ b ”

$$b = N \left[1 - \left(\frac{1}{D_f} \right) \right]^{(1/n)} \quad (2.41)$$

and slope, “ m ”

$$m = -bN \left(\frac{3}{D_f} \right)^{-1} \quad (2.42)$$

can be obtained from a linear regression of the data. Hence, the ratio of the radius of the agglomerate to the radius of the primary particle is given by

$$\frac{r_{agg}}{r_p} = \sqrt{-mb^{n-1}} \quad (2.43)$$

In addition, the fractal dimension, D_f , can be calculated from

$$D_f = \frac{2}{\frac{\ln(m/-b)}{n \ln b} + 1} + 1 \quad (2.44)$$

This value can then be replaced in Equation 2.41 or Equation 2.42 for finding the number of primary particles, N .

In the results shown, an R-Z index of 5 was assumed; the results are relatively insensitive to changes in the R-Z index in the order of +/- 1. Figure 2.46 shows the plot of the non-dimensional velocity against the solid fraction for APF nanopowders. Similarly, Figure 2.47 shows the corresponding plot for ABF nanopowders. In addition, Table 2.6 summarizes the parameters corresponding to these plots. It can be seen that data corresponding to the jet assisted fluidization shifts towards the left, and then the void

space in the fluidized bed has increased significantly; indicating a better dispersion of the powder.

The results given in Table 2.6 are somewhat inconclusive because the model predicts larger than expected agglomerate sizes based on the average sizes obtained from the measurements with the FBRM Lasentec probe. From these results, it seems that the current method to estimate agglomerate sizes based on the fractal dimension and the Richardson-Zaki criterion may work for conventional fluidization but not for assisted fluidization.

Table 2.6 Parameters Corresponding to the Fractal Analysis Coupled with the R-Z Model for the Estimation of the Agglomerate Size

	Nano-powder	Solid		d_p	Slope	y-inter.	d_{agg}	v_{agg}	ρ_{agg}	Df	N
		Mass	density								
	gr.	kg/m ³	m	"m"	"b"	um	m/s	kg/m ³	[-]	[-]	
Conventional	Aerosil R974	9.45	2200	1.2E-08	-1543.2	25.13	298	0.097	36	2.593	2.49E+11
	Aerosil R974	13	2200	1.2E-08	-1443.9	24.60	276	0.087	37	2.595	2.07E+11
	Aerosil 200	15.7	2200	1.2E-08	-1351.7	24.12	257	0.079	39	2.596	1.75E+11
	Aerosil 90	18.0	2200	1.3E-08	-1019.9	26.11	283	0.137	102	2.633	2.64E+11
	Aeroxide Alu C	22	4000	1.3E-08	-928.16	22.94	208	0.131	99	2.618	1.02E+11
	Aeroxide TiO ₂ P25	60	4000	3.0E-08	-335.18	19.89	217	0.341	237	2.682	2.25E+10
Jet Assisted	Aerosil R974	9.5	2200	1.2E-08	-7655.4	23.94	1560	0.509	7	2.51	6.87E+12
	Aerosil R974	13	2200	1.2E-08	-8333.1	24.32	648	0.082	6	2.464	4.60E+11
	Aerosil 200	15.7	2200	1.2E-08	-5343.2	24.45	524	0.084	10	2.496	3.82E+11
	Aerosil 90	18.0	2200	1.3E-08	-3780.2	24.05	462	0.091	25	2.517	2.86E+11
	Aeroxide Alu C	22	4000	1.3E-08	-2554.6	18.69	230	0.047	29	2.497	4.03E+10
	Aeroxide TiO ₂ P25	60	4000	3.0E-08	-59.209	11.12	29	0.019	751	2.756	1.61E+08

d_p : primary particle diameter

v_{agg} : terminal velocity of the agglomerate

d_{agg} : estimated agglomerate diameter

Richardson-Zaki index used: $n = 5$

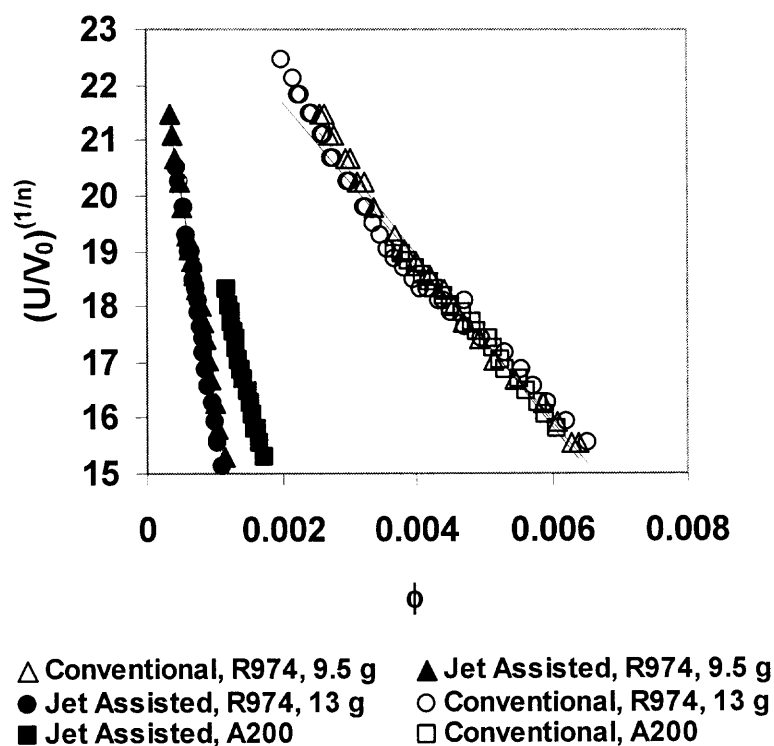


Figure 2.46 Plot corresponding to the fractal analysis coupled with the Richardson-Zaki models for conventional and micro-jet assisted fluidization of APF nanopowders.

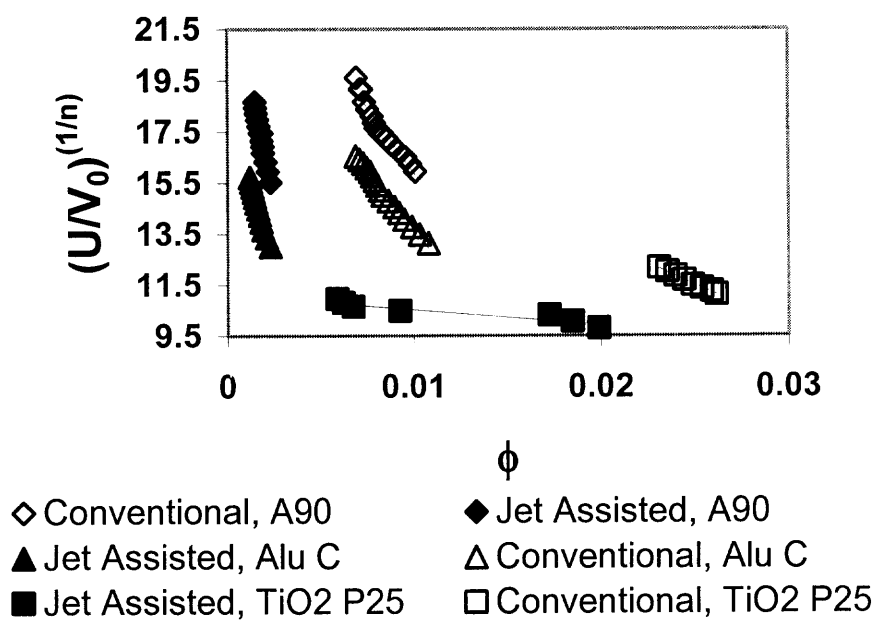


Figure 2.47 Plot corresponding to the fractal analysis coupled with the Richardson-Zaki models for conventional and micro-jet assisted fluidization of ABF nanopowders.

2.4.12 Fluctuations in Pressure Drop Measurements during Fluidization of Nanopowders

In the experimental section method, it has been shown that a highly accurate differential pressure transmitter has been used for the measurement of the pressure drop across the bed of nanopowders. This transmitter can report pressure drops as low as one thousandth of an inch of water ($0.001 \text{ in H}_2\text{O} = 0.25 \text{ Pa} = 0.0025 \text{ mbar}$). While using this instrument for measuring the pressure drop across the fluidized beds it was found that several readings were not constant with respect to time. It is important to recall that Aerosil R974 has a particulate fluidization behavior free of bubbles; therefore, the fluctuations are not generated by bubbling. Fluctuations in pressure drop during bubbling of the fluidized bed were found at gas velocities above the minimum bubbling velocity (about 3 cm/s for Aerosil R974) but these and are not the focus of the current study.

For example, Figure 2.48 shows the pressure drop readings across a fluidized bed of Aerosil R974 with respect to time under reduced electrostatic charge conditions, i.e., using alcohol vapor, at two different gas velocities. In some previous works⁷, it has been reported that the minimum fluidization velocity of Aerosil R974 is about 0.25 cm/s; however, it can be seen that at a gas velocity of 0.33 cm/s, the pressure drop across the bed of nanopowder fluctuates quite considerably when compared to the pressure drop readings at a gas velocity of 1.5 cm/s. From these pressure drop readings, the average and standard deviation can be found to properly describe the pressure drop across the fluidized beds of nanopowders.

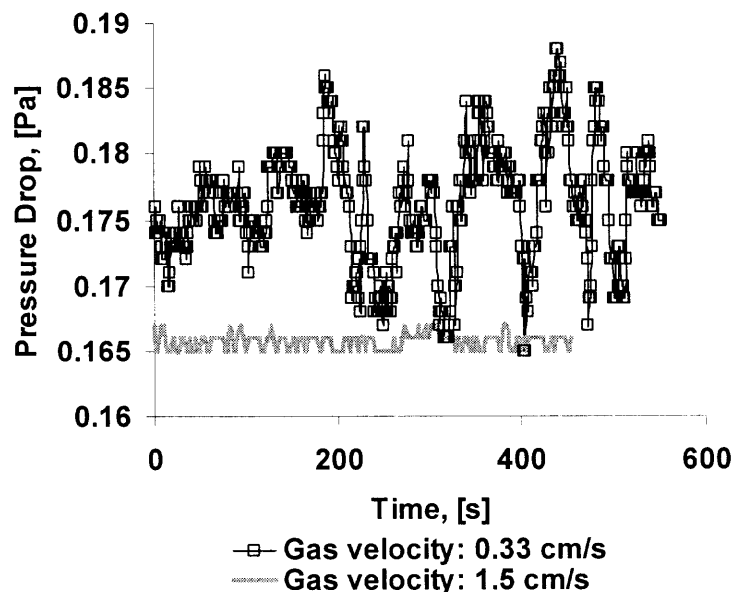


Figure 2.48 Pressure drop data at two different gas velocities obtained during fluidization of Aerosil R974 under reduced electrostatic charge conditions.

For example, Figure 2.49 shows the average pressure drop and their corresponding standard deviations with respect to the superficial gas velocity during conventional fluidization of 20 grams of Aerosil R974. It can be seen that the average pressure drop plateaus at a gas velocity of 0.3 cm/s. This result corresponds to the minimum fluidization velocity (U_{mf}) reported in previous works^{2, 5, 7, 8}. However, the pressure drop fluctuations, represented by the standard deviations, are significant up to a gas velocity of about 1 cm/s. These fluctuations are in the range of +/- 2.5% of the average pressure drop readings and they may have been neglected or not measured at all in past research works. These fluctuations are important because they may indicate a non-fully fluidized state. Moreover, as described in previous works, the pressure drop should increase proportionally to the superficial gas velocity before reaching minimum fluidization velocity, this behavior is not seen when fluidizing nanopowders, and the fluctuations in pressure drop may indicate that, before fluidization, the bed of

nanopowder does not behave like a packed bed but rather like a channeling bed. Furthermore, the gas velocity at which the fluctuations in pressure drops reach a low level may indicate a fully fluidized state of the agglomerates.

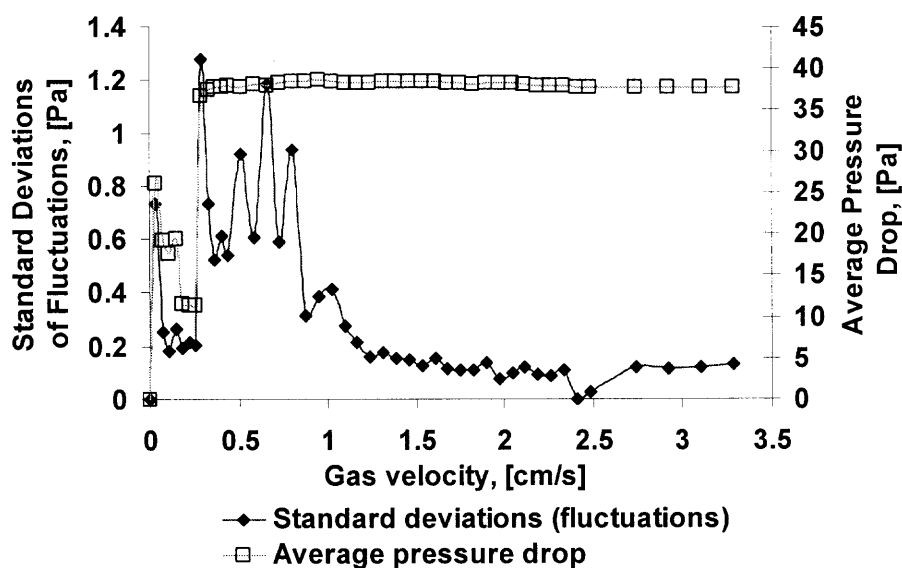


Figure 2.49 Average and standard deviations of the pressure drop with respect to superficial gas velocity during conventional fluidization of 20 grams of Aerosil R974.

It is believed that the fluctuations in pressure drop may arise due to the presence of different interacting forces between the agglomerates that hinder their full fluidized state. For example, Figure 2.50 shows a comparison of the fluctuations given by conventional fluidized beds with and without the presence of electrostatic charges. As explained earlier, the electrostatic charges in a fluidized bed were reduced by using alcohol as additive to the gas phase. This figure shows that the intensity of the pressure fluctuations, given by the standard deviation, is reduced when the electrostatic charge is minimized in the fluidized bed, indicating that a full fluidization condition is reached at lower gas velocities when compared to a fluidized bed with electrostatic charges. This

figure also shows that there is a slightly increase in the fluctuations at gas velocities larger than 3 cm/s and this is due to the appearance of slight bubbling in the fluidized bed.

Also, the effects of using a different fluidizing gas, such as neon, were studied. Neon has a higher viscosity than nitrogen when compared at the same temperature. The higher viscosity leads to a larger drag force on the agglomerates. When studying the pressure drop fluctuations, shown in Figure 2.51, the lowest fluctuation levels are reached at gas velocities of about 1.5 cm/s, for fluidization with nitrogen, and about 1 cm/s for fluidization with Neon. Furthermore, the data obtained when using Neon as the fluidizing gas seem to be shifted towards lower gas velocities (left) when compared to the data collected when using nitrogen. This indicates that a fully fluidized bed of nanoparticles will occur at lower gas velocities by increasing the viscosity of the fluidizing gas.

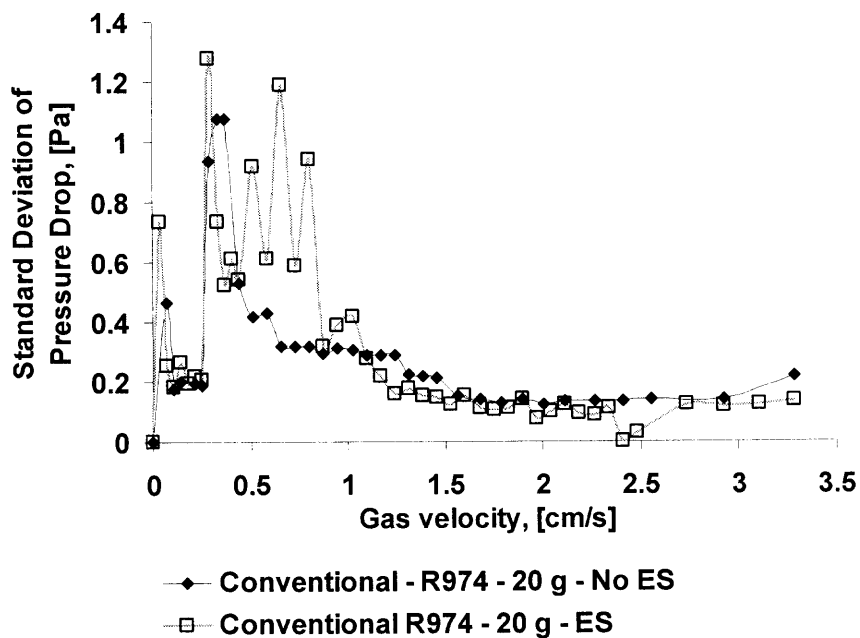


Figure 2.50 Standard deviation of the pressure drop readings as a function of gas velocity during fluidization of Aerosil R974 under different electrostatic charge conditions (ES: Electrostatic).

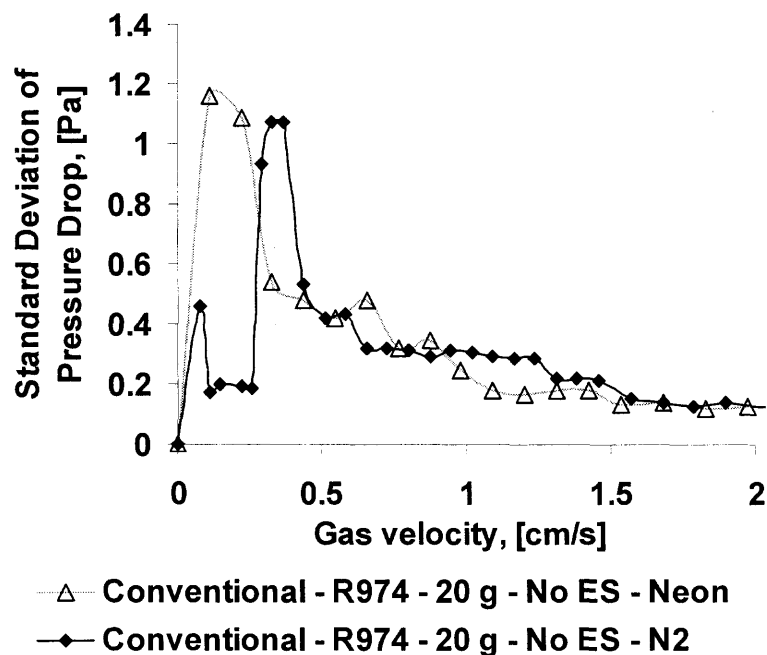


Figure 2.51 Standard deviation of the pressure drop readings as a function of gas velocity during fluidization of Aerosil R974 with different gases and under reduced electrostatic charge conditions (ES: Electrostatic).

Previous works^{7, 8} have reported hysteresis in the measurements of the fluidized bed height and pressure drop when comparing the fluidization data collected when increasing the flow of the fluidizing gas and then decreasing the flow. This hysteresis is also observed somewhat in the pressure drop fluctuations. For example, Figure 2.52 shows compares the pressure drop fluctuations obtained when increasing and decreasing the fluidizing gas velocity under reduced electrostatic charge conditions. It can be seen that the pressure drop fluctuations are slightly lower when the gas velocity is reduced. Moreover, the pressure drop fluctuations are much lower when compared with the results obtained when the electrostatic charge in the fluidized bed was not removed (see Figure 2.50).

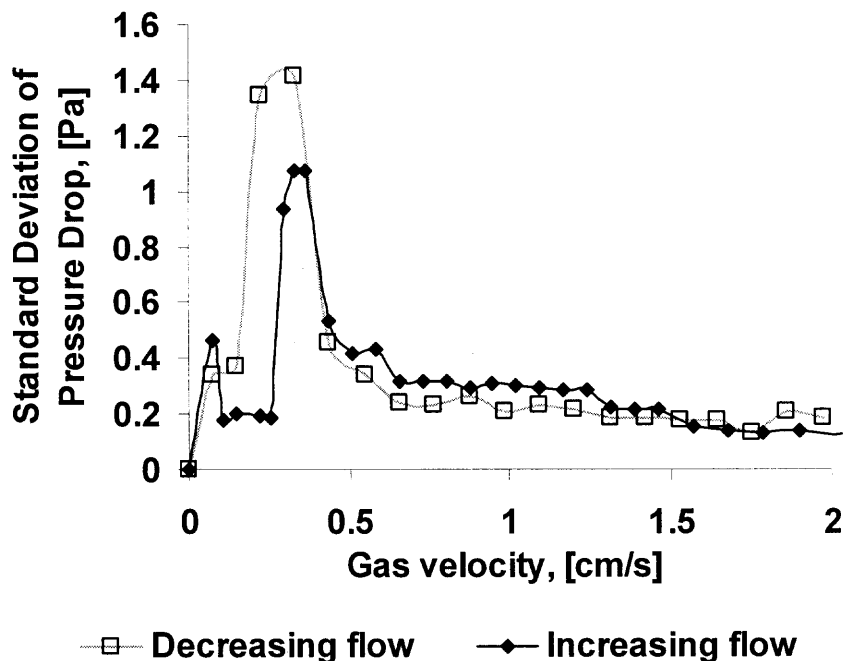


Figure 2.52 Standard deviation of the pressure drop readings as a function of gas velocity during fluidization of Aerosil R974 with nitrogen under reduced electrostatic charge conditions.

2.5 Conclusions

Extensive work has been presented on the fluidization of agglomerates of fumed metal oxide nanoparticles. Among the most significant achievements are the reduction of electrostatic charge in fluidized beds, the enhancement of fluidized beds of agglomerates of nanoparticles by using a jet generated from a micro-nozzle and the successful in-situ imaging and measurement of fluidized agglomerates. The reduction of electrostatic charge in fluidized bed of nanoparticles was critical in the development of other experiments such as the jet assisted fluidization and the in-situ imaging and sizing of the fluidized agglomerates.

It has been shown that by using a downward pointing jet coming from a micro-nozzle, nanopowders that show agglomerate particulate fluidization (APF) behavior expanded several times further relative to the already expanded conventional fluidized bed height. For nanopowders that show agglomerate bubbling fluidization (ABF) behavior, the jet assistance transformed their fluidization behavior into an APF-like characterized by the absence of bubbles and a fluidized bed expansion several times the initial bed height. It has also been shown that jet assistance method improves fluidization regardless of the location and direction of the micro-nozzle(s), although the best performance was achieved by positioning the nozzle relatively close to the gas distributor plate at the bottom of the column and pointing downwards. Under these conditions, full fluidization of the entire amount of powder placed in the column was achieved. These results were verified by measuring the fluidized bed expansion and pressure drops with respect to the fluidizing gas velocities.

Experiments were conducted with nozzles of different sizes (from 100 up to 500 microns) and an upstream pressure of 75 to 120 psig. The size of the micro nozzles were of particular importance, the smaller the nozzle size the higher the shear generated by the jet but also the lower the flow passing through the orifice of the nozzle. For example, for many nanopowders it was found that the optimal nozzle sizes were between 100 and 250 microns. These nozzle sizes provided a jet with enough shear and gas velocity to result in breaking of the agglomerates and generating turbulence. However, some ABF nanopowders, such as Aerioxide TiO₂ P25, only require high turbulence for achieving an APF behavior. For these nanoparticles a larger nozzle size was used (500 μm) but with a lower upstream pressure (20 psig). The rate at which the agglomerates were processed

by the jet was also studied and it was found that it depends on the total superficial gas velocity, the amount of nanopowder, the size and number of the nozzles. Since the main purpose of enhancing the fluidization of these nanopowders was for industrial applications, scaling up of the jet assisted system was also studied. It was demonstrated that the jet assisted fluidization also gives good results at a larger scale. The benefits of the jet assisted fluidization when compared against other assisting fluidization methods such as sound, vibration or moving magnetic particles consists of lower energy consumption, its simplicity and that no addition of foreign particles or materials into the fluidized bed is necessary.

In-situ measurement and imaging of the fluidized agglomerates was achieved by reducing the electrostatic charge and using the FBRM and PVM probes from Lasentec. It has been shown that the probes successfully characterize the agglomerates by giving reasonable size distributions. The images and data show that the probes are able to differentiate between types of powders (such as Aerosil R974 and Aerosil 90) and can also evaluate the effects of jet processing. The results show that the agglomerates are reduced in size and density due to the jet processing.

Methods used in previous works for the determination of the fluidized agglomerate size, such as the conventional Richardson-Zaki and the R-Z method coupled with fractal analysis, do not appear to give good estimates of the size of fluidized agglomerates, especially for the jet assisted experiments, when compared to the results from the Lasentec probes. It should be noted that both of these methods result in a single value of the agglomerate size, whereas in reality, the fluidized agglomerates consist of a broad size distribution. Also for nanopowders, the R-Z exponent " n " depends on the

properties of the powder as well as the hydrodynamics of the fluidized bed, i.e., the Reynolds number. Moreover, the R-Z method was developed based on experiments involving non-porous particles of similar density and size whereas in a fluidized bed of agglomerates of nanoparticles there is a wide size distribution and the density of the agglomerates may vary as shown by the imaging obtained with the PVM probe. Only after jet processing of the agglomerates, would a uniform agglomerate density may be expected (as also shown by the PVM images also). Lastly, the assumption of Stokes flow around the fluidized agglomerates ignores the fact that these agglomerates are very porous, have an irregular surface, and are in contact with or influenced by other agglomerates. Therefore, the drag coefficient may be appreciably different than that for single sphere Stokes flow.

The presence of pressure fluctuations seems to indicate that the method, by which the minimum fluidization velocity is usually found for micron size particles, i.e., the point at which the pressure drop starts to plateau, may not represent a fully fluidized bed condition for agglomerates of nanoparticles. The velocity where the pressure fluctuations become very small (are damped out) may be a better indication of when a fully fluidized bed is achieved. These fluctuations occur due to the channeling (rather than flow through a packed bed) that is seen before the bed of nanopowder begins to fluidize.

CHAPTER 3

EVALUATION OF ASSISTING METHODS ON FLUIDIZATION OF HYDROPHILIC NANOAGGLOMERATES BY MONITORING MOISTURE IN THE GAS PHASE

3.1 Overview

Agglomerates of nanoparticles were fluidized conventionally and under the influence of assisting methods such as vibration and/or moving magnetic particles. The adsorption/desorption rate of moisture of fluidized hydrophilic nanopowders was monitored during humidification/drying of the powder in order to find their adsorption isotherms at room temperature and to evaluate the assisting methods. Adsorption isotherms were verified by a gravimetric method. The nanopowders studied were Degussa Aerosil[®] 200 and Aerosil[®] 90, which were chosen because of their different fluidization behaviors.

The moisture level in the nitrogen gas used to fluidize the powders was monitored on-line by using humidity sensors upstream and downstream of the fluidized bed. Moisture was added to the fluidizing nitrogen by bubbling it through water. The amount of moisture adsorbed/desorbed by the powders was obtained by integration of the time dependant moisture concentration. It was found that when the bed of powder is assisted during fluidization, the mass transfer between the gas and the nanopowder, as measured by the amount of moisture adsorbed/desorbed, is larger than when the powder is conventionally fluidized. Vibration assistance was found to be more effective for Aerosil[®] 200, but magnetic assistance was needed for Aerosil[®] 90 in order to break down the very large agglomerates formed in this powder.

3.2 Introduction

Many industries rely on advantages of gas-solid fluidization to process their products, such as good mixing, high heat and mass transfer rates, improved reaction kinetics and large gas throughput. More specifically, gas-solid fluidization is widely used in reactions such as cracking of hydrocarbons, where the solid particles act as a catalyst, and intermediate processes such as drying, coating, granulation, mixing, and purification of particulate materials.

Research on gas-solid fluidized bed systems is quite extensive, but research related to the dynamics of the powder inside the fluidized bed is somewhat limited, as for powders that do not fluidize well, such as ultra-fine and nanoparticles (Geldart Group C powders). Inadequate fluidization results in poor mixing between the solid and gas phases. When fine particles are attempted to be fluidized at low gas velocities, the fluidizing gas rises in the form of channels, and large bubbles appear at high gas velocities, which bypass the bed of powder that remains more or less motionless, and there is entrainment of the particles.

Amorphous fumed silica nanoparticles used in the present study are produced by the pyrogenic process⁵³. The pyrogenic process involves the use of a flame reactor in which nanoparticles are formed under high temperatures (2000 °F). Because of the high temperatures, fumed metal oxide nanoparticles sinter resulting in aggregates of submicron size⁵⁴. Subsequently, aggregates of nanoparticles come together in the form of chain and net-like structures forming simple agglomerates several microns, or tens of microns in size. It is believed that these agglomerates have a hierarchical fractal structure⁵⁵.

Fumed metal oxide nanoparticles have been conventionally fluidized in the form of large or complex porous agglomerates by many research groups^{1, 7, 9}. The fluidization behavior of agglomerates of nanoparticles has been classified as either agglomerate particulate fluidization, (APF) or agglomerate bubbling fluidization (ABF)¹. APF behavior is characterized by a large bed expansion of several times the initial bed height at zero flow, smooth fluidization, and relatively low minimum fluidization velocities. ABF behavior shows little bed expansion (it increases less than 50% with respect to the initial bed height at zero flow), bubbling, and the bed of powder behaves more like Geldart Group B micron-size particles.

To overcome the difficulties during fluidization, like bubbling or channeling, assisting methods have been developed, such as sound assisted fluidization², centrifugal forces also called rotating fluidized beds¹², vibration⁵ or disrupting the bed by moving magnetic particles in an oscillating magnetic field⁸ to improve the dispersion of the nanopowder in the gas phase. A relatively large literature exists describing the application of magnetic assistance to fluidize micron-sized powders of either magnetic or a mixture of magnetic and non-magnetic powders to eliminate bubbles and gas-bypassing^{56, 57, 58, 59}. However, the studied magnetic assisted fluidization method⁸ is distinctly different; namely, the relatively large magnetic particles do not fluidize along with the nanopowder and remain close to the distributor. In this work, both vibration and moving magnetic particles are used as assisting methods.

It has been previously reported that when using vertical vibration during fluidization of hydrophobic Degussa Aerosil[®] R974 just above the minimum fluidization velocity the bed height increased by about a factor of two and continued to expand up to

five times the original bed height as the gas velocity is increased⁵. Also, it was found that the movement of magnetic particles excited under an oscillating magnetic field improved the dynamics of the fluidized bed of nanopowders. The moving magnetic particles at the bottom of the fluidization column tend to break-up large clusters of agglomerates and also gas bubbles. For example, it has been shown that when fluidizing a mixture of 20% large clusters of agglomerates (larger than 500 μm) and 80% finer agglomerates (smaller than 500 μm) of Aerosil[®] R974, the magnetic assistance increased the bed expansion 3 to 5 times when compared against conventional fluidization⁸.

In this paper, a new method is introduced for quantifying the impact of the assisting methods in the fluidization of agglomerates of nanoparticles. It consists of studying the drying of a hydrophilic bed of agglomerates of nanoparticles by monitoring the release of moisture from the powder to the gas phase. Information on the rate of drying and the total moisture released by the powder is used to compare conventional fluidization against assisted fluidization.

The drying process of porous particles is complex due to the different mechanisms by which the moisture is held at the particle's surface. If the interactions between water molecules and the surface of the particle are strong, chemisorption of water occurs; on the other hand, if the interactions are weak the phenomenon is called physisorption^{60, 61, 62}.

Several experimental and modeling works related to the drying of solids in a fluidized bed have been previously reported with materials other than nanopowders. Hoebnik et al.^{63, 64} modeled the drying of wet solids in a fluidized bed considering the bubble phase and also the impact of diffusion limited drying. Chandran et al.⁶⁵ developed

a kinetic model for the drying of solids in fluidized beds assuming two different drying rates. They compared their model against experimental results from batch and continuous single and spiral fluidized beds with good agreement. Chen and Pei⁶⁶ developed a mathematical model to describe the drying of several non-hygroscopic and hygroscopic materials. Davidson et al.⁶⁷ studied the drying rate of wetted porous silica-alumina particles in an air-fluidized bed by mounting the fluidized bed on a balance and by measuring the inlet and outlet air humidity by wet and dry bulb thermometers. A model for describing batch fluidized-bed drying of moist porous particles shows that capillary flow and vapor diffusion both affect the moisture transfer⁶⁸. The drying rate of porous spherical brick balls of 50 mm in diameter placed inside of a fluidized bed of glass beads was studied by measuring the water content of the sample using a hot wire method^{69, 70}. Modeling work and experiments for drying grains in a fluidized bed have also been reported^{71, 72}. This work is the first study on drying in a fluidized bed of nanoparticles.

In addition to evaluating the impact of the assisting methods, data related to the adsorption isotherms of the nanopowders is obtained in order to relate the specific surface area of the nanopowders with the amount of moisture adsorbed. It is well known that the adsorption isotherms are essential for understanding the drying or desorption in the porous nanoagglomerates. For example, Mihoubi et al.⁷³ studied the adsorption isotherms of bentonite clay, a porous material composed of alumina-silicates, at different temperatures. Another interesting research work that shows isotherms of silica gel-water that are described by a Henry-type equation has been done by Ng et al.⁷⁴. In this work, it is shown that adsorption isotherms of hydrophilic silica nanopowders follow a similar tendency when exposed to low levels of moisture.

3.3 Experimental Methods

A certain amount of dry fluidized nanopowder is humidified with a nitrogen gas stream that contains a constant amount of moisture. After the moisture in the powder has reached equilibrium with the moisture in the gas, humidification is stopped, and dry gas is sent through the fluidized bed. The amount of moisture released by the fluidized bed of powder is monitored by measuring the moisture content of the gas stream leaving the fluidization column as a function of time.

Based on the procedure described above, an experimental system was designed and built as shown in Figure 3.1. The system was composed of a fluidization column, equipment that provided either vertical vibration or magnetic assistance, and instruments to measure the flow of gas, the pressure drop across the bed and the moisture levels in the fluidizing gas. The fluidization column was made of acrylic plastic and its diameter was selected depending on the assisting method used. At the bottom of the column, a 0.002 m thick sintered stainless steel metal plate with pore size of 100 μm and a pore fraction of about 40% was used as the gas distributor.

For vibrated assisted fluidization experiments, the fluidization column diameter was 0.0762 m with a height of 1.82 m, whereas for magnetic assisted fluidization experiments, the column diameter was 0.0635 m with a height of 1.52 m. It is important to note that the large bed expansion contributed to a large length/diameter (L/D) ratio. Both fluidization columns were surrounded by a self-regulating heater of 5 watts/ft placed helicoidally around the column with an axial spacing of about 1 inch in each turn.

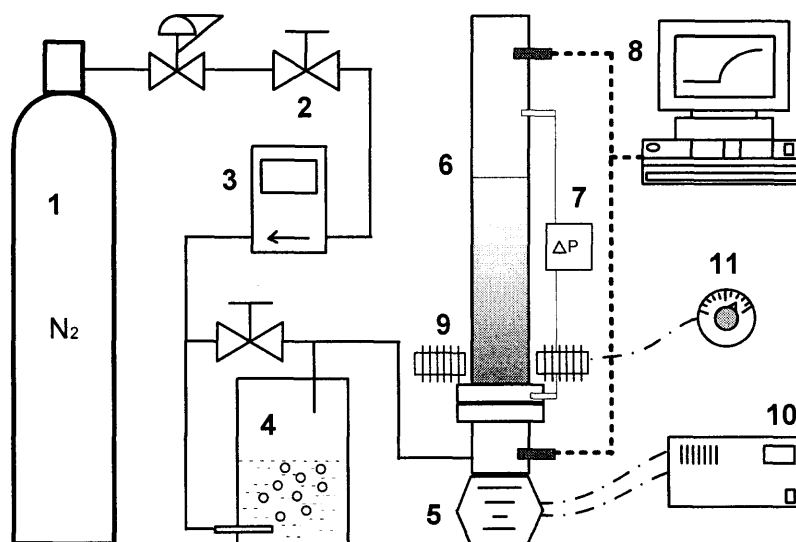


Figure 3.1 Schematic of the experimental apparatus for evaluating the drying process in a fluidized bed of nanopowder. (1) Gas cylinder with pressurized N_2 ; (2) valve; (3) mass flowmeter; (4) humidifier; (5) vibrating device; (6) fluidized bed column; (7) pressure drop display; (8) data acquisition system for humidity sensors; (9) electromagnetic coils; (10) control unit for the vibrator; (11) voltage regulator for the electromagnetic coils.

A flow of dry nitrogen gas, supplied by a pressurized gas cylinder, was adjusted by a needle valve and measured by a 0 to 5 lpm mass flowmeter (Model FMA1818 from Omega), which was connected to a digital display. The flow of nitrogen gas could be directed towards the humidifier or directly to the fluidized bed depending on the stage of the experiment. This could be done by switching a valve that bypassed the humidifier. The humidifier consisted of a water tank made of acrylic plastic and spargers that generated small gas bubbles. In addition, the temperature of the water could be increased with a heater Model ARTM-1000 supplied by Omega for increasing the amount of moisture in the gas stream, if necessary. The temperature of the water was adjusted by a microcontroller that activated the heater according to the temperature value entered in the set point.

For magnetic assisted fluidization, two electromagnetic coils were placed at opposite sides outside of the column in the area right above the distributor (see Figure 3.1). These coils were connected through voltage regulators to an AC power source, and generated an oscillating magnetic field inside the column. Barium ferrite magnetic particles of about 1 to 3 mm in diameter moved (translation and rotation) due to the presence of the magnetic field. However, the magnetic particles do not fluidize along with the powder and tend to remain at the bottom of the bed above the distributor. Since the electromagnetic coils heated up due to the resistance of the wire coils, a cooling system composed of a blower and air ducts provided a constant airflow around the coils for cooling. The intensity of the magnetic field was controlled by adjusting the voltage of the power supply to the electromagnetic coils.

Vertical vibration was supplied to the fluidization column using a Ling Dynamic system composed of an electrodynamic shaker Model V650, a digital sine controller DSC4, a PA1000L Amplifier and a FPS10L field power supply. The fluidization column was mounted directly above the electrodynamic shaker so that the column was vibrated vertically. The vibration of the system was controlled by adjusting the force of the vibration, given in gravity force units, and the frequency of the oscillation measured in hertz.

Two different kinds of powders were supplied by the Degussa Corporation for these experiments: Aerosil[®] 200, which shows agglomerate particulate fluidization (APF) behavior, and Aerosil[®] 90, which shows agglomerating bubbling fluidization (ABF) behavior. These powders were delivered under special conditions to reduce densification due to storage; thereby, these nanopowders have similar characteristics to those used in

the production process. In addition, depending on the experiment, densification of the powder was reduced by sieving using sieve orifice sizes of 500 μm and 700 μm and then discarding the large dense agglomerates. A visual inspection of Aerosil[®] 200 shows that it is composed mainly of very fluffy, low density, agglomerates and that there are not many large clusters of agglomerates (larger than 1 mm) present. In contrast to Aerosil[®] 200, Aerosil[®] 90 contains denser agglomerates and a significant fraction of large agglomerates when compared with Aerosil[®] 200. Both powders are hydrophilic, which means that they will adsorb moisture. It is also important to note that Aerosil[®] 200 and Aerosil[®] 90 have a primary particle size of 12 nm and 20 nm, and a specific surface area of 200 m^2/g and 90 m^2/g , respectively, since the surface area plays a major role in the adsorption process.

During each experiment, the relative humidity data (dew point) of the gas stream at the bottom and at the top of the column was collected every 2 seconds (in some cases every 10 seconds). A micro server (Model iTHX-W from Newport Electronics) that came with 2 humidity probes was used to send the data through an Ethernet port to a personal computer and the values were displayed in an Excel[®] spreadsheet in real time. The humidity sensors have an operational range from about 5% to 95% of relative humidity; below 5% of relative humidity the sensor will still give readings, but with increased error, since the calibration line for the sensor does not hold at lower moisture concentrations. The fluidized bed height was visually measured and the bed pressure drop was measured with a high sensitivity low differential pressure transmitter with a range from 0 to 1 inches of water (Cole-Parmer, Model #EW-68071-22) connected to a digital display (Cole-Parmer, Model #EW-93284-02). The vibration parameters (vibration intensity and

frequency) for vibration assistance, the voltage supplied to the electromagnetic coils and the amount of magnetic particles for magnetic assistance were also recorded and kept fixed in the experiments.

Four different sets of experiments were performed: experiments to determine if the fluidization assisting methods speed-up the transfer of moisture from the gas to the powder, experiments to determine the adsorption isotherm of the powder by monitoring moisture in the gas phase, experiments to determine the adsorption isotherm of the powder by a gravimetric method and experiments for monitoring the overall rate of release of moisture by the bed during drying of the powder.

3.3.1 Isotherm Experiments by Monitoring Moisture in the Gas Phase

The thermodynamic equilibrium of the moisture between the gas and the solid phase is established by an adsorption isotherm, which represents the relationship between the moisture content of the solid and the moisture in the gas phase at a fixed temperature. The total amount of powder and the gas velocity can be arbitrarily chosen as long as the moisture in the gas phase reaches equilibrium with the moisture adsorbed by the powder; thus a long-time experiment is necessary in order to let the moisture reach equilibrium in both phases. For convenience, experiments to find the adsorption isotherms were run in the vibrated assisted fluidization column and at room temperature.

In order to reduce uncertainties in the results due to the presence of large agglomerates in the powder, i.e., agglomerates larger than 500 μm for Aerosil[®] 200 and 700 μm for Aerosil[®] 90, and to improve the flow dynamics of the bed, the powder was sieved using sieve meshes having the corresponding apertures. A certain amount of

powder was then collected, weighed and placed in the fluidized column, usually 40 grams for Aerosil[®] 200 and 100 grams for Aerosil[®] 90. The flow of dry nitrogen gas was adjusted to a desired value (usually 4.2 lpm and kept constant during the entire experimental run), and the powder was initially dried for at least half an hour starting when the humidity sensor at the top showed no moisture.

Once the powder was dry, a portion of the gas flow was directed towards the humidifier in such a way that the level of moisture in the gas stream could be adjusted by passing more or less of the gas through the humidifier. The relative humidity of the gas stream going to the fluidized bed was monitored carefully using the humidity sensor and it remained steady as long as the temperature of the experiment was not changed. The dew point of the gas stream at the inlet of the column was monitored and kept steady, assuring a constant partial pressure of water in the gas stream for the duration of the humidification part of the experiment. Usually, the humidification period lasted from 1.5 up to 3 hours in order to assure equilibrium conditions.

After the dew point reading from the sensor at the top of the bed became constant and matched the dew point reading from the sensor at the bottom, the drying process was started by bypassing the humidifier and sending dry gas into the fluidized bed. The moisture content in the gas was recorded during drying and the experiment ended once there was no moisture detected by the sensor. It is important to note that if the powder is releasing moisture at a low rate, such that the moisture content in the gas stream is too low (in parts per million), then it will not be measured by the humidity sensor, underestimating the amount of moisture in the powder.

3.3.2 Isotherm Experiments by Monitoring Moisture in the Solid Phase

The humidification part of the process was performed as described above, and once the powder was fully saturated, several samples of about 1 gram of powder were taken from the fluidized bed and the moisture in the powder was quantified by following the procedure according to ISO 787-2⁷⁵. An empty crucible was weighed (W_{tare}), then 1 gram of Aerosil[®] was placed in the crucible which was reweighed. Its new weight was recorded (W_{start}). The crucible, with its lid in tilted position, was then heated in an oven at 105°C for exactly 2 hours. Next, the crucible was carefully placed in a dessicator and allowed to cool down for 30 minutes. Finally, the crucible and its content were reweighed (W_{dry}). The percentage of moisture content was calculated by the equation,

$$\%LD = \frac{W_{start} - W_{dry}}{W_{start} - W_{tare}} \times 100 \quad (3.1)$$

By changing the moisture level in the gas phase in different runs, and taking samples of fully saturated powder at different conditions, the isotherm plot could be obtained; no drying of the powder after the humidification was carried out.

3.3.3 Monitoring of the Moisture in the Gas Phase during Drying

These experiments were carried out similarly to the experiments for finding the adsorption isotherms by monitoring the moisture in the gas phase. In these runs, the dew point (absolute humidity) was kept constant during humidification of the powder. Also, the moisture leaving the fluidization column was monitored during drying of the powder. Two series of experiments were performed for comparison purposes, fluidization assisted by vibration or magnetic excitation and fluidization without assistance, i.e., conventional fluidization.

3.3.4 Short Time Experiments

The purpose of these experiments was to show that the assisting methods improve the dynamics of the fluidized bed by keeping all other variables fixed. Moreover, the gas velocity was kept very low so that without assistance the bed of powder is not fully fluidized, i.e., the gas velocity is less than the minimum fluidization velocity. However, as soon as the assistance is activated, the bed becomes fully fluidized at the same gas velocity.

For measuring the effect of the assisting methods on the mass transfer during fluidization, experiments were done as follows: a certain amount of powder taken right out of the container, i.e., without sieving, was placed inside the fluidization column; if magnetic assistance was to be used, then a measured amount of magnetic particles was added before the powder in order to make sure that all the magnetic particles were located right above the gas distributor. Dry nitrogen gas flow was adjusted to a desired value, by reading the mass flowmeter, and the powder was left to dry for at least half an hour, until the sensor at the top of the bed showed no humidity. Simultaneously, column and gas heaters were turned on in order to avoid any condensation of moisture at the surfaces of either the column or tubing; this was required since most of the experiments were carried out at high moisture conditions; in fact, dew points higher than ambient temperature lead to condensation of moisture and overestimation of the moisture content in the powder. Once the powder was dry, the assisting method was activated and the humidification process was started by humidifying the gas flow that entered the fluidization column, a process that lasted for about 5, 10 or 20 minutes depending on the experiment. The powder was then dried by sending dry gas to the fluidized bed

(bypassing the humidifier), and the moisture content in the gas stream was monitored. A similar experiment was run at the same operating conditions, i.e., temperature, gas flow, humidifying time and mass of powder, but without activating the assisting method (conventional fluidization). These experiments are called “short time experiments”, since the entire amount of powder in the bed is not fully saturated with moisture because the humidification is carried out only for short times.

3.3.5 Experiments for Studying the Residence Time Distribution (RTD) of Gas Molecules in Packed and Fluidized Beds of Porous Hydrophobic Agglomerates of Nanoparticles

It is believed that the sizes of the agglomerates of nanoparticles in fluidized beds play an important role in transport processes such as desorption of byproducts from the agglomerates. Depending on the size distribution of the pores in the agglomerates, diffusion processes may arise that can delay transport. Residence Time Distribution (RTD) studies shed light on the real mean residence time that molecules spend in the reactor, i.e., the fluidized bed, and allow for the identification of any non-ideality present in the reactor such as bypassing, dead spaces, and diffusion among others. In this context, humidity was used as tracer in packed beds and fluidized beds of hydrophobic fumed silica agglomerates to find the mixing behavior and the impact of having large agglomerates in the fluidization column. The use of moisture as tracer and hydrophobic agglomerates was to avoid any type of interaction or adsorption, between the surface of the agglomerates and the tracer.

The experimental setup is shown in Figure 3.2. When dry nitrogen gas is bubbled through the tank, it picks some moisture. The level of moisture will remain constant since the gas flow and temperature of the water do not change. The levels of moisture in these

experiments were kept low, under 60% relative humidity, in order to avoid condensation of water that would distort the experimental data. Moisture levels in the gas phase were given by two humidity sensors located at the bottom (entrance) and at the top (exit) of the fluidization column. The humidity sensor at the top of the column was located at 57.5 inches from the gas distributor plate. The humidity probes provided dew point data every 2 seconds. They were connected to a micro server Model iTHX-W (Newport Electronics) which recorded the data in an Excel spreadsheet. Also, a portable dewpoint meter Model XPDM (Cosa Instruments) was used to compare the moisture readings from the humidity probes under low moisture conditions (below 5% RH).

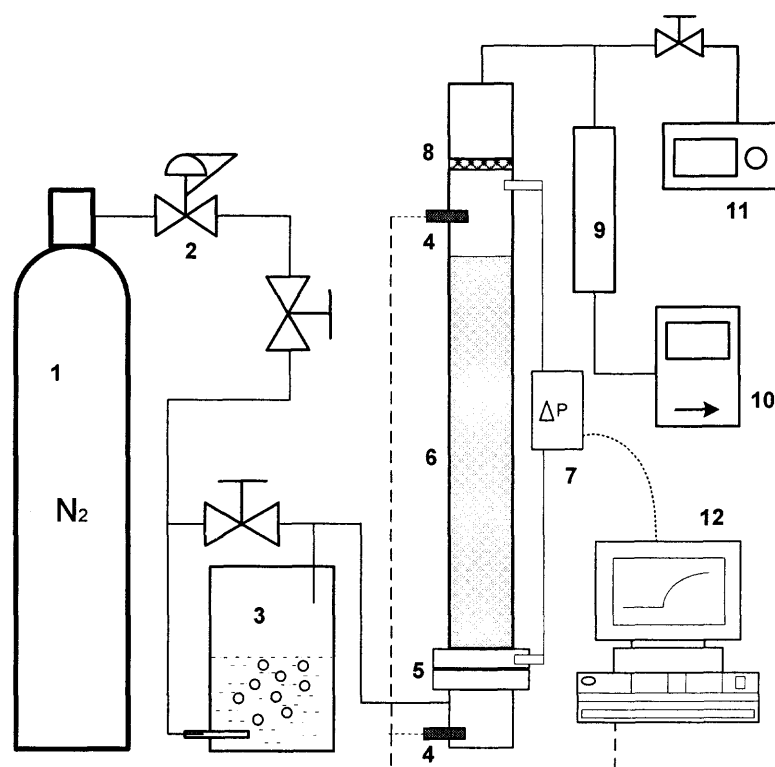


Figure 3.2 Schematic showing the setup used for the Residence Time Distribution studies of packed beds and fluidized beds of hydrophobic agglomerates of nanoparticles. (1) compressed dry N₂ cylinder, (2) pressure regulator for low pressure, (3) tank holding water, (4) humidity sensors, (5) sintered metal plate-distributor, (6) fluidization column, (7) differential pressure drop transmitter, (8) filtering mesh, (9) HEPA filter, (10) flowmeter (11) absolute humidity sensor (low range), and (12) computer for data acquisition.

The nanopowder used for these experiments was Aerosil R974, either as a packed bed or as a fluidized bed. Aerosil R974 is a hydrophobic nanopowder. Also, in order to compare the effects of tortuosity and porosity of the particles on the tracer, a packed bed of agglomerates of Aerosil R974 was prepared and compared against a packed bed of nonporous glass beads. The size of the agglomerates was in the range of 1.4 to 2.3 mm while the size of the glass beads was of about 2.5 to 3.2 mm. For the fluidized bed, two types of agglomerates were studied: agglomerates sieved under 500 microns and agglomerates sieved under 500 microns but also processed in a jet assisted fluidized bed. The agglomerates of Aerosil R974 and the glass beads used in the packed beds are shown in Figure 3.3.

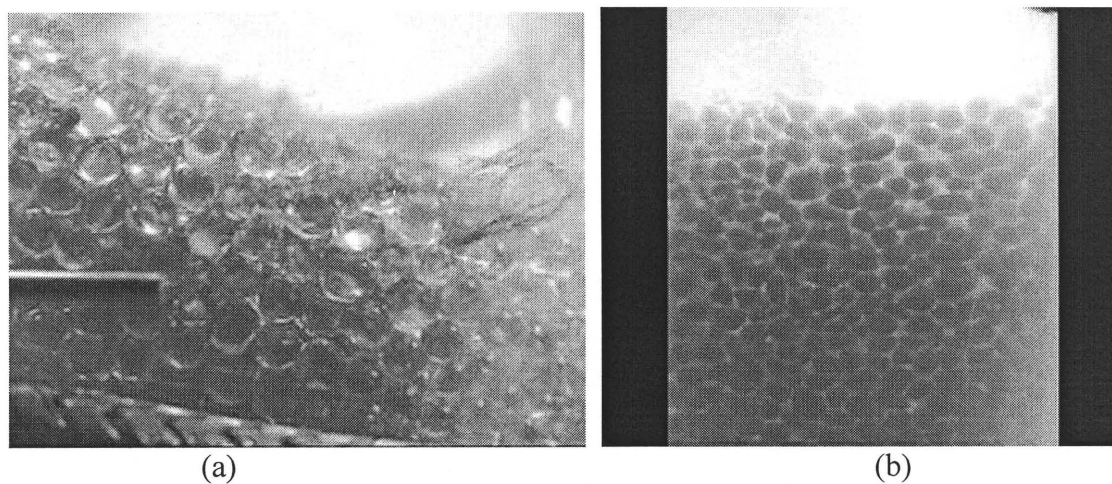


Figure 3.3 Packed beds for the RTD studies; (a) packed bed of glass beads, (b) packed bed of clusters of agglomerates of nanoparticles.

3.4 Results and Discussion

Dew point values in degrees Celsius were collected as data and were used to calculate the partial pressure of water in the gas stream⁷⁶

$$P_{H_2O} = 610.78 \left(\exp \left(\frac{17.2694 \cdot DP}{DP + 238.3} \right) \right) \quad (3.2)$$

where DP stands for the dew point in degrees Celsius and P_{H_2O} is the partial pressure of water in Pascals. This equation is similar to the one introduced by Bolton⁷⁷ and it is also used for the calculation of the vapor pressure at the temperature of the experiment.

To evaluate the moisture in the gas stream, the absolute humidity is calculated as a function of the partial pressure of water using the equation,

$$AH = \frac{0.622 \cdot P_{H_2O}}{101300 - P_{H_2O}} \quad (3.3)$$

where AH stands for absolute humidity, which is non-dimensional since it represents the ratio of mass of water per mass of dry gas.

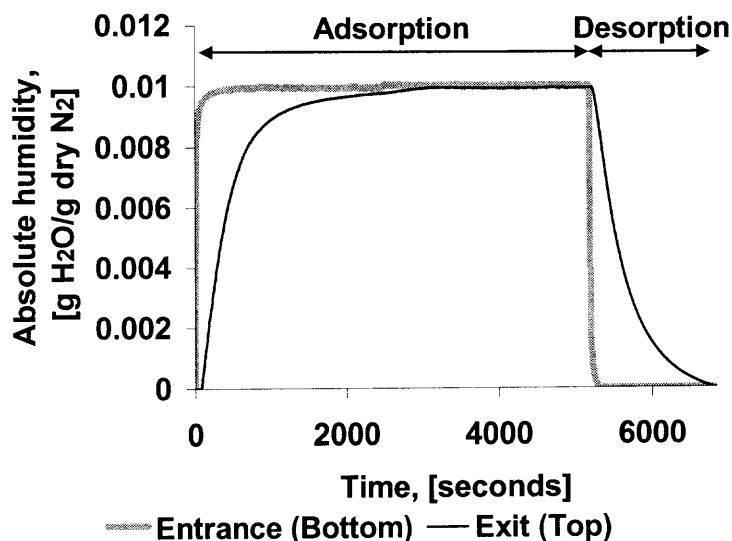


Figure 3.4 Absolute humidity as a function of time during humidification and drying of Aerosil[®] 200.

Figure 3.4 shows an example of the moisture data collected by the humidity sensors after being converted to absolute humidity. Two stages can be clearly identified taking as a reference the moisture at the entrance (bottom) of the column, the humidification (or adsorption of moisture) of the powder when the nitrogen gas contains moisture, and the drying (or desorption) of the powder when the nitrogen gas is dry.

In order to evaluate the amount of moisture released by the powder during the drying process, the absolute humidity obtained from the dew point values given by the sensor at the top of the bed was multiplied by the mass flow of dry gas and then multiplied by the time to yield the mass of water at every time interval since the drying process began. Finally, a summation or integration of the mass of water as a function of time gives the total amount of water that was adsorbed by the powder. A typical result is shown schematically in Figure 3.5.

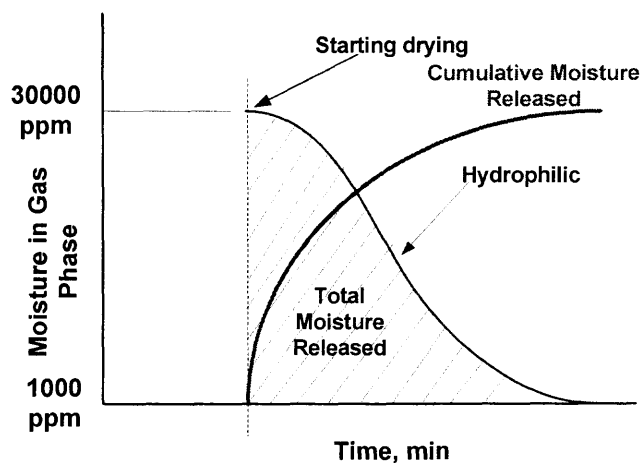


Figure 3.5 Schematic showing the procedure to find the moisture released by the powder during drying from data collected by the sensor at the top of the column.

The following equations summarize the procedure described above. For each time interval, for example, 2 seconds:

$$(M_{H_2O})_i = F_{gas} \cdot \rho_{gas} \cdot AH_i \cdot (t_i - t_{i-1}) \quad (3.4)$$

where $(M_{H_2O})_i$ is the mass of water released at each time period $(t_i - t_{i-1})$, F_{gas} is the volumetric flow of gas, ρ_{gas} is the density of the gas, AH_i is the absolute humidity, and t_i is the time in seconds corresponding to the data point. Next, the total amount of water released by the powder is found by adding the moisture released at each time interval.

$$M_{H_2O} = \sum_i (M_{H_2O})_i \quad (3.5)$$

In order to find the adsorption isotherms, the total amount of moisture, M_{H_2O} , was divided by the total amount of powder, either M_{A200} or M_{A90} ; and plotted against the partial pressure of water in the gas phase at the temperature of the experiment. Adsorption isotherms are shown as plots where the abscissa corresponds to the partial pressure (mbar) and the ordinate corresponds to the mass fraction (mg/g) of water released.

The total amount of moisture released, M_{H_2O} , is also used as a parameter for comparing conventional against assisted fluidization since the moisture adsorbed by the powder is related to the amount of powder suspended in the gas phase, and therefore, an indication of the degree of dispersion of the powder in the fluidized bed. For example, if there are clusters of agglomerates in the fluidized bed, less moisture will be adsorbed because the agglomerates inside of the clusters are not exposed to the gas phase.

3.4.1 Adsorption Isotherms by Monitoring the Gas Phase

Adsorption isotherms at room temperature were found for both powders, Aerosil[®] 200 and Aerosil[®] 90. Similar amounts of powder were used in all the experimental runs. As shown in Figure 3.6 for Aerosil[®] 200 and Figure 3.7 for Aerosil[®] 90, the powder was humidified with gas having different amounts of moisture (as given by the relative humidity or dewpoint) until saturation is obtained. At saturation, no additional moisture is adsorbed and the absolute humidity given by the sensors at the bottom and at the top of the column match. After saturation of the powder, data collected during drying was used to find the amount of moisture adsorbed by the powder.

While most of the experiments were run at a gas velocity of 1.54 cm/s, one experimental run for each powder was done at a higher gas velocity (1.74 cm/s) to verify that the isotherm was not dependant on the gas velocity. Also, all the experiments were done at room temperature (73°F).

Experimental data related to the adsorption isotherms are summarized in Table 3.1 and Table 3.2, and Figure 3.8 shows the corresponding adsorption isotherms found by monitoring the moisture in the gas phase for Aerosil[®] 200 and Aerosil[®] 90. As can be seen from the tables, humidification times were not held constant for all experiment runs. Even though in some of the experiments the powder was humidified for a longer time, all of the data points followed the linear regression, indicating that the powder was in equilibrium with the moisture in the gas before being dried.

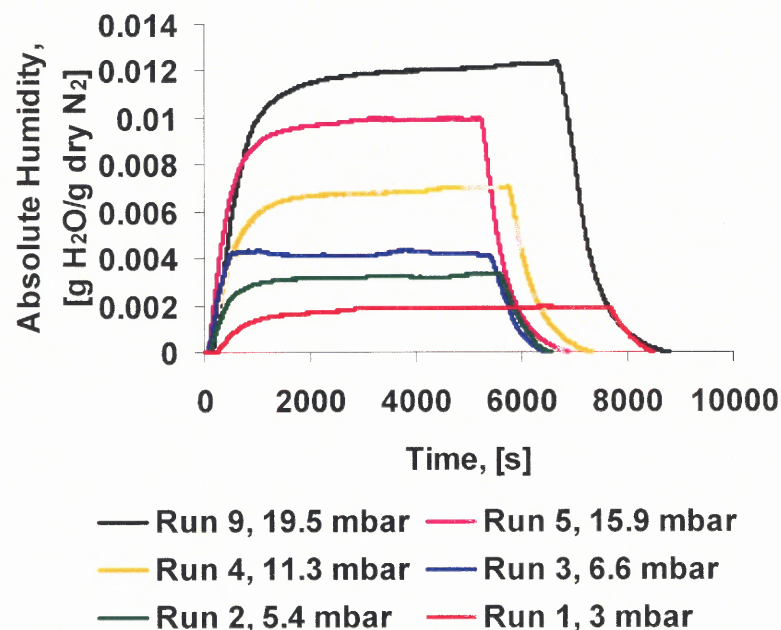


Figure 3.6 Moisture levels obtained from the sensor at the top of the column showing the humidification and drying runs at different partial pressures for finding the adsorption isotherm of Aerosil[®] 200.

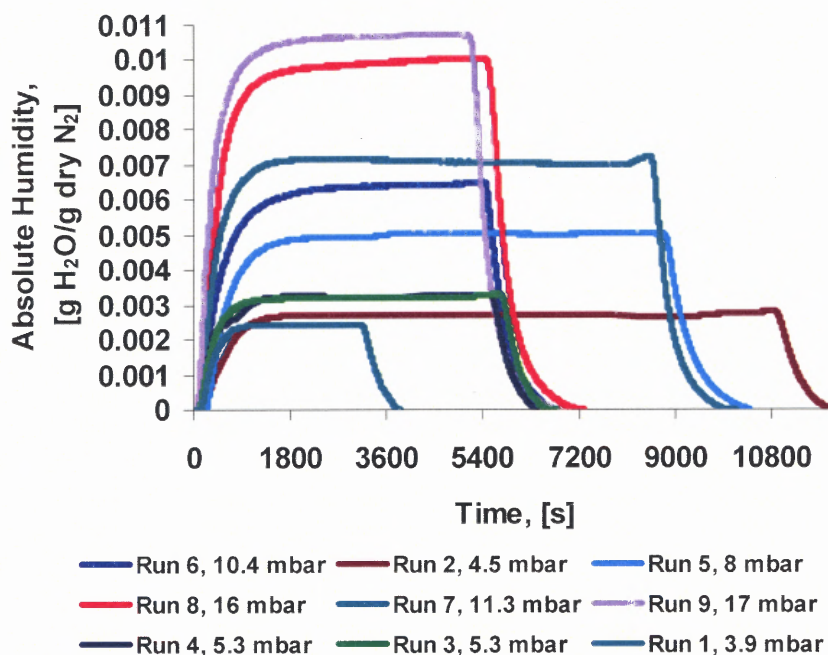


Figure 3.7 Moisture levels obtained from the sensor at the top of the column showing the humidification and drying runs at different partial pressures for finding the adsorption isotherm of Aerosil[®] 90.

Table 3.1 Data Corresponding to the Adsorption Isotherm of Aerosil® 200 by Monitoring Moisture in the Gas Phase

Run (#)	Partial Pressure H ₂ O (mbar)	Moisture in Powder (mg/g)	Gas Velocity (cm/s)	Humidification Time (min)
1	3	1.4	1.54	127
2	5.4	2.6	1.54	92
3	6.6	3.4	1.54	89
4	11.3	6.6	1.54	95
5	15.9	10.1	1.73	87
6	17	11.9	1.54	29
7	19.5	13.1	1.54	111

Table 3.2 Data Corresponding to the Adsorption Isotherm of Aerosil® 90 by Monitoring Moisture in the Gas Phase

Run (#)	Partial Pressure H ₂ O (mbar)	Moisture in Powder (mg/g)	Gas Velocity (cm/s)	Humidification Time (min)
1	3.9	0.531	1.54	50
2	4.5	0.767	1.54	181
3	5.27	0.787	1.54	95
4	5.25	0.82	1.54	92
5	8	1.71	1.54	146
6	10.4	1.96	1.72	90
7	11.25	2.14	1.54	141
8	16	3.255	1.54	90
9	17	3.274	1.54	85

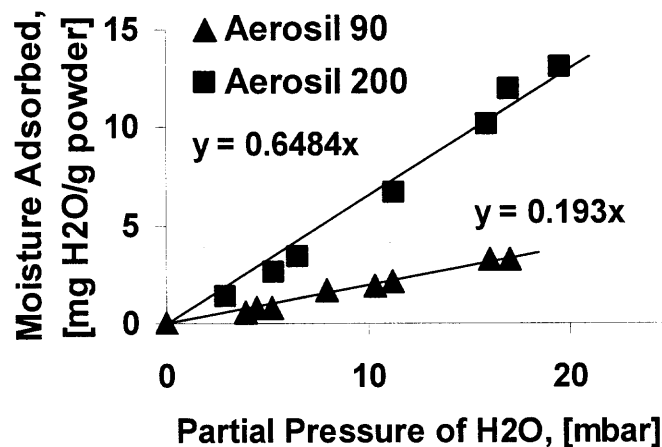


Figure 3.8 Adsorption isotherms of Aerosil[®] 200 and Aerosil[®] 90 found by monitoring the moisture in the gas phase.

3.4.2 Adsorption Isotherms by the Gravimetric Method

In order to validate the adsorption isotherm data obtained in the previous section, the adsorption isotherms were also found by using the gravimetric method. These results are shown in Figure 3.9 for Aerosil[®] 200 and Aerosil[®] 90. Although not exactly the same (because the gravimetric method uses a powder sample that is fully fluidized), the isotherms obtained by both methods are quite similar. The difference in slope of the linear regression for both powders, when comparing the gravimetric method against the gas-phase monitoring method, may be due to the axial dispersion of the moisture inside of the fluidized bed. The delay in the release of moisture from the fluidized bed due to axial dispersion results in an increased slope for both powders, and it is related to the residence time distribution of the moisture in the fluidized bed.

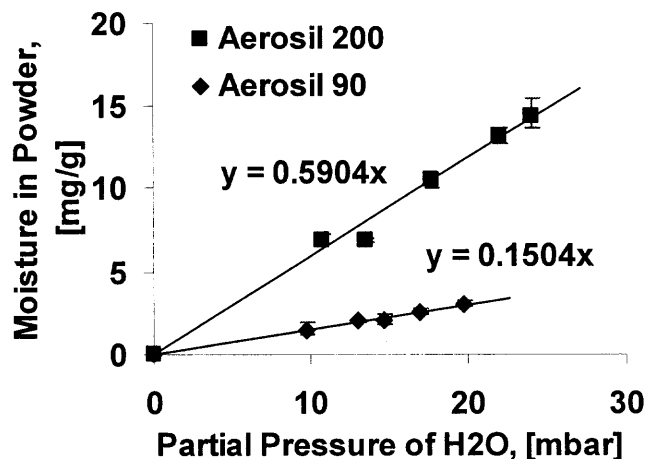


Figure 3.9 Adsorption isotherms of Aerosil[®] 200 and Aerosil[®] 90 at room temperature found by using the gravimetric method.

3.4.3 Short Time Experiments

Short-time humidification experiments were designed to demonstrate that the assisting methods contribute to the dynamics of the powder in the fluidized bed. In the following example, 40 grams of Aerosil[®] 200 were fluidized conventionally and under vibration at the same operating conditions. The powder was humidified for a short time (5 minutes) and dried immediately to analyze the rate at which moisture was released from the fluidized bed with and without assistance. In this experiment, the operating conditions were as follows: partial pressure was about 57 mbar, gas velocity of 1.5 cm/s and temperature of about 128°F measured by the sensor at the top. It is important to note that the gas velocity has been selected in a way that it corresponds to the minimum fluidization velocity when vibration is used; if no assistance is used, the bed is not fully fluidized. The corresponding experimental data are shown in Figure 3.10.

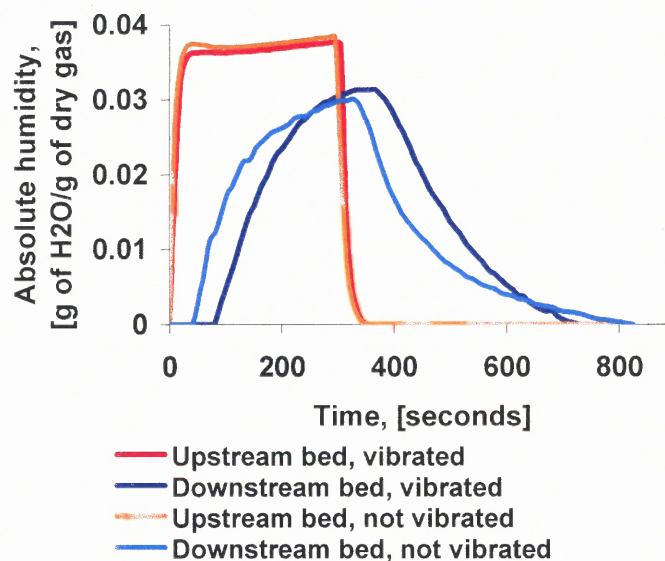


Figure 3.10 Data from two short time experiments for assessing the impact of vibration. 40 grams of Aerosil[®] 200 were humidified for about 5 minutes. Gas velocity was 1.5 cm/s and the temperature of the experiment was 128°F.

During humidification of the powder (high moisture at the bottom), Figure 3.10 shows the sensor at the top of the bed picks up a delay, which is shorter for fluidization without assistance, indicating gas-bypassing in the bed. This delay is longer for vibration assisted fluidization, indicating that there is less gas-bypassing and hence better mixing. Also, it can be seen that the slope of the curves as given by the data from the sensor at the top of the bed (blue and light blue curves) are positive while humidifying, but then become negative during drying. The time for the drying process starts when the slope changes sign. When looking at the drying of the bed of powder, it takes longer to dry the conventional fluidized bed of powder.

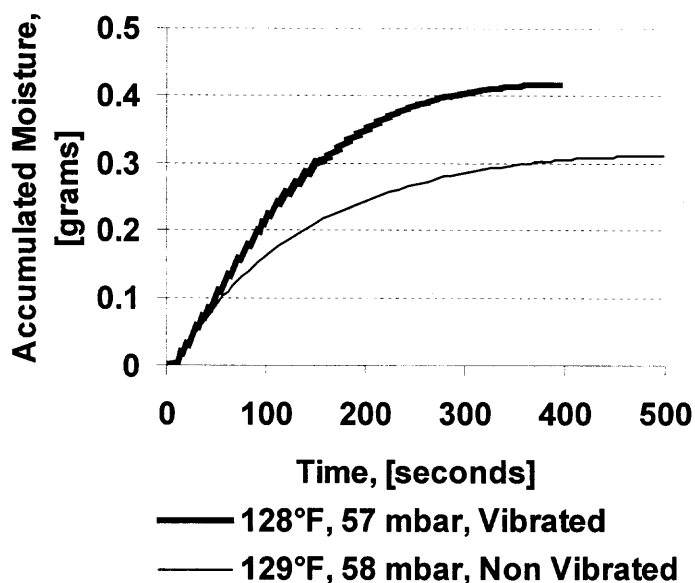


Figure 3.11 Short time experiment showing the effect of vibration applied to the fluidized bed of Aerosil® 200. Gas velocity was 1.5 cm/s and full fluidization was obtained when vibration was applied; without vibration, channeling occurred.

Figure 3.11 shows the cumulative moisture released by the powder with respect to time based on the moisture readings from the gas stream at the sensor at the top of the column shown in Figure 3.10. The fluidized bed of powder retains more moisture and it releases it quicker when vibration is applied, a clear indication of enhancement in the dynamics of the fluidized bed by the assisting method.

3.4.4 Comparison of Conventional and Assisted Fluidization by Monitoring Moisture in the Gas-Phase during Drying

In these results, the powder was saturated with moisture at a constant concentration for a period of time longer than 90 minutes as explained in the experimental procedures. In this way, a valid comparison of the conventional and assisted fluidization methods can be made since any differences in the amount of moisture adsorbed by the fluidized bed of powder will be due to powder that is not exposed to the fluidizing gas.

Figure 3.12 shows the moisture levels given by the sensor at the top of the bed with respect to time while drying a fluidized bed of Aerosil[®] 200. The drying in a conventional fluidized bed is compared against assisted fluidization. At the beginning of the drying, it is seen that the moisture drops at a faster rate for the conventionally fluidized bed, because the fluidizing gas, dry N₂, easily reaches the sensor at the top and dilutes the moisture being released by the bed of powder. For the vibrated bed, the moisture levels drop at a slower pace because more powder is suspended or dispersed in the gas phase releasing more moisture into the fluidizing gas.

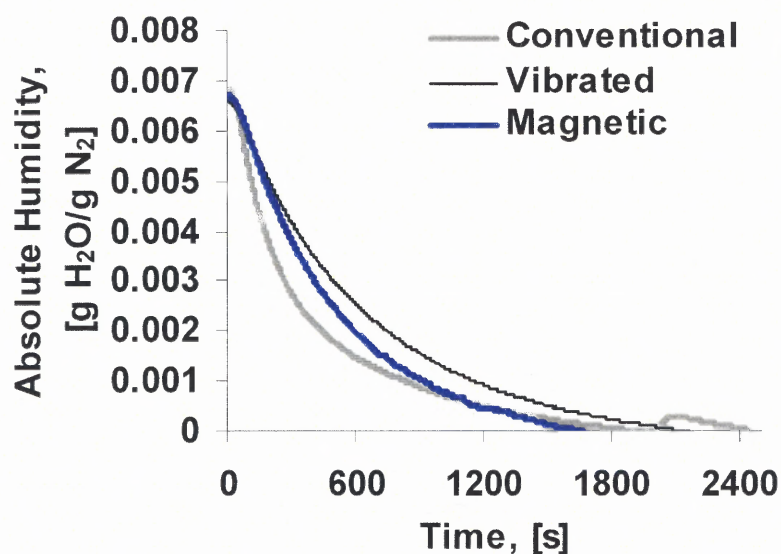


Figure 3.12 Comparison of the moisture data obtained from the sensor at the top of the column for conventional and assisted fluidized bed drying of Aerosil[®] 200.

Figure 3.13 shows the cumulative moisture with respect to time during drying of a fluidized bed of Aerosil[®] 200 based on the information obtained from Figure 3.12. When the fluidized bed of powder is vibrated, it retains more moisture and releases it faster than when using conventional fluidization. In a similar way, when magnetic assistance is

applied, the powder dries faster than under conventional conditions; however, taking into account the adsorption isotherm, the powder does not retain as much moisture as expected. Since the magnetic assistance acts only at the bottom of the fluidized bed, any powder that attaches to the wall of the column does not participate in the fluidization process reducing the total amount of moisture adsorbed; this particular problem is overcome when using vibration which acts along the entire length of the column. In addition, a smooth fluidization is obtained when Aerosil[®] A200 is fluidized with vibration assistance regardless of whether the powder has been sieved or not. In contrast, during conventional fluidization channeling and bubbling occur, increasing elutriation of particles in addition to having some regions of powder that are not participating in the fluidization, diminishing the effective mass of fluidized powder in the bed, and therefore, showing less than the expected amount of moisture adsorbed.

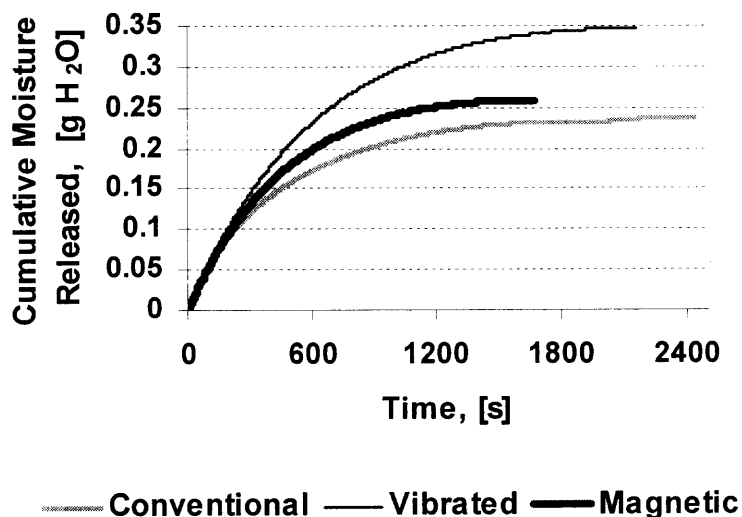


Figure 3.13 Effect of assistance on fluidized bed drying of Aerosil[®] 200 (not sieved). Mass of powder 40 grams, gas velocity 1.5 cm/s, humidification time 90 minutes, 3 inch column diameter.

Aerosil[®] 90 contains a much larger fraction of large agglomerates, (clusters >700 μm), than Aerosil[®] 200. These clusters do not allow for a good distribution of the gas in the bed causing large channels and bubbles (typical ABF behavior). It is seen in Figure 3.14 that when vibration is applied to the fluidization of 200 grams of non-sieved Aerosil[®] 90 (powder taken directly from the container) there is no difference in the moisture adsorbed by the powder as compared to conventional fluidization. The intensity and amplitude of the vibration (3 times normal gravity) are not strong enough to break-down the large agglomerates; however, it may be possible to break the large agglomerates under a higher intensity vibration. When visually inspected, the fluidized bed is composed of two sections, a packed bed of large agglomerates at the bottom and a spouting fluidized bed of smaller agglomerates over the packed bed, a behavior that is observed during both conventional and vibrated assisted fluidizations. In addition, the large agglomerates reduce the effective amount of powder that participates in fluidization and the bed of powder adsorbs less moisture than expected due to the poor mixing and dispersion of the hydrophilic nanopowder.

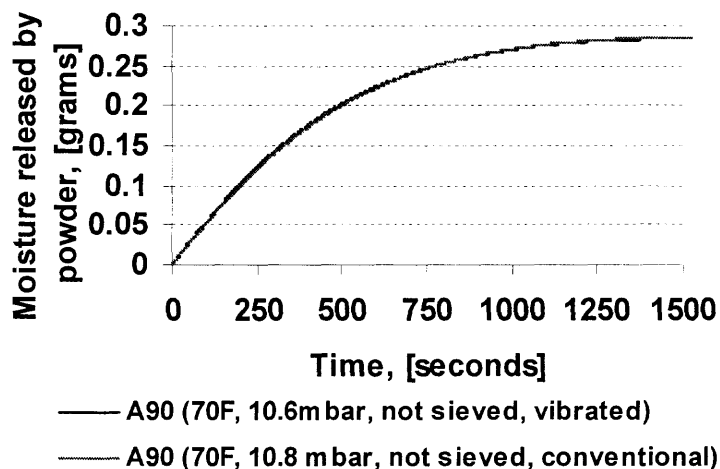


Figure 3.14 Accumulated moisture released from Aerosil[®] 90 (not sieved) showing relatively no effect of vibration as compared to conventional fluidization. Experimental conditions: 200 gr. of Aerosil[®] 90, gas velocity 1.5 cm/s, 3 inch diameter column.

Also, 40 grams of non-sieved Aerosil[®] 90 were fluidized using the magnetic assisting method and Figure 3.15 shows the moisture levels collected by the sensor at the top as a function of time. The cumulative moisture released from the powder during drying is compared to conventional fluidization data as shown in Figure 3.16. It can be seen that when magnetic assistance is used, the fluidized bed of powder adsorbs about 20% more moisture than when conventional fluidization is used. The moving magnetic particles break the large agglomerates and improve the dynamics of the fluidized bed which is reflected by its fluidization behavior. Visual inspection of the powder after being fluidized with magnetic assistance shows a significant reduction in the fraction of large agglomerates, which can even disappear entirely depending on the time the magnetic assistance is applied. It is important to note that even though data shown in Figure 3.14 and Figure 3.16 have been collected from experiments at similar operating conditions, i.e., moisture levels, due to the difference in the amount of powder used and the diameter of the column, the residence time distribution of the moisture in the fluidized bed changes resulting in dissimilar drying curves.

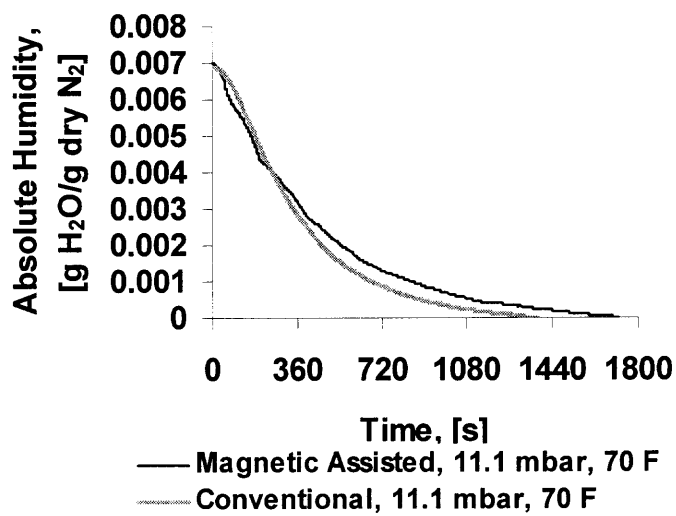


Figure 3.15 Comparison of the moisture data obtained from the sensor at the top of the column for conventional and magnetically assisted fluidized bed drying of Aerosil[®] 90.

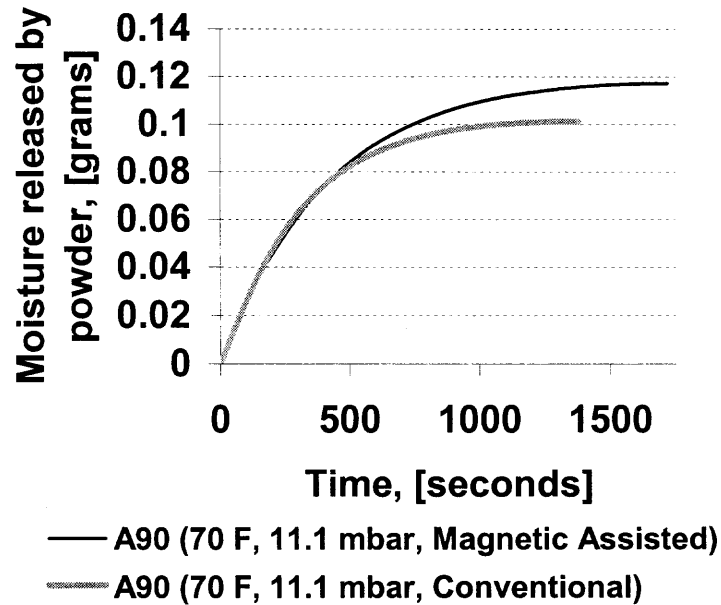


Figure 3.16 Accumulated moisture released from Aerosil[®] 90 (not sieved) comparing magnetically assisted and conventional fluidization. Experimental conditions: 40 grams of Aerosil[®] 90, gas velocity 1.5 cm/s, humidification time 90 minutes, 2.5 inch diameter column.

3.4.5 Fluidization Characteristics of the Nanopowders Studied

As indicated in the experimental methods, Aerosil[®] 200 shows APF behavior which is characterized by a smoother and much more homogeneous fluidization than Aerosil[®] 90's ABF behavior. However, it could be seen that these powders, when dry, have a significant amount of electrostatic charge that hinders fluidization. If conventional fluidization experiments were done without first reducing the electrostatic charge, it is very difficult to get good repeatability of the data. In the experiments, electrostatic charge was somewhat reduced by using moisture before characterizing the fluidization of the powder. Fluidization quality is generally characterized by data related to the fluidized bed pressure drop and bed expansion as a function of gas velocities. These particular experiments were done in a fluidization column of 0.0762 m (3 inches) internal diameter.

Figure 3.17 shows the fluidized bed pressure drop as a function of gas velocity for 16 grams of sieved Aerosil[®] 200 with and without vibration assistance. The large difference in the pressure drop is due to the fact that vibration was used in combination with a reduction of electrostatic charge by humidifying the powder. The minimum fluidization velocity during conventional fluidization is about 0.017 m/s (1.7 cm/s) and it is reduced to about 0.007 m/s (0.7 cm/s) due to vibration assistance. Figure 3.18 shows the non-dimensional bed expansion, which is the actual bed height divided by the bed height at zero gas velocity, as a function of the superficial gas velocity. The larger bed expansion is an indication of a much better dispersion of the powder in the fluidizing gas.

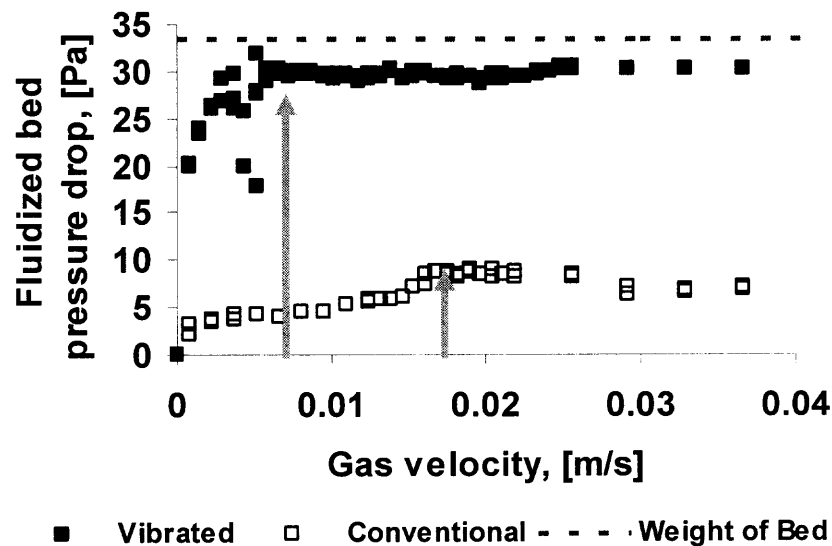


Figure 3.17 Comparison of the fluidized bed pressure drop of Aerosil[®] 200 for conventional fluidization without reducing electrostatic charge, and for vibrated assisted fluidization with reduced electrostatic charge.

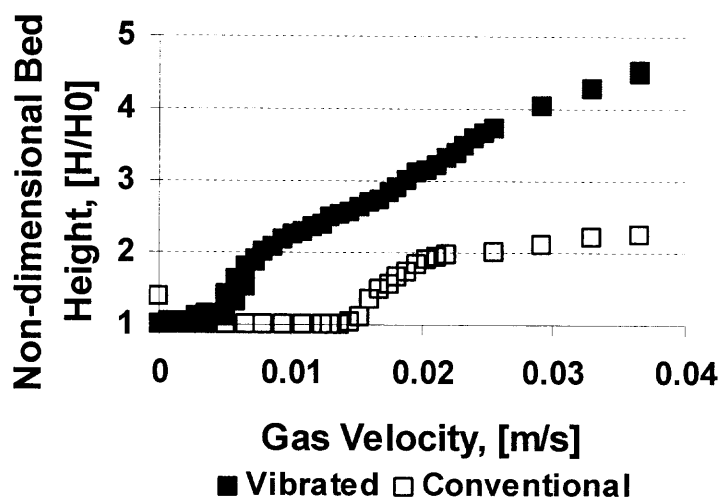


Figure 3.18 Comparison of bed expansion of Aerosil® 200 for conventional fluidization without reducing electrostatic charge, and for vibrated assisted fluidization with reduced electrostatic charge.

Similarly, Figure 3.19 shows the fluidized bed pressure drop as a function of superficial gas velocity for 31 grams of sieved Aerosil® 90. Conventional fluidization is compared against assisted fluidization. For this experiment, magnetic assistance has been coupled with vibration in order to better disperse the powder and break large agglomerates. As for Aerosil® 200, the minimum fluidization velocity has been reduced from 0.015 m/s (1.5 cm/s) for conventional fluidization to 0.007 m/s (0.7 cm/s) during assisted fluidization. Also the fluidized bed pressure drop increases when the assisting methods are used because more powder is suspended by the fluidizing gas. Figure 3.20 shows a comparison of the non-dimensional bed height as a function of superficial gas velocity between the conventional and the assisted fluidized beds. A large difference in the bed expansion can be seen due to the better dispersion of the powder in the fluidizing gas because of the breaking up of the agglomerates and their better dispersion by the vibration.

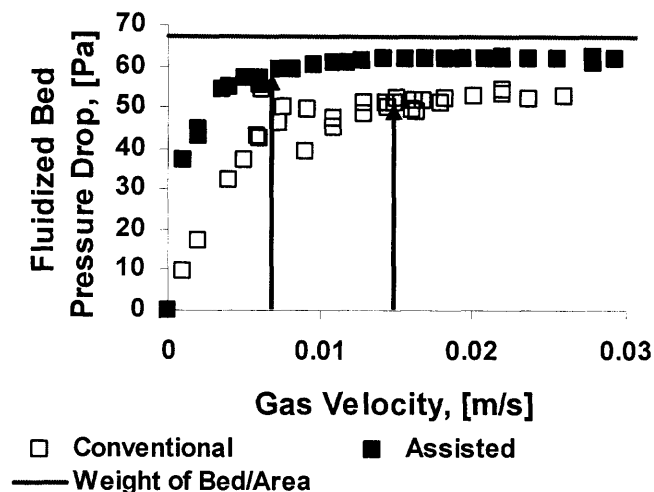


Figure 3.19 Comparison of the fluidized bed pressure drop of Aerosil[®] 90 for conventional and assisted fluidization (magnetically assisted coupled with vibration).

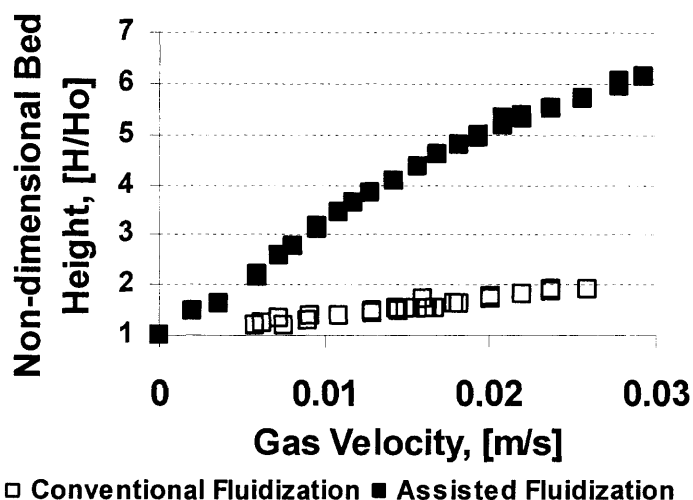


Figure 3.20 Comparison of the fluidized bed expansion of Aerosil[®] 90 for conventional and assisted fluidization (magnetically assisted coupled with vibration).

The homogeneity of the fluidized bed depends on the presence of bubbles. Figure 3.21 shows how bubbling is identified in a conventional fluidized bed of Aerosil[®] 200 during humidification of the powder. Since the bubbles contains gas having a moisture concentration similar to that at the entrance (bottom, of the column) the humidity sensor at the top of the column senses an increase in moisture due to bursting of the bubbles at the surface of the fluidized bed.

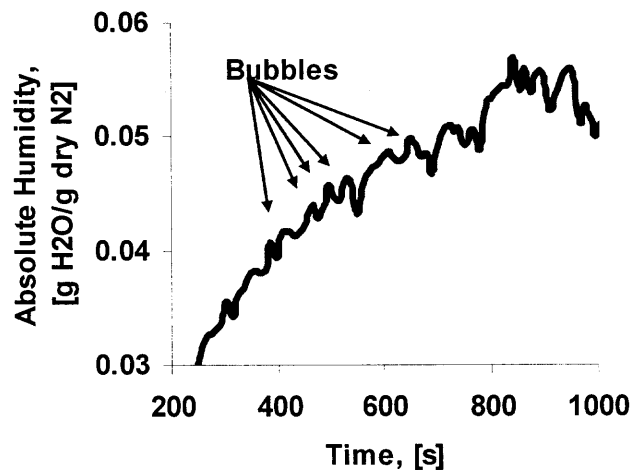


Figure 3.21 Sudden changes in moisture concentration seen at the sensor at the top of the column due to bursting of bubbles.

3.4.6 Residence Time Distribution (RTD) of Packed and Fluidized Beds of Hydrophobic Agglomerates of Aerosil R974

As pointed out in the experimental section, residence time distribution (RTD) studies allow for the identification of non-idealities in reactors. In other words, an RTD function is a characteristic of the degree of mixing that occurs in a chemical reactor⁸⁴.

The RTD is related to the time that molecules of a tracer spend in a reactor. The time that molecules spend in an ideal reactor is given by the space-time (τ), which is obtained by dividing the reactor volume by the volumetric flow rate entering the reactor. In these experiments, the fluidization column is composed of two volumes, a fluidized (F.B.) or packed bed (P.B.) volume and the empty volume above it, upstream the humidity sensor located at the top of the column as shown in Figure 3.22. The space-time values calculated for the different experiments represent the ideal conditions, i.e., without diffusion, and they are used as a point of comparison for the mean residence time obtained from the RTD functions. When calculating the space-time for a packed bed or a fluidized bed, the porosity (void fraction) has to be taken into account. The Blake-

Kozeny equation was used to estimate the void fraction, of around 0.35. Using this value of the void fraction for the packed and fluidized beds, the space-time (τ) can be approximated by the following equation

$$\tau_{total} = \tau_{Bed} + \tau_{Empty} = \frac{H_{bed}\epsilon}{U_g} + \frac{H_{empty}}{U_g} \quad (3.6)$$

where H is the height of the volume, U_g is the superficial velocity and ϵ is the void fraction of the bed. The calculated space-time values are shown in Table 3.3.

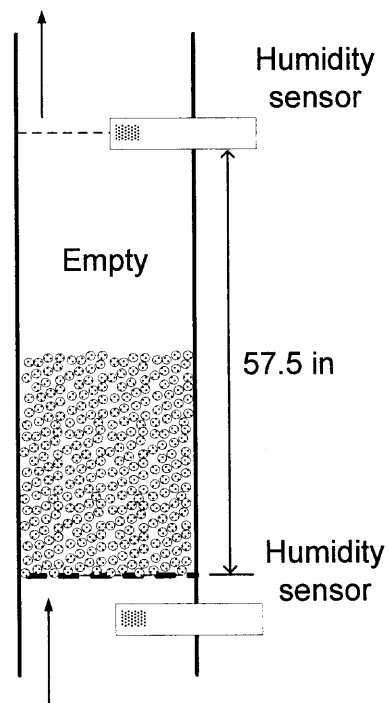


Figure 3.22 Schematic showing the regions of interest inside of the fluidization column.

Table 3.3 Space-Time for the Different Experiments of the RTD Studies

Column	Gas	Length	Space- time τ
	velocity		
	(cm/s)	(cm)	(s)
Empty	1.5	146	100
	2.2	146	67
P.B. Glass Beads	1.5	53	76
	2.2	53	51
P.B. R974	1.5	52	76
	2.2	52	51
	1.5	104	52
F.B. R974	2.2	104	35
	1.5	53	76
	2.2	53	51
	1.5	104	54
	2.2	107	35

From Table 3.3, longer space-time values correspond to the empty column and shorter space-times for packed or fluidized beds. This was expected because the available volume of the empty column is larger than the volume of the packed column.

The absolute humidity in the nitrogen gas has been used as the concentration of the tracer in the gas phase. There are two differences between the RTD results presented below and the experimental results concerning the evaluation of the assisting methods. Experiments for evaluating the assisting methods were done with hydrophilic nanopowders and experiments for finding the RTDs were done with a hydrophobic nanopowder. The second difference is that drying data is analyzed for the evaluation of the assisting methods while humidifying data is analyzed for obtaining the RTDs.

Figure 3.23 shows examples of the data measured by the humidity sensors after being converted to absolute humidity values. Two types of input signals can be issued upstream of the column, pulse and step inputs; however a pulse input is inaccurate

because of the broadening of the peak and the fact that the concentration of tracer entering the column is not infinite. For these reasons, a step input has been used for the RTD studies.

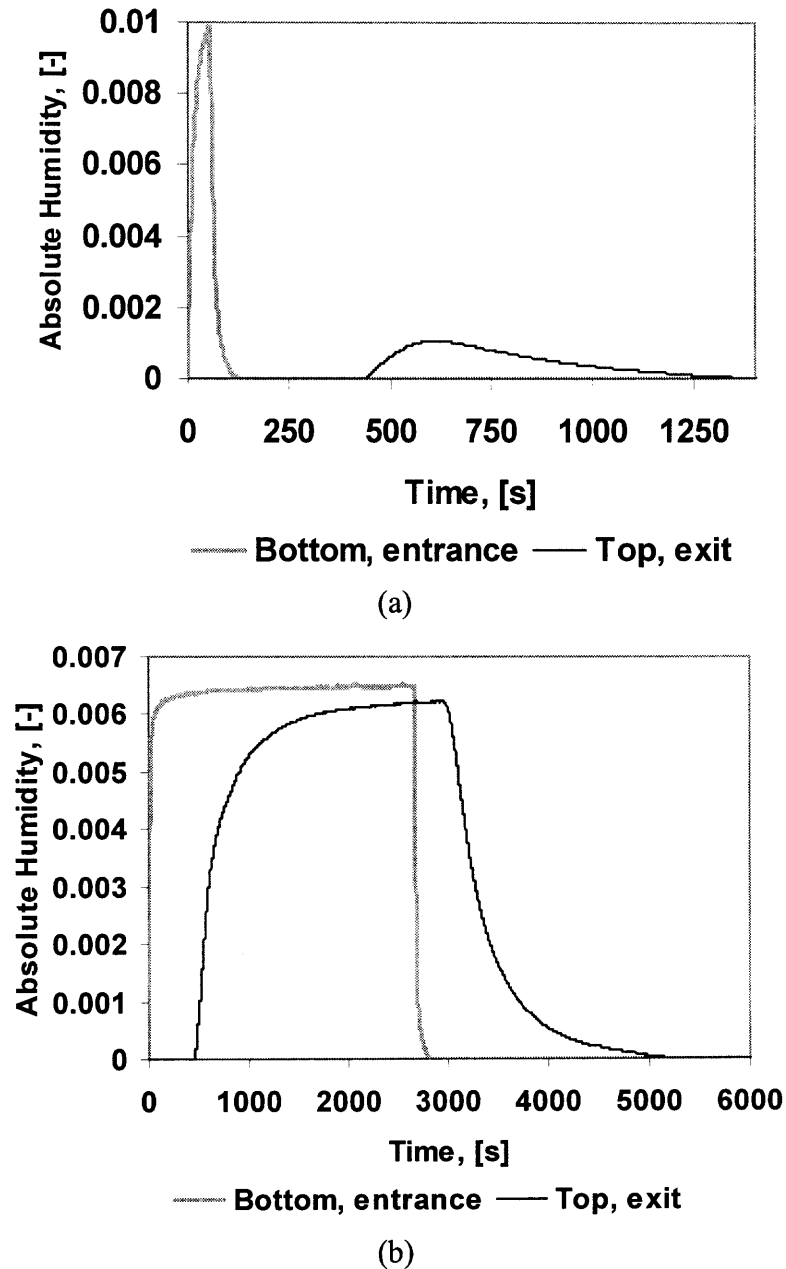


Figure 3.23 Examples of the absolute humidity data given by the sensors during RTD studies, moisture at the bottom of the column or input signal in red and moisture at the outlet of the column or response is given in blue, (a) pulse input, (b) step input.

From the absolute humidity data with respect to time, as shown in Figure 3.23, the residence time distribution (RTD) function, $E(t)$, can be obtained by using the equations below⁸⁴. For a pulse input the residence time distribution function is found by

$$E(t) = \frac{C(t)}{\int_0^{\infty} C(t) dt} \quad (3.7)$$

and for a step input, the following equation applies

$$E(t) = \frac{d}{dt} \left[\frac{C(t)}{C_0} \right]_{step} \quad (3.8)$$

It is important to note that the RTD function is always normalized, hence

$$\int_0^{\infty} E(t) dt = 1 \quad (3.9)$$

As mentioned above, a step input has been used because it is easier to apply than the pulse input and is more accurate. From absolute humidity data, the cumulative time distribution function, $F(t)$, can be obtained with the following equation

$$F(t) = \left[\frac{C(t)}{C_0} \right]_{step} \quad (3.10)$$

where $C(t)$ is the absolute humidity at the exit of the column (blue line in Figure 3.23) as a function of time and C_0 is the absolute humidity of the gas at the entrance of the column (red line in Figure 3.23). Hence, the RTD function, $E(t)$, can be found by applying Equation 3.8.

Before going into more detail on the method for processing of the data, it is important to recall the variables that characterize an RTD function. These are the mean residence time, t_m , and the standard deviation, σ . The mean residence time indicates the

average time that the molecules of the tracer spent in the reactor, in this case, the fluidized or packed bed of agglomerates, and it can be found with the following equation

$$t_m = \int_0^{\infty} tE(t) dt \quad (3.11)$$

The standard deviation is the square root of the variance, which indicates the spreading of the tracer (molecules) with respect to time. It can be found from

$$\sigma = \sqrt{\sigma^2} = \sqrt{\int_0^{\infty} (t-t_m)^2 E(t) dt} \quad (3.12)$$

One of the disadvantages of using the step mode input is that noise in the data becomes significant when the concentration of the tracer starts to level off. Data noise affects the estimation of the variables that characterize the RTD function, i.e., the mean residence time and the standard deviation. To remove the noise from the data, the RTD functions obtained from Equation 3.8 were truncated when the $E(t)$ values approached to zero. Then, the functions were normalized and the noise reduced by using the equidistant least square method based on Gram polynomials⁷⁸.

The RTD functions of the empty column and the column containing a packed bed of glass beads were obtained for comparing them to the RTD functions of packed and fluidized beds of agglomerates of nanoparticles. The cumulative, $F(t)$, and the RTD, $E(t)$, functions for a packed bed of agglomerates of Aerosil R974 are shown in Figure 3.24. RTD functions for a conventional fluidized bed of agglomerates of Aerosil R974 are shown in Figure 3.25. Additional plots showing more RTD functions are given in the appendix section.

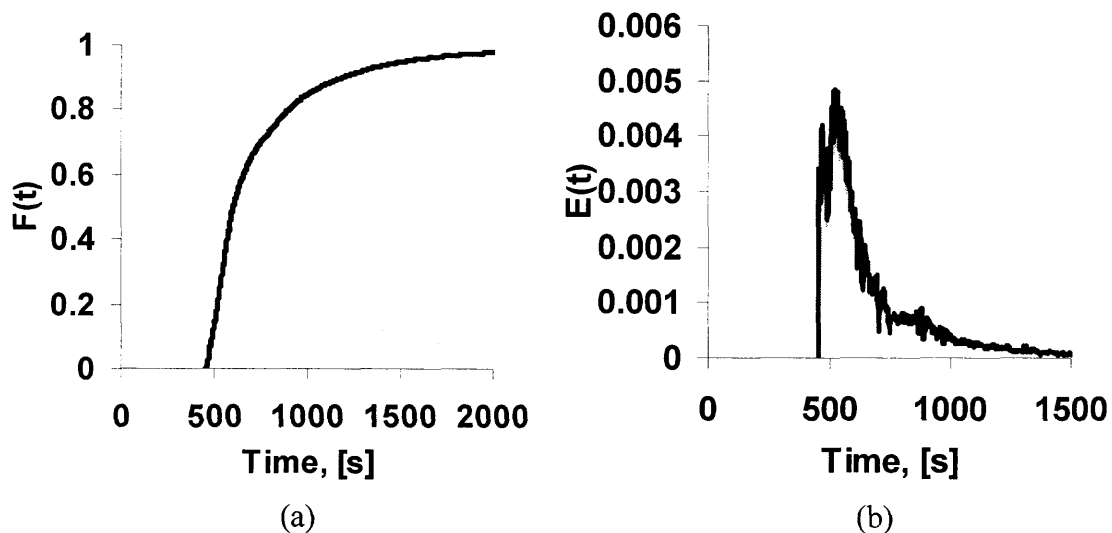


Figure 3.24 Responses obtained when applying a step moisture input to a packed bed of agglomerates of Aerosil R974. (a) cumulative distribution function, $F(t)$; (b) residence time distribution function, $E(t)$.

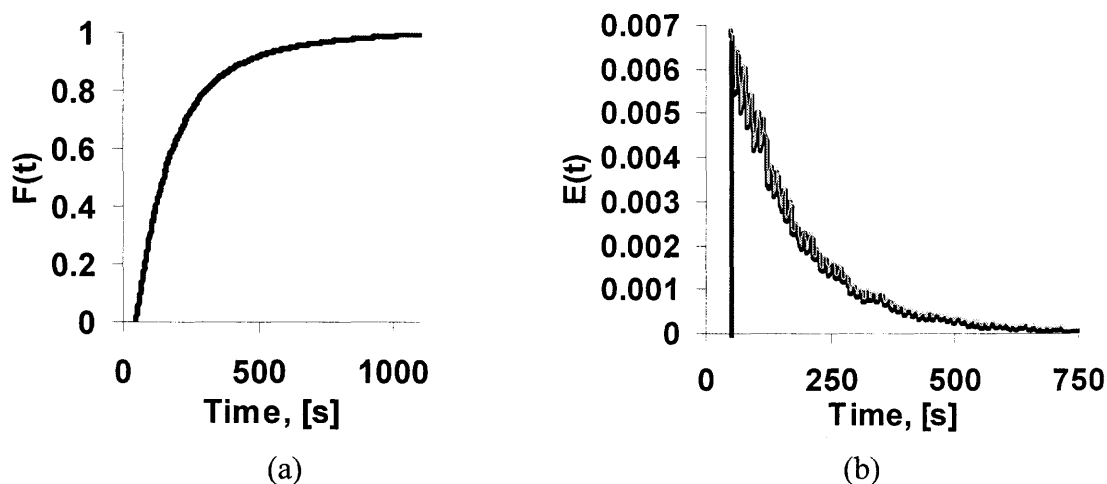


Figure 3.25 Responses obtained when applying a step moisture input to a fluidized bed of agglomerates of Aerosil R974. (a) cumulative distribution function, $F(t)$; (b) residence time distribution function, $E(t)$.

When the RTD functions shown in the figures above are compared, it can be clearly seen that the delay in the exiting of the tracer, moisture, for the packed bed of agglomerates of Aerosil R974 is longer than the time delay shown in the RTD function of the fluidized bed. In both experiments, the concentration of the tracer was approximately

the same, about 10 mbar. A better way to compare the RTD functions is to have their characterizing variables (t_m , τ , σ) plotted on the same graph as shown below.

The RTD functions, $E(t)$, shown in Figure 3.24 and Figure 3.25 are similar to the response from a reactor having a PFR and a CSTR in series. By using this analogy, the RTD function obtained from the experimental data can be characterized by a time delay (similar to the PFR space time), τ_D , and a CSTR-like space time, τ_S . This type of response is shown in Figure 3.26. Actually, the RTD functions obtained from experimental data are very similar to the result corresponding to the axial dispersion of a tracer in a tubular reactor with laminar flow, also known as the Aris-Taylor problem⁸⁴.

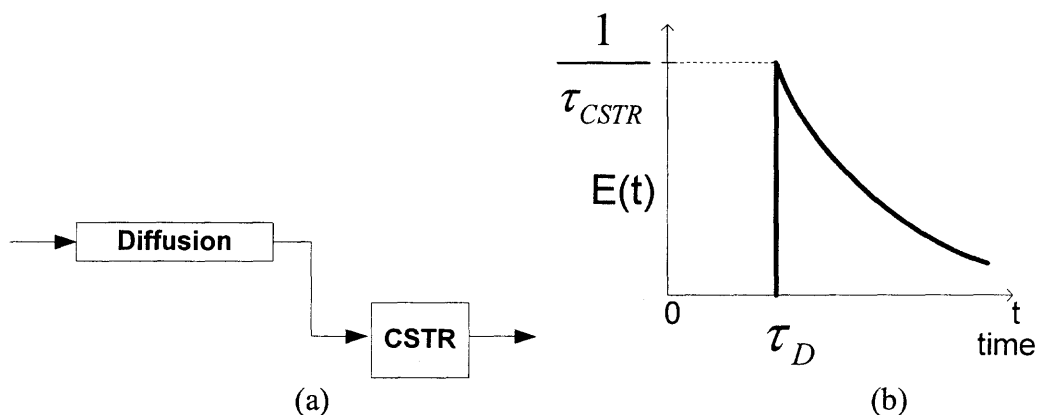


Figure 3.26 RTD for a model incorporating diffusion (as a PFR) and a CSTR in series.

The RTD response from the reactor composed of a PFR and CSTR in series can be modeled by

$$E(t) = \begin{cases} 0 & t < \tau_D \\ \frac{e^{-(t-\tau_D)/\tau_s}}{\tau_s} & t \geq \tau_D \end{cases} \quad (3.13)$$

and can be applied to the RTD responses obtained from the experiments, where the delay due to the diffusion (τ_D) is modeled in a similar way than the space time of a PFR, although such a reactor does not exist in these experiments.

RTD functions of the packed beds of large agglomerates of nanoparticles and non-porous glass beads, and fluidized beds of sieved and jet processed agglomerates were obtained from the experiments. Their corresponding characteristics such as the time delay due to diffusion (τ_D), the mean residence time (t_m) and the standard deviation (σ) were calculated using the equations shown above. Note that the last two variables correspond to the CSTR portion of the RTD functions.

Figure 3.27a shows the time delays (τ_D) and the corresponding mean residence time (t_m) of the RTD functions obtained from the experiments. Note that for these results three different concentration of tracer (5, 10 and 15 mbar) were used in combination with two different gas velocities (1.5 and 2.2 cm/s) and two different bed heights (21 and 41 inches) for each different condition (packed bed of glass beads or clusters of nanoparticles and fluidized beds of agglomerates of nanoparticles). From this figure, it is seen that the time delays are longer for the packed beds of large agglomerates (clusters) of Aerosil R974, represented by the squares, than for the other cases. These time delays are also dependant on concentration which is why they do not match as the concentration of the tracer is changed keeping all the other variables constant. From the figure, the time delays also depend on the gas velocities with higher gas velocities leading to shorter time delays as can be seen by comparing the symbols enclosed by a black border (1.5 cm/s) to the symbols without the black border (2.2 cm/s).

It is believed that the time delay on the tracer is caused by the diffusion of the tracer into the pores of the large agglomerates because the time delay observed for the packed bed of glass beads is significantly shorter, indicating that the diffusion is not due to the dispersion in the porosity of the bed (around the agglomerates) but due to diffusion into the pores of the agglomerates.

Figure 3.27(b) shows a close up of Figure 3.27(a) after removing the data corresponding to the packed bed of the large agglomerates of Aerosil R974. The points corresponding to the empty column and a gas velocity of 2.2 cm/s have a time delay (τ_D) of about 33 s which is approximately half of the space-time shown in Table 3.3 of about 67 s. This is in agreement with the solution to the Aris-Taylor problem⁸⁴ and validates the experimental setup, experimental procedure and results. Also, when the gas velocity is 1.5 cm/s, the time delay (τ_D) is about 42 s which is somewhat close to half of the space time of about 100 s, as predicted by the Aris-Taylor problem, and the mean residence time is larger for the lower velocity because diffusion becomes more important.

For the packed bed of the glass beads, again the diffusion is larger at the low gas velocity which is the reason why the time delay (τ_D) and the mean residence time are longer. Under the operating conditions used in the experiments, no significant diffusion is seen due to the tortuosity of a packed bed indicating that the diffusion effects seen for the packed bed of agglomerates are due to their porosity.

When looking at the data given by the conventional fluidized beds (diamonds), the time delay (τ_D) is longer for the shorter bed (light blue) and shorter for the longer bed (purple). This is due to the difference in the empty column's volume and is in agreement with the space-times reported in Table 3.3.

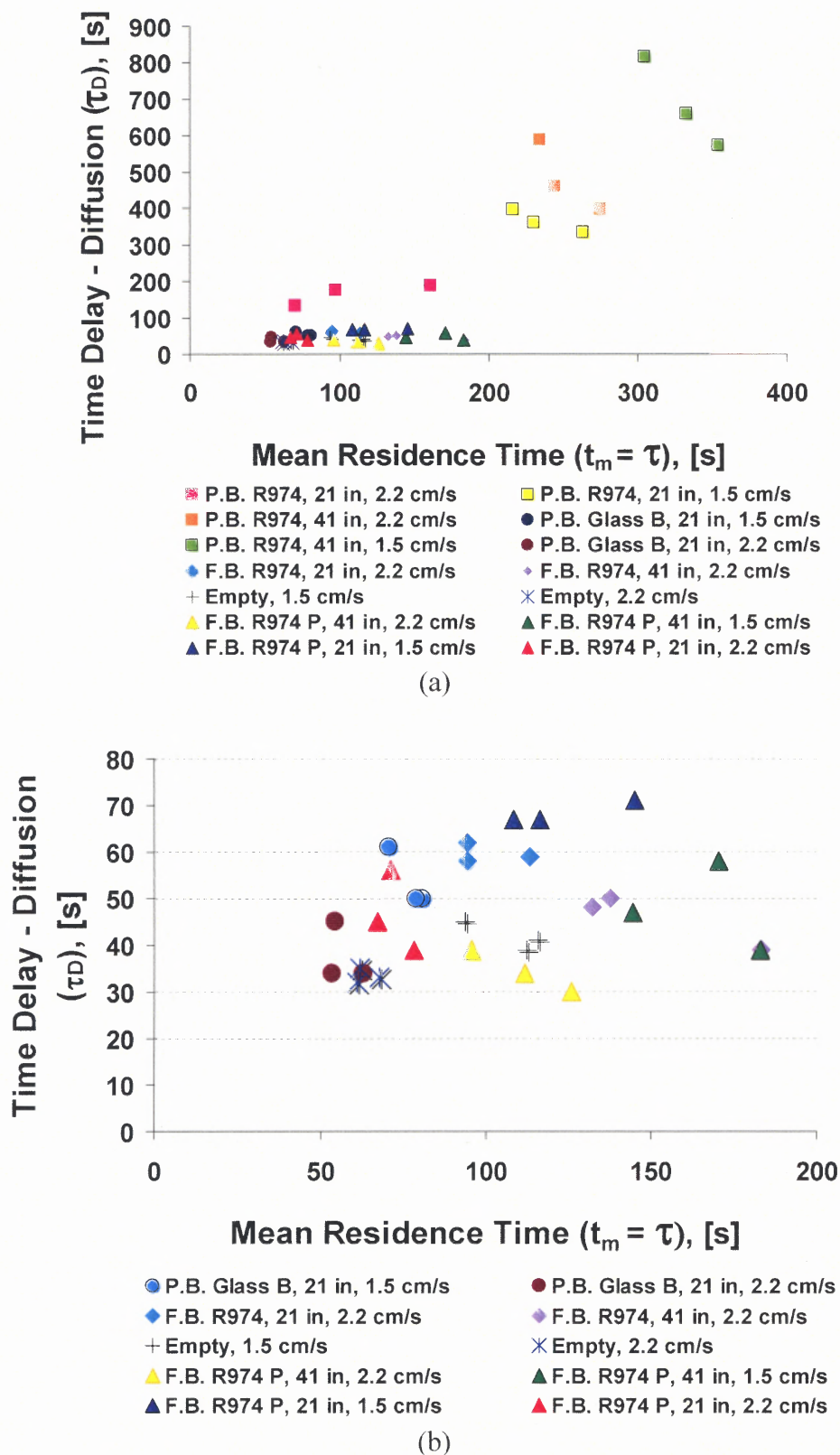


Figure 3.27 Time-delay (τ_D) due to diffusion and mean residence time from the RTD function for the different experiments (P.B., Packed Bed; F.B., Fluidized Bed; P. Processed powder; B., Beads).

In Figure 3.27, when comparing the time delays (τ_D) of the conventionally fluidized nanopowder (diamonds) and the jet processed nanopowder, it can be seen that time delays (τ_D) are slightly shorter for the jet processed nanopowder (see purple diamonds, average of 46 s vs. yellow triangles, average of 34 s and light blue diamonds, average of 60 s vs. red triangles, average of 46.6 s). These results indicate that there is a greater diffusion effect in the conventionally fluidized nanopowder probably due to the presence of larger and denser agglomerates.

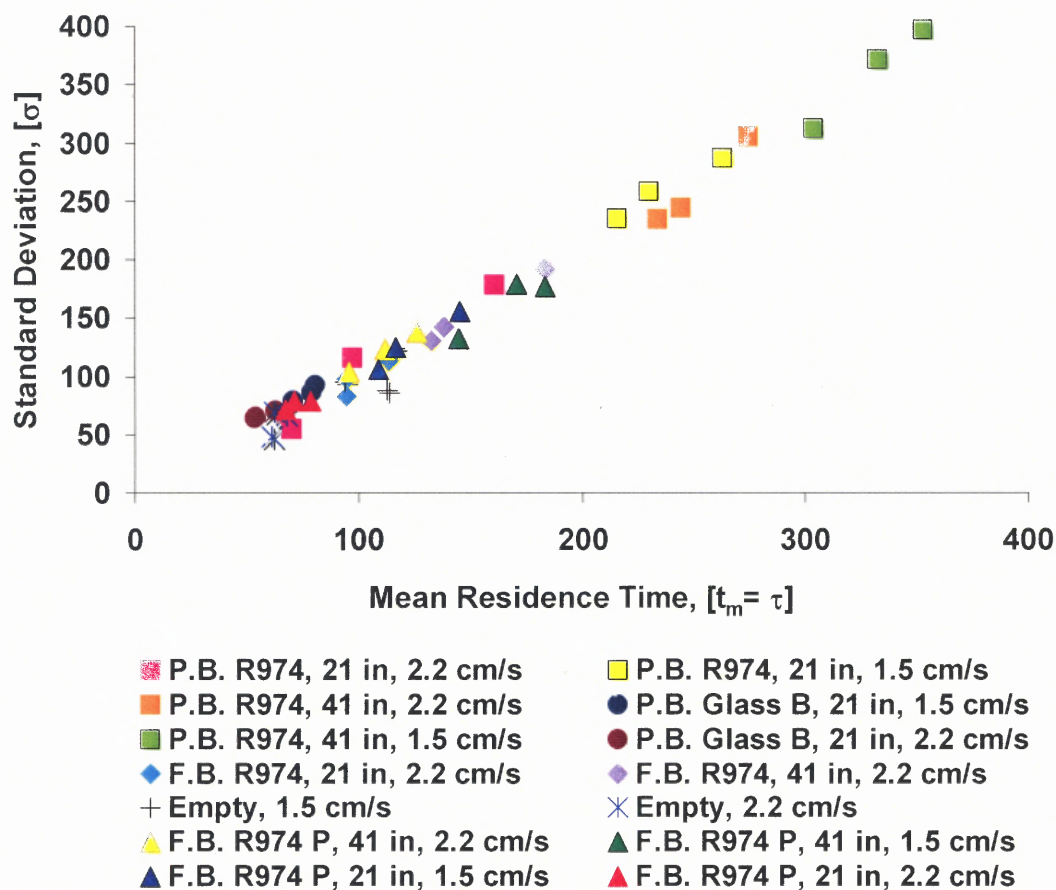


Figure 3.28 Standard deviation and mean residence time of the RTD functions (CSTR portion) obtained from the experimental data.

Figure 3.28 shows the standard deviation plotted against the mean residence time for the different cases studied. The data fits a linear regression of slope equal to unity indicating that the standard deviation (σ) is approximately equal to the mean residence time (t_m) which is a typical characteristic of a CSTR type response. The standard deviation and the mean residence time indicate a greater dispersion of the moisture, as given by their decreasing values, in the following order: packed beds of agglomerates of nanoparticles (squares) > conventional fluidized beds (diamonds) > jet processed fluidized beds (triangles) > empty column (cross, star) and the packed bed of glass beads (dots).

From the data, it has been shown that diffusion effects are expected in a fluidized bed of agglomerates of nanoparticles depending on the presence of large agglomerates. A fluidized bed of jet processed agglomerates shows lesser diffusion effects and can be modeled as a CSTR. In contrast, a conventionally fluidized bed will contain large agglomerates that delay transport due to diffusion; hence, those fluidized beds show a delay in the concentration at the exit.

3.5 Modeling

Detailed modeling of the hydrodynamic and mass transfer characteristics of fluidized beds of nanoparticle agglomerates has been developed⁷⁹, and the contribution from this work was to analyze the existing model, to suggest changes in critical variables and to prepare a program code to compare the model to the experimental results shown. The key non-dimensional numbers related to the hydrodynamic characteristics of the powder that

impact the mass transport are the Reynolds number at terminal velocity (Re_t) and the Archimedes number (Ar)

$$Re_t = \frac{U_t d_p \rho_g}{\mu_g} \quad (3.14)$$

$$Ar = \frac{d_p^3 \rho_g (\rho_p - \rho_g) g}{\mu_g^2} \quad (3.15)$$

By doing a force balance on a fluidized agglomerate, according to Newton's second law the following well known expression is derived

$$C_D Re_t^2 = \frac{4}{3} Ar \quad (3.16)$$

where the drag coefficient can be approximated by using the Schlichting and Gersten, approach⁸⁰

$$C_D \cong \frac{1}{3} \left(\sqrt{\frac{72}{Re_t}} + 1 \right)^2 \quad (3.17)$$

This equation can be substituted into Equation 3.16 to obtain an equation for the Reynolds number as function of the Archimedes number.

$$Re_t = 18 \left(\sqrt{1 + \frac{1}{9} \sqrt{Ar}} - 1 \right)^2 \quad (3.18)$$

To model the concentration of moisture with respect to time at the exit of the batch fluidized bed the following assumptions are made as extracted from the reference⁷⁹:

- Fluidization is homogeneous because of the use of the assisting methods implying the presence of only two phases: the agglomerates and the gas surrounding the agglomerates in the suspension phase. Bubbling does not occur.
- There is no concentration gradient within the agglomerate.

- The outer boundary of the agglomerate is in equilibrium with the surrounding gas phase and can be described by the adsorption isotherm.
- Mixing in the fluidized bed is CSTR-like. The concentration of moisture in the gas phase of the fluidized suspension is equal to the concentration of moisture exiting the fluidized bed, i.e., the concentration of moisture in the gas phase is independent of position in the fluidized bed.

Based on these assumptions, a mass balance is applied to both phases, the agglomerates (solid phase) and the gas phase. A schematic diagram that illustrates the phases and the variables involved in the transport of moisture between the agglomerates and the gas phase is shown in Figure 3.29.

Besides the non-dimensional numbers related to the hydrodynamics of the agglomerates in the fluidized bed, the Schmidt and the Sherwood numbers are related to the mass transport of moisture.

$$Sc = \frac{\nu}{\rho_g D_m} \quad (3.19)$$

$$Sh = 2 + \sqrt{Sh_{lam}^2 + Sh_{turb}^2} \quad (3.20)$$

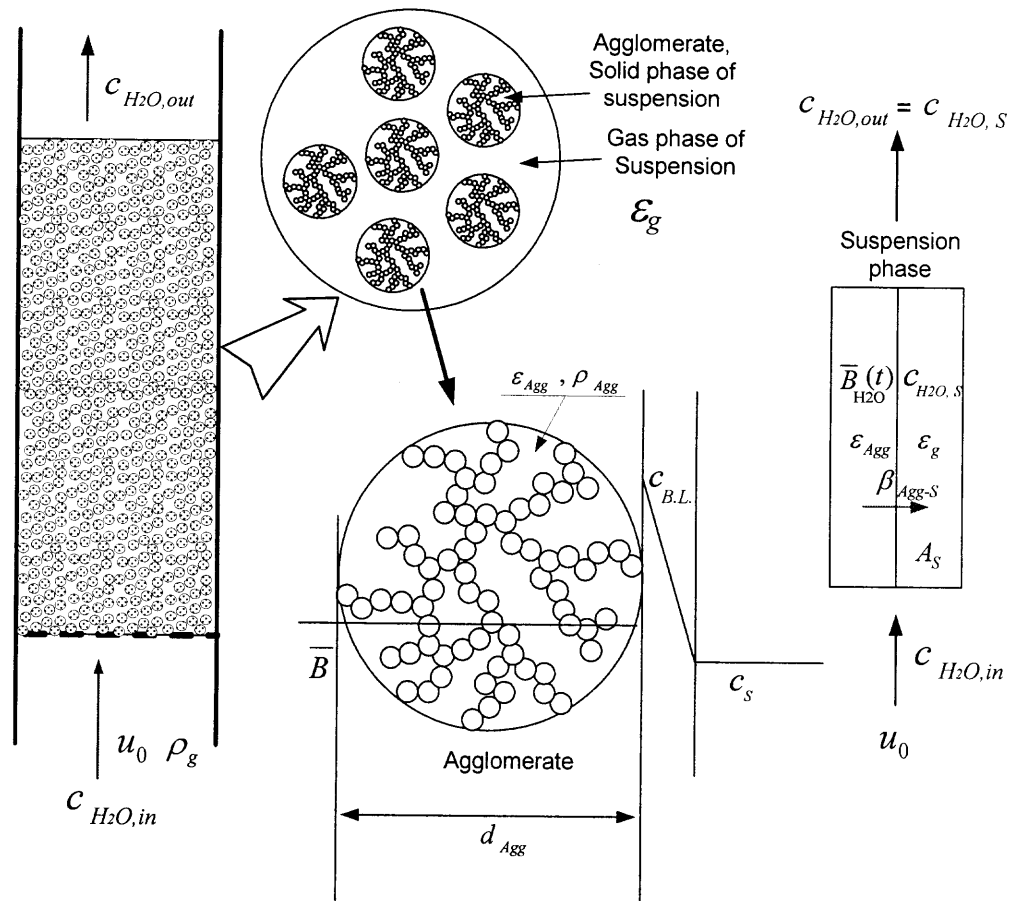


Figure 3.29 Schematic diagram showing homogeneous fluidization of agglomerates of fumed silica nanoparticles and the variables considered in the modeling of the transport of moisture⁷⁹.

where the laminar and turbulent Sherwood numbers can be expressed as⁸¹

$$Sh_{lam} = 0,664\sqrt[3]{Sc}\sqrt{Re_i} \quad (3.21)$$

$$Sh_{turb} \approx 0 \quad (3.22)$$

Here it is assumed that the mass-transfer correlation for flow around a single sphere can be used to estimate the mass transfer from an agglomerate in the fluidized bed, and also the turbulent Sherwood number is neglected because the experiments are under laminar flow conditions.

In Equation 3.19, the binary diffusion coefficient can be estimated^{82, 83}

$$D_m = \frac{10^{-7} T^{1.75} \left(\frac{\tilde{M}_1 + \tilde{M}_2}{\tilde{M}_1 \tilde{M}_2} \right)^{1/2} 1.013}{p \left((\sum v_1)^{1/3} + (\sum v_2)^{1/3} \right)^2} \quad (3.23)$$

where the pressure p is given in bars, the temperature T in degrees Kelvin, and the equation calculates the binary molecular diffusion-coefficient in units of m^2/s . $\tilde{M}_{1,2}$ is the molecular mass (in kg/kmol) of both components and $v_{1,2}$ are molecule specific constants, which can be found in the literature or can be calculated. For the diffusion of water-vapor in air, $v_1 = 12.7$ (water) and $v_2 = 20.1$ (air) were considered.

A moisture mass balance on the agglomerate results in the following equation,

$$M_{SiO_2} \frac{d\bar{B}_{H_2O}}{dt} = -\beta_{Agg-S} n_{Agg} a_{Agg} (c_{H_2O,BL} - c_{H_2O,S}) \quad (3.24)$$

where M_{SiO_2} is the mass of the nanopowder loaded in the fluidization column; \bar{B}_{H_2O} represents the mass of moisture per mass of powder (kg/kg); β_{Agg-S} is the mass transport coefficient of moisture from the agglomerate to the gas in the suspension phase; n_{Agg} is the number of agglomerates in the fluidized bed; a_{Agg} is the area of the surface of the agglomerate; c_{H_2O} represents concentration given in mass of moisture per volume of gas; the subscripts BL and S represent the “boundary layer” and “suspension” phase (gas surrounding the agglomerates), respectively.

The equilibrium relationship between the concentrations of moisture in the gas phase at the boundary layer surrounding the agglomerate ($c_{H_2O,BL}$) and the concentration of moisture in the agglomerate (\bar{B}_{H_2O}) is assumed to follow a modified Henry law which considers that the void fraction in the agglomerate is homogeneous.

$$c_{H_2O,BL} = \frac{\bar{B}_{H_2O}}{K'_c} \quad (3.25)$$

where K'_c is the modified Henry constant considering the porosity of the agglomerate. In addition, by assuming that the agglomerates are spherical and of the same size, the total (outer) surface area of the agglomerates can be written as

$$n_{Agg} a_{Agg} = \frac{6}{d_{Agg}} \frac{V_{SiO_2}}{(1 - \varepsilon_{Agg})} \quad (3.26)$$

Substituting the terms from Equations 3.25 and 3.26 into Equation 3.24, and after simplifying, the concentration of moisture in the agglomerate with respect to time is given as

$$\frac{d\bar{B}_{H_2O}}{dt} = -\beta_{Agg-S} \frac{6}{d_{Agg} \rho_{SiO_2} (1 - \varepsilon_{Agg})} \left(\frac{\bar{B}_{H_2O}}{K'_c} - c_{H_2O,S} \right) \quad (3.27)$$

To obtain the mass transfer from the boundary layer around the agglomerates to the gas phase in the suspension, the mass transfer coefficient is estimated as

$$\beta_{Agg-S} = \frac{Sh D_m}{d_{Agg}} \quad (3.28)$$

for which the Sherwood number and the diffusion coefficient have been calculated according to Equations 3.20 and 3.23, respectively.

Similarly, a moisture mass balance in the gas phase leads to the following equation,

$$\varepsilon_g V_{FB} \frac{dc_{H_2O,S}}{dt} = \beta_{Agg-S} n_{Agg} a_{Agg} \left(\frac{\bar{B}_{H_2O}}{K'_c} - c_{H_2O,S} \right) + u_S \varepsilon_g A_{FB} (c_{H_2O,in} - c_{H_2O,S}) \quad (3.29)$$

which represents the rate of change with respect to time of the moisture in the suspension gas phase. The first term in the right side of the equation comes from the mass transfer of

moisture from the agglomerate into the suspension gas phase, and the second right side term corresponds to the difference in the moisture entering and leaving the bed since $c_{H_2O,S} = c_{H_2O,out}$. In Equation 3.29, ε_g represents the void fraction in the fluidized bed (inter-agglomerate void); V_{FB} is the volume of the fluidized bed, u_s is the interstitial gas velocity and A_{FB} represents the cross sectional area of the fluidized bed. After using Equation 3.26 and a correlation for the porosity in a fluidized bed,

$$\frac{dc_{H_2O,S}}{dt} = \beta_{Agg-S} \frac{6(1-\varepsilon_g)}{d_{Agg}\varepsilon_g} \left(\frac{\bar{B}_{H_2O}}{K'_c} - c_{H_2O,S} \right) + \frac{u_s}{H_{FB}} (c_{H_2O,in} - c_{H_2O,S}) \quad (3.30)$$

Equations 3.27 and 3.30 lead to a system of simultaneous differential equations for the moisture concentration with respect to time. These equations have been solved by using a program written in MATLAB 7.1. A comparison of the moisture concentration at the exit of a fluidized bed of Aerosil[®] 200 with respect to time between the experimental data and the model is shown in Figure 3.30. The experimental data shown in these figure has been obtained by monitoring the moisture at the exit of the vibrated fluidized bed during drying of 40 grams of Aerosil[®] 200 after being humidified under a partial pressure of about 10.7 mbar of moisture. These experimental data have been previously shown in Figure 3.12. The results from the model agree closely with the data; however, it is important to note that some of the assumptions may not fully apply to the fluidized bed system of agglomerates of nanoparticles. In particular, other correlations may need to be applied to make the model closer to reality with regard to the following variables: the surface area of the agglomerates available for mass transport, the void fraction within the agglomerate, the delay due to diffusion in and out of agglomerates and the assumed mono-dispersity of the agglomerates, among others.

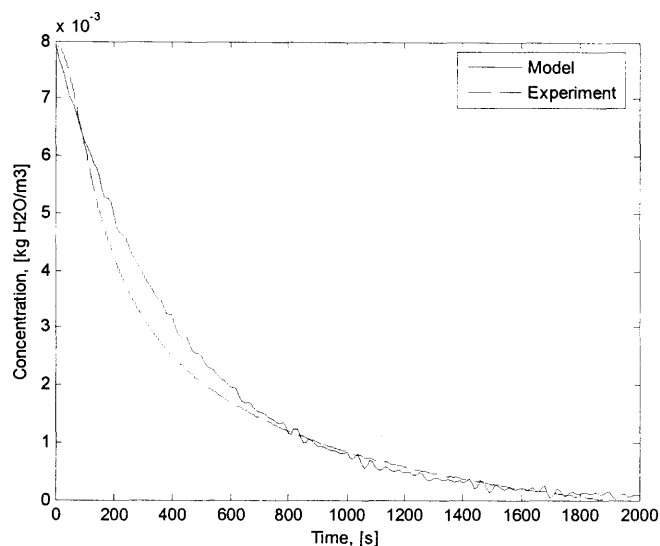


Figure 3.30 Comparison of experimental and modeling data corresponding to the concentration of moisture in the gas phase with respect to time. Experimental data obtained from monitoring moisture in the gas phase at the exit of a vibrated fluidized bed, (data shown in Figure 3.12).

3.6 Conclusions

By monitoring the adsorption/desorption of moisture in the gas phase during fluidization of nanopowders and the fluidization characteristics observed, the fluidization quality of fumed silica nanoparticles is clearly enhanced by applying external force field assistances. In particular, fluidization of Aerosil[®] 200 is enhanced by vibration while magnetic assistance is needed to break up the large agglomerates present during the fluidization of Aerosil[®] 90. For improving the fluidization of Aerosil[®] 90 (a typical ABF nanopowder) a combination of vibration and magnetic assistance gives the best results.

The quantification of moisture in the powders was done by monitoring the moisture in the gas phase to obtain adsorption isotherm data. The absorption isotherms were also obtained by a standard gravimetric method for comparison purposes. By monitoring the moisture content in the gas phase, the overall moisture absorbed in the

entire bed of powder is evaluated. In contrast, when using the gravimetric method only powder that is fully fluidized is analyzed. Isotherm data were obtained for Aerosil[®] 200 and Aerosil[®] 90 showing that the former adsorbs more moisture than the later. It was also found that data collected by monitoring the moisture in the gas phase slightly overestimate the true values of the slopes of the adsorption isotherm plots (as measured gravimetrically) due to the effect of axial dispersion⁸⁴ of the moisture in the fluidized bed.

The dispersion effects, mathematical modeling and residence time distributions will be the object of a future study. For Aerosil[®] 200, the presence of large agglomerates does not affect the amount of moisture retained by the fluidized bed since they are found in small amounts; on the contrary, for Aerosil[®] 90, large agglomerates constitute a significant fraction of the powder and they affect the adsorption of moisture due to the poor mixing between the solid and gas phases, hindering the overall absorption of moisture by the bed of powder.

The enhancement of fluidization due to the assisting methods is reflected by the increase of moisture retained by the overall fluidized bed of powder while humidifying and by reducing the time needed for the bed of powder to release the moisture trapped, as shown by the drying curves obtained by monitoring the gas phase. The improvement is relatively modest for Aerosil[®] 200, an APF type nanopowder that can be fluidized without any assistance; however, for fluidization of Aerosil[®] 90, there is significant enhancement in the fluidization which is shown in the difference in the amount of moisture adsorbed/released when compared to conventional fluidization.

The study of the RTD functions in packed and fluidized beds of agglomerates of nanoparticles indicates that there is a delay in the appearance of the tracer due to its diffusion into the pores of the relatively large agglomerates. The tracer coming from a fluidized bed of jet processed agglomerates, which have been reduced in size and density, shows shorter delay indicating lesser diffusion effects. For modeling of the concentration of moisture at the exit of the fluidized bed, a delay has to be considered if the fluidizing nanopowder has not been jet processed; this time delay can be modeled by similarity to the response from a PFR-CSTR in series reactor.

Modeling of the concentration of moisture in the gas phase exiting the fluidized bed of agglomerates of nanoparticles has been introduced. Differences, between previous models and the one presented here, include the fact that agglomerates of nanoparticles are extremely porous, they fluidize homogeneously, and the proposed model focuses on the adsorption/desorption of moisture at the surface of the agglomerate. Note that for achieving adsorption only, low levels of moisture are required to avoid the formation of a liquid phase at the surface of the agglomerate; hence, condensation/evaporation is not included in the model. The model is based on finding the moisture mass transport from the agglomerate to its boundary layer and then to the bulk gas phase around the suspension. Predicted and measured concentrations of moisture as a function of time show very good agreement.

CHAPTER 4

FLUIDIZATION OF NANOAGGLOMERATES IN A ROTATING FLUIDIZED BED: THE INFLUENCE OF TANGENTIAL GAS MOTION

4.1 Overview

Agglomerates of nanoparticles were fluidized in a Rotating Fluidized Bed (RFB) system at different rotating speeds corresponding to 10, 20, 30 and 40 times the gravity force (9.8 m/s^2). The powders, fumed silica Aerosil[®] R974, Aerosil[®] R972 and Aeroxide[®] TiO₂ P25, with a primary particle size of 12, 16 and 21 nm, respectively, form micron sized nanoagglomerates. The bulk density of these fumed silica nanopowders is low (around 30 kg/m^3) and it is somewhat higher for Aeroxide[®] TiO₂ P25 (about 90 kg/m^3). Their fluidization behaviors are described by the fluidized bed expansion, pressure drop and minimum fluidization velocity (U_{mf}). It was found that the fumed silica agglomerates expanded considerably while the TiO₂ agglomerates showed very little bed expansion. The minimum fluidization velocities for Aerosil[®] R974 and R972 ranged from 0.02 to 0.07 m/s and from 0.13 to 0.20 m/s for Aeroxide[®] TiO₂ P25; U_{mf} increased at higher rotating speeds for all powders.

At gas velocities above U_{mf} , the fluidized bed pressure drop of fumed silica agglomerates was higher than theoretically estimated by mathematical models found in the literature. Thus, it is believed that for these light particles additional tangential momentum effects may increase the bed pressure drop and a revised model is proposed. In addition, the agglomerate size and external void fraction of the bed are predicted by using a fractal analysis coupled with a modified Richardson-Zaki equation for data obtained with Aerosil[®] R972.

4.2 Introduction

Because of their unique properties due to their very small primary particle size and very large surface area per unit mass, nanostructured materials are already being used in the manufacture of drugs, cosmetics, foods, plastics, catalysts, and energetic and bio materials. Therefore, it is necessary to develop processing technologies, which can handle large quantities of nanosized particles, e. g., mixing, transporting, modifying the surface properties (coating)^{85, 86} and downstream processing of nanoparticles to form nanocomposites. Before processing of nanostructured materials can take place, the nanosized particles have to be well dispersed. Gas fluidization is one of the best techniques available to disperse and process powders and is widely used in a variety of industrial applications because of its capability of continuous powder handling, good mixing, large gas-solid contact area and very high rates of heat and mass transfer. Moreover, it has been demonstrated that a rotating fluidizing bed (RFB) system has advantages over conventional fluidized beds in terms of handling very fine powders due to the additional forces generated by the rotation of the assembly⁸⁷.

To date, several studies on fluidization of agglomerates of nanoparticles have been done which include conventional fluidization⁷ and externally assisted fluidization involving the use of additional forces generated by vibratory⁵, acoustic², or magnetic fields⁸ to enhance the dynamics of the powder in the fluidized bed. It also has been found that the nanoparticles form fractal agglomerates⁵, and that the size and porosity of the agglomerates affect the nature of fluidization; therefore, several studies have focused on theoretical predictions of the average agglomerate size^{5,7}, as well as altering its size by external excitations^{2,5,7,8,87}.

Wang et al.⁸⁸ found that when fluidizing different nanoparticles, the fluidization behavior can be classified as either Agglomerate Particulate Fluidization (APF) or Agglomerate Bubbling Fluidization (ABF). APF is characterized by a large bed expansion of up to three to five times the original bed height, smooth fluidization and very low minimum fluidization velocities. ABF shows little bed expansion, bubbling, and the bed behaves more like Geldart Group B micron size particles. This is in agreement with the fluidization behavior observed by Zhu et al.⁷ where some nanoparticles fluidized homogeneously (APF) and others formed large bubbles and channels (ABF).

Among the several studies on rotating fluidized beds, Kroger et al.⁸⁹ estimated the bed pressure drop and flow distribution in both packed and fluidized rotating beds of spherical particles. In a section of their modeling work, they analyzed how the tangential velocity and effective viscosity of the fluidized bed could affect the pressure drop in a fluidized bed. They concluded that in some cases a decrease in the effective viscosity caused by an increase in void fraction could lead to tangential momentum effects within the fluidized bed which would increase its pressure drop. It is believed that this phenomenon also occurs while fluidizing APF agglomerates of nanoparticles, although it should be noted that the modeling done by Kroger et al.⁹⁵ did not consider nanoparticles.

By fluidizing micron size alumina particles and glass beads, Qian et al.⁸⁷ concluded that the fluidization behavior of fine particles can be changed from Geldart Group C to Geldart Group A due to the centrifugal acceleration, the value of which could be adjusted to several times the acceleration of gravity by simply increasing the rotating speed of the distributor. Kao et al.⁹⁰ developed equations for predicting the pressure drop and the minimum fluidization velocity of a fluidized bed of millimeter size particles.

They simplified the equations previously developed by Chen⁹¹, who for modeling purposes assumed that the fluidized bed rotated like a rigid body. Chen⁹⁷ also suggested that in a rotating fluidized bed, the particulate material is fluidized layer by layer from the solid-gas interface outward at increasing radius as the gas velocity is increased. The phenomenon of fluidization, layer by layer, which is caused by the radial velocity being higher and the centrifugal force lower at the bed's interface, is useful to explain the fact that the bed void fraction at the bed's interface, i.e., the freeboard region, is lower than the bed void fraction in the proximity of the distributor.

Extensive modeling and numerical simulations of the flow pattern in a rotating cylinder containing a packed bed was done by Arman⁹². His work describes the different flow regions inside the rotating cylinder that arise as a consequence of the type of flow. He also describes the presence of a significant tangential velocity of the fluid gas right above the packed bed or fluidized bed of particles; this is important for explaining the additional tangential momentum effects that can alter the bed pressure drop.

Watano et al. granulated particles of cornstarch (about 15 microns in size) by using an RFB unit⁸⁵, showing the potential applications of this device for the pharmaceutical industry. Saunders⁹³ study on the entrainment of particles coming from an RFB, explained the importance of the ratio of fluidizing velocity to particle terminal velocity at the surface of the rotating bed.

Recently, Matsuda et al.⁹⁴ fluidized agglomerates of nanoparticles of TiO₂ with a primary particle size of 7 nm, which is smaller in size than the nanosized TiO₂ fluidized in the present work. They presented a model based on an energy balance which predicts a reduction in agglomerate size at higher centrifugal forces. However, the agglomerate

sizes used to validate the model were obtained by measuring minimum fluidization velocities and used correlations from Wen and Yu⁹⁵, rather than by direct agglomerate size measurements.

In this work, nanoparticles agglomerates of fumed silica, namely, Aerosil[®] R974 and Aerosil[®] R972 (provided by Degussa Japan – Nippon Aerosil Co.) and Aeroxide[®] Titanium Dioxide P25 (provided by Degussa Corp. USA) were fluidized while subject to 10, 20, 30 and 40 times normal gravity acceleration. Data such as the fluidized bed height and pressure drop were recorded and used to approximate the minimum fluidization velocity by plotting the bed pressure drop against the gas velocity.

In conventional fluidization, Aerosil[®] R974 and Aerosil[®] R972 show an agglomerate particulate fluidization (APF) behavior which is characterized by a bed expansion of about several times the initial bed height depending on the gas velocity^{2, 5, 7, 8}. It has been found in this work that in an RFB, the initial bed height is almost doubled during fluidization of these powders, and that the fluidized bed pressure drop is higher than that theoretically estimated by Kao's model⁹⁶.

It is believed that the effective viscosity and the Darcy number of the fluidized bed are significantly reduced due to the large total bed void fraction; thus, the tangential velocity component of the gas flow within the fluidized bed may become significant, in particular, in the vicinity of the gas-solid interface. As a result, the fluidized bed pressure drop may increase due to additional forces caused by the tangential momentum effects.

4.3 Experimental Method

Details of the rotating fluidized bed unit, customized by Nara Machinery Co. (Tokyo, Japan), are shown in Figure 4.1. It consists of an air-pressurized chamber, which encloses a cylindrical stainless steel sintered mesh with a diameter of 400 mm and a depth of 100 mm. This 2 millimeter thick mesh has apertures of 20 microns and acts as the gas distributor, it rotates along its horizontally directed axis of symmetry and its angular velocity, measured by a tachometer, can be adjusted by a variable speed electric motor. The fluidization behavior can be observed because the frontal covers of the pressurized chamber and the rotating air distributor are made of translucent acrylic plastic.

A blower (Hitachi VBD-080), driven by a variable speed electric motor, delivers air to the chamber; the flow of air is measured with a variable area type flowmeter. Pressure taps are placed as shown in Figure 4.1 in such a way that the pressure drop is measured along the radial direction; a differential pressure transmitter is connected to the taps and linked to a computer for recording data. In addition, a digital camera is used to record the fluidization of the agglomerates of nanoparticles and a laser-pointer is used to measure the bed height and to see the surface of the fluidized bed. Further details of the rotating fluidized bed unit can be found in Watano et al.⁸⁵.

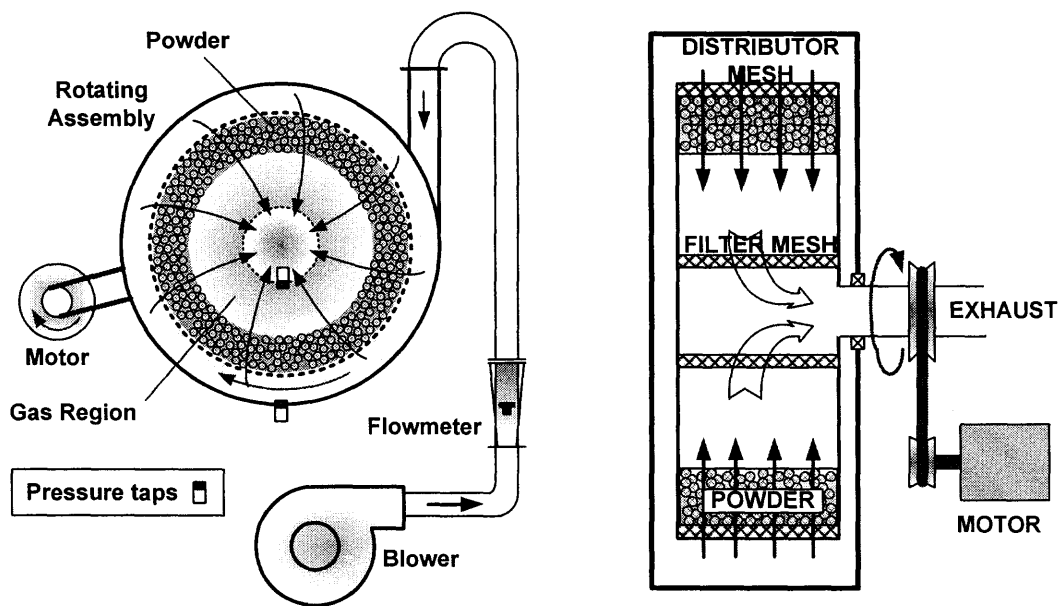


Figure 4.1 Schematic of the Rotating Fluidized Bed Unit.

Under normal gravity conditions, i.e., conventional fluidization, Aerosil[®] R974 and R972 fluidize smoothly, which is characteristic of agglomerate particulate fluidization (APF)¹; on the other hand, Aeroxide[®] TiO₂ P25 fluidizes with the presence of bubbles and a irregular bed surface, typical of an agglomerate bubbling fluidization (ABF) behavior¹. These powders are quite different than Geldart group C powders because they consist of highly porous agglomerates; as a result, the bulk density of these powders is much lower than the bulk density of micron size powders^{2, 5, 7, 8}.

Due to the relatively long period of time that the nanoparticles are stored and/or transported before using, agglomerates of different sizes form because of consolidation due to the cohesive interactions between the nanoparticles, i.e., densification. Therefore, the powders were sieved by using a shaker and a 60 Mesh sieve (mesh opening about 250 μm) to discard large agglomerates and for repeatability purposes; this procedure was

followed since it was observed that the presence of large agglomerates changes the fluidization behavior. Furthermore, fluidization experiments performed with non-sieved agglomerates did not show good bed expansion (data not shown). These observations are also consistent with the observations reported in Zhu et al.⁷ for conventional fluidization.

Fumed silica, Aerosil[®], has a tapped density of about 50 g/l (source, Degussa Corp.) and the average primary particle sizes for Aerosil[®] R974 and R972 are 12 and 16 nanometers, respectively. The bulk density, found experimentally, for both powders was about 30 g/l; 70 grams of powder were used in each experimental run. Aeroxide[®] TiO₂ P25 has an average particle size of 21 nanometers, a tapped density of 130 g/l and a bulk density of about 90 g/l; 250 grams of this powder were used in each experiment. In all experiments the initial bed height was about 0.02 meters.

For each different nanopowder, the experimental procedure can be summarized as follows. For a particular rotating speed (set centrifugal force) the air distributor mesh's pressure drop was measured as the air flow rate was gradually increased before loading any powder into the unit, i.e., for an empty distributor. The rotating speed was then increased to the next level and the procedure repeated; this was done to obtain the pressure drop across the air distributor as a function of the air flow at different rotational speeds.

The angular speeds selected for the experiments were 22, 31, 38 and 44 rad/s that correspond to centrifugal accelerations of 10, 20, 30 and 40 times gravity acceleration, respectively. A weighed batch of powder was then loaded into the unit, the rotating speed was set, and the air flow was gradually increased in order to record data such as air flow, pressure drop and bed height. A similar procedure was followed for each angular

velocity. The fluidized bed pressure drop was obtained by subtracting the distributor's pressure drop from the pressure drop measured when the unit was loaded with powder at the same flow rate and rotating speed.

4.4 Results and Discussion

Figure 4.2, Figure 4.3 and Figure 4.4 show the fluidized bed pressure drop as a function of radial air velocity at the four different centrifugal accelerations for Aerosil[®] R974, R972 and Aeroxide[®] P25, respectively. In general, the pressure drop increases until the minimum fluidization velocity is reached, then an approximately constant pressure drop is observed. In some cases, it was not possible to measure the pressure drop at very low gas velocities, and the pressure drop did not maintain a linear trend before reaching U_{mf} probably due to the instability of the non-fully fluidized bed. It was observed that the fluidized bed pressure drop could be affected by entrainment of powder at gas velocities higher than the minimum fluidization velocity, and as will be explained below, due to the presence of tangential momentum effects that may increase the fluidized bed pressure drop.

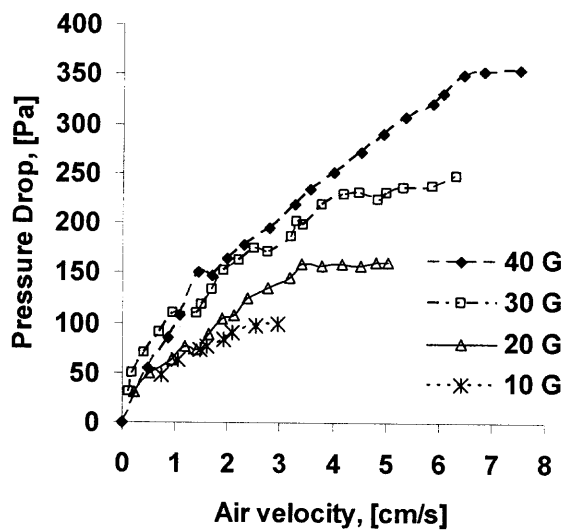


Figure 4.2 Bed pressure drop of Aerosil® R974 vs. air velocity at different centrifugal accelerations ($1\text{ G} = 9.8\text{ m/s}^2$).

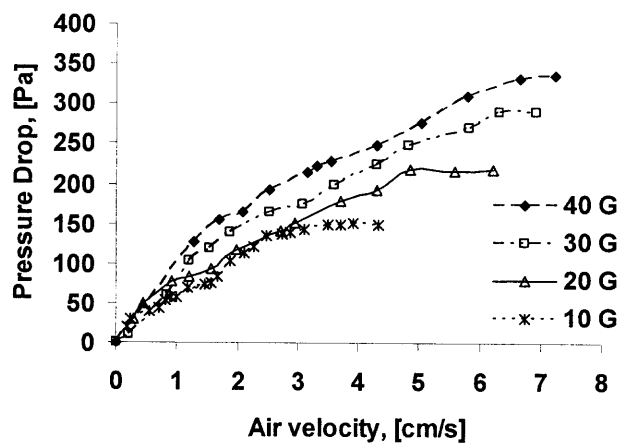


Figure 4.3 Bed pressure drop against air velocity of Aerosil® R972 vs. air velocity at different centrifugal accelerations ($1\text{ G} = 9.8\text{ m/s}^2$).

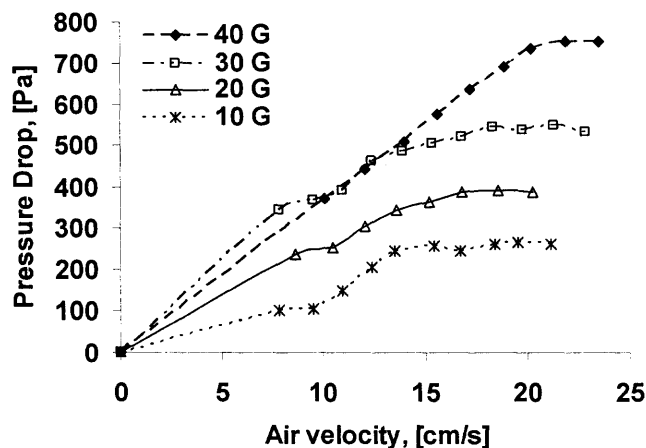


Figure 4.4 Bed pressure drop against air velocity of Aeroxide® TiO₂ P25 vs. air velocity at different centrifugal accelerations (1 G = 9.8 m/s²).

The values of the minimum fluidization velocities (U_{mf}) at different rotating speeds are obtained from Figure 4.2, Figure 4.3 and Figure 4.4 by selecting the air radial velocity at which the pressure drops becomes constant and plotted against the centrifugal acceleration in terms of artificial gravity, G. As seen in Figure 4.5, the minimum fluidization velocities appear to be proportional to the centrifugal acceleration in the range from 10 to 40 Gs. However, this linear relationship between the U_{mf} and the centrifugal acceleration fails if the minimum fluidization velocity at 1 G (open symbols in Figure 4.5) obtained during fluidization of the powders in a conventional fluidized bed is included. The linear relationship may also not hold for higher rotational speeds as shown by the results of Matsuda et al.¹⁰⁰ at 81.5 G. However, the linear relationship in the range of 10 to 40 G was also found by Watano et al.⁸⁵ and Qian et al.⁸⁷ in their RFB experiments using solid micron sized particles.

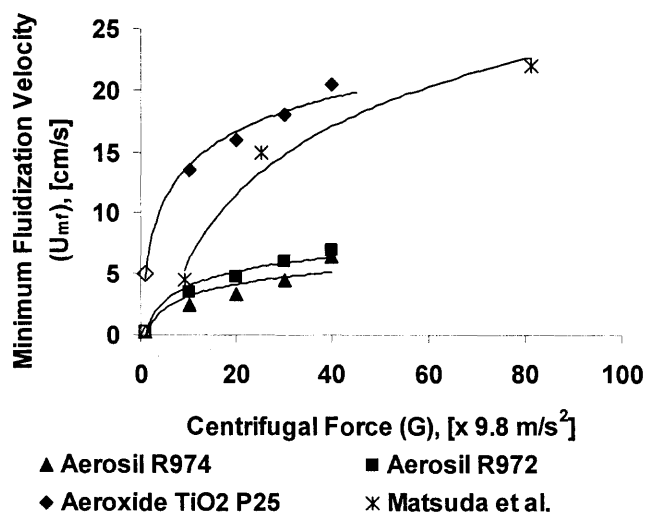


Figure 4.5 Minimum fluidization velocities of the powders at different rotating speeds (G). The open symbols are U_{mf} data obtained for these powders in a conventional fluidized bed (Zhu et al.⁷).

Unlike in a conventional gravity-driven fluidized bed, the relationship between the minimum fluidization velocity and the centrifugal force can also be affected by the geometry of the RFB unit since the intensity of the tangential momentum effects depends, among other things, on the existence of a well developed vortex flow in the freeboard region. Therefore, a plot of the minimum fluidization velocity against the centrifugal force may show different tendencies depending on the nature of the powder, the geometry of the unit and the range of the centrifugal force. For all of these reasons, more research needs to be done to elucidate the relationship between the U_{mf} and the centrifugal force.

The non-dimensional fluidized bed height, actual bed height divided by initial bed height, plotted against air velocity at different values of centrifugal force are shown in Figure 4.6, Figure 4.7 and Figure 4.8 for Aerosil[®] R974, R972 and Aeroxide[®] P25, respectively. There is a significant bed expansion when fluidizing type APF agglomerates of nanoparticles (R974 & R972) that is almost double the initial bed height at air velocity values slightly higher than the minimum fluidization velocity. The

stepwise changes seen in Figure 4.6 and Figure 4.7 are probably due to inaccuracies in measuring the bed height at different velocities since this was done with a scale rather than using an automated sensor. Entrainment of powder takes place if the airflow is further increased, which changes the bed pressure drop readings. For Aeroxide[®] P25, an ABF type powder, the bed expansion was very small and entrainment was also less when compared to the APF type nanopowders.

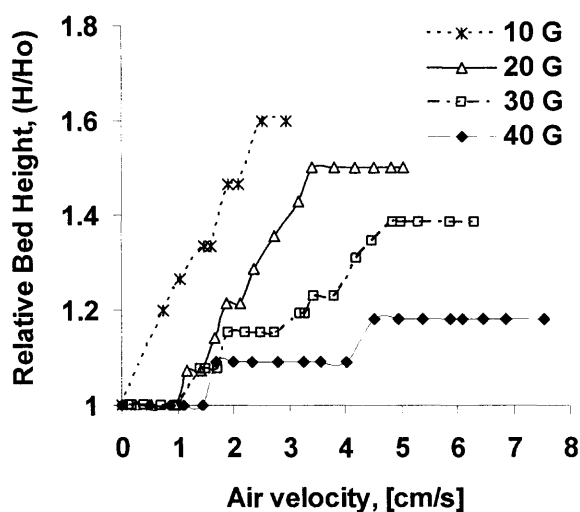


Figure 4.6 Relative bed height against air velocity of Aerosil[®] R974 vs. air velocity observed during fluidization at different centrifugal accelerations (1 G = 9.8 m/s²).

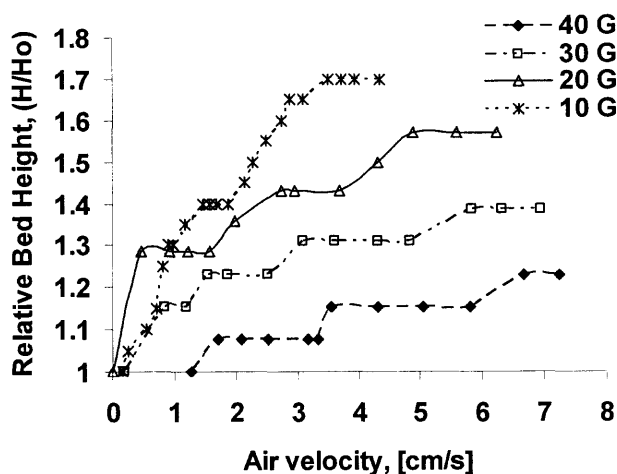


Figure 4.7 Relative bed height against air velocity of Aerosil[®] R972 vs. air velocity observed during fluidization at different centrifugal accelerations (1 G = 9.8 m/s²).

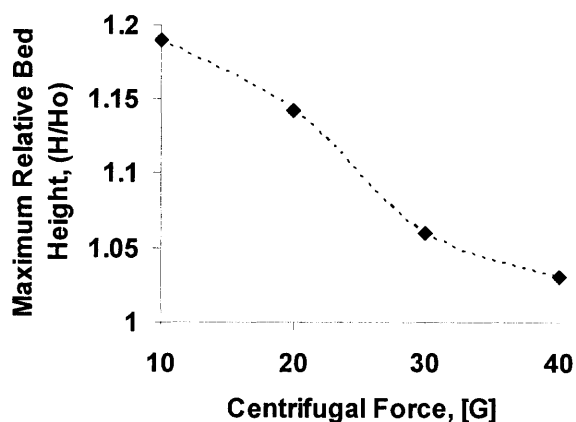


Figure 4.8 Relative bed height of Aeroxide[®] TiO₂ P25 vs. air velocity observed during fluidization at different centrifugal accelerations (1 G = 9.8 m/s²).

Furthermore, it was observed that the fluidized bed expansion reduces due to the higher centrifugal force when the rotating speed is increased. It is noted that, unlike R974 and R972 for which the bed expansion is a strong sign of the fully fluidized state, the bed expansion of the TiO₂ P25 is poor giving little clue about its fluidization state, and one must rely solely on the pressure drop data to infer anything about its fluidization behavior.

Experimental measurements of fluidized bed pressure drop at air radial velocities higher than the minimum fluidization velocities are compared against theoretical calculations using the equations presented by Kao et al.⁹⁶. Figure 4.9a shows that the experimental bed pressure drop values for APF type powders, R974 and R972, are higher than the theoretically calculated values. On the other hand, Figure 4.9b shows that the experimental bed pressure drops of Aeroxide[®] TiO₂ P25, an ABF type powder, are close to (or below) the theoretical calculations, and are in general agreement with the results reported by Matsuda et al.¹⁰⁰ who found fluidized bed pressure drops of TiO₂ to be lower than the theoretical values due to some loss of particles during the experiments.

The dissimilarity between the experimental bed pressure drops of APF and ABF type powders can be explained by the fact that the bed expansion of APF type powders (R974 & R972) is much larger than for ABF powders (TiO_2 P25); moreover, this significant bed expansion is not seen during fluidization of micron size powders. The additional bed expansion means an increase in the void space within the fluidized bed; therefore, it is believed that the high tangential flow of air from the region above the fluidized bed, i.e., freeboard-surface interface, can extend into the fluidized bed close to the interface as shown in Figure 4.10b, resulting in additional tangential momentum effects⁹⁵; this phenomenon is explained more in detail in the next section.

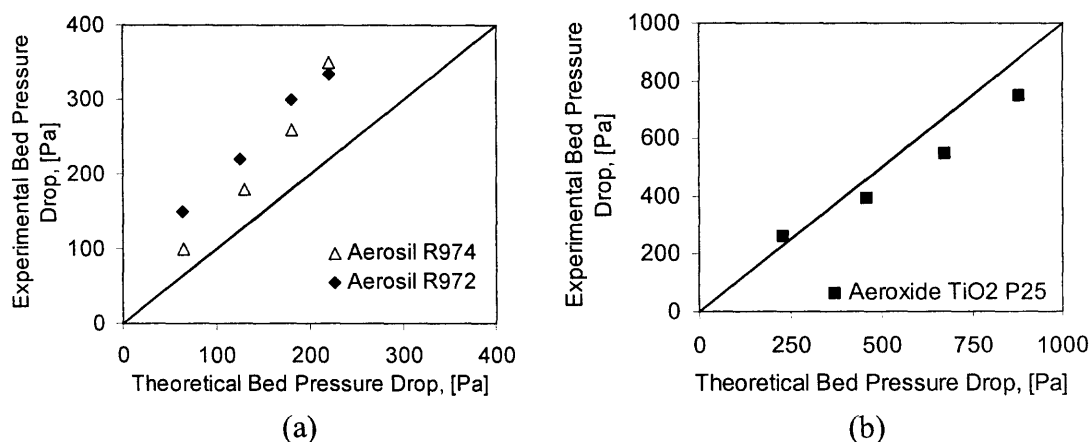


Figure 4.9 Comparison of the experimental data (dots) of the fluidized bed pressure drop at gas velocities higher than the minimum fluidization velocity against the theoretical estimation using Kao's model; (a) Agglomerates of nanoparticles APF type (Aerosil® R974 and R972), (b) Agglomerates of nanoparticles ABF type (Aeroxide® TiO_2 P25).

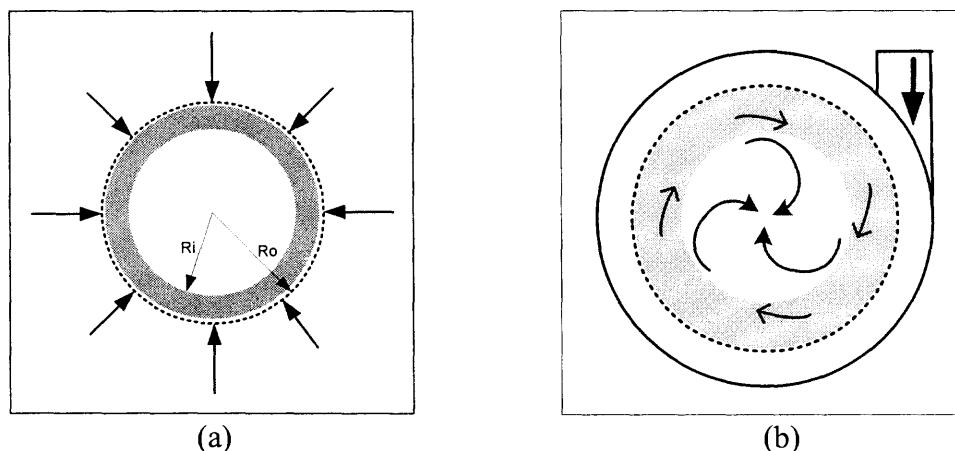


Figure 4.10 Comparison between the modeling of the flow in a RFB: (a) Schematic according to Chen⁹⁷ in which a rigid body rotation is assumed for the fluidized bed, valid for modeling micron size and ABF type particles; (b) Schematic when fluidizing APF agglomerates of nanoparticles. Light gray represents the expanded fluidized bed and the blue arrows stand for the flow of air in the RFB.

4.4.1 Flow Regime in the RFB when Fluidizing Agglomerates of Nanoparticles

When performing numerical simulations on the flow pattern in a rotating cylinder, Arman⁹⁸ described in detail the several flow regions inside of an RFB unit. Furthermore, he performed calculations on a rotating packed bed and he found that the radial velocity component is important within the bed while the tangential velocity component is significant in the region right above of it⁹⁸; in addition, he also found that the tangential velocity within the bed increased as the porosity of the bed increases.

In an RFB, an increase in void fraction within the fluidized bed decreases its effective viscosity, and if the porosity is large enough, the fluidized bed pressure drop will be increased due to the tangential effects produced by the extension of the tangential flow of the gas from the region above the fluidized bed into it⁹⁵. Since the fluidized bed total void fraction of APF type agglomerates of nanoparticles, before and during fluidization, is larger than the total void fraction of any other class of fluidized powder, it is possible for the fluid gas to have a significant tangential velocity component within the

fluidized bed. In addition, the very low minimum fluidization velocity observed during conventional fluidization of silica nanoagglomerates^{1,7} indicates that these agglomerates are fluffy and light; therefore, a low terminal velocity is expected indicating that these agglomerates can be easily entrained in the direction of the fluid flow, i.e., radially and/or tangentially.

A description of the fluid flow in an empty rotating cylinder gives a better understanding of the system. Equation 4.1 is the non-dimensional form of the Navier-Stokes equation for the motion of the fluid inside of a rotating cylinder considering a rotating frame of reference^{96,97}

$$R_o (\vec{u} \cdot \vec{\nabla}) \vec{u} + 2\vec{k} \times \vec{u} = -\vec{\nabla} p + E_k \nabla^2 \vec{u} \quad (4.1)$$

and the non-dimensional pressure includes the effect of the centrifugal force

$$\nabla p = \nabla \left[p^* + \rho \Phi - \frac{1}{2} \rho (\Omega \times \mathbf{r}) \cdot (\Omega \times \mathbf{r}) \right] \quad (4.2)$$

where R_o and E_k represent the Rossby and Ekman non-dimensional numbers,

$$R_o = \frac{U}{\Omega L} = \frac{U}{\Omega R} \quad (4.3)$$

$$E_k = \frac{\nu}{\Omega L^2} = \frac{\nu}{\Omega W^2} \quad (4.4)$$

and U is the fluid velocity, Ω is the rotational speed, ν is the kinematic viscosity and L describes a geometric length scale related to the fluid flow analysis.

The Rossby and Ekman numbers determine the flow regime within the RFB system; there are five possibilities^{92,98}, linear flow ($1 \gg E_k^{1/4} \gg Ro$), weakly linear flow ($1 \gg E_k^{1/4} > Ro \sim E_k^{1/2}$), weakly non linear flow ($1 \gg E_k^{1/4} \sim Ro$), non-linear flow

($1 \geq Ro \gg E_k^{1/4}$) and turbulent flow ($Ro > 1 \gg E_k^{1/4}$). As mentioned above, it is important to note that the geometry of the chamber, i.e., the radius and width of the rotating distributor, can change the flow regime because the Rossby and Ekman numbers depend on the dimensions of the chamber.

Based on the Rossby and Ekman numbers (Table 4.1) calculated accordingly to the experimental conditions when fluidizing agglomerates of nanoparticles, the flow regime in the experiments can be classified as weakly non-linear. Therefore, the fluid flow in the empty chamber will be dominated by the tangential velocity component. Similarly, when the unit is loaded with powder, the tangential velocity, will also dominate the freeboard region (above the fluidized bed).

Table 4.1 Estimated Values of the Dimensionless Numbers for Gas Flowing Through the Bed during Fluidization of APF Powders. Average Particle Diameter Assumed to Be 80 μm

Porosity (epsilon)	Gas velocity (m/s)	Angular Speed (rad/s)	Centrifugal Acceleration (1g=9.8 m/s ²)	Non-dimensional numbers			
				Rosby	Ekman	Darcy	Forcheimmer
0.3	0.05	22	10 g	1.E-02	2.E-05	368894	445
0.4	0.05	22	10 g	1.E-02	2.E-05	114338	161
0.5	0.05	22	10 g	1.E-02	2.E-05	40654	69
0.6	0.05	22	10 g	1.E-02	2.E-05	15057	32
0.7	0.05	22	10 g	1.E-02	2.E-05	5334	15
0.8	0.05	22	10 g	1.E-02	2.E-05	1588	7
0.9	0.05	22	10 g	1.E-02	2.E-05	279	2
0.98	0.05	22	10 g	1.E-02	2.E-05	9	0
0.3	0.05	44	40 g	6.E-03	9.E-06	184447	222
0.4	0.05	44	40 g	6.E-03	9.E-06	57169	80
0.5	0.05	44	40 g	6.E-03	9.E-06	20327	34
0.6	0.05	44	40 g	6.E-03	9.E-06	7528	16
0.7	0.05	44	40 g	6.E-03	9.E-06	2667	8
0.8	0.05	44	40 g	6.E-03	9.E-06	794	3
0.9	0.05	44	40 g	6.E-03	9.E-06	139	1
0.98	0.05	44	40 g	6.E-03	9.E-06	4	0

4.4.2 Computational Simulations of an Empty Rotating Cylinder

The fact that the flow pattern of air inside of a rotating cylinder is different than a rigid body rotation can be demonstrated by performing simulations using Fluent 6.1. The simulation region was set up in accord with the dimensions of the experimental apparatus; the gas media properties used were those of air. Since the gas speed is relatively high inside the computational field, it is treated as a compressible media instead of incompressible. The standard κ - ϵ turbulence model is used to describe the turbulent behavior of the gas.

Figure 4.11 (a, b, c and d) show the velocity profiles of the fluid (gas) inside of the RFB unit as calculated by Fluent[®]. The simulations were run by changing the gas velocity at the inlet of the chamber while keeping the rotating speed constant at 211 rpm (10 times the gravity force). The simulations show that the tangential velocity component is highly dependant on the air velocity at the inlet of the chamber; additional simulations run at 411 rpm (40 times gravity force) indicated that the flow was also dependant on the rotating speed of the distributor. From the simulations, it can be concluded that the fluid velocity in the chamber is mostly tangential, i.e., vortex like, and that the velocity increases as the flow of air to the chamber is increased. Thus the fluid flow in an RFB is far from being like a rigid body rotation. The dependence of the tangential velocity on the gas flow fed to the RFB chamber was verified experimentally by placing flags inside the chamber. At a constant rotating speed of the distributor, the flags bended more as the flow to the chamber was increased. The bending of the flags occurred due to the increase in the drag force because of higher tangential velocities.

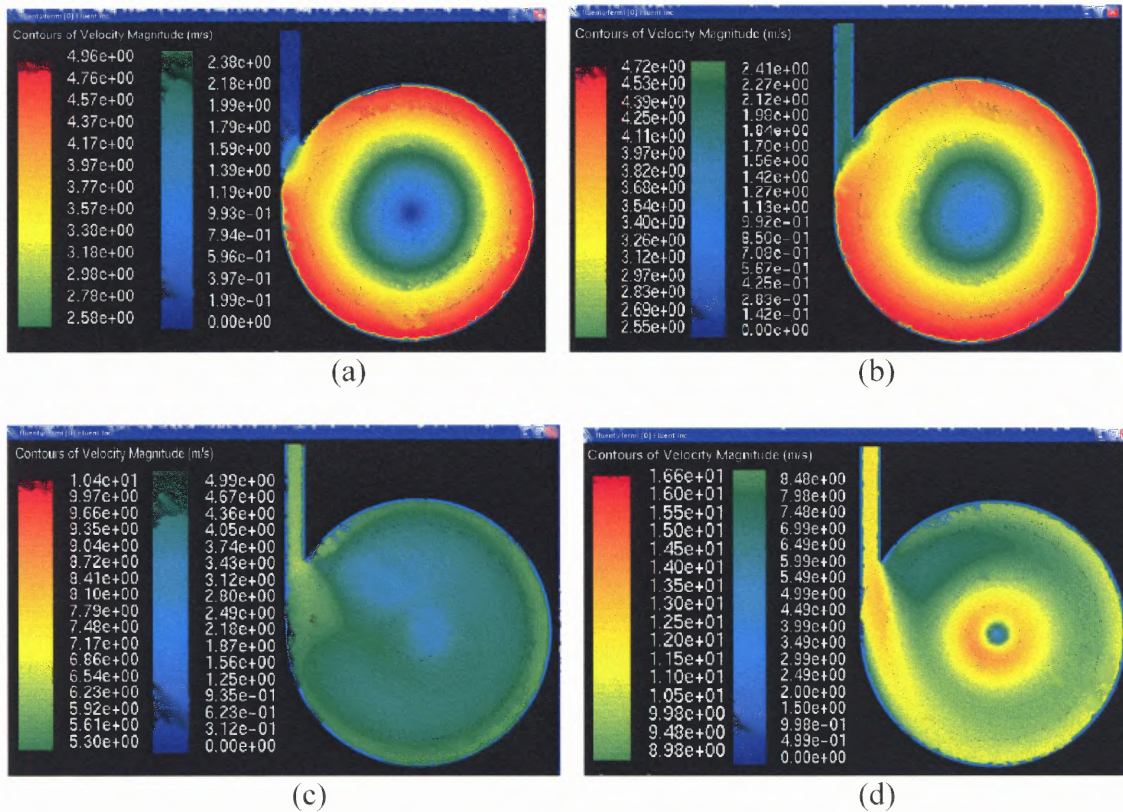


Figure 4.11 Contours of velocity magnitude of the air inside the rotating cylinder; velocity mostly tangential. The distributor (dotted circle) rotated at 211 rpm (10 times gravity). These figures show that the tangential velocity in the freeboard changes as a function of the velocity at the inlet of the chamber. (a) inlet velocity of 2 m/s equivalent to a radial velocity at the distributor of 0.095 m/s; (b) inlet velocity of 6 m/s equivalent to a radial velocity at the distributor of 0.286 m/s; (c) inlet velocity of 12 m/s equivalent to a radial velocity at the distributor of 0.573 m/s.

Figure 4.12 shows the simulated tangential velocity of the fluid considering the rotating frame as reference; these values were obtained by subtracting the tangential velocity of the frame (rigid body, Ωr) from the contours of velocity obtained from the results shown in Figure 4.11. Figure 4.12 clearly shows how the tangential velocity of the fluid increases due to the change in the inlet velocity. The abscissa represents the radial distance from the center of the chamber in meters such that the distributor is located at 0.2 meters from the center of the chamber (right extreme); while the ordinate gives the values of the velocity of the fluid, mostly tangential. It is important to note that

while the radial velocity at the distributor is in the range of 0.01 to 0.1 m/s, the corresponding tangential velocity has values in the range of 1 to 5 m/s, which means that the tangential velocity is at least an order of magnitude larger than the radial velocity.

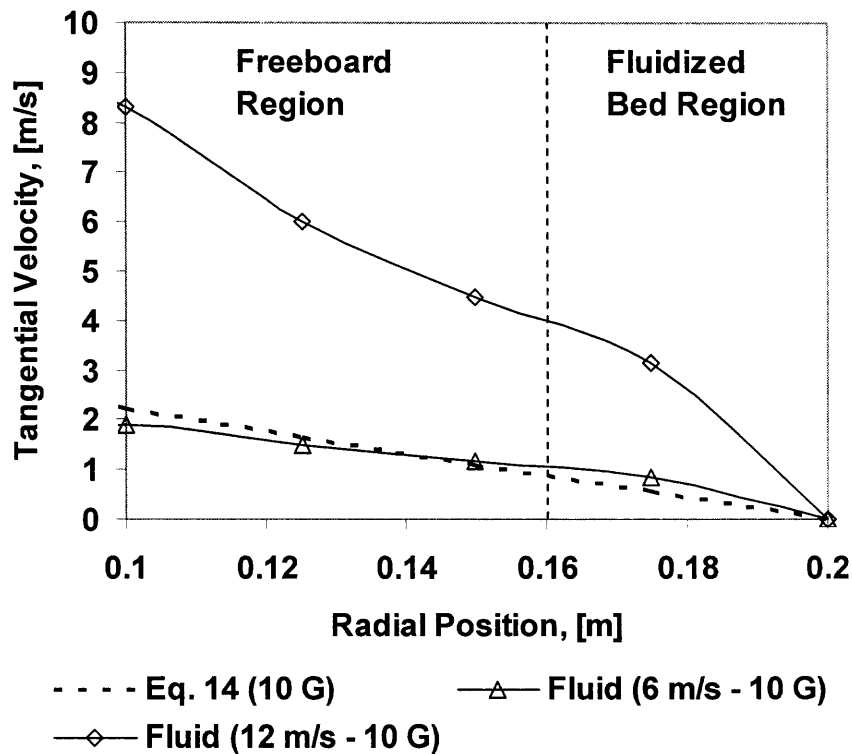


Figure 4.12 Tangential velocities of the fluid with respect to the rotating frame as function of the radial position in chamber. Solid lines correspond to the results from the numerical simulations from Figure 4.11 and the dotted line corresponds to Equation 4.13. The vertical dotted line separates the fluidized bed region from the freeboard.

4.4.3 Tangential Momentum Effects

Considering the fluid flow within a rotating packed bed, Arman's simulation results⁹⁸ show that the radial velocity component dominates the fluid flow pattern within a packed bed of large particles (about 1000 μm) held inside a rotating cylinder; indicating that the tangential velocity component is negligible within a bed of large particles. His conclusions are in agreement with several experimental results on fluidization of several

hundred microns or millimeter size particles in an RFB. Kroger et al.⁸⁹ further explained that in fluidization of large size particles (larger than 500 μm), the fluidized bed rotates like a solid body because of the large effective viscosity (μ_e). However, Kroger⁸⁹ concluded that the tangential velocity component within the bed depends on the effective viscosity (μ_e); therefore, for low values of the effective viscosity, the tangential velocity component within the bed would become significant and it would increase the pressure drop across the bed.

The effective viscosity is strongly affected by the size of the particles; the larger the diameter of the solids, the higher the effective viscosity, as indicated by Kunii and Levenspiel⁹⁹. The effective viscosity also decreases when the porosity of the bed increases¹⁰⁰; e.g., at gas velocities higher than the minimum fluidization velocity^{99, 100, 101} when the bed expands. Thus the effective viscosity of a fluidized bed of APF type agglomerates of nanoparticles, characterized by a significant bed expansion, should be much lower than the effective viscosity of a bed of solid micron size particles. Kroger et al.⁸⁹ concluded that the tangential velocity is related to the effective viscosity in such a way that if the effective viscosity is large, as for a bed of micron or larger size particles, the tangential velocity profile of the bed is similar to a solid body rotation ($v_\theta = \Omega r$); on the other hand, if the effective viscosity is small, approaching to zero, then the tangential velocity profile is similar to a free vortex ($v_\theta = C \frac{r_0}{r}$).

Furthermore, Arman⁹² concluded that for a rotating fluidized bed, the equation for the radial dependant tangential velocity considering a fixed frame of reference is related to the void fraction of the bed, represented by its permeability, which is included in the Darcy number (D) as shown in the equation below

$$V_{\theta} = \Omega r + \frac{2|v_{r0}|}{D} \frac{1}{1 + \frac{r}{r_0}} \quad (4.5)$$

where r_0 is the distributor radius, v_{r0} is the radial velocity passing through the distributor and D is the Darcy non-dimensional number,

$$D = \frac{\nu}{\Omega \kappa} \quad (4.6)$$

where ν is the kinematic viscosity of the fluid and κ the permeability.

The total fluidized bed void fraction can be calculated by several correlations; for example, using the equation given by Kroger⁸⁹

$$\rho_s (1 - \varepsilon) = \frac{M_{sh}}{\pi (r_0^2 - r_i^2)} \quad (4.7)$$

where M_{sh} stands for the bed mass per unit height, r_i is the distance from the center to the surface of the expanded bed, ρ_s is the density of the solid particles and ε is the total bed void fraction. The total void fraction for a bed of solid micron size particles, as calculated by Equation 4.7, is about 0.3 to 0.4 while the total void fraction for type APF agglomerates of nanoparticles is about 0.92 to 0.98. Therefore, the Darcy non-dimensional number is of the order of several thousands for micron size particles. so that the second term in Equation 4.5 for the tangential velocity is negligible; whereas, the Darcy number for a bed of agglomerates of nanoparticles is at least two orders of magnitude smaller (values from 10 to 60), so that the second term of Equation 4.5 cannot be neglected.

The total void fraction of the bed has been used in calculating the Darcy number. If the external fluidized bed void fraction (interagglomerate void fraction) were used

instead, the Darcy number would be much higher, and of the same order as for micron sized particles (see Table 4.1). However, the very large internal porosity of the nanoagglomerates should affect the permeability κ , and is also an important factor (as discussed above) in determining the effective viscosity of the fluidized bed. For example, for agglomerates of nanoparticles which are 98-99% porous, even though their diameter is of the order of hundreds of microns, their mass or inertia is about 2 orders of magnitude lower than of a solid micron particle of similar diameter. Hence, the effective viscosity of the fluidized bed will be much lower, reducing the Darcy number by about 2 orders of magnitude, in addition to the reduction of the Darcy number due to the increase in permeability. The effective viscosity has not been considered in the calculations of the Darcy number in Table 4.1, and for this reason a total porosity was used to account for the much lower effective viscosity, rather than the external void fraction.

4.4.4 Model That Predicts a Higher Bed Pressure Drop

Results from simulations using Fluent[®] and the low effective viscosity of the bed due to the large total porosity of APF nanoagglomerates indicate that a large tangential velocity component within the flow pattern of the rotating fluidized bed (RFB) of APF powder may occur. Therefore, it is necessary to reformulate the problem using the Navier-Stokes for a steady axisymmetric, incompressible, non-linear fluid flow through a bed of particles in a rotating cylindrical frame of reference⁹²

$$R_o \left(\vec{u} \cdot \vec{\nabla} \right) \vec{u} + 2 \left(\vec{k} \times \vec{u} \right) = -\vec{\nabla} p + E_k \nabla^2 \vec{u} - D \vec{u} - F \left| \vec{u} \right| \vec{u} \quad (4.8)$$

Equation 8 incorporates the non-dimensional numbers R_o , E_k , D and F , where D is the Darcy number and F is the Forcheimmer number. The Darcy and the Forcheimmer

numbers appear in the equation due to the presence of the bed of particles⁹²; the Darcy number has been discussed in detail above, and the Forcheimmer number is given by

$$F = \frac{cU_o}{\Omega\sqrt{\kappa}} \quad (4.9)$$

where

$$c = 0.045\varepsilon^{-3/2} \quad (4.10)$$

and κ has been introduced in Equation 6.

Assuming a fluidization particle diameter of 80 microns (either a nanoagglomerate or a solid particle), the non-dimensional numbers (R_o , E_k , D , F) have been calculated accordingly to the experimental conditions, and are listed in Table 4.1. From this table, the Darcy number is the most relevant since the other non-dimensional numbers are very small and can be neglected. Furthermore, the Darcy number is large when the porosity is low, i.e., for solid micron size powders, and it is small when the porosity is large, i.e., for a fluidized bed of agglomerates of nanoparticles. Considering the values of the non-dimensional numbers, Equation 4.8 can be simplified

$$2(\vec{k} \times \vec{u}) = -\vec{\nabla} p \quad (4.11)$$

where p is the non-dimensional pressure term that includes the centrifugal force as shown in Equation 4.2.

By expanding Equation 4.11, returning back to dimensional terms, simplifying and considering only the radial direction due to the axisymmetric flow, the following equation is obtained

$$\frac{1}{\rho} \frac{\partial P}{\partial r} \underline{i}_r = \Omega^2 r \underline{i}_r + 2\Omega \cdot v_\theta \underline{i}_r \quad (4.12)$$

This equation is applicable when fluidizing APF type agglomerates of nanoparticles, Aerosil[®] R974 and R972, at gas velocities higher than the minimum fluidization velocity. Equation 4.12 explains the higher experimental pressure drops observed than expected from models that do not consider tangential effects, i.e., the Coriolis force.

In other words, as can be seen from Equation 4.5, the fluidized agglomerates may have tangential velocities higher than the tangential velocity of the rotating frame (rigid body rotation, Ωr); this means that the agglomerates may rotate at higher speeds than the rotating distributor due to gas entrainment in the tangential direction; therefore, the pressure drop across the bed can be increased due to the additional centrifugal acceleration.

In order to solve Equation 4.12, a value for the tangential velocity has to be assumed. For example, considering a rotating frame of reference, the relative tangential velocity of the fluid can be found by subtracting the tangential velocity of the rotating frame of reference from the tangential velocity of the fluid obtained from a fixed frame of reference. As a first approximation, a fluid tangential velocity equal to the distributor's tangential velocity was assumed. In fact, the actual tangential velocity of the fluid can be larger, as shown by the simulations in Figure 4.11 and Figure 4.12; nevertheless, it can be seen that when the gas velocity at the inlet of the chamber is 6 m/s, the fluid velocity from the simulations can be approximated by the equation

$$v_{\theta} = \Omega R - \Omega r \quad (4.13)$$

Substituting this tangential velocity equation into Equation 4.12,

$$\frac{1}{\rho} \frac{dP}{dr} = 2\Omega^2 R - \Omega^2 r \quad (4.14)$$

Equation 4.14 can be compared against the model of Kao et al.⁹⁰ for the fluidized bed pressure drop at gas velocities higher than the minimum fluidization velocity

$$\frac{dP}{dr} = (\rho_g - \rho_f)(1 - \varepsilon)r\Omega^2 \quad \text{Kao et al.}^{90} \quad (4.15)$$

$$\frac{dP}{dr} = (\rho_g - \rho_f)(1 - \varepsilon)(\Omega^2 r + 2\Omega \cdot v_\theta) \quad \text{This model} \quad (4.16)$$

The model, Equation 4.16, has an additional term due to the Coriolis force that represents the additional tangential effects that occur during fluidization of APF type powders.

By defining the distance from the fluidized bed surface to the center of the RFB as a fraction of the distributor's radius, "x," Equations 4.15 and 4.16 can be integrated according to the boundary conditions (P_1 at R_1 , radius of the bed surface; P_2 at R , distributor's radius)

$$\Delta P = \rho_b \Omega^2 \left(\frac{R^2}{2} - \frac{R_1^2}{2} \right) \quad (4.17)$$

$$\Delta P = \rho_b \Omega^2 \left[2R(R - R_1) - \left(\frac{R^2}{2} - \frac{R_1^2}{2} \right) \right] \quad (4.18)$$

But

$$R_1 = xR \quad 0.5 < x < 1 \quad (4.19)$$

$$\Delta P = \frac{\rho_b \Omega^2 R^2}{2} (1 - x^2) \quad (4.20)$$

$$\Delta P = \frac{\rho_b \Omega^2 R^2}{2} (x^2 - 4x + 3) \quad (4.21)$$

As can be seen, Equations 4.20 and 4.21, which correspond to the model of Kao et al.⁹⁰ and the proposed model, respectively, differ by a factor that depends on the fraction, x . For example, if the surface of the fluidized bed is at 0.15 m from the center, for a fluidized bed height of 0.05 m, then $x = 0.75$. Hence, the pressure drop calculated with the proposed model is 30% larger than the estimated by Kao et al's model. However, it should be noted that this assumption is based on a fluidized bed tangential velocity equal to the tangential velocity of the distributor, considering a fixed frame of reference. The actual tangential velocity may be even higher depending on the flow of air at the inlet of the chamber as seen by the simulations in Figure 4.11 and Figure 4.12.

4.5 Concluding Remarks

Experimental data show that it is possible to fluidize nanopowders in a rotating fluidized bed and different nanopowders show quite different behavior during fluidization. For example, Aerosil[®] R974 and R972 fluidized with a significant bed expansion while Aeroxide[®] TiO₂ P25 did not show any appreciable bed expansion at all.

Some of the advantages of the rotating fluidized bed over conventional fluidization are: less elutriation of powder, fluidization at much higher gas velocities resulting in a much higher gas throughput per unit area of distributor, smaller footprint, thin beds resulting in either no bubbles or very small bubbles, very little gas bypassing and shorter time of processing. For example, the minimum fluidization velocity for Aerosil[®] R974 in conventional fluidization^{5, 7, 8} is about 0.0025 m/s while the minimum

fluidization velocity of the same powder in a RFB at 10 times gravity acceleration is about 0.02 m/s, an order of magnitude higher.

Numerical simulations of the fluid flow pattern inside of a rotating cylinder show that the tangential velocity component is predominant over the radial component and the hydrodynamics depend on the flow rate directed to the chamber, as well as the rotating speed of the distributor. The tangential velocity component of the fluid flow is very different from rigid body rotation which has been assumed in most of the previous literature references.

It has been found that the pressure drop of a fluidized bed of APF type agglomerates of nanoparticles is higher than that estimated using available mathematical models for RFBs. This phenomenon can be explained based on the existence of tangential momentum effects that arise because of the large porosity and reduced effective viscosity of the fluidized bed of agglomerates of nanoparticles. For these nanoagglomerates, estimating the bed pressure drop becomes difficult, and it depends not only on the centrifugal acceleration, but also on the fluidized bed expansion and tangential velocity component of the fluid bed. The tangential velocity component within the fluidized bed of APF type agglomerates of nanoparticles is significant in the expanded bed, i.e., in the fluidized bed region close to the interface or bed surface, because the tangential velocity component from the empty geostropic region expands into the fluidized bed through the porous interface. The extension of the tangential flow into the fluidized bed is also promoted by its low effective viscosity, which results from the significant fluidized bed expansion of APF nanoparticles that increases the porosity of the bed.

Previous models on fluidization of solid micron size particles in a RFB, such as those formulated by Chen⁹¹ and Kao et al.⁹⁰ neglected the Coriolis term in the fluid equation; these models gave reasonable results when compared with experiments where the effective viscosity was large, i.e., large particles in beds of low porosity. Therefore, the tangential velocity within the fluidized beds was negligible and only the radial component was important.

When the effective viscosity is small, however, it is believed that the tangential velocity component within the fluidized bed entrains the agglomerates in the direction of the flow, i.e., tangentially. If this tangential velocity is larger than the tangential velocity of the rigid rotating frame then the agglomerates are subject to an additional centrifugal acceleration that increases the fluidized bed pressure drop.

CHAPTER 5

AGGLOMERATES AND GRANULES OF NANOPARTICLES AS FILTER MEDIA FOR SUBMICRON PARTICLES

5.1 Overview

An experimental study on filtration of submicron particles by using a filter media composed of agglomerates or granules of nanoparticles is described in the present work. Fumed silica nanoagglomerates, nanoporous hydrophobic aerogel, carbon black, silica shells, activated carbon granules and glass beads were among the granular filter media tested and compared to a commercially available HEPA fiber based filter. The primary particle size of the agglomerates/granules is in the nanometer scale, but they agglomerate forming porous structures of about several hundreds of microns. These agglomerates were customized as packed (deep bed) or fluidized bed filters and challenged against submicron solid and liquid aerosols. For packed bed filters, the size of the granules has been optimized to a range of 150 to 500 microns with a filter thickness of 1 to 3 inches. Fluidized beds required granules smaller than 150 microns and the height of the bed was in the range of 15 to 40 cm. Solid aerosols were composed of polystyrene latex spheres of sizes in the range of 0.13 to 0.6 microns, and liquid oil-based aerosols had a median of about 0.15 microns.

The customized filters were challenged simultaneously with a HEPA filter against the same aerosol under equal superficial gas velocities. Optimal gas velocities for the granular systems are less than 4 cm/s.

In particular, when using carbon black or aerogel granules as filter media, collection efficiencies comparable or even higher than HEPA fiber based filters are obtained; but with the advantage of extra filtration capacity due to the deep bed configuration and the absorption of liquids into the porosity of the media.

5.2 Introduction

High efficiency particulate air filters (HEPA) perform with at least 99.97% collection efficiency for particles larger than 0.3 microns. They are used by industries that control contamination in their facilities such as pharmaceutical, medical, nuclear, semiconductor, food and electronics. Commercially available HEPA filters are usually based on surface filtration. These filter media are made of polymeric fibers of small diameter holes and arranged in a net-like configuration.

Frames for filter media are characterized by their face surface area and their thickness or depth. These dimensions change depending on the application; for example, HEPA filters for domestic use are relatively small in size while HEPA filters for industrial applications such as ventilation systems have much larger dimensions¹⁰². A domestic HEPA filter usually is less than one inch thick; in contrast, industrial filters can have thickness of up to ten inches if located in-line. While size is a limiting factor for domestic-use HEPA filters, power consumption and capacity performance are of more concern for industrial-use filters. Hence, the criterion for designing HEPA filters depends on their application.

There are a variety of qualities of HEPA fiber based filters^{103, 104}; according to the EN 1882 standard, there are five levels of HEPA filters: H10, H11, H12, H13 and H14

that correspond to collection efficiencies of 85, 95, 99.5, 99.95 and 99.995 percent respectively. Ultra low penetration air (ULPA) filters are also classified in the following levels: U15, U16 and U17 which correspond to collection efficiencies of 99.9995, 99.99995 and 99.999995 percent respectively. Wepfer¹⁰⁵ characterized fiber-based HEPA and ULPA filter according to European standards.

The main difference between HEPA fiber based and granular based filters is related to the filtration modes. There are two well defined filtration modes, cake or surface filtration and deep bed filtration. In the cake filtration mode, everything happens in a “bi-dimensional” context, the filter media is a layer of fibers and the collected particles form a layer or cake. The formation of a cake of particles increases the collection efficiency of the initial fiber layer, but it also increases the resistance through it. The collection of particles in a granular or fluidized bed filter happens in a “tri-dimensional” context, the filter media has an additional dimension, depth. There is a volume of filter media in which the collectors provide the surface for the capturing of the particles. Since the filter media has a depth, which can be changed, the filtration capacity as well as the resistance through the filter can be optimized.

The collectors or granules of a packed bed can trap aerosol particles by different mechanisms such as inertial, interception, diffusion and electrostatic forces. Fiber based filters mainly capture particles by inertial and interception mechanisms which work pretty well for capturing particles larger than 0.3 microns. Highly porous granules made of nanoparticles can trap aerosols by diffusion because the aerosol particles can diffuse into the pores of the collectors after diffusing to the surface. The porosity of the collectors makes them extremely effective for capturing particles smaller than 0.3 microns.

Variables that are monitored when testing filter media are collection efficiency, and resistance or pressure drop. These are obtained at different face gas velocities and upstream concentrations of aerosol. The filter's dimensions can be changed in order to optimize operating conditions; for example, for a deep bed filter, the thickness can be increased in order to improve the collection efficiency. However, this would also lead to an increase in resistance. Another parameter that can be changed in the granular filter's design is the size of the collectors or granules; large collectors will give lower resistance and lower collection efficiency when compared against smaller collectors because of the difference in size of the voids.

Porosity of the collectors is of significant importance because of the diffusion mechanism needed for the collection of submicron particles. Some agglomerates of fumed silica nano-particles are highly porous. For example, porosity values close to 98% have been found during fluidization of fumed silica agglomerates^{1, 2, 5}. The high porosity and the net-like structure may be favorable for filtration purposes since they provide lower resistance and extended surface area.

As mentioned above, the most important characteristics of filters are their resistance or pressure drop (ΔP) and the collection efficiency (E) or penetration ($P=1-E$); more recently, Podgorski et al.¹⁰⁶ have introduced the filter utility factor (FUF), which takes into account the total cost of filtration. This parameter is used for comparison of filters and to determine the optimal filtration time.

Fiber based filters have been extensively studied, Japuntich et al.¹⁰⁷ studied the efficiency of fiber based filters of different thickness and void sizes; they also studied the performance of the filters after the formation of a cake on their surface. During the

filtration of submicron particles in a fiber based HEPA filter, Thomas et al.¹⁰⁸ believed that filtration of the Most Penetrating Particle Size (MPPS) initially took place in the depth of the filter, and that after the upstream layers got clogged, most of the filtration occurred at the filter's surface. They observed that collected particles form dendrites that can act as newly formed fibers increasing the collection efficiency but also the resistance of the filter. It is believed that this phenomenon also occurs for granular bed filters where the void spaces are partially filled with dendrites increasing both the collection efficiency and resistance of the granular filter.

Among several other studies involving HEPA filters, Penicot et al.¹⁰⁹ studied the clogging process of HEPA fibrous filters when challenged against solid and liquid aerosols; they showed that the pressure drop across a HEPA fiber based filter increases linearly when collecting solid particles and exponentially when collecting oil droplets with respect to filtration time. Another interesting work related to the collection of liquid aerosols has been done by Raynor et al.¹¹⁰. They showed that the liquid aerosol droplets can move from the front to the back of the fiber filter but they did not observe re-entrainment of the oil droplets from the filter to the air stream under their experimental conditions. Frising et al.¹¹¹ (2005) studied the clogging of fibrous HEPA filters by liquid aerosol particles. They showed that the pressure drop across a HEPA filter increases suddenly about 100% under certain surface loading indicating that the saturation of the filter has been reached. In other related works, Balazy et al.¹¹² studied and modeled the filtration of submicron size particles by fibrous filters. Podgorski¹¹³ established that the morphology of the fiber may play a role on the collection efficiency of fibrous filters.

In regard of granular bed filters, silica based aerogel granules were used as filter media by Guise et al.¹¹⁴, who customized aerogel granules of 120 microns in a packed bed filter of 1.75 cm thickness. Otani et al.¹¹⁵ (1989) did extensive experimental and theoretical work for characterizing granular bed filters at several face gas velocities; many of their correlations are used in this work to compare experimental to theoretical results. Podgorski et al.¹⁰⁶ (1996) studied the deposition of fibrous aerosol particles in granular beds. Marre et al.^{116, 117} modeled the effects of flow slip, Brownian diffusion and direct interception for estimating the efficiency of granular ceramic filters. Granular filtration of polydispersed aerosols was studied experimentally by Wu et al.¹¹⁸ (1994); extensive work has also been done on granular filters by Tien's group^{119, 120}.

The impact of the challenging aerosol's characteristics on the performance of filters has also been the object of study. For example, Leibold et al.¹²¹ (1991) studied the response of HEPA filter media to high concentrations of aerosols, they found that the penetration decreased as the particle loading was increased indicating that a better collection efficiency is to be expected at higher concentrations of aerosol; however, resistance also increased. The aerosol particle size determined the rates of increase in resistance or collection efficiency. The effects of the challenging aerosol's polydispersity on the collection efficiency were studied by Kim et al.¹²² (2000) for fibrous and granular filters. Computational Fluid Dynamics (CFD) has also been used as a tool for predicting the collection efficiency for fibers as reported by Mortimer et al.¹²³ (1996).

There has also been some research regarding granular filtration in a fluidized bed. Mei et al.¹²⁴ (1995) studied a fluidized bed of sand particles of about 100 microns and acrylic powder of about 53 microns as a fluidizing media for capturing solid particles.

The amount of solids in the gas stream was measured with a Particle Counter-Sizer-Velocimeter (PCSV). They obtained about 90% collection efficiency for particles larger than 3 microns but poor collection efficiency for particles smaller than 3 microns.

In this work, several different filter media have been prepared using agglomerates or granules made of nanoparticles and other materials customized as granular bed filters. These filter media have been arranged in the following configurations: granular (packed bed) and fluidized bed filters. These customized filters and a HEPA fiber-based filter have been challenged against solid and liquid submicron aerosols to find their collection efficiencies and capacities for comparison purposes. It will be shown that, in particular, customized filters made of porous granules, such as carbon black and aerogel, have collection efficiencies similar to, or higher than HEPA filters but with the advantage of having extra filtration capacity before cleaning or changing the filter is necessary, i.e., having a longer lifetime.

5.3 Experimental Methods

The experimental setup is described in this section. Several experimental procedures are discussed, such as, the preparation of customized filters, solutions for the generation of solid and liquid aerosols, among others.

5.3.1 Description of the Experimental Setup

A detailed schematic diagram of the experimental setup is given in Figure 5.1. Instrument air at 100 psig is purified by removing oil mist, humidity and particles with a coalescer, a silica-based dryer and filters respectively. The filters used for cleaning the

instrument air guaranteed almost zero particles; the final filter media used was a HEPA Capsule (PN 12144) provided by Pall Corporation. The concentration of particles in the cleaned air was measured to be around 0.01 particles/cm³. The clean air was divided in two streams, one at 80 psig that fed the aerosol diluter and the other at about 20 psig (10 to 35 psig) that was supplied to the atomizer. A Constant Output Atomizer (Model 3075, TSI Inc.) was used to generate the aerosol from a solution of solid particles in water or oil in ethanol. The pressure upstream of the atomizer determined the concentration of aerosol. After the solution was atomized, the droplets were dried with a Diffusion Dryer (Model 3062, TSI Inc.). After removal of the solvent, any charges on the aerosol particles were neutralized with an Aerosol Neutralizer (Model 3077, TSI Inc.). The concentrated aerosol was diluted with clean air resulting in the final aerosol.

The concentration of aerosol particles was characterized by a Condensation Particle Counter (CPC) (Model 3760A, TSI Inc.). However, since the concentration of the aerosol before the filters was high, a Dilution System (VKL-100, Palas GmbH) was used to reduce the concentration about 100 times. During the experiments, the concentration of upstream aerosol was kept constant particularly when comparing the upstream to the downstream concentrations at certain gas velocity. The aerosol size distribution was also found by using a Scanning Mobility Particle Sizer, described below¹²⁵. There is a vent located upstream of the filters that allows adjusting the concentration of the aerosol due to changing operating conditions. The aerosol stream flow rate was measured with a flow transmitter (FMA 1720, Omega) with a range of 0 to 10 lpm. This transmitter was connected to an i3200 Process Monitor (Newport Electronics Inc.).

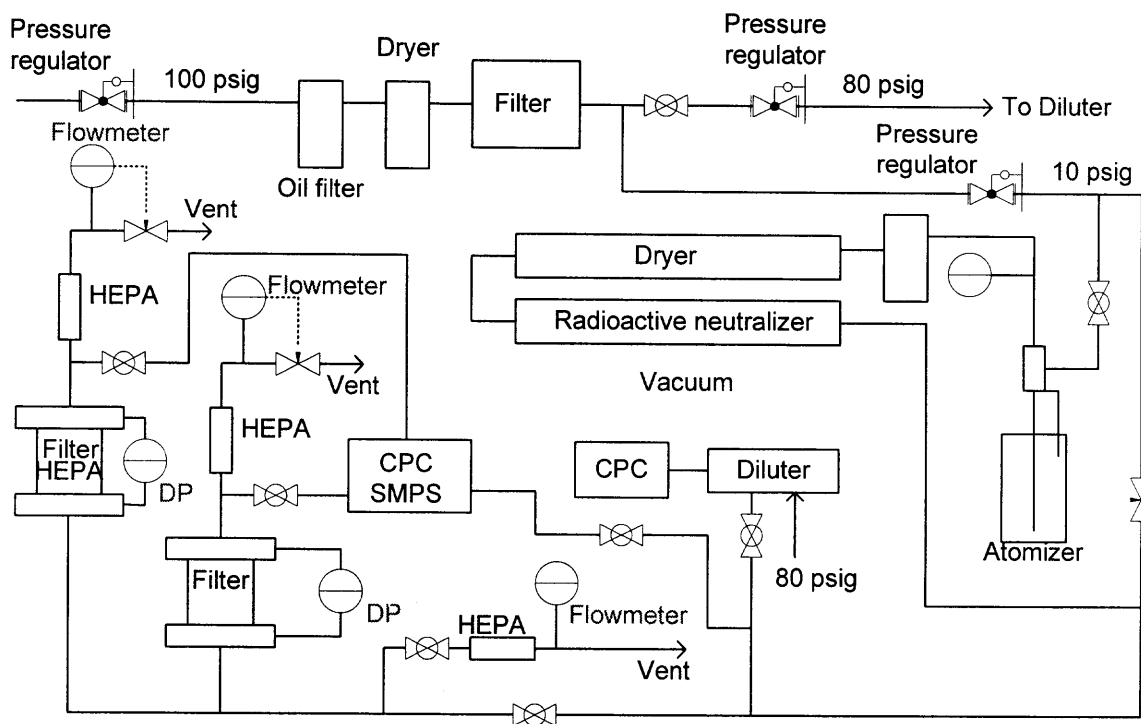


Figure 5.1 Schematic diagram of the experimental setup for the testing of customized filter media against submicron aerosols.

As it can be seen in Figure 5.1, the flow of gas containing the aerosol passed through both the customized and the HEPA filters simultaneously. The flow was regulated by mass flow controllers, FMA 5423 Omega, with a range of 0 to 15 lpm. These controllers were connected to displays with Ethernet ports, i800 EI Process Monitor (Newport Electronics Inc.) that allowed recording the values in a computer. The set point was adjusted in the mass flow controllers which regulated the flow through the filters with a control needle valve attached. These flow controllers malfunction in the presence of particulate matter; therefore, HEPA Capsule filters (PN 12144, Pall Corp.) were placed before them.

The pressure drop across the filter media, the HEPA and the customized filter, was measured by using highly accurate low-differential pressure transmitters with a range

from 0 to 10 inches of water column (Cole-Parmer, C-68071-12). These transmitters were connected to i800 EI Process Monitors (Newport Electronics Inc.) that allowed recording the data in a computer.

The aerosol coming out of the filters was characterized using a Scanning Mobility Particle Sizer (SMPS) which is composed of an Electrostatic Classifier (Model 3080, TSI Inc.), a Condensation Particle Counter (CPC) (Model 3010, TSI, Inc.), two HEPA Capsules and a flowmeter with a range from 0 to 1 lpm (Cole-Parmer, Model 32907-14). The purpose of the HEPA Capsule filters was to provide particle-free air for cleaning the SMPS system. The aerosol sample entered the Electrostatic Classifier, which separated aerosol particles in a certain size range. The aerosol exited the Electrostatic Classifier and entered the Condensation Particle Counter where the count of particles was measured. By mapping different particle sizes the SMPS gave the particle size distribution^{126, 127}. The flowmeter (0 to 1 lpm) was used to measure the flow of air that compensated the flow of aerosol entering the CPC 3010, because the flow sampled by the Electrostatic Separator could change from 0.2 to 0.3 lpm and the required flow for the CPC is 1 lpm. Aerosol Instrument Manager Software for CPC and SMPS allowed interconnecting the Electrostatic Classifier with the CPC and a computer in order to record data on the characteristics of the aerosol.

5.3.2 Filter Media Preparation

Several different materials were tested as filter media, such as, carbon black, activated carbon, aerogel, glass beads, silica shells and fumed silica. These materials were prepared for being customized mainly as granular filter media in a packed bed; aerogel granules

and fumed silica were also used in a fluidized bed filter. The different types of particles used in these experiments are shown in Table 5.1. Glass beads (spheres) were acquired from MO-SCI Specialty Products, L.L.C. The glass beads were bought under the denomination of Precision Glass Spheres (Class V). Two sizes were selected: small sizes in the range of 180 to 212 microns (-70/+80 Sieve size) and larger ones in the range of 355 to 425 microns (-40/+45 Sieve size). Activated carbon particles were supplied by NORIT Americas Inc. The grade of activated carbon selected was DARCO 20 x 40. Two types of fumed silica were supplied by Cabot Corporation: hydrophobic (TS-530) and hydrophilic (EH-5). Several grades of carbon black, such as Black Pearls, Monarch, Regal, were supplied from Cabot Corp. They were pre-screened by running experiments which are not shown in this work. The pre-screening process identified the carbon black grades that were not suitable as filter media due to the release of particles. It was also found that the best carbon black granules for use in a packed bed filter are Regal 660 A69.

Table 5.1 List of the Particles Used as Filter Media

Material	Type	Provider
Hydrophobic Fumed Silica	TS-530	
Hydrophilic Fumed Silica	EH-5	
Aerogel	Nanogel	Cabot
Carbon Black	Black Pearls 460 Regal 660 A69	
Glass Beads	Class V	MO-Sci
Activated carbon	Darco 20 x 40	NORIT Americas

Regarding the preparation of the granular media, the particles were sieved using U.S Standard Sieves to get the required size range. The selected sizes were: less than 150 micron for the fluidized bed filter made of aerogel; 150 – 250, 250 – 500 and 500 – 850 microns for granular packed bed filters, and less than 500 microns for fluidized bed filters made of fumed silica. Prior work not shown, lead to the selection of the collector size ranges abovementioned. Sieving is the most important step in the preparation of the filter media since if done improperly it could lead to the addition of particles to the stream of gas instead of removal. Glass beads were not sieved since they were sieved at the supplier. Carbon black granules were sieved to select the desired size and to remove fines. Granulated carbon black was selected against other types due to their consistency and low generation of fines. Silica shell granules are similar to carbon black granules but produced by the granulation of fumed silica nanoparticles. Fumed silica granules were also separated from fines by sieving. In addition to the separation of the granules, vibration consolidated the fumed silica granules increasing their density and making them stiffer thereby keeping their granular shape when packed. If too much vibration was applied during the separation of the granules, they were broken, and if vibration was not enough, then fines were not properly removed from the granules and released into the gas stream.

After the selection of the granules by their size, a certain amount were weighed and poured into an acrylic plastic module whose preparation will be detailed below. For the fluidized bed filters, fines of fumed silica were selected and aerogel granules were prepared by grinding larger aerogel particles on a 150 micron sieve.

5.3.3 Module Preparation

Module preparation is one of the most important steps in the aerosol filtration setup. A module is the part of the setup which includes the filter media housing and the filter media. Two different types of modules, one for the packed bed, and another for the fluidized bed, were constructed.

5.3.3.1 Packed Bed Module Preparation. The filter media housing for the packed bed is made of square blocks of acrylic plastic (3.2 x 3.2 inches with a thickness of 0.5 inches, with a cylindrical hole drilled in the center of 1.75 inches of diameter) stacked together with silicon glue in such a way that the center holes coincide with each other. The stacking of the square blocks of acrylic is done in order to get the required thickness of the filter housing, since the filter media is to be packed in the cylindrical space of the module. The use of these blocks allows for changing the thickness of the filter by adding or removing square blocks and it also allows incorporating baffles in the filter housing. More details on the filter modules are shown in Figure 5.2.

One of the two cylindrical openings of the filter housing was closed with a cloth or a wire mesh, so that the filter media could be poured into the module from the opposite end. The cloth or the wire mesh were fixed to the face of the module by gluing it with silicon glue selected and the apertures were selected in such a way that the filter media granules do not pass through them. The cloth consisted of a polyester filtering fabric (Rayon/Polyester, Snofil) with a thickness of 6 mils and a micron rating of 60, indicating that only particles larger than 60 microns are held by the cloth. The cloth was tested against submicron particles showing no collection at all. The apertures in the wire mesh were about 20 microns. The wire mesh was used only when the filter media was

composed of fumed silica particles. The reason why the cloth was preferred is because of its lower cost when compared against the wire mesh. In a commercial application, the use of cloth as the support of the filter media will make the granular filter media economically more feasible.

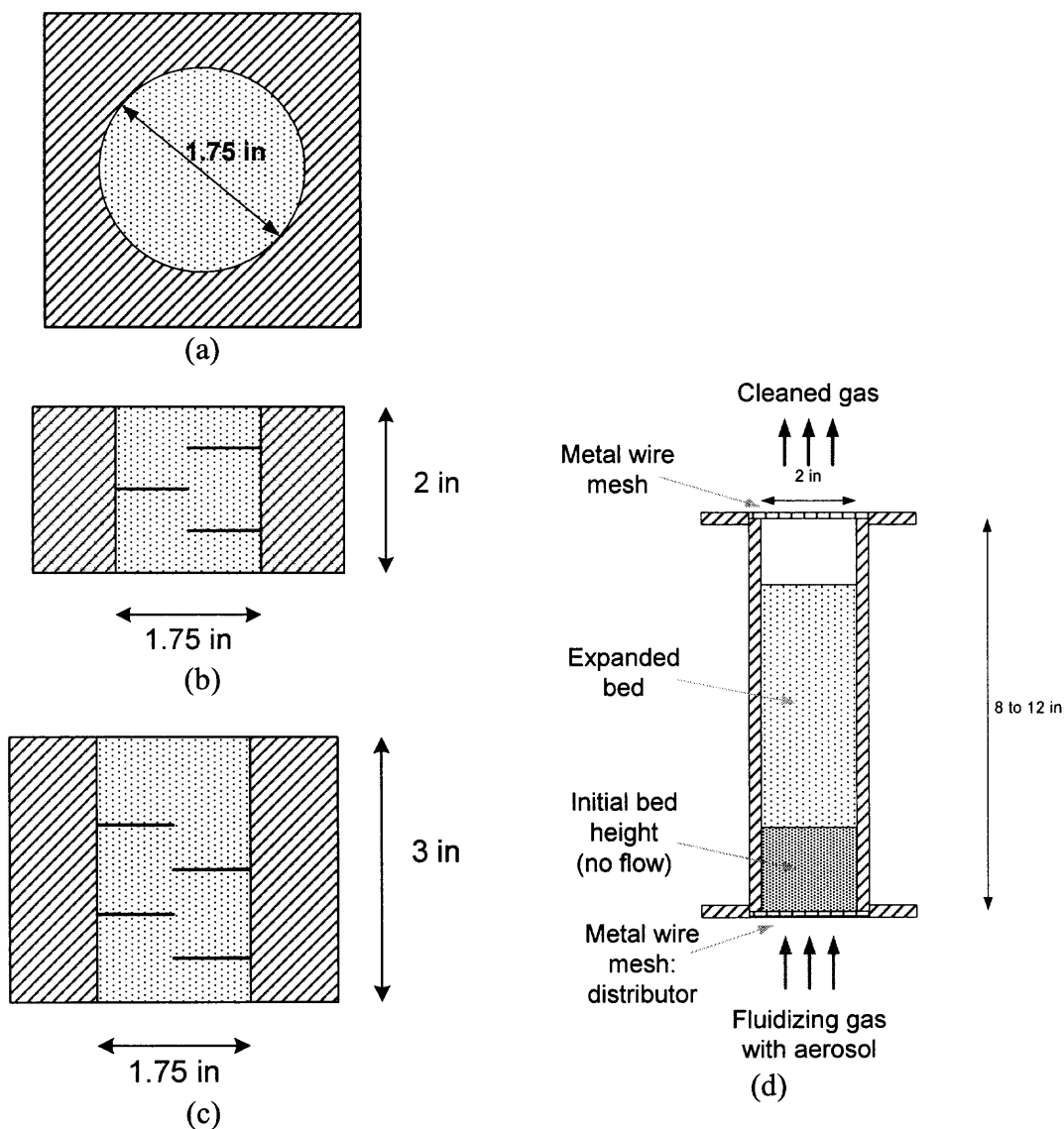


Figure 5.2 Schematic diagram of the different filter modules. (a) cross sectional view, (b) axial view showing the thickness of the module and the baffles, (c) axial view of a 3 inches thick module, and (d) view of a fluidized bed filter module.

In order to pack the particles in the module, the particles were slowly added while the module was shaken until the entire cavity of the module was filled. Once the granular media was poured and packed in the filter module, the second opening was closed with the cloth or wire mesh. Since the cloth was very thin, at least three pieces of cloth were glued one on top of the other to ensure that the filter media particles do not escape from the module. When preparing a baffled packed bed module, pieces of aluminum foil were placed between each square block of acrylic while gluing them together. The pieces of aluminum foil were placed in the module in such a way that the air had to pass through the filter in a zig-zag path, thereby increasing the pathway of the gas to be filtered.

5.3.3.2 Fluidized Bed Module Preparation. The filter housing of the fluidized bed module was prepared using an acrylic cylinder tube in the center with two square acrylic blocks with cylindrical holes of diameter equal to the outside diameter of the cylindrical column, attached at each end of it. The two square pieces were similar to the ones used in packed bed modules. The bottom end of the fluidization column was closed with three layers of cloth (which acted as the distributor), and a certain amount of filter media particles were loaded from the top into the fluidization column. Then, the top end of the fluidization column was closed with cloth or wire mesh in a similar way as was done for the packed bed module. In this case, the amount of powder was small with respect to the entire volume of the column because the powder expanded during fluidization several times its original bed height. Since, during fluidization of fumed silica, small particles are entrained, the wire mesh with 20 micron apertures was used at the top of the housing instead of cloth.

5.3.3.3 Preparation of HEPA Module. A module holding a sheet of HEPA fiber based filter was prepared for use as a reference or control. The HEPA filter was challenged against the same aerosol challenging the customized granular packed bed filter and at the same gas velocity. The HEPA module consisted of a layer of HEPA paper-cloth obtained from a Shop-Vac HEPA filter element (Code number 90340). The Shop-Vac HEPA filter is basically a filter cloth made of Gore[®] arranged in a zigzag pattern and supported by a wire mesh. This filter cloth has a smooth surface on one side and the other side is comparatively rough. A piece of this cloth was carefully cut and straightened without damaging its smooth surface. This cloth was then fixed with glue between two acrylic square blocks of dimensions given earlier. It is to be noted that the smooth surface was kept facing the air stream entering the HEPA module.

5.3.3.4 Preparation of Solutions to be used for Aerosol Generation. The solutions used for generating solid submicron aerosol particles were prepared as follows: about 1 to 0.3 ml of a concentrated solution containing polystyrene latex spheres (PSLS, HEPA-CHECK[™] Filter Challenge Particles, from Duke Scientific Corp.) were added to 500 ml of deionized water and agitated to mix. Three different nominal sizes of PSLS were available for the preparation of the suspensions: latex microsphere suspension 5060A of 0.60 microns, and filter challenge particles with a diameter of 0.20 microns (HF-20) and 0.30 microns (HF-30). The suspensions to be atomized contained a mixture of submicron spheres of different sizes, i.e., a mixture of HF-20 and HF-30 for example.

For the generation of liquid submicron aerosols, oil was dissolved in alcohol by taking about 0.1 to 0.3 ml of vegetable oil using a pipette into a conical flask (250 ml)

and then filling up the flask till the 250 ml mark with 99.5% pure ethanol. It should be noted that the aerosol size distribution from an oil/ethanol solution is quite wide, and there are sharp peaks indicating a high number of particles at the nominal particle sizes for the solid aerosol size distribution.

5.3.4 Experimental Procedure

After preparing the customized filter module, it was fitted in the filter assembly which included a zone before the filter for proper distribution of air entering the module and a zone at end of the filter to take a representative sample of the filtered air coming out of the module.

The experimental runs were conducted as follows. First, all of the equipments such as the SMPS, the CPC, the flow meters, and the displays were started so that they warm up. The clean air flow was started through both the HEPA module and the test filter module. The pressure drop across the customized filter was measured at different superficial air velocities in order to find its permeability. The air upstream and downstream of the customized filter was sampled to confirm the purity of the air and release of particles from the customized filter, if any. Then, the atomizer was started. The pressurized air feeding the atomizer's nozzle controlled the amount of atomized solution. A needle valve controlled the flow of diluting air. Hence, the concentration of aerosol was adjusted by these two variables. An upstream sample was taken using the CPC 3760A to see if the concentration of the generated aerosol was constant.

The SMPS system was cleaned before using it to sample the aerosol stream. This was done by passing clean air through the SMPS before and after each aerosol sample

and checking the concentration of particles. Tubing allowed connecting the SMPS system and the CPCs to the sampling points. It should be noted that all tubing transporting aerosol were of the conducting type to avoid adhesion of the aerosol particles to the wall of the hoses. For characterizing the collection efficiency of the filters, samples downstream and upstream of the filters were taken when the filters were exposed to three different superficial velocities of the aerosol stream. The concentration of aerosol upstream of the filters was maintained relatively constant for comparison purposes. The pressure drops across the customized and the HEPA filter modules were measured using two differential pressure transmitters. In experiments to measure the capacity of the filters, the flow rate of aerosol and its concentration were kept constant, and the concentration and the particle size distribution upstream and downstream of both the customized and HEPA filters were measured after a long interval of time. The data were then analyzed to find the collection efficiency and capacity of the filter modules.

5.4 Results and Discussion

As explained in the experimental methods section, several different experiments were performed to find the collection efficiency of different types of customized filters. This section will be divided accordingly to the several cases studied.

Regarding calculations of the experimental collection efficiency, a channel can be defined as a size range given by the instruments during measurement of aerosols. The number of particles per channel, number particle size distribution, is found by using the SMPS as explained in the experimental methods section¹²⁶. The aerosol concentration, or

number of particles per unit volume, is measured upstream (C_{up}) and downstream of the filters (C_{dn}). These values are used to find the collection efficiency of each channel by using the following equation,

$$E = 1 - \frac{C_{dn}}{C_{up}} \quad (5.1)$$

where E is the total collection efficiency, which can be calculated for each channel or for the total concentration of particles in all the channels, i.e., entire particle size distribution. For example, given “ n ” channels, each of them corresponding to a particular size range, there will be “ n ” number concentrations upstream and “ n ” downstream, so the collection efficiency for a particular channel “ i ” is given by

$$E_i = 1 - \frac{C_{dn_i}}{C_{up_i}} \quad (5.2)$$

However, when plotting the collection efficiency of each channel, it appears very spiky. For this reason, a plot of the cumulative collection efficiency is preferred. The equation used to find the cumulative collection efficiency from the lowest particle size up to channel “ m ” is given by

$$E_m = 1 - \frac{\sum_{j=1}^m C_{dn_j}}{\sum_{j=1}^n C_{up_j}} \quad (5.3)$$

The experimental collection efficiencies are presented as the cumulative collection efficiency per particle size or channel, and they are plotted against particle size to compare the filtration efficiency of the different filters.

5.4.1 Filtration of Submicron Solid Aerosol Particles

A solution containing solid polystyrene latex spheres (PSLS) of sizes 0.2 and 0.3 μm was prepared as indicated in the experimental methods section. This solution in particular will be called “Solution A.” Figure 5.3 shows the particles size distribution and the cumulative number of particles corresponding to the aerosol generated with “Solution A”. There are two peaks in the particle size distribution given in Figure 5.3, these correspond to the particles sizes of 0.2 and 0.3 microns. There are also several smaller peaks below and above the nominal sizes. These occur due to the agglomeration of the particles or due to the presence of the solid particles generated by other substances present in the atomized solution such as dispersants. The plot shown in Figure 5.3 was obtained when the flow through the system was 4.6 lpm, the number of particles may change slightly when the flow through the system is changed but the shape of the plot corresponding to the PSD remains unchanged.

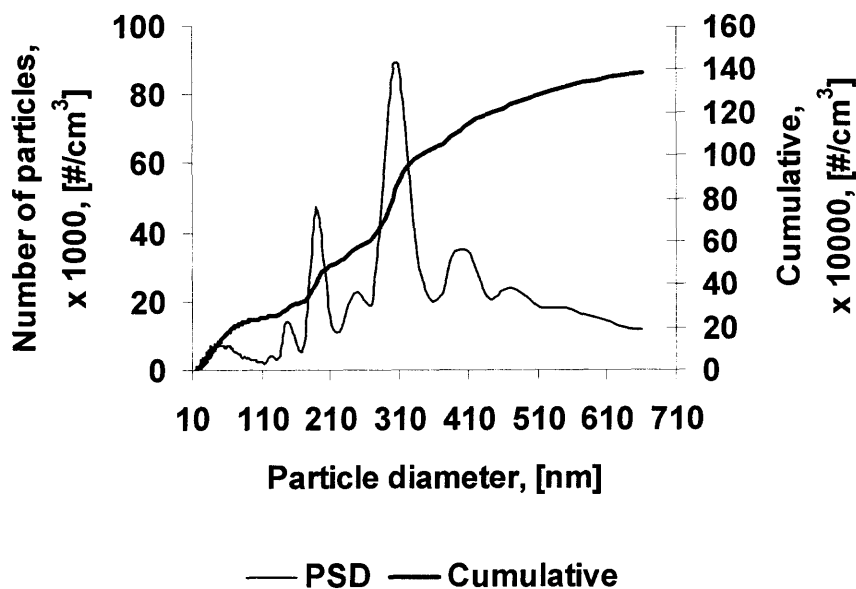


Figure 5.3 Particle size distribution (PSD) and cumulative number of particles (blue) corresponding to the solid aerosol from a suspension of polystyrene latex spheres of 0.2 and 0.3 μm in size (peaks).

5.4.1.1 Collection Efficiency of HEPA Filter Media. A sheet of a HEPA fiber-based filter was tested against solid aerosol particles produced with “Solution A”. The HEPA filter was supported in an acrylic plastic frame as explained above in the experimental methods section. Figure 5.4 shows the characteristics of the solid aerosol before and after the HEPA filter. Clearly, a reduction in the number of particles of about three orders of magnitude can be seen. Figure 5.5 shows the cumulative collection efficiencies of a brand new HEPA fiber-based filter (a), the same filter after being used for about 2 hours (b), and after 5 hours (c). The collection efficiency of a new HEPA filter is lower than the standard (99.97%), but as it traps particles and a cake at its surface is formed, its collection efficiency improves fairly quickly after 2 hours to over 99.85%. The HEPA filter was inspected visually after 2 hours and no thick particle layer could be seen, indicating that the filter was far from being clogged. It is important to note that after the formation of a cake on the surface of the filter, the penetration of large submicron particles is reduced as indicated a leveling off of the cumulative number collection efficiency as shown in Figure 5.5 (b). As time passes and the thickness of the cake increases due to the collection of submicron particles, the collection efficiency of the filter increases as seen in Figure 5.5 (c).

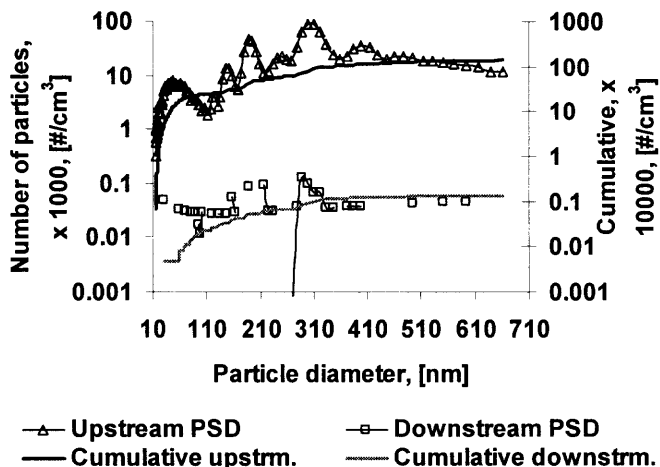


Figure 5.4 Particle size distributions and cumulative plots of the solid aerosol before and after the HEPA filter challenged simultaneously with the customized granular filter.

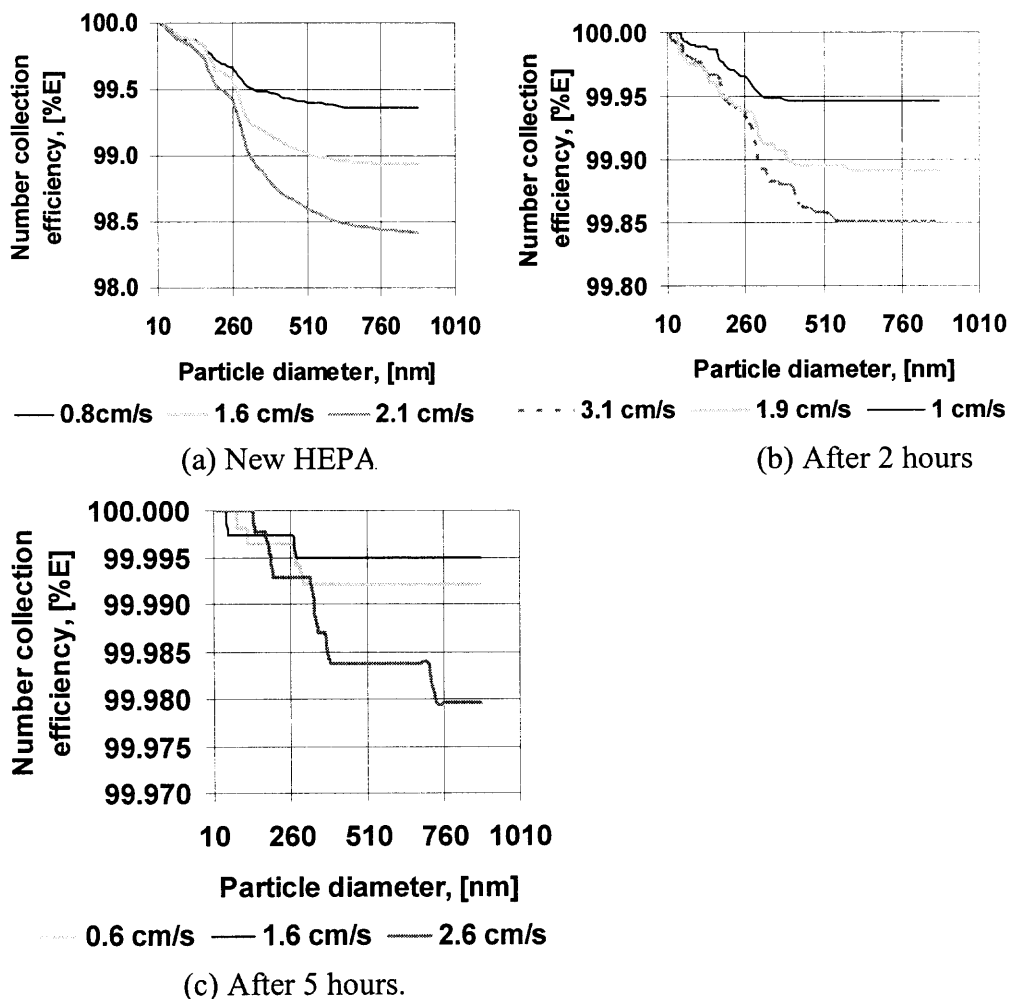


Figure 5.5 Cumulative collection efficiency of a brand new HEPA fiber based filter sheet and a used HEPA filter when challenged against solid submicron aerosol at different gas velocities.

5.4.1.2 Collection Efficiency of a Filter Media Made of Glass Beads. Glass

beads with sizes of about 180 to 220 μm were placed in an acrylic plastic module with 2 inches thickness. In this case, the cylindrical cavity in the acrylic module had a diameter of 1.75 inches (4.4 cm). The customized filter was challenged against solid aerosol particles as described in Figure 5.3. Figure 5.6 shows the number collection efficiency of the glass beads bed filter at different gas velocities. This filter was tested to have a point of comparison between solid and porous spherical collectors customized as granular packed bed filters.

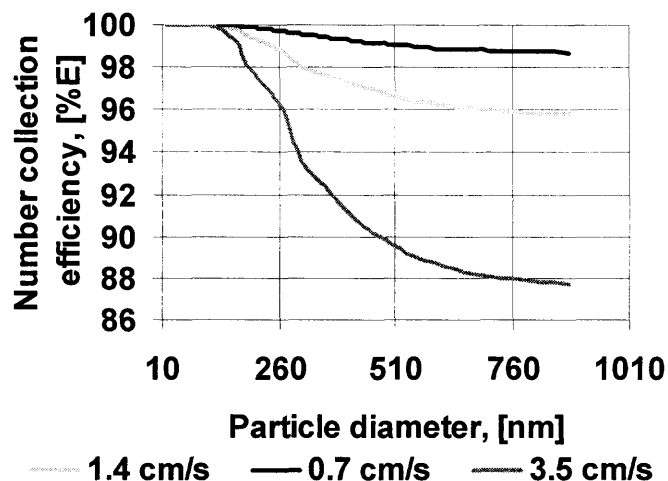


Figure 5.6 Cumulative collection efficiency of a 2 inches thick packed bed of glass beads (180-220 μm) at different gas velocities.

5.4.1.3 Collection Efficiency of a Filter Media Made of Activated Carbon. A

customized filter made of activated carbon particles was also challenged against solid aerosol submicron particles. The filter was 3 inches thick and had baffles. The particle size selected was 250 to 500 microns. Figure 5.7 shows the cumulative number collection efficiency corresponding to the activated carbon based granular filter. Data was gathered at three different gas velocities.

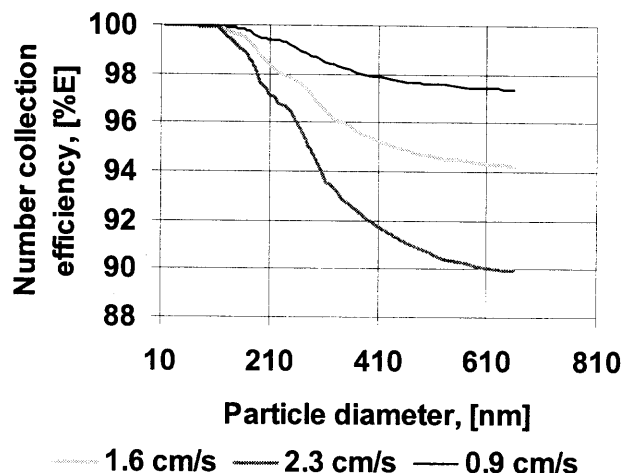


Figure 5.7 Cumulative collection efficiency of a 3 inches thick packed bed of activated carbon particles (250 – 500 μm) with baffles at different gas velocities.

5.4.1.4 Collection Efficiency of a Filter Media Made of Agglomerates of Fumed Silica.

Hydrophobic fumed silica's agglomerates of about 500 to 850 μm were customized as a granular filter media with a 3 inch thickness. The customized filter media was challenged against solid aerosol with a particle size distribution described in Figure 5.3. Figure 5.8a shows the number collection efficiencies of the customized filters made of fumed silica nanoparticles' agglomerates. Hydrophilic fumed silica's agglomerates of about 500 to 850 μm were also customized as a 3 inches thick granular filter media. The customized filter media was challenged against the same solid aerosol used in the previous experiments. Figure 5.8b shows the number collection efficiency of the customized filter.

As explained in the experimental methods section, another silica based material tested was Silica Shells, from Cabot. A cut size from 250 to 500 microns was selected, because there were no particles of the preferred size of 150 to 250 microns. The granules were customized in a 3 inch thick filter module with baffles and challenged against solid aerosol particles at different gas velocities. The cumulative number collection efficiencies

of a clean filter of Silica Shells are shown in Figure 5.9(a). This filter was also tested for capacity by continuously challenging it against the solid aerosol for about 25 hours. The collection efficiency was measured after certain time intervals. Figure 5.9(b) shows the collection efficiency at each of these time intervals, the collection efficiency improves as the voids in the filter are being filled.

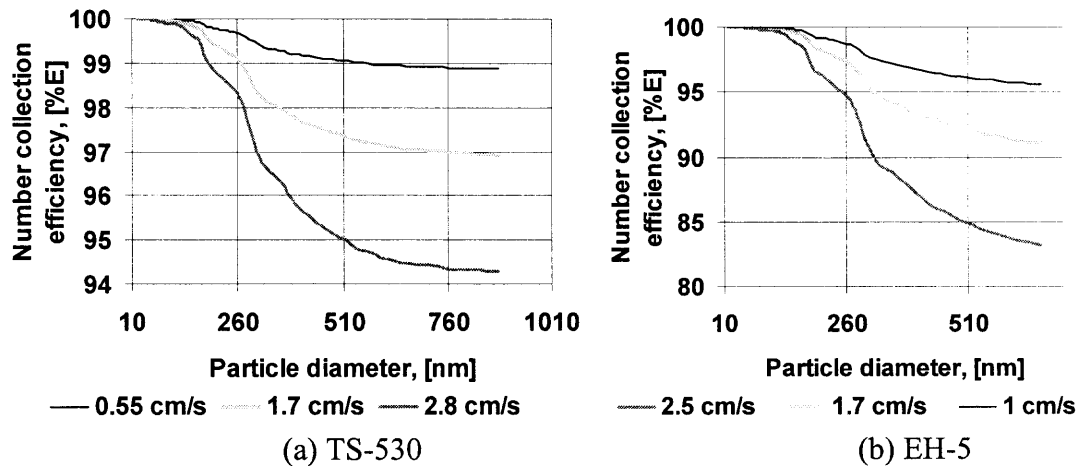


Figure 5.8 Cumulative collection efficiencies of 3 inches thick packed beds of agglomerates of fumed silica of about 500 to 850 μm in size at different gas velocities. (a) hydrophobic agglomerates of TS-530, and (b) hydrophilic agglomerates of EH-5

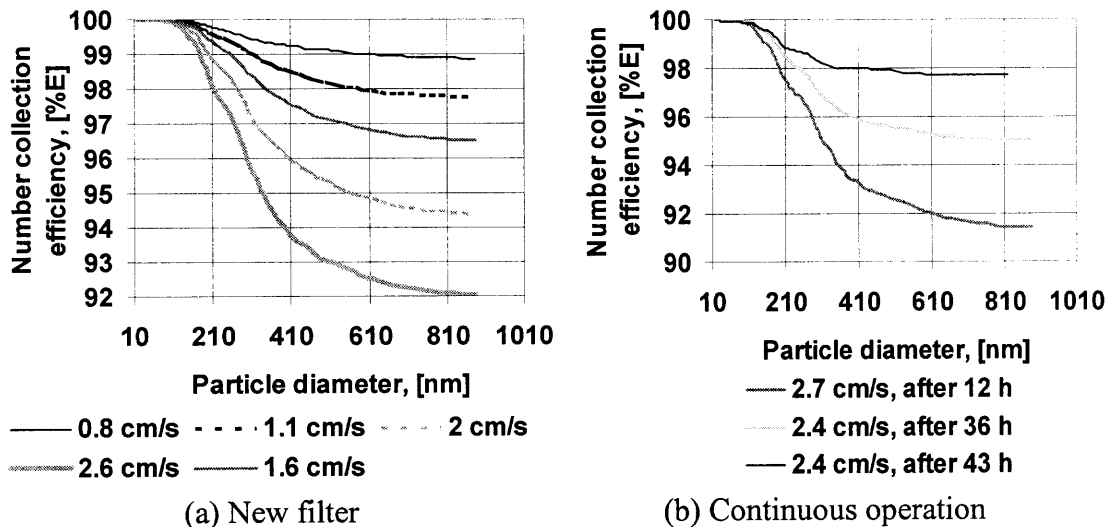


Figure 5.9 Cumulative number collection efficiency of a 3 inches thick packed bed of silica shells (250-500 μm) with baffles at different gas velocities.

5.4.1.5 Collection Efficiency of a Filter Media Made of Carbon Black Granules.

Different carbon black based filter media were tested against solid aerosol particles with a particle size distribution as shown in Figure 5.3. The preparation of the different filter modules has been described in the experimental methods section.

Granules of carbon black, Black Pearl 460, with sizes between 250 to 500 microns were customized as a granular filter media of 3 inches thickness with baffles. Figure 5.10 shows the number collection efficiency of the customized filter made of carbon black granules.

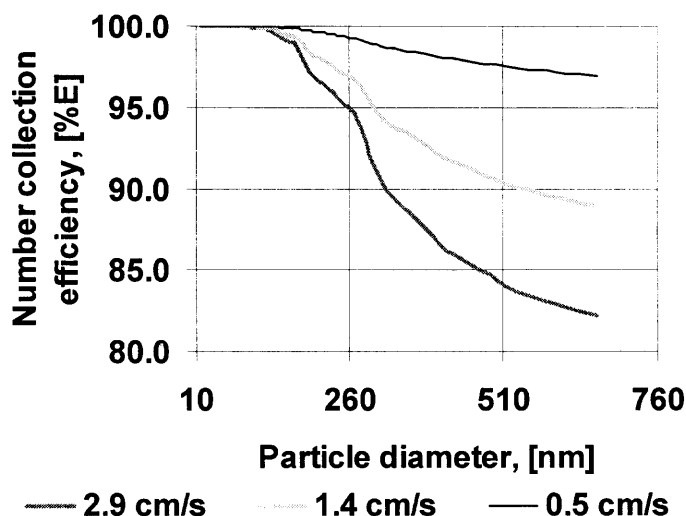


Figure 5.10 Cumulative collection efficiency of a 3 inches thick packed bed of granules of carbon black (250 – 500 μm , Black Pearl 460) at different gas velocities.

Similarly, granules of carbon black, Regal 660 A69, with sizes between 150 to 250 microns were customized in a 2 inch thick filter module and challenged against the solid aerosol particles. Figure 5.11 shows the cumulative collection efficiency of the customized filter at different gas velocities. These granules were also placed in a filter module of similar dimensions but with baffles. Figure 5.12 shows a comparison between the aerosol upstream and downstream of the customized granular filter; a significant

reduction in the concentration of aerosol can be seen. In this case in particular, the gas velocity through the filter was about 2.5 cm/s. Figure 5.13 shows the cumulative collection efficiency corresponding to the filter with baffles; the collection efficiency at 2.5 cm/s has improved from 91.5% without baffles to 98.4% with baffles.

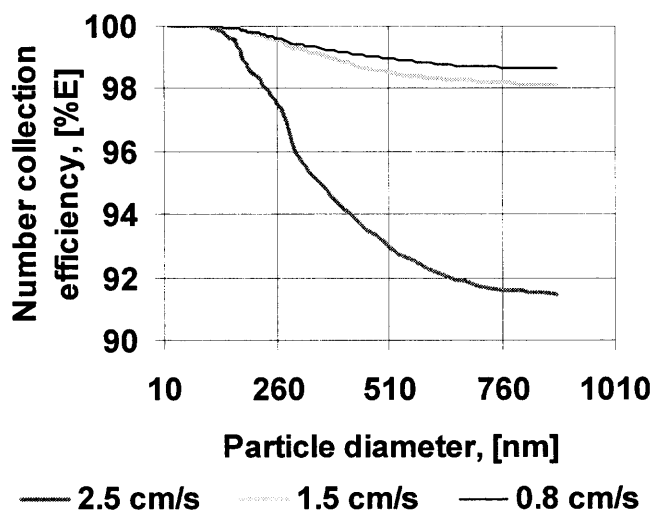


Figure 5.11 Cumulative collection efficiency of a 2 inches thick packed bed of granules of carbon black (150 – 250 μm , Regal 660 A69) at different gas velocities.

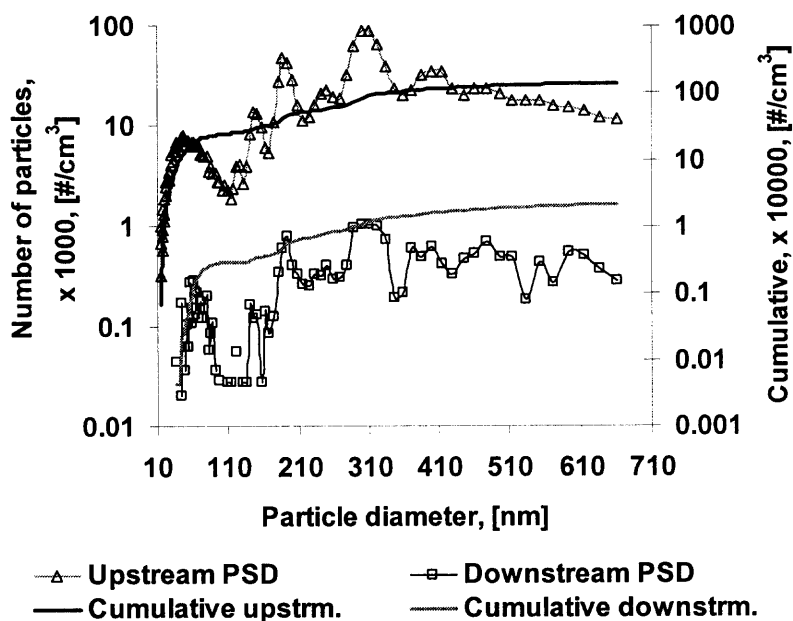


Figure 5.12 Particle size distributions and cumulative plots of the solid aerosol before and after the customized granular filter (Regal 660, 150-250 μm , 2 in. thick + baffles).

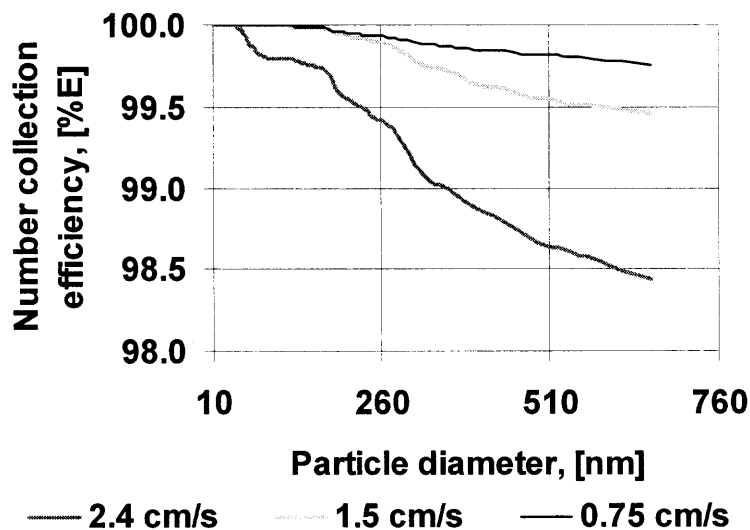


Figure 5.13 Cumulative collection efficiency of a 2 inches thick packed bed of granules of carbon black (150 – 250 μm , Regal 660 A69) with baffles at different gas velocities.

5.4.1.6 Collection Efficiency of a Filter Media Made of Aerogel Granules.

Another granular media studied were hydrophobic aerogel granules, Nanogel[®] supplied by Cabot Corp. Granular filters of 3 inches thickness were customized as explained in the experimental methods section. These filters were challenged against submicron solid aerosol particles. Figure 5.14 shows two plots, (a) corresponds to granules with sizes between 150 to 250 μm and (b) corresponds to granule sizes between 250 to 500 μm . The cumulative number collection efficiency corresponding to the small granules is similar to the HEPA filter. However, as the granule size is increased the collection efficiency drops as can be seen in (b).

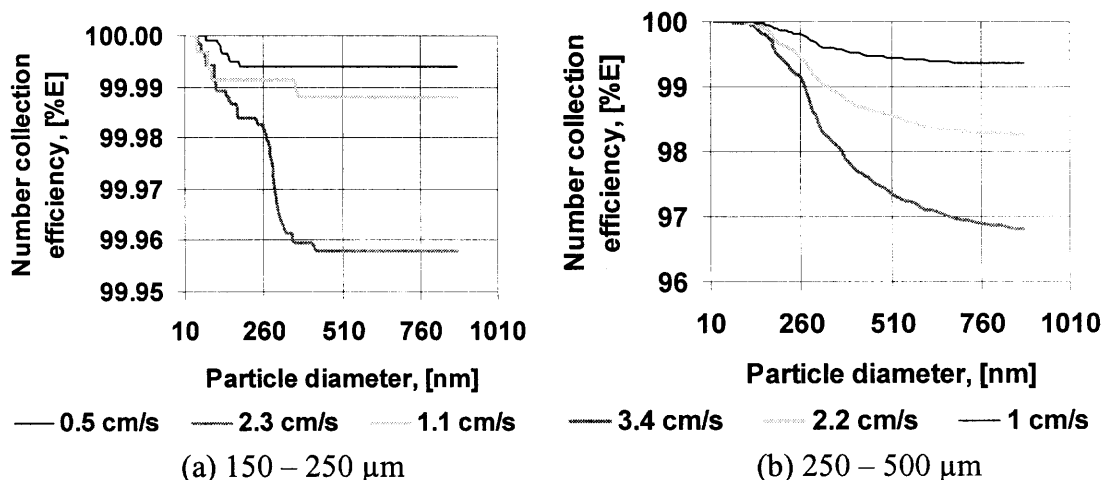


Figure 5.14 Cumulative collection efficiency of a 3 inches thick packed bed of aerogel granules at different gas velocities. (a) granules of sizes between 150 – 250 μm , (b) granules of sizes between 250 to 500 μm .

5.4.1.7 Summary of Filtration Results Corresponding to Solid Aerosol Particles.

All the cumulative collection efficiency results corresponding to customized granular bed filters challenged against solid submicron size particles are summarized in Figure 5.15 and Table 5.2. The gas velocities used for testing the filters are relatively low, less than 3 cm/s.

Table 5.2 Summary of the Cumulative Collection Efficiencies of the Filters When Challenged Against Solid Aerosols

Filter Media Material	Symbol Fig. 16	Size um	Thickness in	Baffles (Yes/No)	Gas velocity		Efficiency		Gas velocity		Efficiency	
					cm/s	%	cm/s	%	cm/s	%		
Activated carbon	P	250-500	3	Y	0.9	97.34	1.6	94.24	2.3	89.84		
Glass Beads	OT	180-212	2	N	0.7	98.72	1.4	95.82	3.5	87.7		
EH5	CID	500-800	3	N	1	95.6	1.7	91.07	2.5	83.2		
TS530	LBD	500-800	3	N	0.55	98.88	1.7	96.91	2.8	94.28		
Silica shells	BkSt	250-500	3	Y	1.1	97.77	1.6	96.53	2.6	92.04		
Black pearls 460	CIC	250-500	3	Y	0.5	96.978	1.4	88.97	2.9	82.21		
Regal 660 A69	RC	150-250	2	Y	0.75	99.75	1.5	99.45	2.4	98.44		
Nanogel II	BkS	150-250	3	N	0.5	99.994	1.1	99.988	2.3	99.957		
Nanogel II	BIS	250-500	3	N	1	99.36	2.2	98.27	3.4	96.82		

Legend:

P: Plus sign

CID : Clear Diamond

BkSt: Black Star

BIS: Blue Square

RC: Red Circle

OT: Orange Triangle

LBD: Light Blue Diamond

CIC: Clear Circle

BkS: Black Square

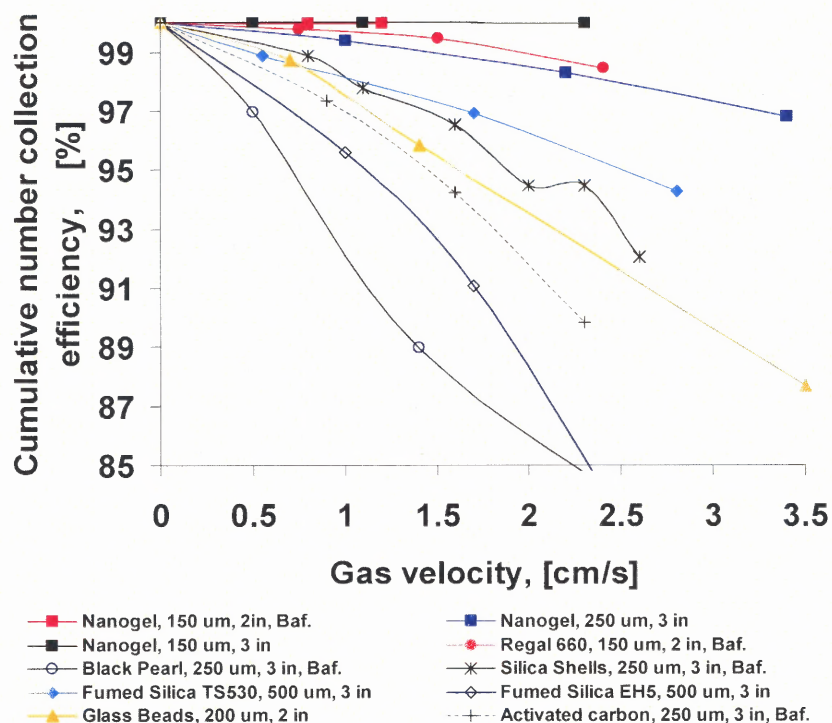


Figure 5.15 Cumulative collection efficiencies with respect to gas velocity of the customized filters challenged against solid submicron aerosol.

The cumulative number collection efficiencies are inversely proportional to the gas velocities and the data fall within a linear regression for each different filter. It can be seen that the filters that perform with collection efficiencies compared to HEPA are aerogel (Nanogel[®]) granules of 150 to 250 microns and 250 to 500 microns as well as carbon black Regal 660 A69 granules of 150 to 250 microns. Collection efficiencies of filter media with granules between 150 to 250 microns show that there is a significant improvement due to the porosity and irregular surface of the nanoagglomerates when comparing them against solid glass beads. Similarly, when comparing granules of sizes in the range of 250 to 500 microns, the porosity of Nanogel[®] aerogel granules seems to make its collection efficiency better than the much denser filter media granules such as silica shells or activated carbon.

5.4.2 Filtration of Submicron Liquid Aerosol Droplets

It is well known that the collection efficiency of fiber based filters is lower when challenged against liquid aerosols than when challenged against solid particles. For example, some commercially available HEPA filters have a collection efficiency of about 99.97% on 0.3 microns particles but only 95% filtration efficiency for oil droplets of 0.3 microns. Oil droplets are more difficult to be trapped by fibers, because they do not form a cake like solid particles do. Oil droplets coalesce at the surface of the fibers and it has been reported that the collection efficiency drops as the fibers get saturated with oil at their surface¹¹⁰. There is also a possibility of re-entrainment of droplets from the filters if there is an oil film at the back of the fiber filter.

In this work, the customized filter media were also challenged against oil droplets. Because the porous filter media is quite different than solid fibers, a difference in collection efficiency and capacity was expected. For these experiments, a solution of oil in ethanol was prepared for the generation of oil-based aerosol as indicated in the experimental methods section. The experiments were run similarly to the ones when using solid aerosol particles. The droplet size distribution is shown in Figure 5.16. The liquid aerosol is characterized for having droplets with a number mean size of about 170 nm and a volume mean size of about 414 nm, very close to the Most Penetrating Particle Size (MPPS).

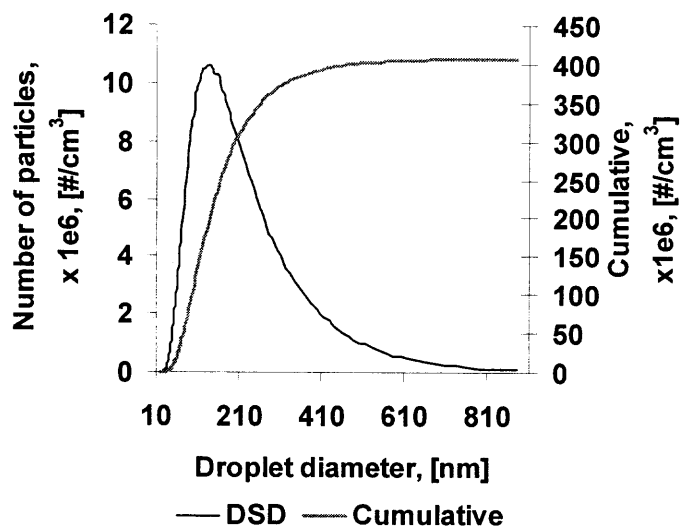


Figure 5.16 Droplet size distribution (PSD) and cumulative number of droplets corresponding to liquid aerosol generated from a solution of oil in ethanol.

5.4.2.1 Collection Efficiency of HEPA Filter Media. Customized filters were tested simultaneously with a HEPA fiber-based filter for comparison purposes. The module with a HEPA sheet was challenged against liquid submicron aerosol. Figure 5.17 shows the cumulative collection efficiency for a clean and used HEPA filter at different gas velocities. As the gas velocity is increased, collection efficiency drops. In addition, as time lapses, the collection efficiency also drops contrary to the case when solid particles are collected. This occurs because when collecting liquid droplets, the formation of a cake does not exist. Liquid droplets coalesce and form larger droplets that can appear at the back side of the filter and open the possibility for re-entrainment or release of small droplets due to the shear force of the gas and collisions with other incoming droplets.

As explained above, the plateau of the collection efficiency as the droplet diameter increases is a characteristic property of HEPA, because these filters have a collection efficiency of about 99.97% for aerosols larger than 0.3 microns. Hence, the collection efficiency does not change much above 0.3 microns.

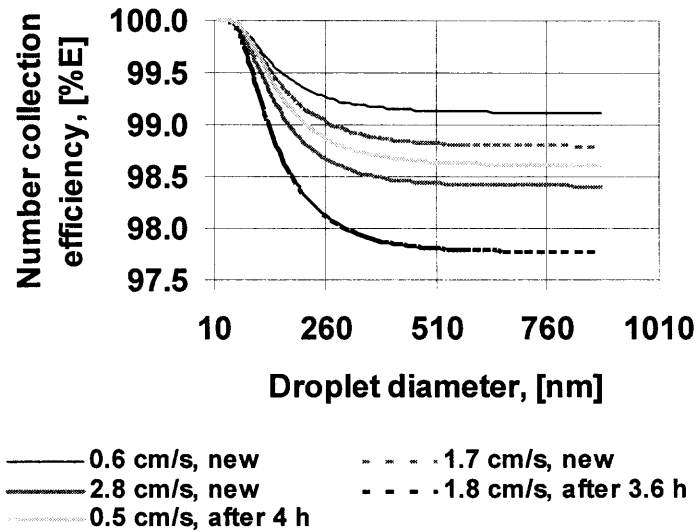


Figure 5.17 Cumulative number collection efficiency of HEPA Shop-Vac fiber based filter when challenged against oil submicron size droplets (liquid aerosol).

5.4.2.2 Collection Efficiency of Filter Media Made of Glass Beads. Similar to the experiments done when using solid aerosol particles, two filtration modules containing packed beds of glass beads of different sizes were tested against oil-based submicron aerosol. The purpose is to compare results from solid and porous particles used as filter media. The sizes of the glass beads were 180 to 220 microns and 380 to 420 microns. The collection efficiencies of these filters can be compared to the results obtained by using granules of sizes in the range of 150 to 250 microns and 250 to 500 microns, respectively.

The packed bed with large particles, shown in Figure 5.18a, gives poorer collection efficiency than the packed bed with smaller ones, Figure 5.18b. In both cases, at any gas velocity, the collection efficiencies do not reach a constant value (plateau) with size indicating that even large droplets are not completely trapped by the filter media.

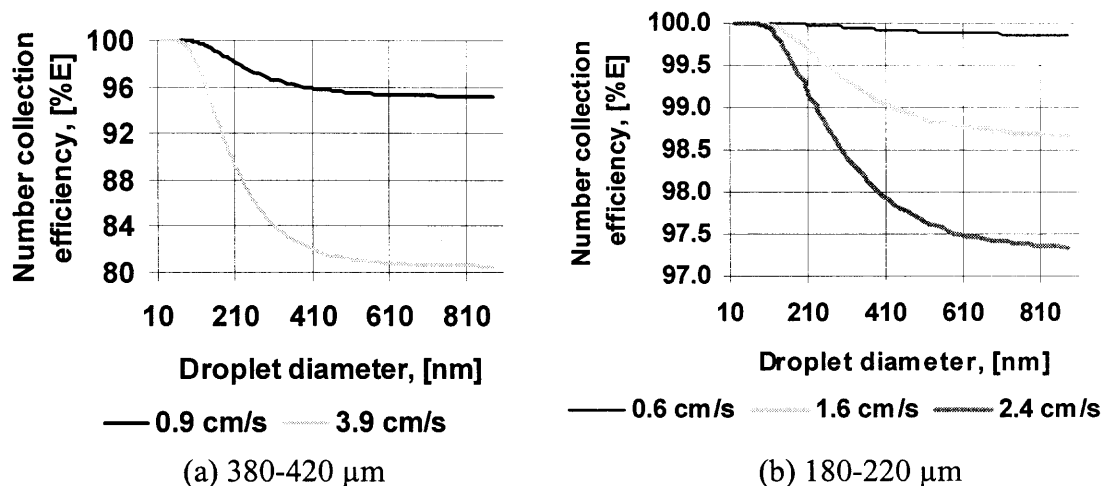


Figure 5.18 Cumulative collection efficiency of 2 inches thick packed beds of glass beads at different gas velocities when challenged against oily submicron aerosol.

5.4.2.3 Collection Efficiency of Filters Made of Agglomerates of Fumed Silica.

Two filter modules containing hydrophilic and hydrophobic consolidated granules of fumed silica were challenged against oil-based aerosol. The collection efficiencies of the hydrophilic and hydrophobic granular filters are shown in Figure 5.19(a) and 5.19(b), respectively. The granular filter made of hydrophilic fumed silica granules shows poorer collection efficiency than the hydrophobic granule based filter. This indicates that the oil droplets were more likely to be trapped in the hydrophobic granular filter because of a greater affinity with the surfaces of the granules. For the hydrophobic granules, the collection efficiencies reach a constant value (plateau) for droplets larger than 500 nm, indicating that large droplets are trapped in the filter media. Nevertheless, the collection efficiencies are far from the desired values shown by the HEPA filter. The main reason for the poor collection efficiency of these filter media is the agglomerate size. Agglomerate sizes smaller than 500 μm were very difficult to obtain. Actually, the collection efficiency corresponding to solid spheres of similar sizes is even lower as will be shown below.

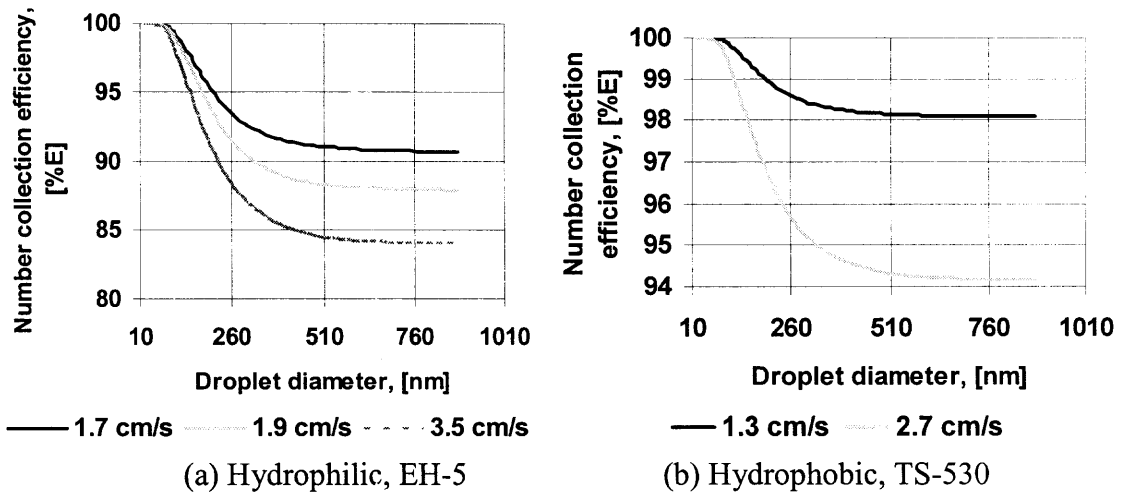


Figure 5.19 Cumulative collection efficiency of 3 inches thick packed beds of fumed silica consolidated agglomerates (500 – 800 μm) at different gas velocities when challenged against oily submicron aerosol.

5.4.2.4 Collection Efficiency of Filter Media Made of Carbon Black Granules.

Two customized filters made of carbon black granules were tested against oil-based submicron aerosol. Figure 5.20 (a) shows the results obtained with a 3 inch thick filter made of granules with sizes in the range from 250 to 500 microns, and Figure 5.20 (b) shows the results corresponding to a 2 inch thick filter of granules with sizes between 150 to 250 microns. The type of carbon black used is Regal 660 A69, which is well granulated and has almost no fines. Once again, better collection efficiency is obtained with the bed made up of smaller granules. However, the collection efficiencies are lower than HEPA filter but it may be possible that the collection efficiency of these carbon-black based granular filters does not change with time as happens with HEPA because of the porosity of the granules. Analysis of the capacity of the filters will be introduced in a later section.

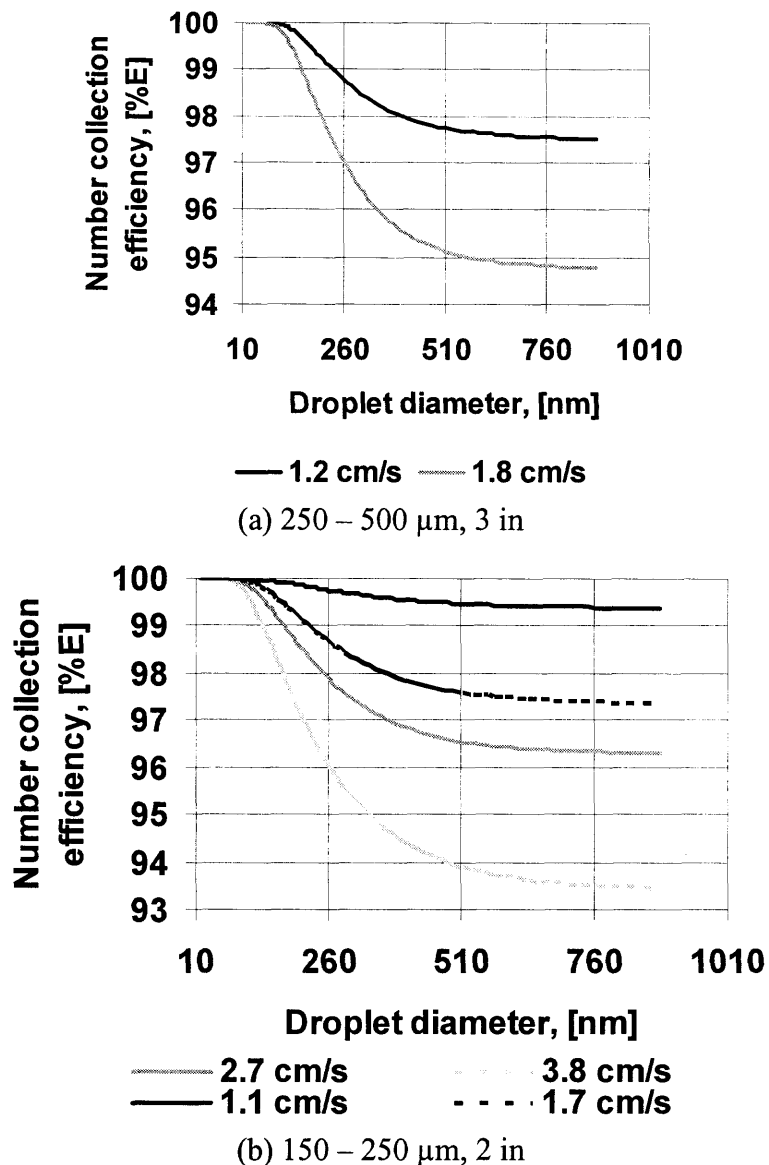
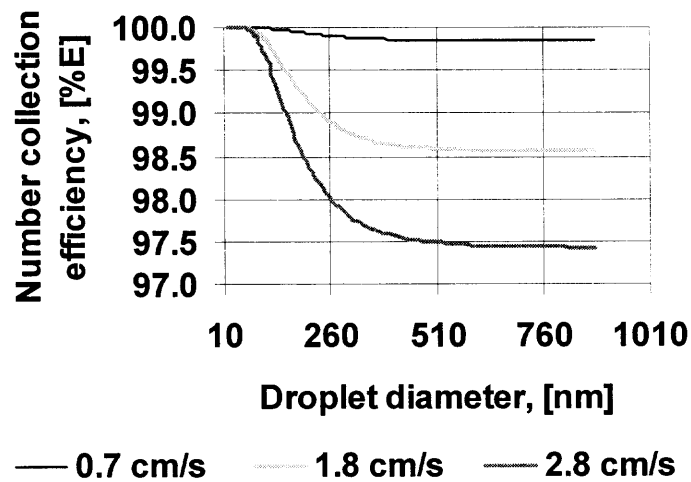


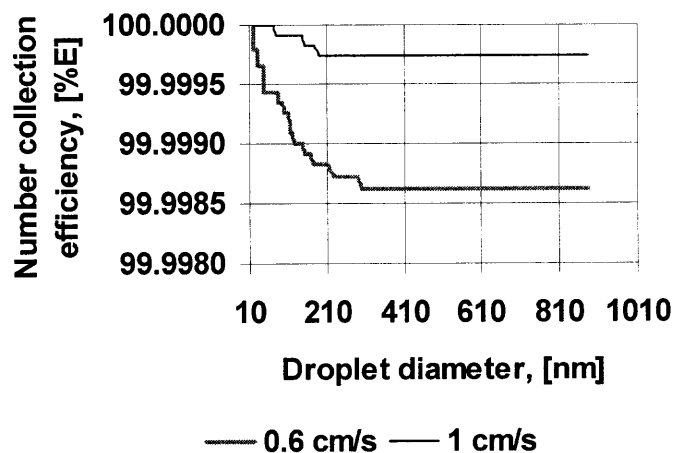
Figure 5.20 Cumulative collection efficiency of packed beds of carbon black granules (Regal 660 A69) at different gas velocities when challenged against oily submicron aerosol.

5.4.2.5 Collection Efficiency of Filter Media Made of Aerogel Granules. The aerogel silica-based granules used in these experiments have a surface treatment that makes them hydrophobic. This hydrophobicity coupled with the fact that these aerogel granules are extremely porous provides a material with a high capacity to adsorb oil; therefore, higher collection efficiencies are expected. The customized filters have a

thickness of about 3 inches; one is filled with granules with sizes between 250 to 500 microns, Figure 5.21 (a), and the other with granules in the range of 150 to 250 microns, Figure 5.21 (b). The collection efficiencies given by the filter containing the larger granules are similar to HEPA, and they are expected to remain constant rather than decrease as is observed with HEPA filters. The collection efficiencies of the filter with smaller granules show values much higher than HEPA, but because of the high resistance through the filter media, it can only be used at very low flows.



(a) 3 in, 250-500 μm



(b) 3 in, 150-250 μm

Figure 5.21 Cumulative collection efficiency of packed beds of aerogel granules (Nanogel OGD) at different gas velocities when challenged against oily submicron aerosol.

5.4.2.6 Summary of Filtration Results Corresponding to Oil-Based Aerosol Experiments. Figure 5.22 shows the different cumulative collection efficiencies of the customized filters at different gas velocities when challenged against oil droplets. The different experimental conditions and results are summarized in Table 5.3. By taking as a reference the performance of the HEPA fiber-based filter, it can be seen that several customized filter media perform similar to HEPA. For instance, at low gas velocities, even a packed bed of glass beads with sizes between 180 to 220 microns has collection efficiencies similar to HEPA. However, the packed bed is more likely to saturate and the liquid will fill the voids increasing its resistance to the flow. For porous materials, such as carbon black or aerogel granules, the oil is absorbed leaving the resistance through the filter, i.e., the pressure drop, unchanged. The collection efficiency of a packed bed of aerogel granules of about 250 to 500 μm provides similar collection efficiency than HEPA. A packed bed with smaller granules of about 150 to 250 microns performs better than HEPA when challenged against oil droplets.

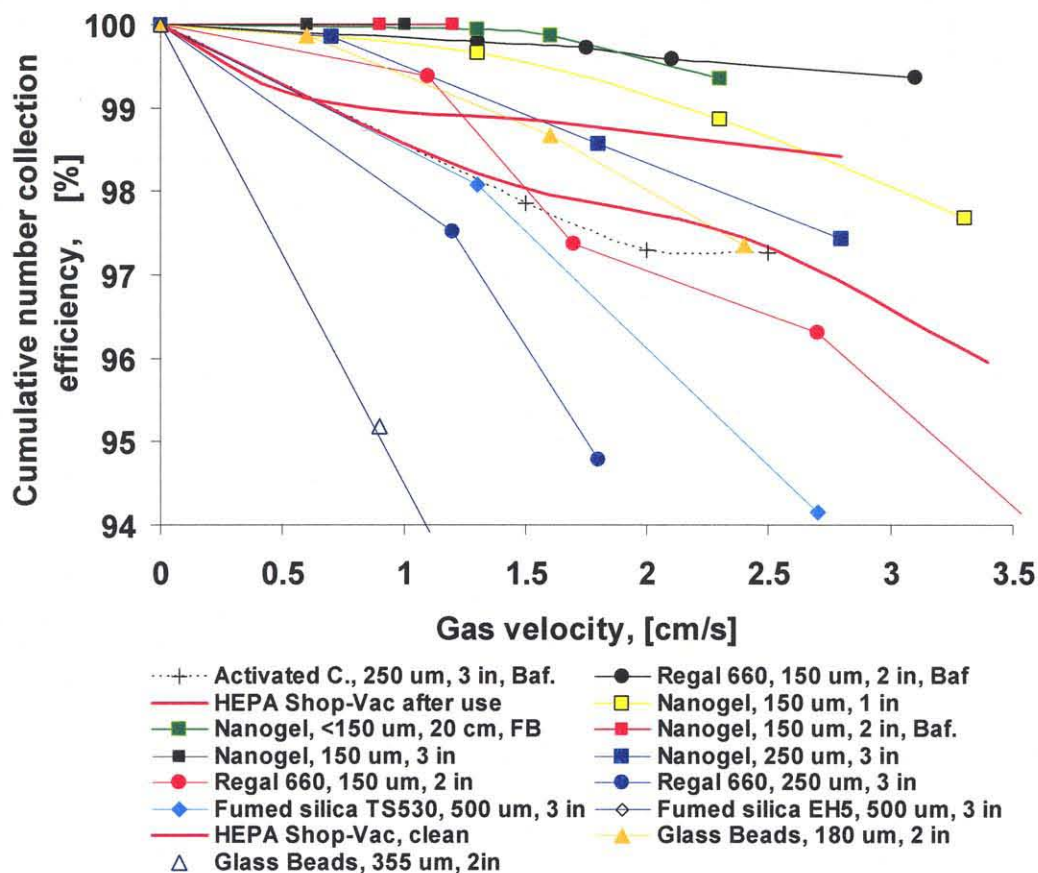


Figure 5.22 Cumulative collection efficiencies with respect to gas velocity of the customized filters challenged against liquid submicron oil-based aerosol.

Table 5.3 Summary of the Cumulative Collection Efficiencies of the Filters When Challenged against Liquid Oily-droplets Aerosol

Filter Media Material	Symbol	Granule Size um	Thickness in	Baffles (Yes/No)	Gas velocity		Efficiency		Gas velocity		Efficiency	
					cm/s	%	cm/s	%	cm/s	%		
HEPA	RL				0.6	99.12	1.7	98.797	2.8	98.413		
Glass Beads	CIT	355-425	2	N	0.9	95.18	3.9	80.53				
Glass Beads	OT	180-212	2	N	0.6	99.87	1.6	98.67	2.4	97.35		
EH5	CID	500-800	3	N	1.7	90.66	1.9	87.88	3.5	84.04		
TS530	LBD	500-800	3	N	1.3	98.085	2.7	94.15				
Regal 660 A69	RC	250-500	3	N	1.2	97.51	1.8	94.78				
Regal 660 A69	BIC	150-250	2	N	1.1	99.38	2.7	96.3	3.8	93.46		
Nanogel II	BIS	250-500	3	N	0.7	99.85	1.8	98.56	2.8	97.43		
Nanogel II	BkS	150-250	3	N	0.6	99.9997	1	99.9986				

Legend:

CIT: Clear Triangle
OT: Orange Triangle

CID: Clear Diamond
LBD: Light Blue Diamond

BkSt: Black Star
BIC: Blue Circle

BIS: Blue Square
BkS: Black Square

RC: Red Circle
RL: Red Line

5.4.3 Pressure Drop across Filter Media and Evaluation of Capacity

The resistance across filter media is of extreme importance since it is directly related to operating costs, the higher the resistance the more expensive it is to run the filtration system. Also, it is well known that the pressure drop across a clean fiber-based filter is usually about 1 inch of water column (25 mm), and that the maximum pressure drop allowed during operation of the filter is about 4 to 5 inches of water (102 to 127 mm). Figure 5.23 shows the resistance, expressed as pressure drop, across the different clean filter media tested as function of gas velocity. The plot has different backgrounds depending on the allowed resistance for a clean filter, light green, and the allowed resistance during operation, light yellow. The HEPA pressure drop is plotted as a red line for reference.

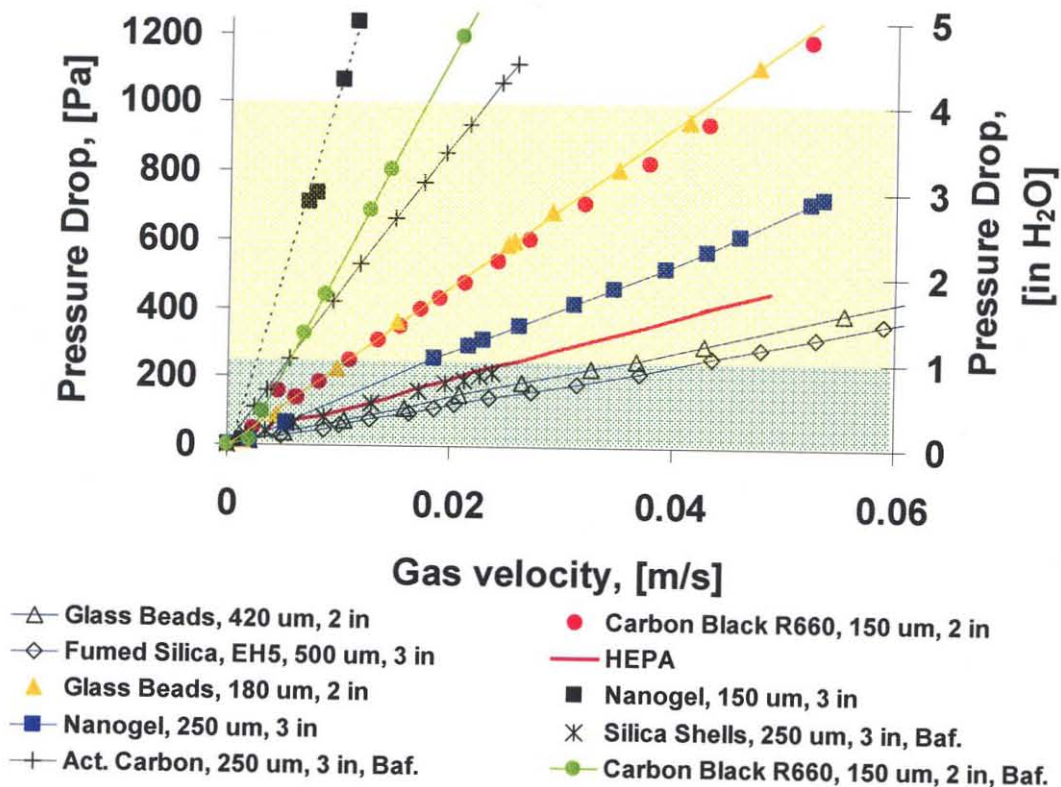


Figure 5.23 Resistance of clean filters tested in the experiments. (Legend: Material, granule size in microns, thickness in inches and with baffles-BAF).

The granular bed filters with relatively large particles such as glass beads of about 420 microns, fumed silica of 500 microns and silica shells gave a lower resistance than HEPA but, as shown in the previous sections, their collection efficiency was poor when compared to HEPA. The granular filter made of carbon black R660 (150 microns, 2 inches thick without baffles), which has an acceptable collection efficiency, has a pressure drop of about 1 inch of water column at a gas velocity of about 1 cm/s. A gas velocity of 1 cm/s would be considered as the minimum velocity during operation. The filters that performed the best, such as carbon black R660 (150 microns, 2 inches thick with baffles) and Nanogel[®] granules (150 μm , 3 inches thick), show higher pressure drop making them suitable for running only at low gas velocities such as 1 cm/s.

Even though the resistance across clean granular filters is higher than clean HEPA filters, during operation, the resistance across the granular filters will increase only slightly when compared to the resistance increase across HEPA filters. It will be shown below that for HEPA filters, the pressure drop increases dramatically as they collect particles, so their initial resistance is doubled or tripled. For example, Figure 5.24 shows the evolution of the resistance across a HEPA and a carbon black-based granular filter with respect to time when challenged against the same aerosol simultaneously. In these tests, the aerosol was composed of polystyrene latex spheres as explained in the experimental section. It can be seen that while the pressure across the granular filter rises less than 20% in a period of about 70 hours, the pressure drop across the HEPA filter rises about 250%. After 70 hours in operation, the pressure across the HEPA filter has reached a similar value than the one given by the carbon black granular filter. In addition, the rate at which the pressure drop across the HEPA filter is increasing is about 5 times

faster than the carbon black filter. This means that the filtration capacity of the granular filter is much larger than the HEPA filter. The changes in the slope of the pressure drop with respect to time are due to the changes in the concentration of the challenging aerosol.

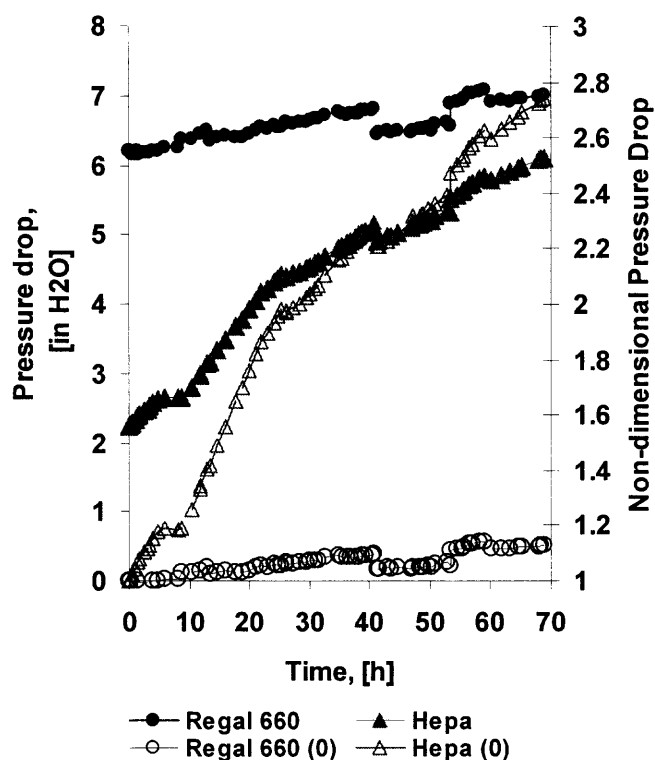


Figure 5.24 Resistance across HEPA and granular carbon black-based filters as a function of time during filtration of solid submicron particles.

In a similar way, a granular filter composed of Silica Shells and a HEPA filter were challenged simultaneously against solid aerosol. Figure 5.25 shows the evolution of the resistance of both filters with respect to time; it is seen that the pressure drop across the HEPA filter increases about 2.5 times its initial pressure drop while the granular filter only increases to 1.1 times its clean filter pressure drop. Regarding the collection efficiency of the granular filter, it started at about 93%, but it increased as more particles were collected to about 98% as shown in Figure 5.9b. As the granular filter collects more

particles, better collection efficiency is expected without a significant change in its pressure drop. The better collection efficiency may be due to the filling of the void spaces between granules and the formation of dendrites with the collected particles that become part of the collectors.

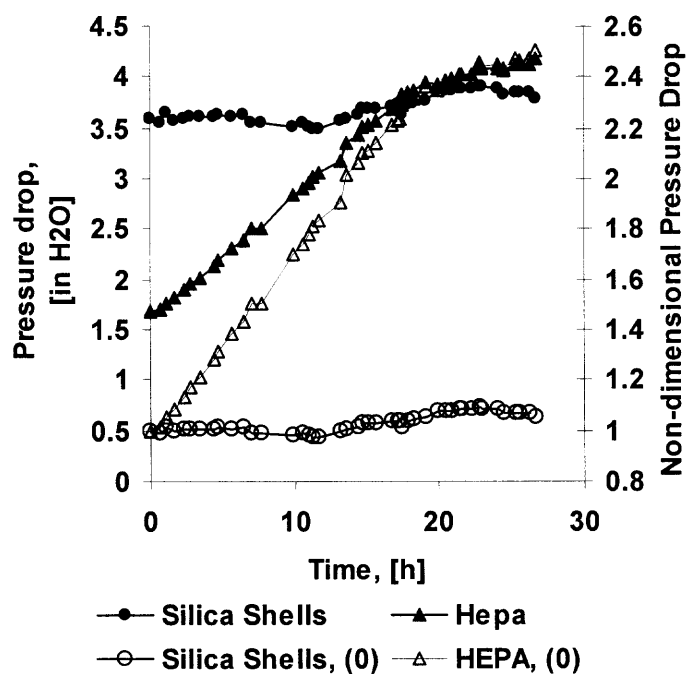


Figure 5.25 Resistance across HEPA and granular Silica Shells-based filters as a function of time during filtration of solid submicron particles.

Granular filters composed of porous collectors such as carbon black or aerogel granules are expected to have a larger filtration capacity than HEPA when removing oil-based aerosols. Similarly for comparing the capacity of the filters towards solid submicron aerosols, the customized filter and a HEPA filter were challenged against an oil-based aerosol for long time and their collection efficiencies and resistances were compared. Figure 5.26a shows the cumulative collection efficiency of a granular bed filter made of carbon black granules, Regal 660. The size of the granules was in the range of 150 to 250 microns placed in a 2 inch thick acrylic module. Its collection efficiency

remains above 99 % during the entire run. Figure 5.26b shows the corresponding cumulative collection efficiency for a HEPA filter sheet that was arranged as explained above. Its collection efficiency drops dramatically, below 90%, as the filter becomes saturated with oil droplets. The superficial gas velocity through both filters was about 1.6 cm/s. Figure 5.27 shows the pressure drop across both filters during the experiment. At the beginning, the pressure drop of the granular bed filter is larger than the HEPA, but as the HEPA filter becomes saturated, its pressure drop increases exponentially surpassing the pressure drop across the granular filter. This is an indication of the larger filtration capacity of the granular filter.

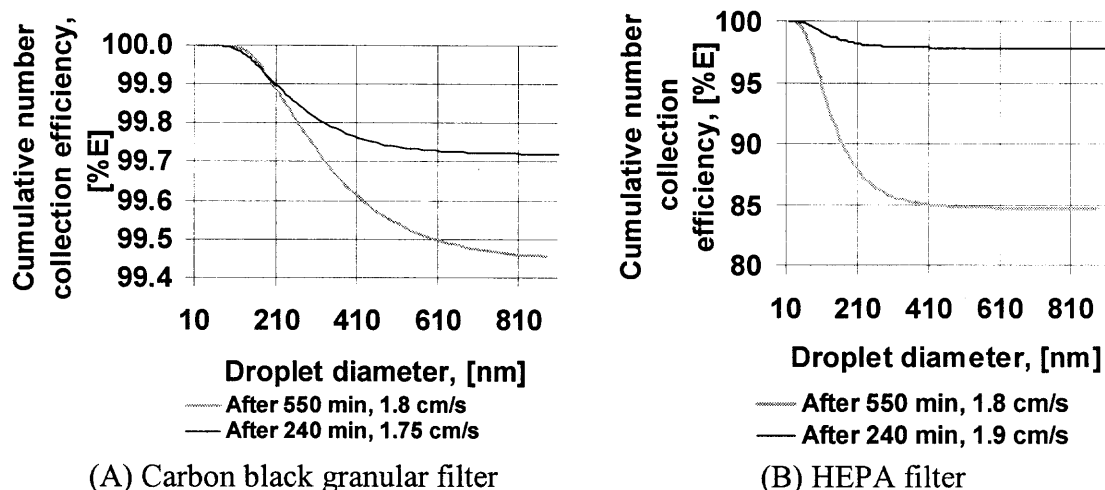


Figure 5.26 Collection efficiencies of (A) a packed bed filter and (B) a HEPA filter with respect to time during an experiment to compare their removal capacity when challenged against oil-based aerosols. 2 in thick packed bed filter of Regal 660 granules with sizes between 150 to 250 microns with baffles.

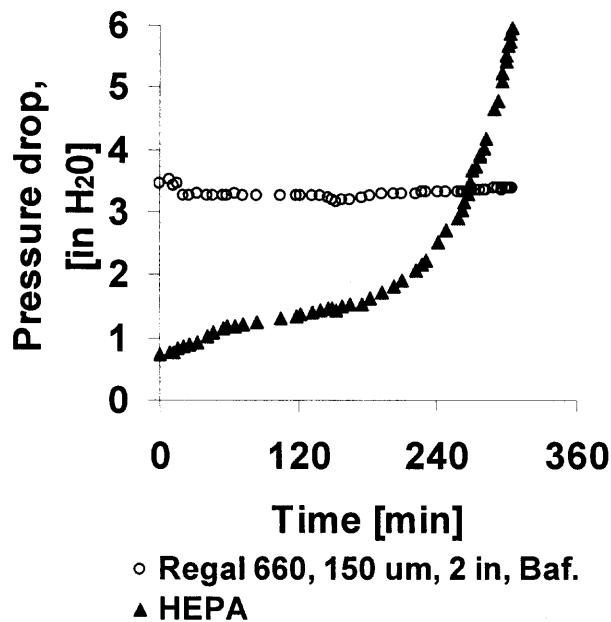


Figure 5.27 Pressure drop across HEPA and a packed bed of carbon black (Regal 660) with respect to time to compare their capacity for collecting oil-based aerosol.

Hydrophobic aerogel granules, such as Nanogel[®], are known for their high absorption capacity for oil, of about several times their weight. Figure 5.28 shows the cumulative collection efficiencies of a packed bed of aerogel granules (A) and a HEPA filter (B) when challenged against the same oil-based aerosol for long periods of time to compare their capacity. The gas velocity through both filters was kept constant at about 3.2 cm/s. The collection efficiency of the aerogel based filter is higher than HEPA in all the measurements, although it decreases with respect to time in a similar way as the HEPA. For the granular filter, since the aerogel granules shrink and fuse in the presence of oil, it is believed that due to the absorption of oil into the aerogel granules more void spaces are generated leading to a reduction in collection efficiency, although still better than the HEPA. This is verified by the pressure drop readings as function of time as shown in Figure 5.29. It can be seen that the pressure drop across the packed bed

granular filter decreases with respect to time while for HEPA it increases exponentially. This phenomenon shows that HEPA filter has a lesser removal capacity than a customized packed bed of aerogel granules.

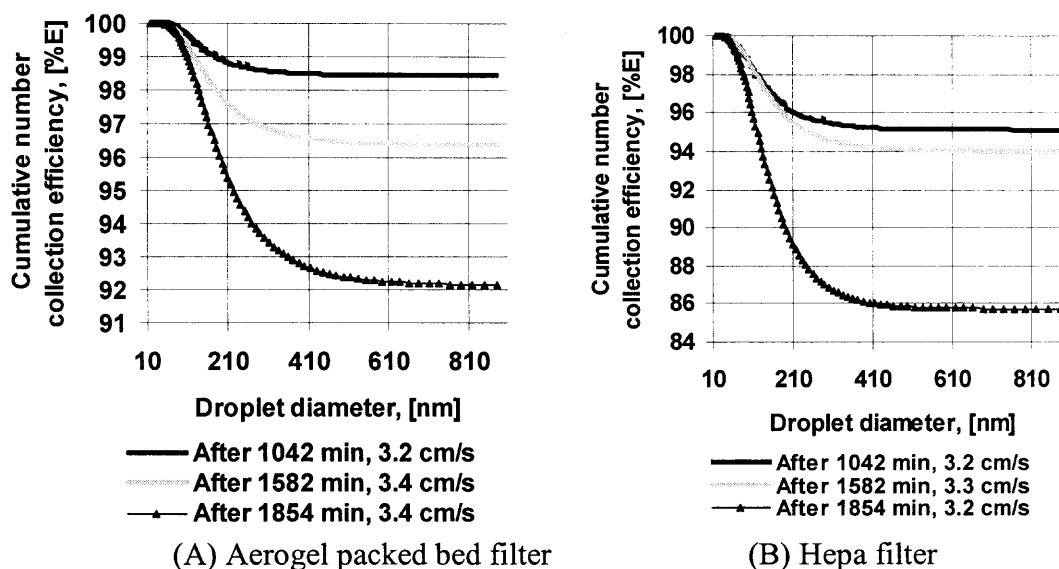


Figure 5.28 Collection efficiencies of (A) a packed bed filter and (B) a HEPA filter with respect to time during an experiment to compare their removal capacity when challenged against oil-based aerosols. 1 inch thick packed bed filter (without baffles) of aerogel, Nanogel, granules with sizes between 150 to 250 microns.

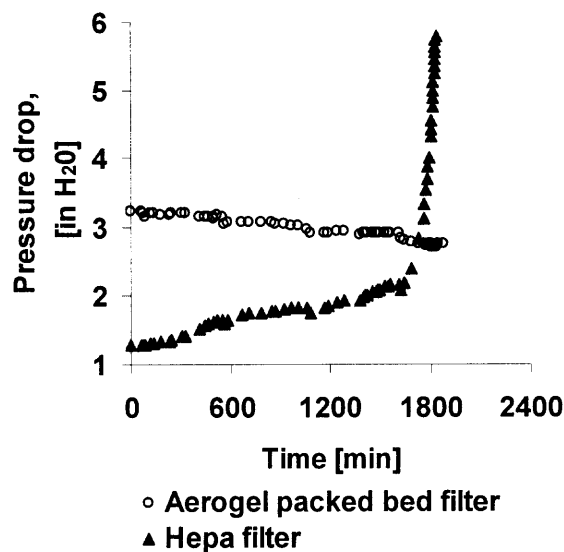


Figure 5.29 Pressure drop across HEPA and a packed bed of aerogel granules with respect to time when challenged against oil-based aerosol.

5.4.4 Fluidized Bed Filter

Another concept studied was the fluidized bed filter. Fluidization of agglomerates of fumed silica nanoparticles is well known and has been extensively studied (see Chapter 2 of this Dissertation). The fluidized agglomerates are highly porous which make them potentially suitable for collecting submicron particles by diffusion and interception mechanisms with reduced resistance. Figure 5.30 shows the cumulative number collection efficiency of a fluidized bed of hydrophobic fumed silica agglomerates when challenged against an oil-based submicron aerosol. Even though the collection efficiency of the fluidized bed of agglomerates of fumed silica nanoparticles was lower than that of several granular bed filters, it does not plateau. In addition, when clean air was used to fluidize the agglomerates, it was found that the fluidized bed released particles (data not shown), which was one of the reasons why the collection efficiency did not plateau at particle sizes larger than 0.3 microns. This was expected because the fluidized bed of agglomerates of nanoparticles is composed of a broad particle size distribution that includes submicron particles.

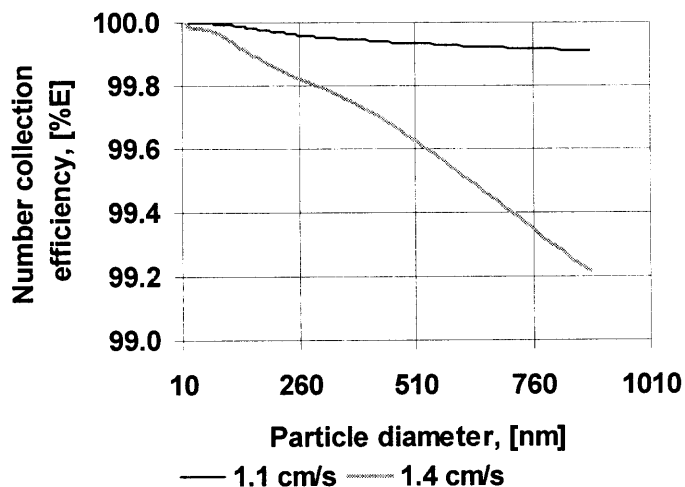


Figure 5.30 Cumulative number collection efficiency of a fluidized bed of hydrophobic fumed silica (TS-530) when challenged against oil-based aerosol.

Another fluidized bed filter containing silica based aerogel granules (Nanogel[®]) was tested. Granules of less than 150 microns in diameter were fluidized. They are somewhat similar to the agglomerates of nanoparticles in the sense that they have a highly nanoporous structure, but with the advantages of being tougher (more robust in structure) and their particle size distribution does not show as much fines as agglomerates of nanoparticles. The aerogel granules used in the experiments have a surface treatment that makes them hydrophobic; this property improves their collection efficiency for oil mists.

Figure 5.31 shows a sequence of the fluidization stages of aerogel granules when going from a packed bed to a fluidized bed. At low velocity, when the fluidized bed shows gas channels, oil droplets are found downstream of the bed indicating that the oil droplets managed to pass through the bed in the channels. However, as soon as homogeneous fluidization is obtained no oil-based aerosol was detected downstream. The homogeneous fluidized bed is reached at gas velocities above the minimum fluidization velocity, which was found to be about 0.3 cm/s as seen in the plot of the fluidized bed pressure drop as a function of the gas velocity in Figure 5.32. The pressure drop across the fluidized bed is very small, about 0.2 inches of water column, and it is not dependant on the gas velocity as in a packed bed. In general, the pressure drop across a fluidized bed is independent of the gas velocity and it is given by

$$\Delta P = \frac{mg}{A} \quad (5.4)$$

This equation relates the pressure drop during fluidization to the apparent weight of the particles. Here m is the mass of the fluidized granules, g is the acceleration of gravity and A is the cross-sectional area of the column.

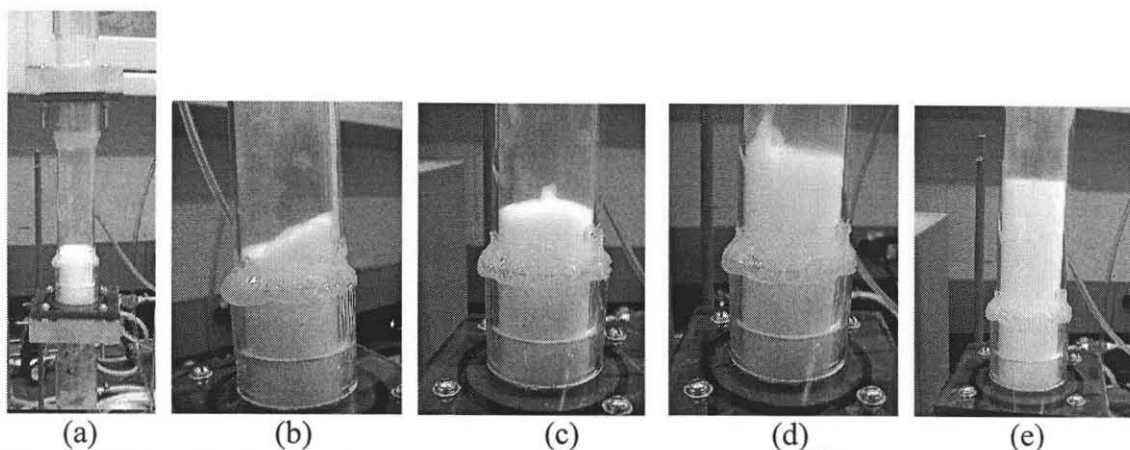


Figure 5.31 Bed expansion of the fluidized bed of Nanogel[®]. (a) Packed bed, no flow passing through the bed; (b-d) flow has been increased but bed not fully fluidized and channels are present; (e) fully fluidized state, a clear horizontal liquid-like interface can be seen.

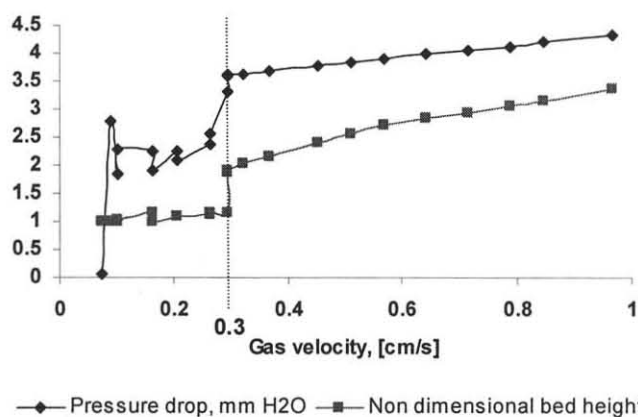


Figure 5.32 Fluidization hydrodynamic characteristics of a fluidized bed of 65 μm aerogel granules (Nanogel).

During fluidization, the aerogel granules release a very small amount of particles when compared against the concentration of the challenging aerosol and they do not affect the collection efficiency. A fluidized bed of aerogel granules was challenged against solid submicron aerosol resulting in the collection efficiencies shown in Figure 5.33a. Clearly, the collection efficiency is comparable to HEPA although the gas velocity is relatively low. When the fluidized bed of aerogel granules was challenged against oil-

based aerosol, the resulting collection efficiency was higher than HEPA filters as shown in Figure 5.33b. In this particular experiment, about 6 grams of aerogel granules were used in the fluidized bed resulting in a bed height of about 40 cm. During fluidization the bed expands (see Figure 5.32) and the large bed expansion provides a better collection efficiency because of the longer time required for the aerosol to go through the fluidized bed. The bed height can be adjusted by adding more granules (powder) to the column and also by increasing the gas flow, although only slightly. The excellent collection efficiency observed for oil-based aerosol is of particular importance and is probably due to the high oil absorption capacity of aerogel granules such as Nanogel[®]. Under the proper operating conditions, a fluidized bed filter of aerogel granules will provide not only better collection efficiency than HEPA filters, but much larger capacity, making them suitable for applications where oil mists need to be removed from gas streams.

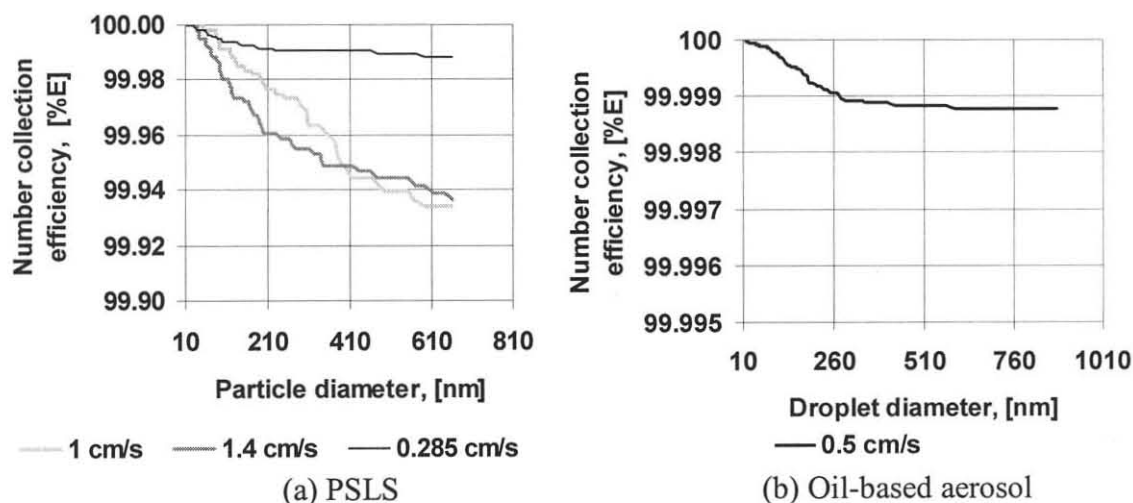


Figure 5.33 Cumulative number collection efficiency of a fluidized bed of aerogel granules of less than 150 microns. (a) fluidized bed challenged against solid aerosol particles, (b) fluidized bed challenged against oil droplets.

To show the importance of the fluidized bed's height and the gas flow in the collection efficiency of the fluidized bed of aerogel granules, an experiment was done with approximately half the amount of powder used in the experiment that resulted in Figure 5.33. In this run, about 3 grams of aerogel granules were used and they provided a fluidized bed height of about 20 cm (half the previous example). Also, the fluidized bed height changed from 19 cm at a gas velocity of about 1.3 cm/s to 22 cm for a gas velocity of about 2.3 cm/s. This increase in gas velocity also affects also the collection efficiency because of the increase in the void fraction of the bed, allowing the aerosol an easier passage through the fluidized bed. However, this could have been compensated for by increasing the amount of powder, but the purpose of the experiment was to find the limiting operating conditions. Figure 5.34 shows the collection efficiencies of the fluidized bed just discussed at three different gas velocities.

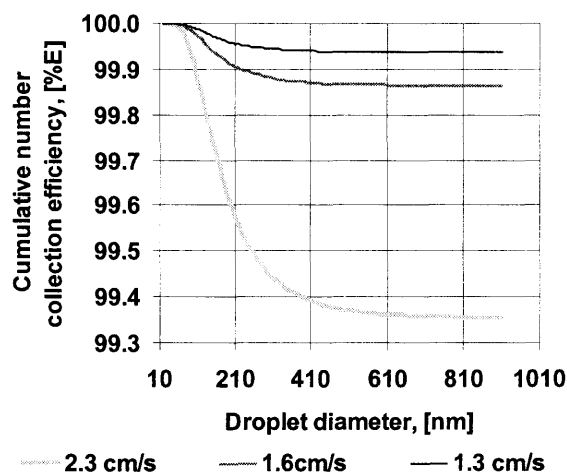


Figure 5.34 Cumulative number collection efficiency corresponding to a fluidized bed of aerogel granules when challenged against oil-based aerosols at different gas velocities.

An example comparing the collection efficiencies and capacities of a fluidized bed of aerogel granules and a HEPA fiber-based filter when challenged against oil droplets is seen in Figure 5.35 and Figure 5.36, respectively. Here, both filters were

challenged against the same aerosol at a constant gas velocity of 0.82 cm/s during the entire run. As explained above, a sheet of HEPA filter was held between 2 acrylic modules with an aperture of 1.5 inches in diameter, and the fluidized bed filter was held in an acrylic tube of 1.5 inches in diameter containing about 3 grams of aerogel granules of less than 150 microns in size. Figure 5.35a shows that the collection efficiency of the fluidized bed remains unchanged with respect to time while the collection efficiency of the HEPA drops significantly down to 66 % after 626 minutes as shown in Figure 5.35b. Regarding the capacities of the filters, the pressure drop across the HEPA filter (triangles) increases exponentially when it is saturated with oil, whereas the pressure drop across the fluidized bed filter increased just a little as shown in Figure 5.36. The pressure drop across the HEPA filter has increased about 14.2 times (1420 %) while it has increased only 50% for the fluidized bed filter.

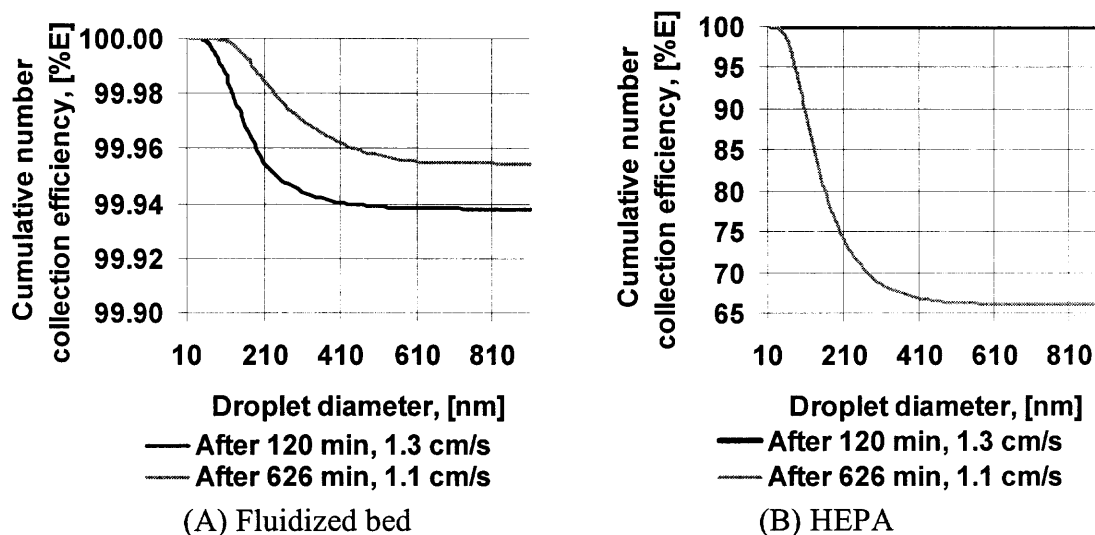
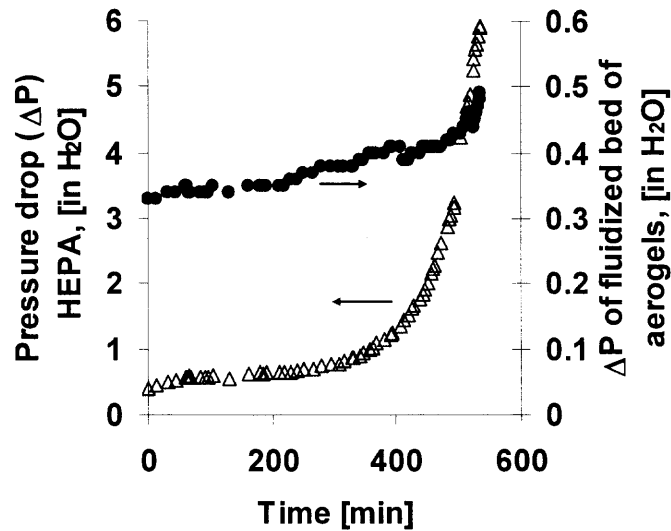


Figure 5.35 Collection efficiencies of a fluidized bed of aerogel granules (A) and a HEPA fiber based filter (B) with respect to time.



△ Hepa • Nanogel, <150 μm, F.B.

Figure 5.36 Pressure drop or resistance across a HEPA fiber based filter and a fluidized bed of aerogel with respect to time when challenged against the same oil-based aerosol.

5.4.5 Discussion on the Filtration Mechanisms and Collection Efficiency

Liquid and solid aerosols of sizes lower than 1 micron have been used to challenge customized filters and compare them to HEPA. The size of the aerosol particles establishes the importance of each of the collection mechanisms. The following filtration mechanisms are well known: diffusion, interception, inertial impaction and electrostatic charges. The effects of electrostatic charges will not be discussed since the charges in the aerosol stream were neutralized as explained in the experimental methods section.

The first question to answer for a granular bed filter is: What is the flow regime around the collectors? This can be solved by calculating the Reynolds number corresponding to the experiments as

$$\text{Re} = \frac{\rho V d_g}{\mu} \quad (5.5)$$

where V , is the superficial gas velocity (Q/A) and d_g is the diameter of the collector or granule.

Figure 5.37 shows the calculated Reynolds number values corresponding to the experimental conditions. The diameter of the collector or granule varies from 65 microns, for a fluidized bed, to about 675 microns (the average size of granules between 500 to 850 microns).

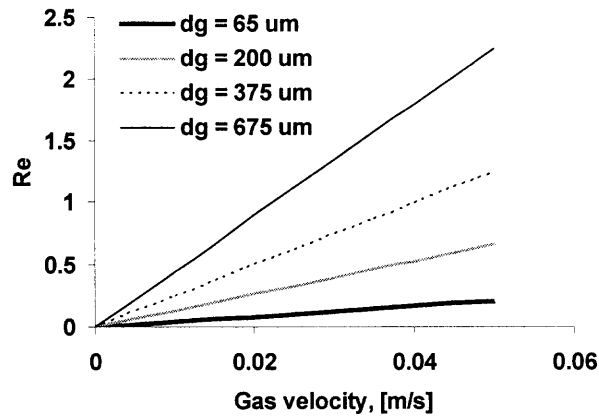


Figure 5.37 Reynolds number corresponding to the experimental conditions.

In a laminar flow regime, the Blake-Kozeny equation, shown below, is valid for describing the pressure drop across a packed bed of spheres¹²⁸.

$$\frac{\Delta P}{L} = 150 \left(\frac{\mu V}{d_g^2} \right) \frac{(1-\varepsilon)^2}{\varepsilon^3} \quad (5.6)$$

The porosity of the packed bed can be calculated from this equation since the other variables are known from experimental data. Table 5.4 shows the different values of the porosity of the bed (ε) as calculated by using experimental data and Equation 2. In this table, the bulk density can be found from the mass of granules divided by the volume of

the filtration module. The material density of the granules is given by different sources.

The granule density is calculated with the following equation

$$\rho_g = \frac{\rho_b}{(1 - \varepsilon)} \quad (5.7)$$

from which the porosity of the granule (ε_g) can be estimated. It is believed that the porosity of the collectors plays an important role in trapping the submicron aerosol particles by the diffusion mechanism. The granule's porosity is given by

$$\varepsilon_g = 1 - \frac{\rho_g}{\rho_m} \quad (5.8)$$

Table 5.4 Summary of Characteristics of the Packed Beds of the Customized Filters

Material	Collector Size	L/dg	Thickness	Bed Porosity	Bulk Density	Granule Density	Material Density	Granule Porosity
	um		in	ε	g/cm ³	g/cm ³	g/cm ³	ε_g
Nanogel OGD	250 - 500 (375)	203	3	0.356	0.075	0.116	2.2	0.95
Nanogel OGD	150 - 250 (200)	381	3	0.290	0.080	0.113	2.2	0.95
Glass Beads	180 - 220 (200)	254	2	0.383	1.517	2.461	2.4	0.00
Glass Beads	380 - 420 (400)	127	2	0.366	1.517	2.392	2.4	0.00
Fumed Silica EH5	500 - 850 (675)	113	3	0.325	0.065	0.097	2.2	0.96
Carbon Black R660	150 - 250 (200)	254	2	0.385	0.519	0.843	2.267	0.63
Carbon Black R660	250 - 500 (375)	135	2	0.312	0.511	0.742	2.267	0.67
Silica Shells	250 - 500 (375)	203	3	0.360	0.178	0.278	2.2	0.87

The porosity of the bed (ε) is important for the calculation of the granules' density, porosity and the conversion of the total bed efficiency (E) to the single-sphere efficiency by using the following equation given by Tardos et al.¹²⁹

$$\eta = -\frac{2}{3} \frac{\varepsilon}{1-\varepsilon} \frac{d_g}{L} \ln(1-E) \quad (5.9)$$

The single-sphere efficiency will be used in combination with other non-dimensional numbers to compare the different filtration efficiencies found in the experiments. Assuming that electrostatic effects are negligible because of the use of the Aerosol Neutralizer, as explained in the experimental methods section, the single-sphere efficiency is a function of the following parameters¹¹⁵:

$$\eta = \eta(Pe, G, Stk, R, Re, \varepsilon) \quad (5.10)$$

where Pe , G , Stk and R are non-dimensional parameters which are the measures of Brownian diffusion, gravitational settling, inertial impaction, and interception, and Re and ε are parameters related to the flow and the configuration of the granular bed. In the experiments, the gravitational settling was neglected because of the small size of the aerosol particles, i.e., submicron. It is also commonly assumed that the single-sphere efficiency is equal to the summation of the efficiencies due to the individual filtration mechanisms

$$\eta = \eta_D + \eta_G + \eta_I + \eta_R \quad (5.11)$$

$$\eta = \eta_D(Pe, Re, \varepsilon) + \eta_G(G, Re, \varepsilon) + \eta_I(Stk, Re, \varepsilon) + \eta_R(R, Re, \varepsilon) \quad (5.12)$$

Before doing an analysis of the total single-sphere efficiency, it is important to determine which of the filtration mechanisms are relevant. In addition to neglecting electrostatic forces, it is quite reasonable to assume that gravitational settling is negligible in the experiments because of the small size of the aerosol particles, i.e., submicron. Hence

$$\eta_G(G, \text{Re}, \varepsilon) \approx 0 \quad (5.13)$$

Among the parameters related to the flow and configuration of the granular bed, the void fraction has been found previously and the only thing left to estimate is the Reynolds numbers. The Reynolds numbers for the different aerosol particle sizes are calculated by

$$\text{Re}_0 = \frac{\rho_g V_0 d_p}{\mu} \quad (5.14)$$

and it is assumed that the aerosol particle of diameter (d_p) is traveling at the same velocity, (V_0), as the gas. The Reynolds numbers are used in the calculation of the stopping distance (S)

$$S = \frac{\rho_p d_p}{\rho_f} \left[\text{Re}_0^{1/3} - \sqrt{6} \arctan\left(\frac{\text{Re}_0^{1/3}}{\sqrt{6}}\right) \right] \quad (5.15)$$

Subsequently, these values are used in the calculation of the Stokes numbers

$$\text{Stk} = \frac{S}{d_g} \quad \text{for } \text{Re}_0 < 1.0 \quad (5.16)$$

Considering the effects of the small size of aerosol particles on drag force, the Stokes number may be slightly different. For this reason, the Cunningham correction factor is incorporated in the equation for the Stokes number and it is calculated from

$$C_c = 1 + \frac{\lambda}{d_p} \left[2.34 + 1.05 \exp\left(-0.39 \frac{d_p}{\lambda}\right) \right] \quad (5.17)$$

In this equation, λ represents the mean free path of air molecules (0.066 microns, @293 K and 101 kPa). The Cunningham correction factor is then used in the calculation of the Stokes numbers by using the following equation.

$$Stk = \frac{\rho_p d_p^2 V_0 C_c}{18\eta d_g} \quad (5.18)$$

Figure 5.38 shows the Stokes numbers as calculated from Equation 18 for the different collector sizes used in the experiments and a gas velocity of 4 cm/s, which is one of the higher used. From these low values of the Stokes number, $Stk \ll 1$, the probability of having inertial deposition is low. Therefore, it can be safely assumed that the single-sphere collection efficiency corresponding to the inertial impaction mechanism is negligible

$$\eta_i(Stk, Re, \varepsilon) \approx 0 \quad (5.19)$$

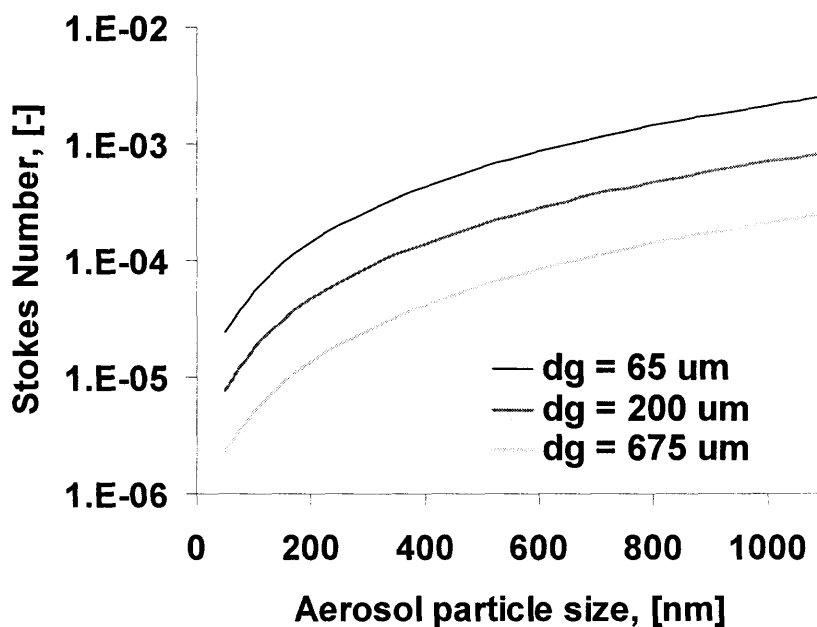


Figure 5.38 Stokes number (Eq. 5.18) as a function of aerosol particle size and collector size (d_g) for the specified experimental conditions.

Another filtration mechanism to consider is interception, although this mechanism has been studied as the residual collection efficiency after subtracting the collection efficiencies from other filtration mechanisms from the single-sphere efficiency. Otani et

al.¹¹⁵ formulated the following empirical equation for the interception efficiency that fitted their experimental data

$$\eta_R = 16R^{2-\text{Re}/(\text{Re}^{1/3}+1)^3} \quad (5.20)$$

Where R is the interception parameter given by

$$R = \frac{d_p}{d_g} \quad (5.21)$$

The collection efficiency corresponding to the interception mechanism, E_R , has been calculated by using the experimental data and Equations 9 and 20. Figure 5.39 shows the calculated values of the collection efficiency due to interception, E_R , as a function of aerosol particle size at 4 cm/s for the different collector sizes. From the figure, better interception collection efficiencies are obtained as the collector size is reduced and for larger aerosol particle's size. A collector size of 65 microns has been used in the fluidized bed filter experiments and collectors with sizes larger than 150 microns have been used in packed beds. Clearly, interception collection efficiency is an important fraction of the total collection efficiency in these experiments.

It is intuitive that given the sizes of the aerosol particles and the gas velocities used in the experiments, the diffusion collection mechanism is the most important in the total collection efficiency of the filter. Brownian motion is very important for small particles and its extent needs to be evaluated; therefore, the Brownian diffusivity of the particle has to be calculated. For this, the mean free path of air is considered ($\lambda = 0.066 \mu\text{m}$, @ 293K, 101 kPa). The Knudsen number gives the ratio of the mean-free path of gas molecules to the particle radius

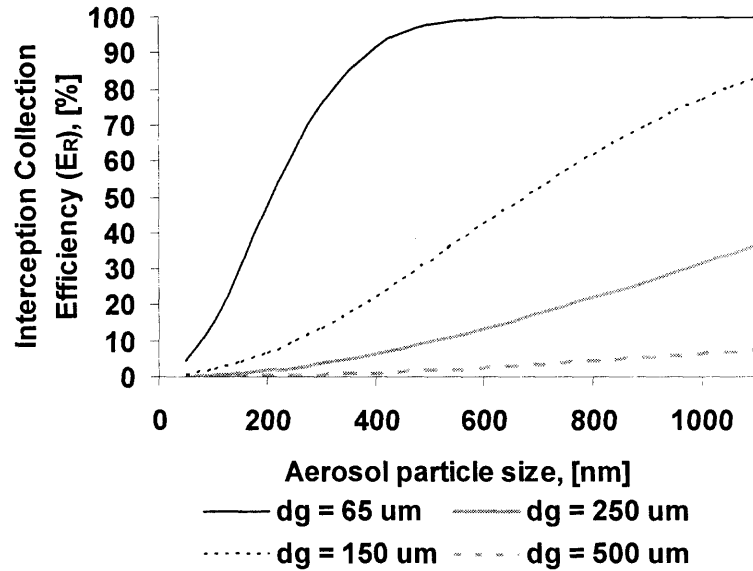


Figure 5.39 Interception based single-sphere collection efficiency corresponding to the specified experimental conditions at 4 cm/s for different collector sizes (d_g) and a packed bed of about 2 inches thick.

$$Kn = \frac{2\lambda}{d_p} \quad (5.22)$$

The Knudsen number is used for the calculation of the Cunningham correction factor given by the following equation

$$C_c = 1 + Kn(1.257 + 0.4 \exp(-1.1/Kn)) \quad (5.23)$$

which is equal to Equation 5.17 but as function of the Knudsen number.

The equation of the Brownian diffusivity of the aerosol particles is calculated by

$$D = \frac{kT}{f} = \frac{kTC_c}{3\pi\mu d_p} \quad (5.24)$$

The Brownian diffusivity is used to calculate the distance that the particle moves due to diffusion. This quantity is represented by the mean-square displacement given by

$$\overline{x^2} = 2Dt \quad (5.25)$$

where t is the time scale in the analysis. The time scale is estimated from the superficial velocity of the fluid and the size of the collector and not the length of the packed bed.

$$t = \frac{d_g}{V} \quad (5.26)$$

The mean-square displacements have been calculated for the experiments by using Equations 5.22 to 5.26; these values are plotted in Figure 5.40. It can be seen that the mean-square displacement increases significantly for aerosol sizes smaller than 400 microns indicating that those particles are very likely to be captured by the diffusion mechanism.

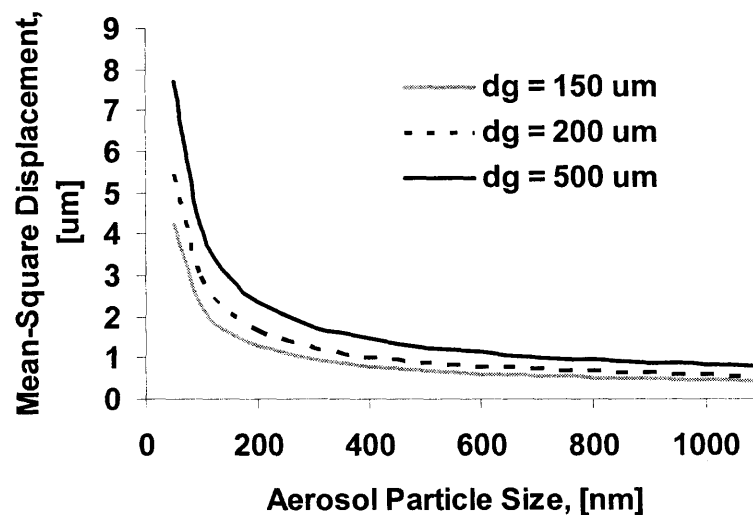


Figure 5.40 Mean-square displacement values corresponding to the aerosol particle sizes used in this study. The gas velocity was 4 cm/s and d_g represents the collector size.

Otani et al.¹¹⁵ estimated the diffusion-collection efficiency by using a correlation dependant on non-dimensional numbers. This correlation has been applied to the experimental conditions. First, the Schmidt (Sc) number was calculated,

$$Sc = \frac{\nu}{D} \quad (5.27)$$

and the Peclet number (Pe) is the product of the Schmidt's and Reynolds numbers.

$$Pe = Sc \cdot Re \quad (5.28)$$

For very low Reynolds numbers such as in these experimental conditions, the following correlation applies:

$$\eta_D = 8Pe^{-2/3} \quad \text{for } Re \rightarrow 0 \quad (5.29)$$

After calculation of the diffusion collection efficiency of a single-sphere, the corresponding value of the total diffusion collection efficiency (E_D) is found by using Equation 5.9. It can be seen that the diffusion collection efficiency is favored by smaller collector and aerosol particle sizes. The collection efficiency due to diffusion mechanism is shown in Figure 5.41.

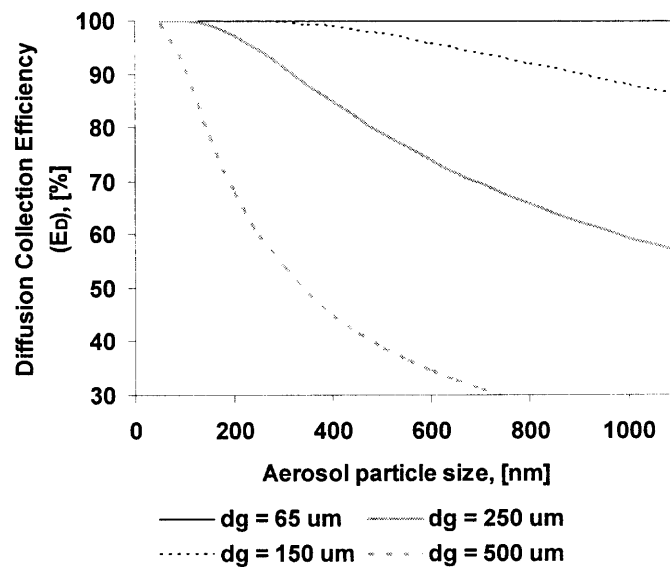


Figure 5.41 Diffusion collection efficiency as calculated by Equations 5.9 and 5.29 for aerosols of different sizes as a function of the collector size (gas velocity of 4 cm/s).

Since the single-sphere collection efficiencies for each of the filtration mechanisms have been found, the total single-sphere collection efficiency can be found with Equation 5.12. Then, Equation 5.9 can be used to calculate the total bed collection

efficiency (E). Figure 5.42 shows the cumulative theoretical total collection efficiency for a 2 inches thick packed bed of spheres having a face velocity of 4 cm/s. Here, the experimental particle size distributions of the PSLS and oil based aerosol have been used for calculation of the cumulative total collection efficiency.

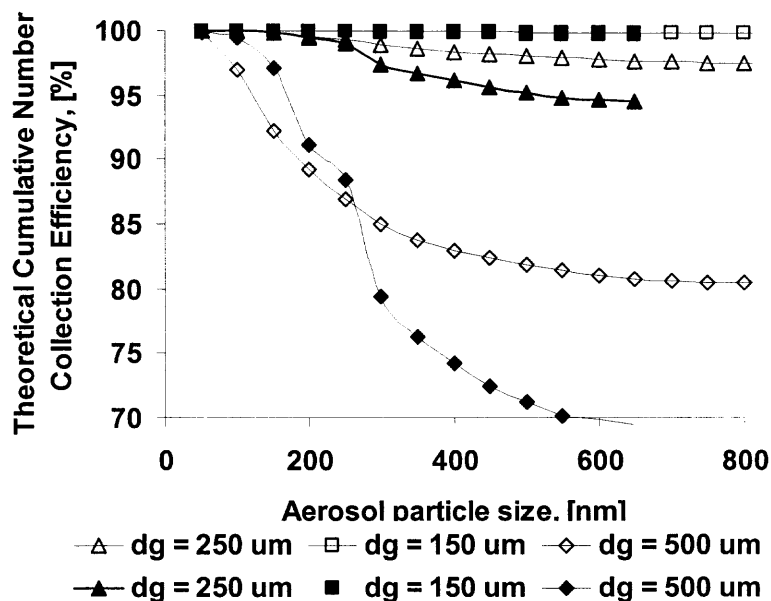


Figure 5.42 Theoretically calculated cumulative collection efficiencies corresponding to the size distributions of the PSLS and oil based aerosols used in these experiments. Gas velocity was about 4 cm/s and the thickness of the filter was 2 inches (background: clear = oil, black = PSLS).

5.5 Conclusions

In the present work, granular and fluidized bed filters made of different materials have been customized to be used for filtration of submicron aerosol particles. Some of the materials are highly porous. These customized filters have been compared against commercially available HEPA fiber based filters in regard to their collection efficiency and filtration capacity. For these purposes, the customized and the HEPA filters were challenged against the same aerosol at the same operating conditions, i.e., superficial gas

velocity. An experimental setup was built for the simultaneous testing of the filters. The setup allowed for the determination of the collection efficiency, pressure drop, and capacity of the filters.

In the preparation of the customized packed bed filters, the size of the granules was optimized according to current available models for the collection efficiency of granular bed filters. Key variables in the design of the granular filters are the collector size and bed thickness. From the experimental results, it was found that the optimal collector size for the packed bed filters was about 150 to 500 microns with a thickness from 1 up to 3 inches. Since submicron particles are to be removed, low superficial velocities favor the collection of the particles by diffusion. Low superficial gas velocities, lower than 4 cm/s, were found to be optimal for the operation of the granular bed filters because they led to higher collection efficiencies and acceptable pressure drops. By adding baffles to the granular bed filters, the volume of the filters was reduced and their collection efficiency increased, but at the expense of higher resistance.

Two different types of aerosol were used for filter testing, oil-based and solid aerosols. Oil-based aerosols were obtained by the atomization of a solution containing ethanol and vegetable oil. Solid aerosols were obtained from a suspension of polystyrene latex spheres (PCLS) in water. The collection efficiency results obtained when challenging HEPA fiber based filters against these aerosols agree with previous works characterizing HEPA filters, which is an indication of the reliability of the present experimental setup. In filtration of solid submicron aerosol particles, it has been shown that a granular bed filter of porous collectors such as carbon black or aerogel granules provide a collection efficiency similar to HEPA fiber based filters. Similar to the

performance of HEPA filters, the collection efficiency of the customized granular filters increases with respect to time as the void spaces are filled with the aerosol particles; however, the resistance of HEPA filters increases at a rate much higher than for granular bed filters. It has also been shown that the customized granular bed filters have a larger filtration capacity than HEPA and their life time is longer than HEPA. This was verified by a plot of the pressure drop as a function of the filtration time. Although the pressure drop of the customized clean bed filters is higher than a clean HEPA filter at the beginning of experiments, the pressure drop of the HEPA filter increased at a much higher rate than the granular bed filters during filtration. At some point, the pressure drop of the HEPA filter surpasses the pressure drop of the granular bed filter.

Regarding the filtration of oil-based submicron aerosols, packed beds of porous materials, such as aerogel granules, give better collection efficiency than HEPA filters. In addition, from a filtration capacity standpoint, granular filters of porous materials such as aerogel granules or carbon black provide larger filtration capacity than HEPA fiber-based filters. For HEPA filters, the oil trapped on the surface of the fibers reduces the collection efficiency because the number of available collectors gets reduced; on the contrary, the captured oil droplets are absorbed into the hydrophobic porous granules, leaving available surface for further aerosol removal. For aerogel granules, in addition to the better collection efficiency, a larger filtration capacity has been found since aerogel granules can absorb more than 7 times their weight of oil.

Small aerogel granules can be fluidized. A fluidized bed filter presents further advantages in regard to the filtration capacity and resistance. It has been shown that a fluidized bed of aerogel granules not only provides higher collection efficiency and larger

capacity than HEPA fiber based filters when challenged against oil-based aerosols but also for solid aerosols. Furthermore, a fluidized bed filter has an extremely low pressure drop compared to a packed bed filter and can be operated continuously.

In summary, it has been shown that porous granular filter media arranged in a packed bed or fluidized bed, when properly designed, offers a collection efficiency equivalent or better than HEPA but with the advantage of a larger filtration capacity.

CHAPTER 6

REMOVAL OF OIL FROM WATER BY INVERSE FLUIDIZATION OF AEROGELS

6.1 Overview

Surface-treated hydrophobic aerogel (Nanogel[®]) particles of sizes between 500 to 850 μm , 1.7 to 2.3 mm and 0.5 to 2.3 mm are fluidized with a downward flow in an inverse fluidization mode. Aerogel particles are extremely hydrophobic with a strong affinity for oil and other hydrocarbons, extremely porous, and have a large surface area; these desirable properties make them an ideal filter media for the removal of oil from wastewater. They also are very light, with a density of about 100 kg/m^3 which makes them suitable for inverse fluidization. Oil concentrations of about 2000 mg/l in water were reduced to less than 10 mg/l during the inverse fluidization process. The oil concentration was correlated to the chemical oxygen demand (COD) which was measured with a HACH[®] colorimeter.

Other advantages of this process are the extremely low energy consumption (low pressure drop) during oil removal by inverse fluidization and the large adsorption capacity when compared against a packed bed filter. Also, the process can be operated continuously because the oil-saturated aerogel particles will fall to the bottom of the bed, and exit the fluidization column and they can be easily removed from the stream of cleaned water by a filter or cyclone.

6.2 Introduction

There are many industrial companies that produce or handle organic compounds, both miscible and immiscible in water. Some of these materials are released accidentally (or on purpose) into the environment. Examples of organic compounds that harm the environment are found in soil and water remediation, removal of waste oils and VOCs formed as byproducts in industrial plants, illegal dumping of waste oils, runoff and ground water; shore oil spills, oil well extraction, among others.

The American Petroleum Institute (API) reports that over 200 million of the 1.3 billion gallons of used oil generated in the U.S. yearly is not collected, but rather dumped into sewers, streams, drains, landfills and backyards:

- 200 million gallons is the equivalent of nearly 20 Exxon Valdez spills each year.
- One gallon of used oil can contaminate up to one million gallons of fresh drinking water.
- One quart of used oil can create a two-acre slick on surface water.
- 40% of the pollution in U.S. waterways is from used motor oil.

Petroleum and petrochemical plants can generate an oil source for polluting inland water caused by runoff from oil fields, refineries and process effluents¹³⁰. Steel manufacturing and metal working are also major sources of oily wastes¹³¹. Municipal wastewater contains up to 36% of oily substances derived from vegetable oils and animal fats¹³².

Current technologies for oil removal include filtration, gravity separation, induced flotation, ultrafiltration, adsorption and biological treatment. An oil and water mixture can be classified as free oil¹³³, for oil droplets larger than 150 μm ; dispersed oil, with oil droplets in the range of 20 to 150 μm , and emulsified oil mixture, water with oil droplets

smaller than $20\ \mu\text{m}$ ¹³⁴. A wastewater, where the oil in the oil-water mixture is not present in the form of droplets, is said to be soluble¹³¹. Figure 6.1 summarizes the classification of oil-water mixtures according to oil droplet size and the corresponding removal methods. Biological treatment of oil-water mixtures is limited only to low concentrations of oil in water since the microorganisms do not stand high oil concentrations and therefore its use is limited to very specific applications.

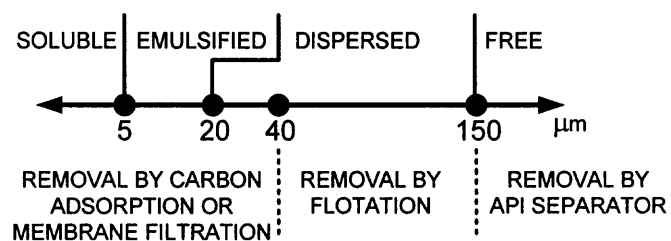


Figure 6.1 Classification of oil-water mixtures according to droplet size and corresponding removal methods.

API separators are used to remove free oil from waste water and they work based on the floating velocity of the oil droplets, and require a sufficiently large residence time for the droplets to coalesce and form an oil layer that can be skimmed off. A maximum of 70% removal of oil can be achieved within 40 minutes after which further removal becomes difficult. Dissolve air flotation (DAF) devices are said to produce an effluent with 1 to 20 mg/l of oil in water, DAF devices are more efficient because the buoyancy is enhanced by the small air bubbles injected¹³⁵. DAF units are very effective in removal of dispersed oil; however, they require the injection of air and addition of pH regulators and coagulants which contribute to the operating costs. DAF units as well as Induced Air Flotation (IAF) units, when properly designed, can achieve an efficiency of 98% and 95% of oil removal, respectively. A good reference on gravity driven separation is given

by Gaaseidnes et al.¹³⁶ Several oil and water separators are explained; among them, gravity driven, gravity coalescing, inverted cone, floating oil-water, and centrifugal separators.

Removal of dissolved and emulsified oils is achieved by using carbon adsorption or membrane filtration¹³⁷. The effluent from these operations contains no oil; however, due to the limited removal capacity of the activated carbon and the very high pressures and high quality feed required by membrane filtration, large capital and operating costs are associated with these devices; hence, they are not commonly used.

Filtration provides good removal, but capacity and energy consumption have to be considered when designing these systems. All filter media have certain permeability which determines the resistance of the media to water flowing through it. The permeability is commonly monitored by the pressure drop across the filter media and generally increases as the filter media gets saturated with the contaminants. As a result, either the amount of water passing through the filter has to be reduced or the pumping power has to be increased leading to a reduction in efficiency from an energy standpoint.

Among examples of the use of filtration for the treatment of oil-water mixture, Cambiella et al.¹³⁸ studied the performance of sawdust as filter media of an oil-water emulsion. They claimed a 99% removal of oil at very small flows (20 ml/h) and with a pressure drop of about 7 psi (50 KPa). They experienced an increase in the resistance of the filter at higher flow rates and due to clogging of the filter media; both of which are common problems in a packed bed filter.

Several types of filter media have been studied for the removal of oil from water by a packed bed filter such as activated carbon and peat¹³⁹, and also bentonite and

organoclay. Mysore et al.¹⁴⁰ studied the efficacy of vermiculite, alumina-silicate resembling mica, as a filter media for oil-in-water emulsions; they found a 30 to 80% removal of oil depending on operating conditions. Filter media based on reed canary grass, flax or hemp fiber were studied by Pasila¹⁴¹ showing that in some cases the media adsorbed 2 to 4 times its weight in oil. Ribeiro et al.¹⁴² studied dried hydrophobic aquatic plants as a filter media showing that *Salvinia* sp. adsorbed 1.33 g of oil/ g of biomass which is much higher than that adsorbed by Peat Sorb (0.26 g of oil/ g Peat Sorb), also used as an oil adsorbent.

A discussion about the use of different commercially available sorbent materials to remove oil from storm waters is presented in an EPA report¹⁴³. This report recalls the work of Stenstrom et al.¹⁴⁴ related to the removal efficiency of oil and grease in a Continuous Deflection Separation (CDS) device using five different sorbents (Nanofiber, OARS[®], Rubberizer[®], Sponge Rok, and Xsorb) and the work of Alsaigh et al.¹⁴⁵ related to the efficiency of four different Best Management Practices (BMPs) that use sorbent materials (Hydrocartridge[®], StreamGuard[®], Gullywasher[®], Grate Inlet Skimmer Box).

The most commonly used material for removal of organic compounds is activated carbon. The main reason for the use of activated carbon in removal of contaminants from water is its highly porous structure that provides large internal surfaces for adsorbed molecules to reside. However, it has been reported that silica aerogels, such as Cabot Nanogel[®], when used in combination with activated carbon during the removal of oil-hydrocarbon-water mixtures, have a much larger adsorption capacity¹⁴⁶. For example, it was reported that silica aerogel adsorbed at least ten times more contaminants by weight than activated carbon. The high oil-adsorption capacity makes aerogels, such as

Nanogel[®], an ideal material for enhancing the removal of organic compounds from water when using activated carbon. An immediate application of Nanogel[®] would be in the removal of immiscible organic compounds such as oils and several hydrocarbons that will readily wet the surfaces of the Nanogel[®] and subsequently be adsorbed into its porous structure. Extensive descriptions of the use of aerogels can be found in government research laboratory websites and reports, such as the Lawrence Berkeley National Laboratory¹⁴⁷ and the Lawrence Livermore National Laboratory¹⁴⁸.

The principles of liquid –solid fluidization have been extensively studied. A key work in the field was presented by Richardson and Zaki³⁹ more than 50 years ago, who found that the superficial velocity divided by the terminal velocity of a single particle is an exponential function of the void fraction in the bed. When the density of the particulate material is less than the density of the fluid, inverse liquid – solid fluidization can be applied to disperse the solid particles in liquids; since aerogels, such as Nanogel[®], have a density lower than water, they can be inversely fluidized. The benefits of inverse fluidization are similar to those found in conventional liquid – solid fluidization: a low and constant pressure drop when operating above the minimum fluidization velocity, optimal mixing between the solid particles and the liquid, good heat and mass transfer rates, and an adjustable voidage of the fluidized bed by changing the fluid velocity. These desirable properties may also result in a large capacity when removing oily compounds from water. On the contrary, filtration carried out using packed beds of granular materials has the following disadvantages: pressure drop increases proportionally to the flow rate, and the bed voidage reduces as the filter saturates with the contaminants. Both of these lead to a lower removal capacity.

Among previous research works with inverse fluidized beds, Fan et al.¹⁴⁹ studied the hydrodynamic characteristics of inverse fluidization in liquid-solid and three phase gas-liquid –solid systems. Low density spherical particles made of polyethylene and polypropylene were used in their experiments and correlations for the bed expansion and the drag force were presented. Nikov et al.¹⁵⁰ used an electrochemical method, based on electromechanical reduction of ferricyanide ions at the surface of a spherical cathode, for liquid-solid mass transfer measurements and proposed an equation which describes the mass transfer in an inverse fluidized bed. Karamanev et al.¹⁵¹ studied bed expansion characteristics of two-phase inverse fluidization using polystyrene and polyethylene spheres of varied sizes and densities. Their experimental data showed good agreement with Richardson and Zaki correlations. Ibrahim et al.¹⁵² studied a three-phase inverse fluidized bed in which the gas and the continuous liquid phase flow counter currently, fluidizing particles lighter than water. Vertical profiles of the gas, liquid and solid holdup were given by static pressure and conductivity measurements. Garcia-Calderon et al.¹⁵³ studied the hydrodynamics of an inverse fluidized bed of ground Perlite[®] particles as support in an anaerobic reactor focusing on the effects of the biofilm thickness on bed expansion and terminal velocity; they also used the Richardson and Zaki equation and drag force models to correlate their experimental data. Other interesting studies of inverse fluidization fundamentals and applications can be found in Bendict et al.¹⁵⁴, Lee et al.¹⁵⁵, Cho et al.¹⁵⁶ and a series of papers by Renganathan et al.^{157, 158, 159, 160}.

In the present work two sizes of sieved Cabot Nanogel[®], hydrophobic granules 500 to 850 μm and 1.7 to 2.3 mm are used to remove oil from water using inverse fluidization since the aerogel granules are lighter than water, Non-sieved Cabot Nanogel[®]

granules having a larger particle size distribution from 0.5 up to 2.3 mm are also used in the experiments. As already discussed above, the main advantages of this system are low pressure drop, high oil removal efficiency, high capacity, and continuous operation.

6.3 Experimental Methods

A schematic diagram of the experimental setup used for inverse fluidization of aerogel granules by water is shown in Figure 6.2. It consists of a fluidization column, valves and piping, flowmeters, a metering pump, static mixer, pressure gauge and a differential pressure transmitter with a display. A summary of an experimental run can be described as follows: the desired size and amount of aerogel granules were selected; next, the granules were loaded in the column; then, the air in the system was purged by filling it with water; this was followed by adjusting the water flow which entered the fluidization column from the top flowing through a distributor, flowing downwards and fluidizing the particles. Experiments' objectives were to study the fluidization hydrodynamics characteristics of aerogel granules and to evaluate the oil removal. The former implies that the fluid velocity was changed in order to find the relationship between the fluidized bed pressure drop and height to the flow velocity, and the later required to run a constant flow of water but with the addition of oil into the system. At the beginning of all the experiments, aerogel granules, which have a bulk density lower than that of water, remain as a packed bed at the top of the column due to buoyancy; after increasing the flow of water, they are fluidized and expand in the downward direction.

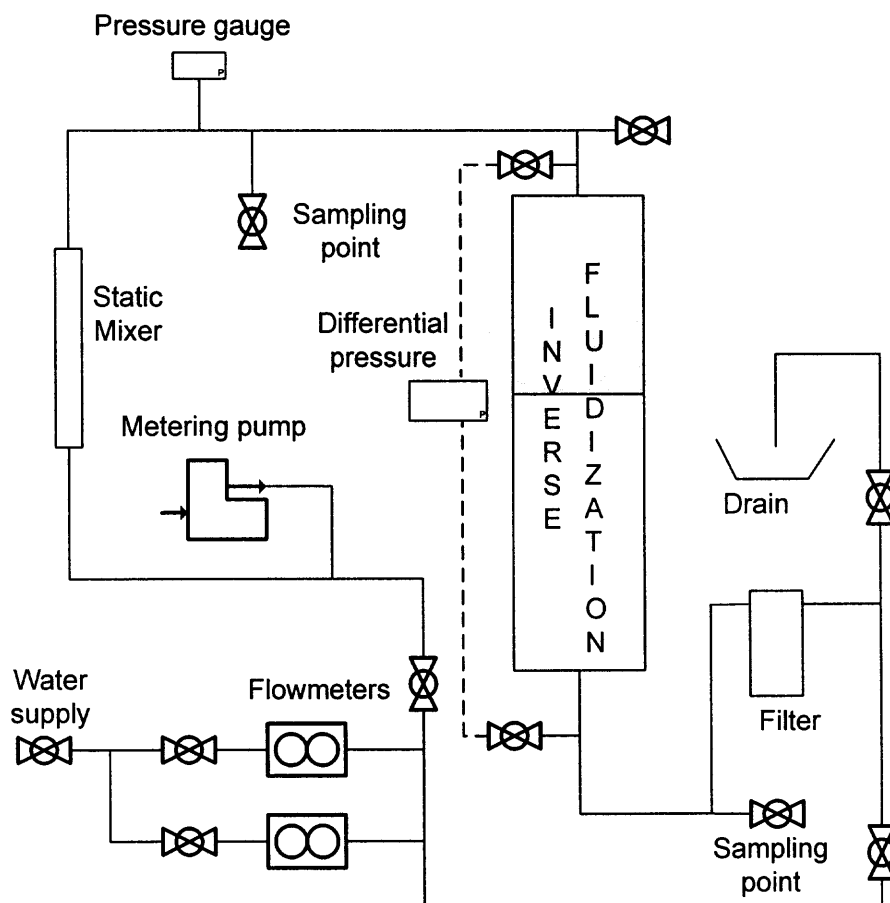


Figure 6.2 Schematic diagram of the inverse fluidization experimental setup.

The fluidization column is made of acrylic plastic with an internal diameter (ID) of 0.089 m (3.5 inches) and an outer diameter (OD) of 0.101 m (4 inches); the total length of the column is 0.86 m. The valves and piping are made of PVC and the pipe size is 1 inch. The flow of tap water is adjusted with ball valves, and flow readings are taken by two calibrated electronic digital flow-meters, one for the range between 0 – 3 GPM and the other for the range between 3 – 50 GPM (GPI series A109).

The water flow is fed at the top of the column through a distributor made up of a packed bed of glass beads supported by a steel wire mesh; it exits from the bottom of the column and passes through a Keystone Sediment Filter (Model 2323N) in order to

remove any entrained aerogel granules before being discarded. The top and bottom caps of the column are used for loading and unloading of the particles. It is important to note that no oil was added when the hydrodynamic behavior of the aerogel granules was studied.

A tap before the fluidization column allowed for the reading of static pressure, which is held constant during the runs; this measurement was taken with a WIKA pressure gauge with a range of 0 – 15 psig (0-103 KPa). There are two additional taps before and after the column for measuring the pressure drop using a differential pressure transmitter (Model 645-1, Dwyer Instruments) with a range of 0 – 2 psid (0-13.8 KPa) and an accuracy of 0.1%; the transmitter is connected to a flow display panel meter (C-93284-02, Cole-Parmer) which is connected to a computer through a RJ11 serial communication port and a converter to an RS-232 port. Data is collected by using Meterview[®] software (C-93284-26, Cole-Parmer) which takes readings every 2 seconds.

To measure the oil removal efficiency and capacity, vegetable oil (soybean oil) from a 1 gallon container was injected into the 1 inch PVC pipe size by a diaphragm pump (Pulsatron Series A Plus, 0 – 6 GPD) and the oil-water mixture passed through a static mixer made up of steel wire packing which is incorporated into the PVC pipe. There are two sampling points, one just after the static mixer and another right after the column, to take samples of the oil-water mixture flowing upstream and downstream of the column, respectively.

The solid phase in these experiments consists of two types of hydrophobic aerogel granules (Nanogel[®] from Cabot Corp.): clear aerogel (TLD) and dark aerogel (OGD). The granule size ranges were selected by sieving to obtain granules within 0.5 to 0.85

mm and 1.7 to 2.3 mm; in some cases, aerogel granules were not sieved and their size range was between 0.5 up to 2.3 mm. The aerogel granules have a highly nanoporous structure with a pore size of about 20 nm, a density of about 100 kg/m^3 and a surface area in the range of 600 to $800 \text{ m}^2/\text{g}$, and they are also extremely hydrophobic due to surface treatment.

The concentration of oil in water is measured by analyzing chemical oxygen demand (COD) in the sample. COD levels of tap water are relatively constant at about 10 mg/l; since oil is the only organic substance added to the water it is safe to assume that any increase in COD levels are due to the addition of oil. COD is measured by using a HACH[®] DR/890 Colorimeter following the procedure indicated in the HACH[®] manual, in particular, Method 8000: Reactor digestion method USEPA approved for COD^{161,162}. Figure 6.3 shows that for these experiments, in which tap water have been used, COD levels are proportional to the concentration of oil, validating the use of COD analysis as a way to monitor concentration of miscible and immiscible oil in water.

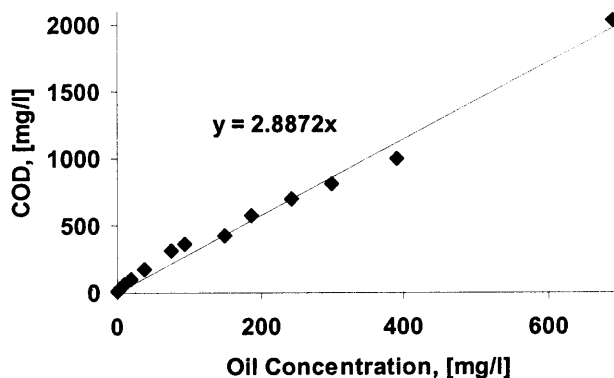


Figure 6.3 Correlation between the oil concentration in water and COD levels measured by HACH DR/890 Colorimeter.

The experimental procedure is as follows. First, the pressure drop across the empty column is measured at different flow rates in order to find a correlation that can be used to determine the pressure drop of the fluidized bed alone; this is done by subtracting the empty column pressure drop from the total fluidized bed pressure drop. The empty column differential pressure is shown in Figure 6.4. Then, the particles to be fluidized are loaded into the fluidization column. Next, the column was filled with water from the bottom and air is completely removed from the system by a vent at a high point. The particles are then inversely fluidized by sending flow from the top (downwards) and the hydrodynamic parameters, bed height and pressure drop, are measured by increasing the flow of water gradually. The increase in the flow of water was stopped when the bed height approached the entire length of the column or if too much entrainment occurred. It is important to note that the static pressure before the column is kept constant to ensure proper readings.

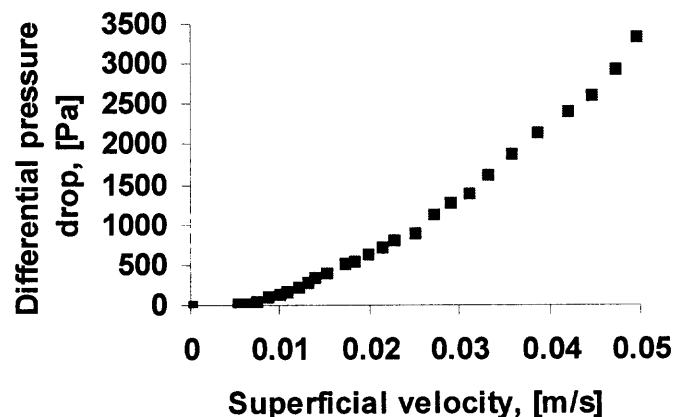


Figure 6.4 Pressure drop across the empty column.

In the experiments for finding the oil removal efficiency and capacity, a constant water superficial velocity above the minimum fluidization velocity is maintained through the column. Injection of oil, upstream the column, is done by starting the metering pump and adjusting its stroke displacement and frequency. Samples of water of about 500 ml, upstream and downstream of the inverse fluidized bed, are taken at regular intervals for COD analysis by the HACH® Colorimeter. Samplings of water as well as the measurement of hydrodynamic parameters are stopped when the bed height approached the entire length of the column or when oil droplets appeared downstream of the fluidized bed. Water samples were mixed thoroughly by using a Hamilton Beach (Model 50256MW) blender to disperse the oil droplets homogeneously. An aliquot (2 ml for 0 – 1500 mg/l COD and 0.2 ml for 0-15000 mg/l COD) from the homogenized sample is taken and inserted into the COD digestion vial which is kept in the digestion reactor (DRB-200, Hach Co.) at 150 °C for 2 hours. Once the digestion was complete, the vial was allowed to cool down and then tested for COD content by the Colorimeter¹⁶².

6.4 Results and Discussion

6.4.1 Hydrodynamics of Inverse Fluidized Beds of Aerogel Granules

The hydrodynamic characteristics of inverse fluidized beds of aerogel granules are represented by the fluidized bed pressure drop and the bed expansion. Plots of these variables against the superficial fluid velocity are used to find the minimum fluidization velocity of the granules (U_{mf}) as shown in Figure 6.5 and Figure 6.6. The minimum fluidization velocity is dependant on the granule size; for example, Figure 6.5 shows that the minimum fluidization velocity for small granules is about 0.007 m/s, and Figure 6.6a

shows that the U_{mf} for large granules (1.7 to 2.3 mm in diameter) is about 0.02 m/s. A mixture of small and large granules, as shown in Figure 6.6b, results in an intermediate minimum fluidization velocity of 0.013 m/s. Besides showing the U_{mf} values, these figures also show that the plateau pressure drop increases proportionally with the amount of powder being fluidized, and that the maximum pressure drop across the fluidized bed of granules remains constant at fluid velocities larger than U_{mf} . The experimentally measured values of U_{mf} will be compared to predicted values using correlations found in the literature.

The fluidized bed heights corresponding to Figure 6.5 and Figure 6.6 are shown in Figure 6.7 and Figure 6.8 respectively. Bed height data will be used to determine the theoretical granule size by using the Richardson-Zaki³⁹ model and to compare it to the measured granule size. Data related to the U_{mf} and the estimation of the particle size from bed height data are of significance since, according to a review of available literature, there are no previous research papers reporting on the fluidization of these specific aerogel granules.

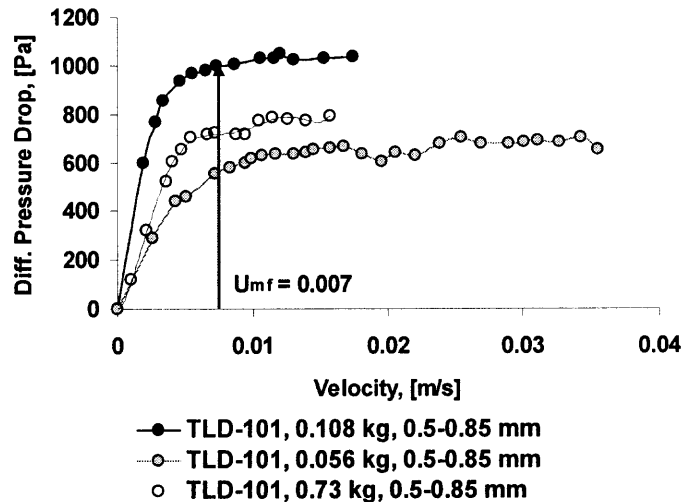


Figure 6.5 Inverse fluidized bed pressure drop vs. superficial fluid velocity of small aerogel granules.

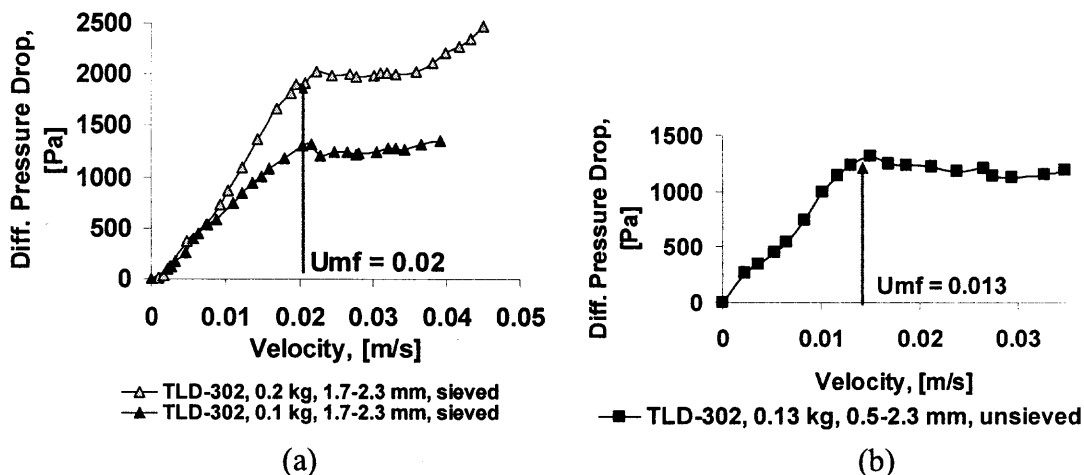


Figure 6.6 Plots showing the inverse fluidized bed pressure drop vs. superficial fluid velocity of large aerogel particles.

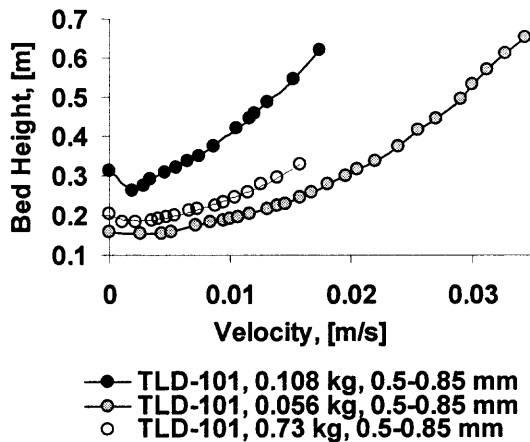


Figure 6.7 Bed height vs. superficial fluid velocity corresponding to the data on Figure 6.5.

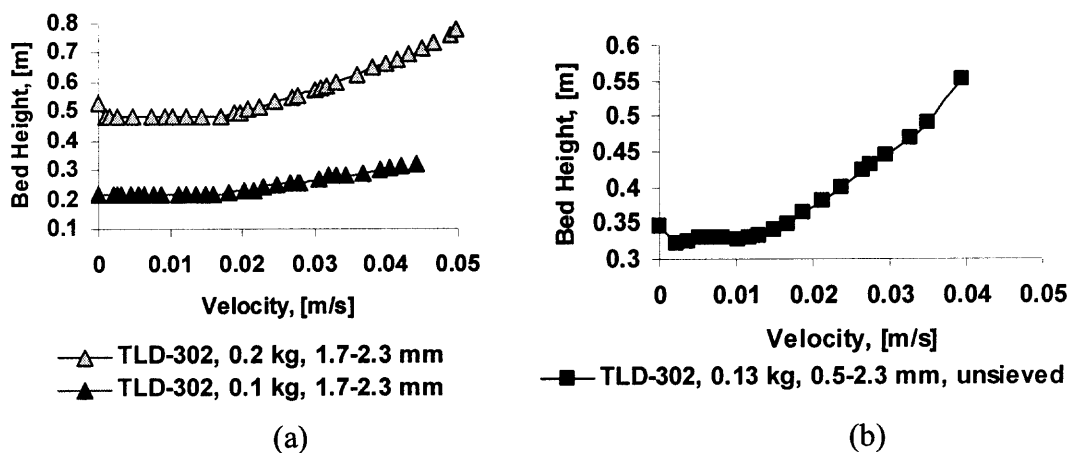


Figure 6.8 Bed height vs. superficial fluid velocity corresponding to data on Figure 6.6.

6.4.1.1 Finding the Density of the Granules (ρ_p) and the Internal Porosity (ε_p)

from Experimental Data. The density of the granules is important to determine the void fraction of the fluidized bed and other hydrodynamic properties. Its value can be calculated from the experimental data by using a force balance, i.e., fluidized aerogel granules in equilibrium are acted on by buoyancy, gravity and drag forces. The buoyancy force is given by

$$F_B = \rho_l V_p g \quad (6.1)$$

while the gravity force can be expressed as

$$F_g = \rho_p V_p g \quad (6.2)$$

and the drag force is represented by

$$F_D = \frac{1}{2} C_D \rho_l U_{mf}^2 \left(\frac{\pi}{4} \right) d_p^2 \quad (6.3)$$

A force balance on the particles gives

$$F_B = F_g + F_D \quad (6.4)$$

The drag force applied on the particles during fluidization is represented by the experimental pressure drop divided by the cross sectional area of the fluidization column.

$$F_D = \Delta P_{\text{exp}} A \quad (6.5)$$

Substituting Equations 6.1, 6.2 and 6.5 into Equation 6.4 gives

$$F_B = F_g + F_D = \rho_p V_p g + \Delta P_{\text{exp}} A = \rho_l V_p g \quad (6.6)$$

After simplification and rearrangement of the terms,

$$\Delta P_{\text{exp}} A = \rho_l V_p g - \rho_p V_p g \quad (6.7)$$

and based on the definition of the density of the granules

$$m_p = \rho_p V_p \quad (6.8)$$

Note that at this point the density of the granules is not known.

Equation 6.7 becomes

$$\Delta P_{\text{exp}} A = \rho_l V_p g - m_p g \quad (6.9)$$

Using Equation 6.9, the volume of the particles is given by

$$V_p = \frac{(\Delta P_{\text{exp}} A + m_p g)}{\rho_l g} \quad (6.10)$$

It is important to note that V_p is independent of the bed height.

The initial bulk density of the bed is given by

$$\rho_{b0} = \frac{m_p}{V_{b0}} = \frac{m_p}{AH_0} \quad (6.11)$$

The void volume can be found by subtracting the volume of the particles (V_p) from the total volume of the fluidized bed (V_b)

$$V_\varepsilon = V_b - V_p \quad (6.12)$$

hence, the void fraction of the fluidized bed is given by

$$\varepsilon = \frac{V_\varepsilon}{V_b} = \frac{V_b - V_p}{V_b} = 1 - \frac{V_p}{V_b} = 1 - \frac{m_p}{\rho_p V_b} = 1 - \frac{m_p}{\rho_p AH} \quad (6.13)$$

the solid fraction is given by

$$\phi = 1 - \varepsilon = \frac{V_p}{V_b} \quad (6.14)$$

and the density of the particles is given by Equation 6.8. Finally, the internal porosity of the particles can be found by

$$\varepsilon_p = 1 - \frac{\rho_p}{\rho_s} \quad (6.15)$$

The aerogel granule density is needed to calculate the void fraction of the fluidized bed, which is used in correlations such as the Richardson-Zaki equation to estimate the granule size and terminal velocity. The aerogel granule densities are estimated using the equations abovementioned, and are listed in Table 6.1. Equation 6.10 is of particular significance since it can be used to calculate the particle density if reliable measurements of pressure drop are available, or it can be used to calculate the pressure drop across the fluidized bed if data on the particle density are available. This equation is also useful in scale-up of the process since it predicts the pressure drop across the fluidized bed.

Table 6.1 Calculation of the Granule Density and the Initial Void Fraction from Experimental Data

Granule Size/Type mm/type	Mass kg	ΔP Pa	Particles Volume m ³	ρ_p (estim.) kg/m ³	Initial Bed Height m	Bulk Density kg/m ³	Void Fraction ε_0
0.5 - 0.85 TLD 101	0.106	1185.9	8.7E-04	121	0.264	65	0.47
	0.05267	579.2	4.3E-04	123	0.143	60	0.52
	0.068	730.8	5.4E-04	126	0.183	60	0.52
1.7 - 2.3 TLD 302	0.197	2240.8	1.6E-03	119	0.484	66	0.45
	0.1	1103.2	8.2E-04	123	0.216	75	0.39
	0.13	1516.8	1.1E-03	117	0.306	68	0.41
0.5 - 2.3 TLD 302	0.1325	1482.4	1.09E-03	121	0.317	67	0.45

6.4.1.2 Finding the Richardson-Zaki Exponent (n), the Terminal Velocity (U_t) and Estimating the Granules' Size (d_p). The Richardson–Zaki correlation³⁹ is among the most useful methods to estimate the terminal velocity and the size of the fluidizing particles/granules. The R-Z equation is

$$\varepsilon^n = \frac{U}{U_i} \quad (6.16)$$

where U is the superficial velocity and U_i is the settling velocity at infinite dilution. The Richardson-Zaki exponent or index (n) is a function of the particle terminal Reynolds number (Re_t) and the particle to column diameter ratio as given below,

$$n = \left(4.4 + 18 \frac{d_p}{D} \right) Re_t^{-0.1} \quad \text{for } 1 < Re_t < 200 \quad (6.17)$$

$$n = 4.4 Re_t^{-0.1} \quad \text{for } 200 < Re_t < 500 \quad (6.18)$$

$$n = 2.4 \quad \text{for } Re_t > 500 \quad (6.19)$$

where Equation 6.17 is specifically applicable for the smaller aerogel particles (0.5 – 0.85 μm) and Equation 6.18 is applicable for the larger aerogel granules (1.7 – 2.3 mm). In these equations the Reynolds number at terminal velocity is defined as

$$Re_t = \frac{U_t \rho_l d_p}{\mu_l} \quad (6.20)$$

The Richardson-Zaki exponent (n) can also be obtained through experimental data by plotting the logarithm of the superficial velocity against the logarithm of the void fraction

$$\ln(U) = n \ln(\varepsilon) + \ln(U_i) \quad (6.21)$$

where the slope of a linear regression of the data gives the Richardson-Zaki exponent (n) and the y-intercept gives the settling velocity at infinite dilution (U_i).

After calculating the void fraction (ε) from Equation 6.13, the experimental data are plotted in Figure 6.9 which shows the relationship between the logarithm of the superficial velocity (U) and the logarithm of the void fraction (ε). From these plots, the values corresponding to the Richardson-Zaki exponent (n) and the settling velocity (U_i) are obtained. The settling velocity (U_i) and the terminal velocity are related as suggested by Richardson-Zaki³⁹,

$$\log U_i = \log U_t - \frac{d_p}{D} \quad (6.22)$$

where the terminal velocity is given by the following equation according to Sakiadis¹⁶³,

$$U_t = \sqrt{\frac{4(\rho_l - \rho_p)gd_p}{3\rho_l C_d}} \quad (6.23)$$

where C_d is the drag coefficient which is a function of the particle Reynolds number,

$$\text{Re}_p = \frac{U \rho_l d_p}{\mu_l} \quad (6.24)$$

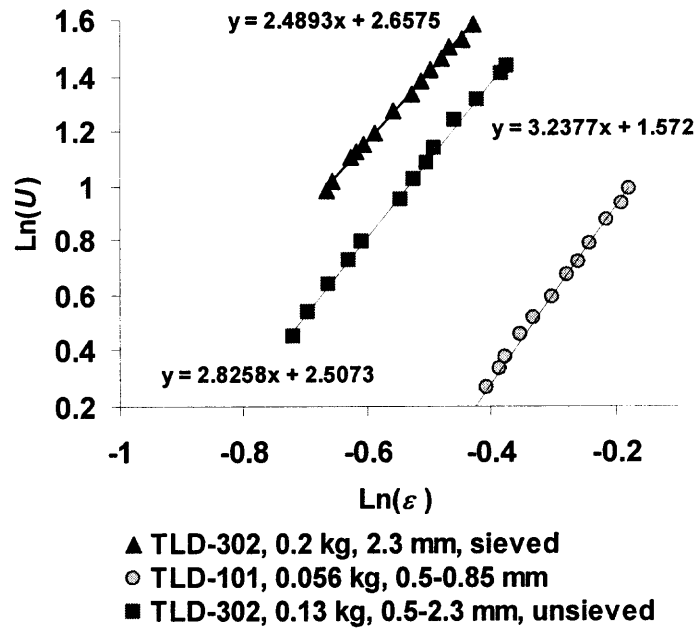


Figure 6.9 Relationship between the superficial velocity and the void fraction of inverse fluidized beds of aerogel granules accordingly to the Richardson-Zaki criterion.

For spherical particles

$$C_d = 24 / Re_p \quad \text{for } Re_p < 0.1 \quad (6.25)$$

$$C_d = (24 / Re_p)(1 + 0.14 Re_p^{0.70}) \quad \text{for } Re_p < 1000 \quad (6.26)$$

$$C_d = 0.445 \quad \text{For } 1000 < Re_p < 350000 \quad (6.27)$$

$$C_d = 0.19 - [(8)(10^4) / Re_p] \quad \text{For } Re_p > 10^6 \quad (6.28)$$

Only Equations 6.25 and 6.26 are applicable to the collected data since Re_p values in the experiments are less than 1000. Based on these experimental data and the equations above, the Richardson – Zaki exponent (n), the terminal velocity (U_t) and the mean particle diameter were calculated for the different experimental runs as shown in Table 6.2.

Table 6.2 Richardson-Zaki Bed Expansion Parameters and Calculation of the Particle Size from Experimental Data

Granule Size/Type mm/type	d_{p0} m	Re_p	C_d (Eq. 6.26)	R-Z "n"	R-Z "ln(U _i)"	U_t (Eq. 6.22) m/s	d_p (Eq. 6.23) mm
0.5 - 0.85	8.5E-04	9.9	3.53	3.20	1.6	0.0487	0.727
1.7 - 2.3	2.3E-03	95.3	1.11	2.49	2.7	0.1514	2.221
0.5 - 2.3	2.3E-03	63.9	1.17	2.83	2.5	0.1303	1.724

6.4.2 Relationship between the Drag Force Function and the Bed Void Fraction

According to Fan et al.¹⁴⁹, correlations to predict bed expansion in an inverse fluidized bed can be developed by expressing a drag force function f , defined as the ratio of the drag force of fluid on particles in a multiparticle system to that in a single particle system,

as a function of the Archimedes number $Ar = \frac{d_p^3 (\rho_l - \rho_p) \rho_l g}{\mu_l^2}$ and the Reynolds number

$Re_p = \frac{U \rho_l d_p}{\mu_l}$. In experiments involving aerogel granules, the Reynolds numbers are within the range $2 < Re < 500$; therefore, the following drag force function, from Fan et al.¹⁴⁹, is used

$$f = \frac{Ar}{13.9 Re^{1.4}} \quad (6.29)$$

In each experimental run, the bed pressure drop and bed expansion were measured as the fluid velocity is increased so that the void fraction, ε , in the fluidized bed could be calculated from the bed expansion at each different fluid velocity. Similarly, the Archimedes and Reynolds numbers and the drag force function f were calculated at each different fluid velocity. Next, the drag force function was plotted against the void fraction as shown in Figure 6.10 for the different sized aerogel granules. Straight lines are obtained for all three granule sizes, the average slope of -4.18 closely agrees with the value of -4.05 suggested by Fan et al¹⁴⁹.

$$f = 3.21 \varepsilon^{-4.05} Ar^{-0.07} \exp\left(3.5 \frac{d_p}{D}\right) \quad (6.30)$$

The range of applicability of Fan's equation is $\varepsilon = 0.4$ to 0.88 , $d_p/D = 0.062$ to 0.250 and $110000 < Ar < 7650000$. The fact that the results agree with Fan's equation indicate that the range of applicability of Equation 6.30 can be extended for particles with Archimedes numbers less than 100000, such as aerogel granules.

Table 6.3 Slopes and Intercepts Corresponding to the Plot of the Drag Force vs. Void Fraction

Granule Size/Type mm/type	d_{p0} mm	Ar	"y" $f = f(\epsilon^{-y})$	$\log(f_0)$
0.5 - 0.85	0.7	2930	-4.18	0.21
1.7 - 2.3	2.3	103329	-4.14	0.19
0.5 - 2.3	1.6	34985	-4.23	0.23

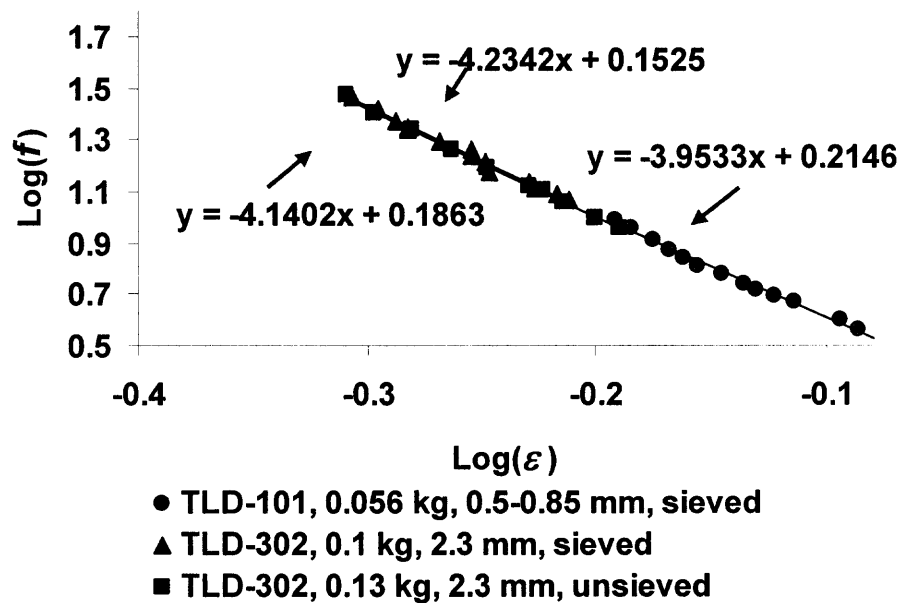


Figure 6.10 Plot showing the relationship between the drag force function “ f ” and the void fraction “ ϵ ”.

6.4.3 Calculation of the Minimum Fluidization Velocity

It is important to compare the experimental minimum fluidization velocity values against values calculated from equations available in the literature. A classical well-known correlation based on the Ergun equation for predicting U_{mf} , in a conventional fluidized bed was introduced by Wen and Yu¹⁶⁴.

$$Re_{mf} = \sqrt{(33.7)^2 + 0.0408Ar} - 33.7 \quad (6.31)$$

This equation should be applicable to inverse fluidization as well, assuming that the drag force of the fluid moving with superficial velocity (U_{mf}) is equal to the buoyancy force less the weight of the particles as has been demonstrated in previous works¹⁵¹. In Table 6.4, the experimentally measured values of U_{mf} are compared against the theoretical values of U_{mf} calculated from Equation 6.31. This equation correctly estimates the minimum fluidization velocity of the large aerogel granules but not the small ones; this could be due to the fact that the Archimedes number for small granules is almost two orders of magnitude lower than that of the large granules.

Table 6.4 Comparison of the Experimental and Theoretical Minimum Fluidization Velocities

Granule Size/Type mm/type	Umf (exp.) m/s	d _p mm	Ar	Re _{mf}	Umf (Eq. 6.32) m/s	Error %
0.5 - 0.85	0.00588	0.7	3341	2.0	0.0027	53
1.7 - 2.3	0.01841	2.3	103290	39	0.017	6
0.5 - 2.3	0.01316	1.8	50039	23	0.01265	3.9

6.4.4 Removal of Oil from Water by Using an Inverse Fluidized Bed of Aerogel Granules

As explained in the experimental methods section, after inversely fluidizing aerogel granules at a certain flow velocity, oil was added to the water to study the oil removal efficiency and the changes in the fluidization characteristics during the adsorption of oil by the aerogel granules. Among the fluidization characteristics monitored during the removal of oil from water are the pressure drop and the bed height. The concentration of oil was monitored also by analyzing the chemical oxygen demand (COD) at several time intervals during the experiments. The operating conditions and measured variables for each of the experiments are listed in Table 6.5. Among the variables that were changed to compare the oil removal efficiency are the fluid superficial velocity, particle size, particle type, amount of particles, initial bed height and concentration of oil upstream the fluidized bed. The variables that were monitored during the oil removal are the bed height and COD levels as measured by the HACH[®] Colorimeter with respect to time. Also, in order to evaluate the oil removal efficiency and capacity of the inverse fluidized bed, the following criterion was adopted: oil removal by an inverse fluidized bed was acceptable only if the COD levels remained below 100 mg/l or 100 ppm. The fluidized bed height and the time, at which the 100 mg/l COD level are reached, are recorded and shown in Table 6.5. This table shows the calculated (not measured) upstream oil concentrations based on the adjustments of the oil pump and the flow of water. The measured COD levels of the oil-water mixture before the fluidized bed are also shown. COD levels before the fluidized bed are measured by analyzing water samples with the Colorimeter. Although the COD concentration is given in mg/l, it is not numerically identical to the concentration of oil in water but proportional. The amount of oil removed

is calculated by multiplying the upstream oil concentration by the water flow rate and the elapsed time to reach a COD level of 100 mg/l downstream the fluidized bed; it has been assumed that this downstream oil concentration (100 mg/l) is negligible compared to the oil concentration upstream. The removal capacity is found by dividing the oil removed by the weight of aerogel granules used in the experiment. It can be seen that in some of the experiments the aerogel granules removed up to 7 times their weight in oil.

Table 6.5 Summary of Results Corresponding to the Oil Removal from Water by Inverse Fluidized Bed of Nanogel[®]

Figure (#)	Fluid Velocity (m/s)	U/Umf Ratio	Particle Type	Particle size (mm)	Mass of Particles (kg)	Upstream Oil Conc. (g of oil/ kg H ₂ O)	COD Entrance (mg/l)	Initial Fluid. Bed Height (m)	Max. Bed Height (m)	Time @ COD =100 (s)	Removal Capacity (kg oil/ kg)
6.12	0.0305	1.5	TLD 302	1.7-2.3	0.054	0.26	490	0.16	0.28	3660	3.3
6.13	0.0305	1.5	OGD 303	1.7-2.3	0.049	0.39	1000	0.14	0.23	2340	3.5
6.14	0.030	4.4	OGD 303	.5-.85	0.056	0.26	490	0.39	0.44	2200	1.9
6.16a	0.030	4.4	OGD 303	.5-.85	0.056	0.18	400	0.39	0.50	3060	1.8
6.16b	0.030	4.4	OGD 303	.5-.85	0.1	0.18	400	0.69	0.78	2820	0.9
6.18a	0.024	3.5	OGD 303	.5-.85	0.056	0.36	900	0.32	0.33	5520	5.3
6.18b	0.024	3.5	TLD 101	.5-.85	0.056	0.36	900	0.34	0.34	4500	4.3
6.19a	0.011	1.5	TLD 101	.5-.85	0.056	0.45	1700	0.14	0.23	13620	7.1
6.19b	0.018	2.6	TLD 101	.5-.85	0.056	0.48	1800	0.22	0.22	6840	6.5
6.21	0.010	1.5	TLD 101	.5-.85	0.108	0.47	1750	0.43	0.44	15360	4.1

A first set of experiments shows a comparison between large (1.7 – 2.3 mm) translucent TLD 302 (Figure 6.11) and large dark OGD 303 (Figure 6.12) granules. According to the calculated oil removal capacity given in Table 6.5, it can be seen that OGD 303 has a slightly larger capacity than TLD302. A run with smaller (0.5 – 0.85 mm) OGD 303 granules, shown in Figure 6.13, indicates that the fluidized bed of smaller

granules has smaller oil removal efficiency. It is important to note that the criterion established for the oil removal considers collection efficiency rather than capacity. When fluidizing small granules, because the fluid velocity is several times larger than the minimum fluidization velocity ($U/U_{mf} = 4.4$), the void fraction is larger and the bed is more expanded; therefore, oil droplets can pass through easier. Even though a COD level of 100 mg/l has been reached downstream of the fluidized bed, this does not mean that the aerogel granules have been fully saturated with oil.

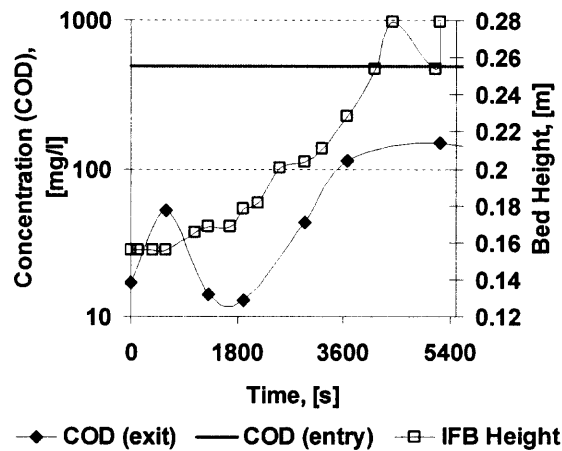


Figure 6.11 Chemical oxygen demand (COD) and inverse fluidized bed expansion (squares) as a function of time of 54 grams of aerogel granules (TLD 302) with sizes between 1.7 to 2.3 mm during removal of oil from water (0.26 g of oil/kg of water and fluid velocity of 0.0305 m/s).

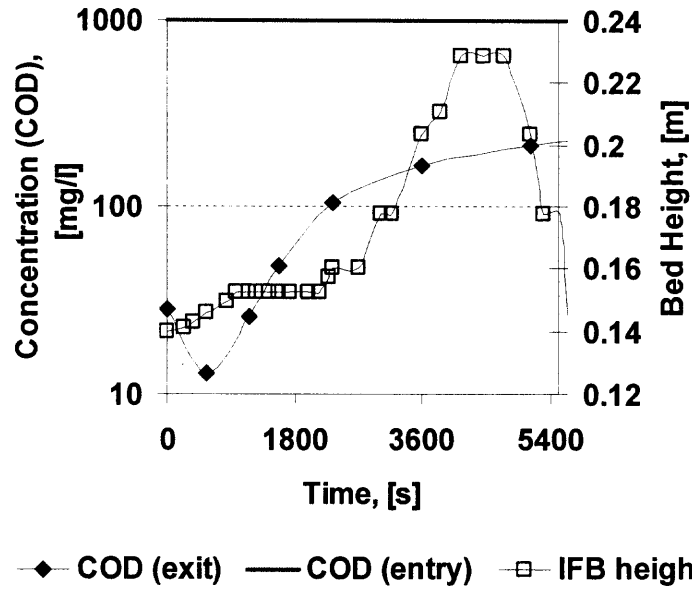


Figure 6.12 Chemical oxygen demand (COD) and inverse fluidized bed expansion (squares) as a function of time of 49 grams of aerogel granules (OGD 303) with sizes between 1.7 to 2.3 mm during removal of oil from water (0.39 g of oil/kg of water and fluid velocity of 0.0305 m/s).

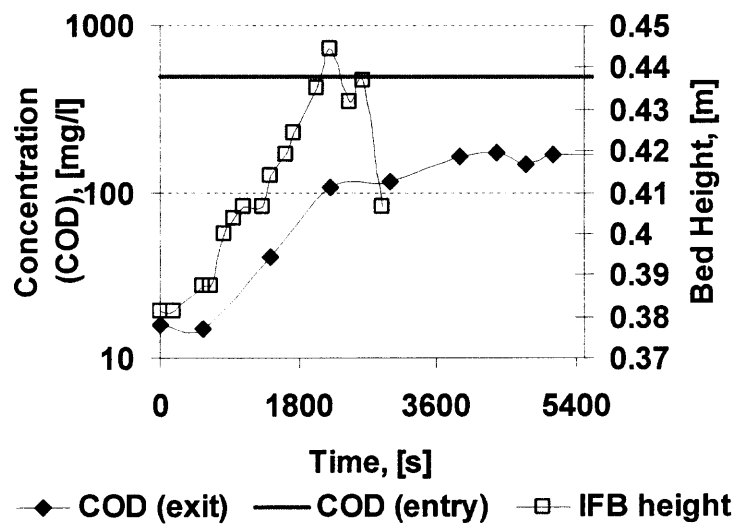


Figure 6.13 Chemical oxygen demand (COD) and inverse fluidized bed expansion (squares) as a function of time of 56 grams of aerogel granules (OGD 303) with sizes between 0.5 to 0.85 mm during removal of oil from water (0.26 g of oil/kg of water and fluid velocity of 0.0305 m/s).

The fluidized bed expansion provides clues about the way the oil droplets are captured and the saturation of the aerogel granules. It is well known that minimum fluidization velocity is proportional to the particle size when comparing similar materials; this also means that at similar fluid velocities, a bed of small granules will have a higher void fraction (larger expansion) than a bed of large granules. A high void fraction in a fluidized bed increases the dynamics in the fluidized bed, i.e., the degree of mixing. If there is a high degree of mixing in the fluidized bed then the concentration of the oil contaminant in the suspension phase can be assumed to be uniform, as in a continuously stirred tank reactor (CSTR). However, if the degree of mixing is poor, the fluidized bed behaves more like a packed bed and the flow through it is similar to a plug flow reactor (PFR).

The degree of mixing in a particulate fluidized bed can be related to the ratio of the actual fluid velocity to the minimum fluidization velocity (U/U_{mf}). A CSTR-like mixing will occur at high U/U_{mf} ratios and a PFR-like mixing will occur at low U/U_{mf} ratios. During oil removal, a CSTR-like mixing leads to a more homogenous saturation of the granules which translates into bed expansion due to the simultaneous reduction in the buoyancy of most of the granules, whereas a PFR-like flow leads to saturation of the granules at the top of the column, and these granules become entrained by the flow due to their more reduced buoyancy than granules in the rest of the bed resulting in a decrease in bed height.

Figure 6.14a shows the differential pressure drop of the inverse fluidized beds corresponding to the three experiments described above. The pressure drop initially increases as oil is added to the water because of the fluidization of small oil droplets; the

flow of water has to overcome their buoyancy force. After a short time, the pressure drop reaches a maximum when equilibrium between the oil added into the fluidization column and the oil adsorbed by the granules is established. At this point of time a decrease in pressure drop occurs because the aerogel granules, as they adsorb oil, become heavier reducing their buoyancy and the drag force needed to fluidize them. The pressure drop would remain constant if oil were not adsorbed by the particles, as shown in Figure 6.14b, because of the formation of an oil layer at the top of the column. The loss of oil-saturated granules entrained from the fluidization column reduces the pressure drop even further. After saturation of the granules occurs, the pressure drop remains constant (see Figure 6.14a), because the oil-saturated granules begin to agglomerate forming a packed bed of agglomerates. The pressure drop across the fluidized bed of granules during oil removal can be used to calculate the oil-removal capacity but not the collection efficiency.

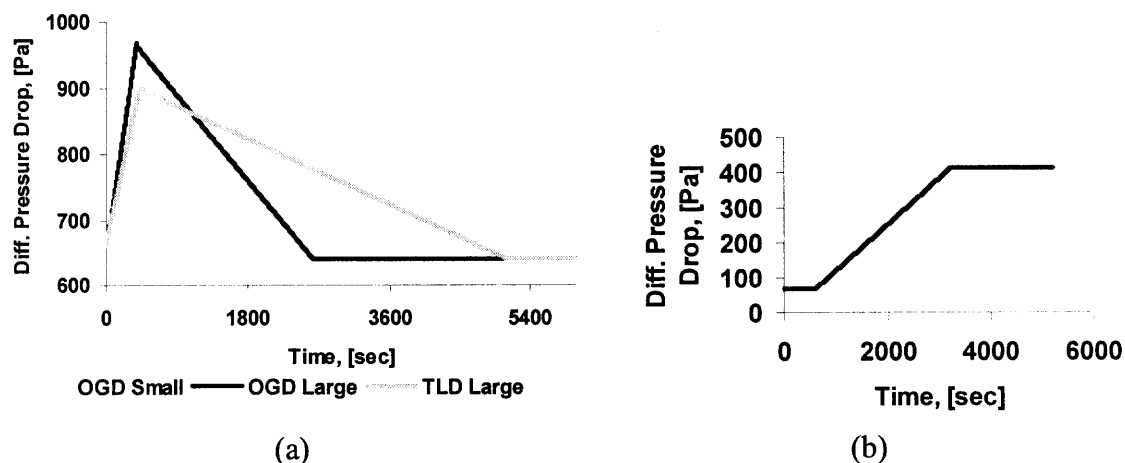


Figure 6.14 (a) Pressure drop across the inversely fluidized beds of aerogel during the removal of oil corresponding to Figures 6.12 to 6.14. Superficial flow velocity was kept constant at 0.0305 m/s. (b) Pressure drop across the column without particles during oil injection.

Another set of experiments was performed to find the effect of using different amounts of fluidized granules on the oil removal efficiency; for these experiments the U/U_{mf} ratio was kept at 4.4. Adding different amounts of granules to the column will result in different initial fluidized bed heights. The residence time of oil droplets in tall fluidized beds (large amount of granules) is larger when compared to short fluidized beds; therefore, in short fluidized beds the oil and granules will be more homogeneously mixed like in a CSTR; whereas, granules at the top will be more saturated than the rest in tall fluidized beds. Figure 6.15a shows the COD levels and the bed expansion of 56 grams of small aerogel granules, it can be seen that there is a significant bed expansion from 40 to 50 cm, indicating a CSTR-type of mixing where most of the granules saturate simultaneously. Figure 6.15b shows COD levels and bed expansion for 100 grams of small aerogel granules exposed to the same concentration of oil and operating conditions as in the experiment using 56 grams described by Figure 6.15a. It can be seen in the figure that the bed height increases slightly at the beginning of the experiment, but then drops off because of the loss of saturated granules during the adsorption of oil. As expected, the fluidized bed with the smaller amount of granules gets saturated faster as seen by the more rapid changes in bed height with time. Note that even though different amounts of aerogel are used, the COD levels at the exit of both fluidized beds are fairly similar; this indicates that the removal efficiency is independent of the length of the bed at relatively high U/U_{mf} ratios ($U/U_{mf} = 4.4$).

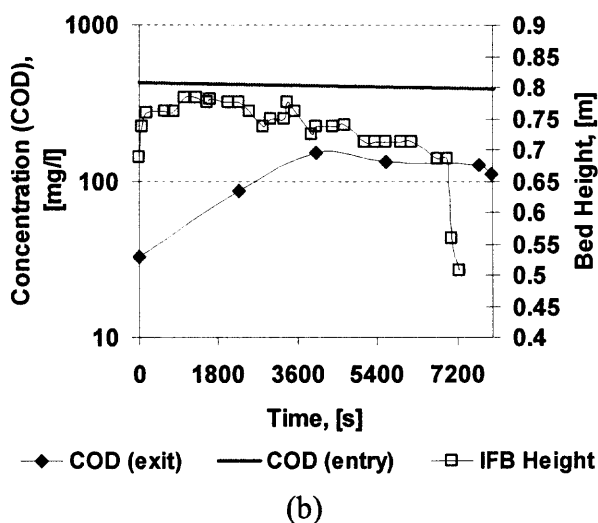
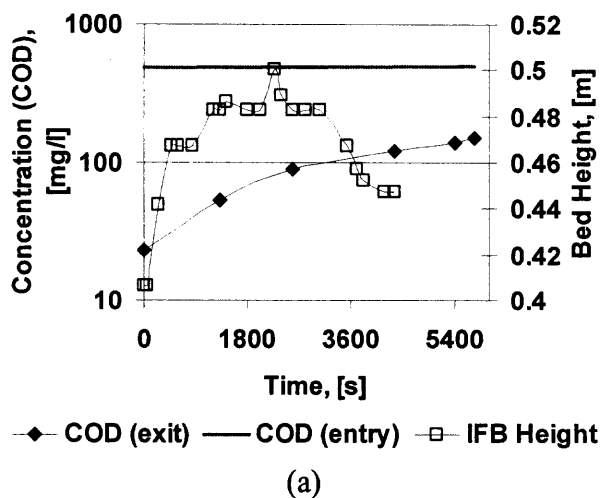


Figure 6.15 Chemical oxygen demand (COD) and inverse fluidized bed expansion (squares) as a function of time of aerogel granules (OGD 303) with sizes between 0.5 to 0.85 mm during removal of oil from water, upstream oil concentration is 0.18 g of oil/kg of water and the fluid velocity is 0.0305 m/s. (a) 56 grams, (b) 100 grams.

Figure 6.16 shows the differential pressure drop across the inverse fluidized beds described by Figure 6.15 during oil removal; as expected, Figure 6.16 shows that the pressure drop is proportional to the amount of fluidized powder in the bed. In both cases, the pressure drop across the bed of granules does not plateau, indicating that the granules did not fully saturate.

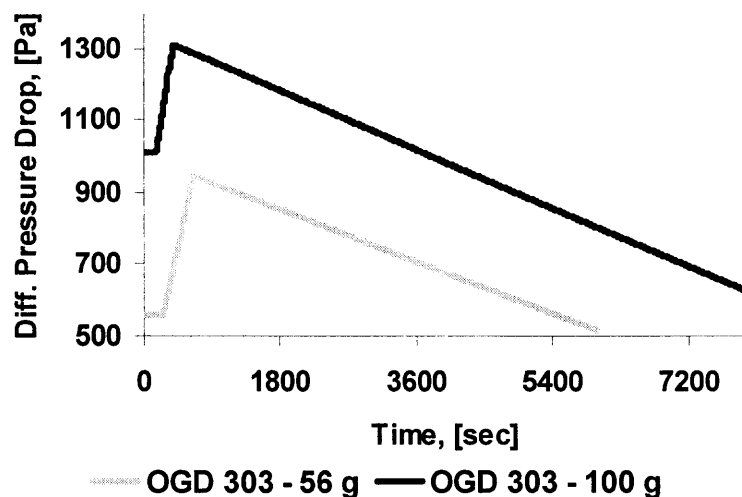
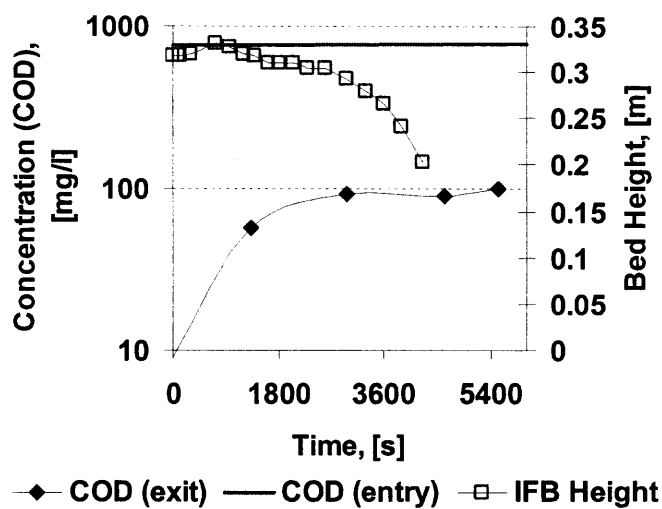
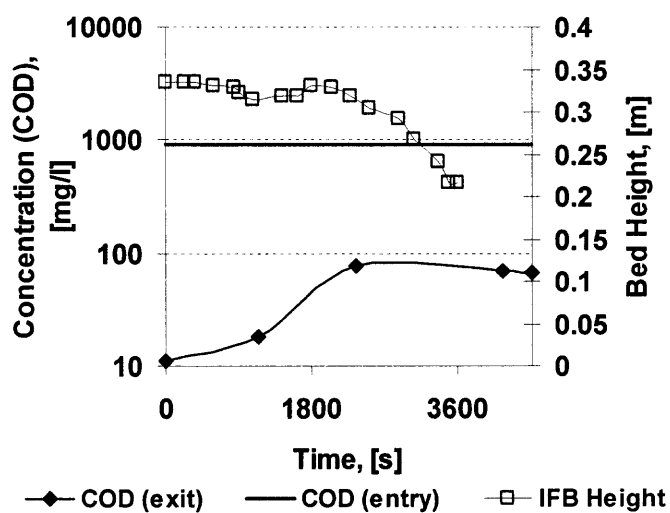


Figure 6.16 Pressure drop across the inversely fluidized beds of aerogel during the removal of oil corresponding to data shown in Figure 15. Superficial flow velocity was kept constant at 0.0305 m/s.

Figure 6.17 shows the removal efficiency of aerogel granules of different type; Figure 6.17a for OGD 303 small granules (0.5 – 0.85 mm) and Figure 6.17b for TLD 101 small granules. As can be seen from the plots and the data reported in Table 6.5, TLD 101 granules adsorbed less oil than OGD 303 granules, i.e., a COD level of 100 mg/l downstream of the fluidized bed is reached after a shorter time when TLD 101 granules are used and a bed height of about 0.2 meters is reached sooner, 3600 seconds, for the TLD granules as compared to 4260 seconds for the OGD granules. Thus, it can be concluded that the OGD granules have a larger oil adsorption capacity.



(a)



(b)

Figure 6.17 Chemical oxygen demand (COD) and inverse fluidized bed expansion (squares) as a function of time of 56 grams of aerogel granules (OGD 303) with sizes between 0.5 to 0.85 mm during removal of oil from water, upstream oil concentration is 0.36 g of oil/kg of water and fluid velocity is 0.0244 m/s (a) OGD 303 granules, (b) TLD 101 granules.

The effect of using a different fluid superficial liquid velocity was also studied, keeping all other operating variables the same, and is shown in Figure 6.18 and Table 6.5. At a low fluid velocity (0.0107 m/s) the collection efficiency is higher since it took more

than 14000 seconds to produce a level of 100 mg/l of COD downstream the bed, as compared to 7000 seconds at higher fluid velocity (0.0183 m/s). It can be seen from the plots and data that a higher oil removal capacity is obtained at the lower flow velocity. Also, at lower fluid velocity, the drag force is lower allowing the granules to saturate more since the resulting force from subtracting the drag force from the buoyancy force is larger. In this case, the bed height remains almost constant for about 2 hours after which the granules become saturated and groups of particles move downwards expanding the bed in a short period of time (3000 seconds). On the other hand, when the fluid velocity is large, voids in the fluidized bed are larger and the drag force is also higher; hence, partially oil-saturated granules leave the bed due to entrainment. This is reflected in the decrease of the fluidized bed height over time.

Figure 6.19 is a plot of the pressure drop across the fluidized bed for the experiments described in Figure 6.18 and shows a change in the rate at which the pressure drop increases/decreases due to the different superficial fluid velocity. At the higher fluid velocity the drag force is larger and entrainment is increased which translates into a faster decrease in the pressure drop across the fluidized bed.

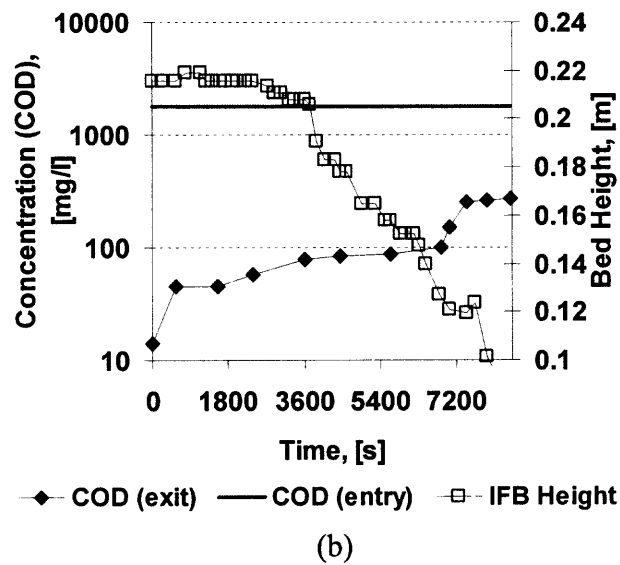
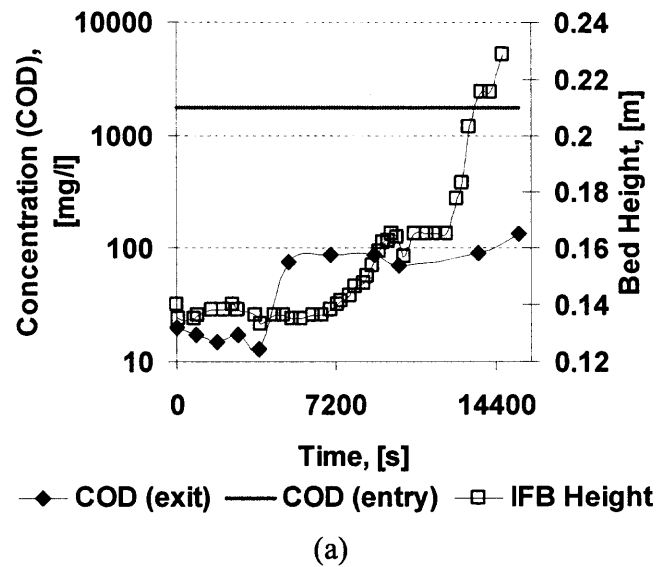


Figure 6.18 Chemical oxygen demand (COD) and inverse fluidized bed expansion (squares) as a function of time of: 56 grams of aerogel granules (TLD 101) with sizes between 0.5 to 0.85 mm during removal of oil from water: (a) Oil concentration is about 0.45 g of oil/kg of water and 0.0107 m/s fluid velocity, and (b) oil concentration is about 0.48 g of oil/kg of water and 0.0183 m/s fluid velocity.

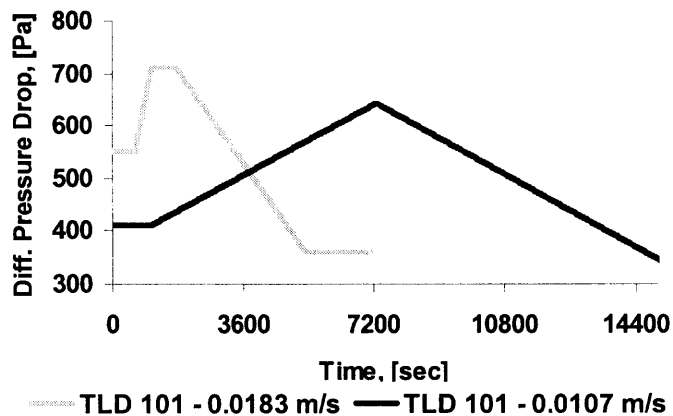


Figure 6.19 Pressure drop across the inversely fluidized beds of aerogel during the removal of oil corresponding to Figure 6.18.

Figure 6.20 shows the COD levels and the bed height of a fluidized bed of 108 grams of TLD 101, which is almost double the amount of granules used in most of the previous experiments. A larger amount of granules results in a taller initial bed height which implies a longer residence time for the oil droplets in the fluidized bed. An immediate consequence of the taller bed height is a better oil removal efficiency. COD levels downstream the fluidized bed containing more granules remain lower than 40 mg/l during the entire experiment before the 100 mg/l COD limit (see Figure 6.20), while in the fluidized bed with less powder but at the same operating conditions (see Figure 6.18a), COD levels remain below 90 mg/l during the experiment before reaching the 100 mg/l COD limit. Regarding the fluidized bed height, as mentioned above, when less powder is used aerogel granules tend to saturate more uniformly because of the CSTR-like mixing, which leads to an increase in bed height. However, for a longer fluidized bed there is a gradient in the concentration of oil along the fluidized bed, so that granules at the top saturate with oil at a faster rate than others, and these saturated granules leave the fluidized bed due to entrainment; therefore, a reduction in the bed height is observed.

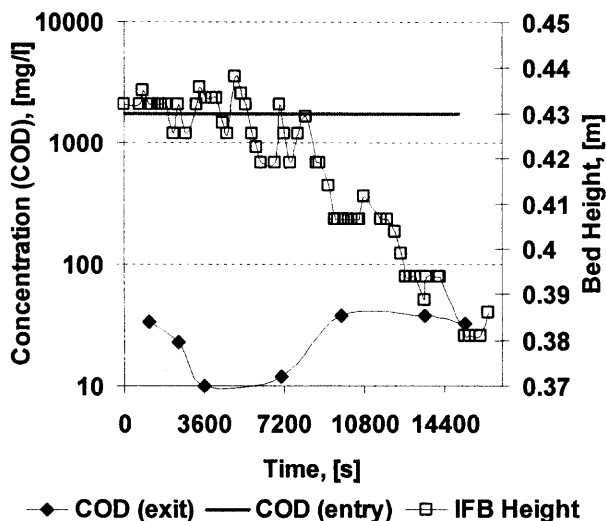


Figure 6.20 Chemical oxygen demand (COD) and inverse fluidized bed expansion (squares) as a function of time of 108 grams of aerogel granules (TLD 101) with sizes between 0.5 to 0.85 mm during removal of oil from water (0.47 g of oil/kg of water and 0.0102 m/s fluid velocity).

6.5 Conclusions

The hydrodynamic characteristics of inverse fluidized beds of aerogel granules were studied by measuring the pressure drop and bed expansion for different operating conditions. The experimental results are in good agreement with previous studies on liquid-solid fluidized beds. The experimentally measured fluidized bed pressure drop, at full fluidization, was used to estimate the volume occupied by the granules so that knowing the mass of granules used, the density and the void fraction of the aerogel granules could be calculated. The void fraction and the fluid velocity data were used to estimate the granules' size and terminal velocity using the Richardson-Zaki approach. It is important to note that the Re_t was in the range of 200 up to 500, so that the Richardson-Zaki index, “ n ,” is around 2.3 which agrees with the experimental data. The calculated

values of the particle size, based on equations for the terminal velocity and drag force, also agree very closely with the actual size of granules.

The drag force approach for multi-particle systems introduced by Fan et al.¹⁴⁹, seems to correlate the aerogel data quite well for the drag force function and the void fraction in the bed. In addition, the minimum fluidization velocity (U_{mf}) can be estimated by using the correlation given by Wen and Yu¹⁶⁴ for the large aerogel granules, but the correlation poorly estimates the U_{mf} for the smaller sized granules.

The oil removal efficiency of aerogel granules depends mainly on the initial height of the fluidized bed (amount of powder used), the void fraction of the bed and the fluid velocity. For continuously removing oil from contaminated water, it is desirable to keep the fluidized bed height constant. This can be achieved by having oil saturated particles entrained from the fluidized bed and then separated from the clean water downstream with a filter or cyclone. To compensate for the loss of particles, fresh granules can be added at the bottom of the fluidization column. With regard to the oil removal capacity, the experiments show that it is better to work with a taller fluidized bed (more granules), smaller granules, and low fluid velocities. The smaller granules will fluidize at lower fluid velocities and result in a lower bed void fraction leading to better removal efficiency. Low fluid velocities allow for a higher saturation of the granules since the drag force is lower and the granules spend more time in the fluidized bed without being entrained.

It has been found that at low flow rates the oil adsorption capacity of aerogel granules can be up to 7 times their weight, and the removal efficiency can be as high as

99%. A typical fluid velocity during operation would be in the range of 1 to 2 cm/s for granules less than one millimeter in size.

A great advantage of the inverse fluidized bed over a packed bed filter is the low pressure drop which translates in low energy consumption. The higher pressure drop obtained in the experiments was of 0.2 psi (1300 Pa) when removing oil with 100 grams of granules. The pressure drop across the inverse fluidized bed will not increase as the oil is adsorbed in the granules; moreover, it decreases unless more granules are added. In a packed bed filter, the pressure drop depends on the flow rate passing through the bed; in a fluidized bed, the pressure drop is only proportional to the amount of granules fluidized. In several applications of packed bed filters, the limiting pressure drop is about 10 psi; this value can be easily reached with a very small amount of granules depending on granule size and fluid velocity. However, in order to reach a differential pressure drop of 10 psi across an inverse fluidized bed of aerogel granules in a column of 3.5 inches internal diameter, as much as 6 kg of aerogel granules could be used. These 6 kg of aerogel granules could adsorb up to 42 kg of oil, and the bed height of the fluidized bed would be about 16 meters (52.5 ft.). Thus, it can be concluded that an inverse fluidized bed of aerogel granules is an excellent candidate for removing oil and other hydrocarbon contaminants from wastewater.

CHAPTER 7

SUMMARY OF CONTRIBUTIONS

This dissertation has focused on three topics: gas-solid fluidization of agglomerates of nanoparticles, filtration of submicron particles using nanoagglomerates or nanostructured granules as a filter media, and liquid-solid inverse fluidization of aerogels for oil removal. These are three different topics related by the general field of particle technology; however, all of the experiments were done using powders made up of primary particles of nanosize or granules having a porous structure in the nanoscale.

The experimental results reported for the fluidization of nanoparticle agglomerates clearly show that the hydrodynamic behavior is quite different than that of solid particles which have been extensively studied. The major contributions and findings related to the gas-solid fluidization of agglomerates of nanoparticles are:

1. The reduction of electrostatic charges in the fluidized bed of agglomerates of nanoparticles allowed the use of optical probes, such as the Focus Beam Reflectance Methods (FBRM) and the Particle Vision and Measurement (PVM) from Lasentec, to characterize the fluidized agglomerates in-situ. Agglomerate size distributions as well as in-situ images were successfully obtained.
2. A new assisting method to enhance the fluidization of agglomerates of nanoparticles has been developed. This method consists of the use of turbulent jets generated by micro-nozzles to increase mixing and promote breaking up of large and denser agglomerates resulting in smaller and fluffier ones. The jet assisted fluidization method provides excellent results. It is well known that the

fluidized bed height is a measurement of the degree of dispersion of the nanopowder in the gas phase. For APF nanopowders, the jet assisting method leads to bed expansions of about several times the conventionally fluidized bed height, for example, bed expansions of about 10 times the expanded conventional fluidized bed has been achieved for Aerosil R974. Moreover, ABF nanopowders, which are very difficult to fluidize, are transformed into APF nanopowders by using the jet assisting method. This method has several advantages over previous assisting methods such as its low energy requirements, absence of foreign material in the fluidized bed, simpler to scale up, and better dispersion of the agglomerates than when using previous methods such as stirring magnetic particles or vertical vibration.

3. A better understanding of the fluidization characteristics of nanopowders can be gained by measuring the pressure fluctuations that occur at gas velocities close to the minimum fluidization velocity. These pressure fluctuations indicate that there may be incomplete fluidization even at gas velocities larger than minimum fluidization velocity; hence, the method to define the minimum fluidization velocity of nanopowders may need to be revised. It also appears that the Blake-Kozeny equation for packed beds does not apply for a non-fully fluidized bed of nanopowders as for larger size solid micron size particles because of channeling and spouting that occurs prior to the fluidization of nanoagglomerates.
4. The application of the conventional Richardson-Zaki (R-Z) method and the Richardson-Zaki (R-Z) method coupled with a fractal analysis for the estimation of fluidized agglomerates sizes seems to indicate the following:

- a. The R-Z index " n " is not only dependant on the Reynolds number but it may also be dependant on the properties of the powder, and it can be used as a parameter to characterize cohesive powders similar to the angle of repose. Other research studies reported in the literature have also found that the " n " index is not limited to the 2.3 to 6 range, and have reported larger values.
 - b. Many of the assumptions made for the R-Z analysis do not apply for agglomerates of nanoparticles in a fluidized bed such as assuming Stokes law for the calculation of the terminal velocity. Also, the fact that agglomerates of nanoparticles have a wide particles size distribution and may even have different densities and a different drag coefficient due to their agglomerate structure and rough surface may lead to incorrect values of the agglomerate size.
5. By monitoring the moisture concentration in the fluidizing gas of conventional and assisted fluidized beds of hydrophilic agglomerates of nanoparticles, mass transport rates as well as the adsorption/desorption phenomenon from the gas phase to the fluidized agglomerate phase can be studied. It was verified quantitatively that assisting methods, such as stirring magnetic particles and vibration, improve the mixing and transport between the two phases.
6. A similar study, monitoring the moisture concentration in the fluidizing gas, but using hydrophobic agglomerates of nanoparticles, was done to find the residence time distribution (RTD) functions in packed beds and fluidized beds. Diffusion of moisture into the porosity of the agglomerates was shown to be important depending on the size of the agglomerate. The larger the agglomerate the more significant the diffusion. The diffusion of the tracer into the pores of the agglomerate delays its appearance at the exit of the fluidized or packed bed. This effect has to be considered in applications that involve mass transport. For example, desorption of a contaminant from the agglomerate may be delayed due to diffusion.

7. During the use of moisture as tracer, it was observed that electrostatic charges in the fluidized bed of powder were reduced. This led to the use of other types of vapors such as alcohol which were added to the fluidizing gas and successfully reduced electrostatic charges allowing for the agglomerates of nanoparticles to be better dispersed in conventional and assisted fluidized beds.
8. Agglomerates of nanoparticles can be fluidized under centrifugal forces. The classification of different nanoparticles into APF type and ABF type behavior as was done for conventional vertical, gravity-driven fluidization a column is also found when the powders are fluidized in rotating fluidized beds. For APF type nanopowders, tangential flows lead to larger pressure drops than expected across the fluidized bed due to the additional centrifugal acceleration of the agglomerates by the tangential flow, which under a different frame of reference, is known as the Coriolis force.
9. The rotating fluidized bed experimental results confirm that the flow velocity profiles and pressure gradients in a rotating fluidized bed are strongly dependant on the geometry of the rotating fluid bed equipment.

The presence of airborne submicron size particles that can affect human health are of major concern. Also, the handling and processing of nanoparticles is increasing due to their unique properties and potential applications in many industries; however, their effects on the human body are not well known yet. This work has introduced using porous granules made of nanoparticles as an alternative filter media to capture submicron and nanosized aerosols. The major contributions and findings related to the filtration of submicron aerosols are:

1. It has been shown that granular bed filters composed of highly porous granules provide collection efficiencies similar to HEPA fiber-based filters when challenged against submicron solid aerosols and collection efficiencies better than HEPA filters when the challenging aerosol is oil-based (liquid droplets). The main advantage of the granular bed filters is their increased filtration capacity when compared to HEPA.
2. The size of the granules of a granular packed bed filter has been optimized considering the thickness of the filter, collection efficiency and pressure drop. It has been found that optimal granule sizes for 2 to 3 inches thick filters is about 150 to 250 microns.
3. Granular filters composed of porous collectors present an excellent collection media for capturing nanoparticles. It is well known that particles smaller than 0.3 microns will be mainly collected by the diffusion-based filtration mechanism. These small particles diffuse into the pores of the collectors increasing the collection efficiency when compared to the non-porous fibers in HEPA filters.
4. Fluidized beds of aerogels have been used for the removal of submicron aerosol with good efficiency in particular when the aerosol is composed of oil droplets. The fluidized bed filters offers an even larger filtration capacity and a very small pressure drop.

The major contributions and findings related to the liquid-solid inverse fluidization of aerogels for removal of oil from water are:

1. Aerogel granules were inversely fluidized in water and their hydrodynamic behavior reported. Inverse fluidization of aerogels has not been previously studied according to the literature review.
2. It has been shown that an inverse fluidized bed of aerogels efficiently reduces oil concentration in water from several thousands down to few parts per million as measured by the Chemical Oxygen Demand (COD) method. The final concentration of oil in water will depend on several variables such as the height of the bed, size of the aerogel granules and the fluid velocity. The use of inverse fluidization of aerogels is much more energy efficient than filtration methods based on using packed beds because the pressure drop across the inverse fluidized bed of aerogel granules is much smaller when compared to the pressure drop across a packed bed containing a similar amount of granules at the same fluid velocity.

APPENDIX A

MATLAB CODE TO MODEL THE CONCENTRATION OF MOISTURE AT THE EXIT OF A FLUIDIZED BED

Modeling of the concentration of moisture with respect to time at the exit of a fluidized bed of agglomerates of nanoparticles has been introduced in Chapter 3. The suggested model was elaborated for a particulate fluidized bed, i.e., free of bubbles. A system of two simultaneous differential equations was the result of the theoretical modeling. This system was solved by writing a program in MatLab 7.1.0. The ordinary differential equation (ODE) solver selected was “ode113.” This solver is designed for nonstiff problems and it was selected because its ability to solve variable order ODE being more efficient when the ODE function is expensive (takes long iteration time). More information on Ode solvers and their syntax can be found in the MatLab Tutorial. The program code is attached below.

```
%Simulation of the drying of a fluidized bed v1.0
%written by Jose A Quevedo in collaboration with Juergen
flesch

%input data
global k1 k2 k3 k4 k5

ldata=input('Do you want to load or enter data
(load:1/enter:2) ');
if (ldata==2)

dagg=input('Agglomerate diameter (um) ');
dF=dagg*1e-6; %to meters
%rhoF=input('Agglomerate density (kg/m3)
= ');
```

```

Ug=input('Gas velocity (cm/s) = ');
Ug=Ug/100; %m/s
Ut=input('Terminal velocity of agglomerate (cm/s)
= ');
Ut=Ut/100; %m/s
Hws=input('Fluidized bed height (m) =
');
epsilonF=input('Agglomerate void fraction
= ');
epsilonG=input('Interagglomerate void fraction
= ');
C2ein=input('moisture concentration at the entrance (kg/m3)
= ');
save modeling.mat
elseif ldata==1
load modeling.mat
end

% gas density is assumed to be nitrogen
rhog=1.16; %kg/m3
nu=0.0000179; %kg/m.s

%silica density
rhosio2=2200;
rhoF=(1-epsilonF)*rhosio2

Texp=293; %temperature in kelvin
R=8.31451; %J/kmol/K
%subscripts: 2 air, 1 water

%pressure
Pdm=1.01325; %bar
%molecular masses
M2=28.97; %kg/kmol air
M1=18.016; %kg/mol water
nu1=12.7;
nu2=20.1;
Dmf=@(T) 1e-
3*T^1.75*((M2+M1)/(M1*M2))^0.5*1.1013/(Pdm*(nu1^(1/3)+nu2^(
1/3))^2);
Dm=Dmf(Texp)/10000; %m2/s
%Henry constant
KcT=@(T) 7.85e-9*R*T*exp(4040/T)/M2; %m3/kg
Kc=KcT(Texp);

```

```

%Schmidt
Sc=nu/(rhog*Dm);
Ar=dF^3*(rhoF-rhog)*rhog*9.8/nu^2;
Ret=18*(sqrt(1+1/9*sqrt(Ar))-1)^2;
Shlam=0.664*Sc^(1/3)*Ret^0.5;
Shturb=0.037*Ret^0.8*Sc/(1+2.443*Ret^-0.1*(Sc^(2/3)-1));
ShEK=2+(Shlam^2+Shturb^2)^0.5;
%mass-transfer coeff
betaFS=ShEK*Dm/dF;
Kcp=Kc+epsilonF/((1-epsilonF)*rhosio2);
Us=Ug/epsilonG;

%constants

A=betaFS*6/(dF*rhosio2*(1-epsilonF));
B=Kcp;
C=betaFS*6*(1-epsilonG)/(dF*epsilonG);
D=Us/Hws;
k1=A/B;
k2=A;
k3=C/B;
k4=C+D;
k5=D*C2ein;

%solvin
iteration=input('Do you want to load or enter the boundary
conditions (Load:1/enter:2) ');

if iteration==2
    tf=input('Final time (s) [20] = ');
X0=input('Initial concentration of moisture in the
agglomerate (kg/kg) [.03] = ');
Y0=input('Initial concentration of moisture in the exiting
gas (kg/kg) [.02] = ');
rele=input('Overall relative error in iteration [1e-3] =
');
abseX=input('Relative error of B in iterations [1e-3] =
');
abseY=input('Relative error of C2,s in iterations [1e-3] =
');
save boundar.mat

elseif iteration==1
load boundar.mat
end

```

```
options = odeset('RelTol',rele,'AbsTol',[abseX abseY]);
[T,Y] = ode113(@massbal,[0 tf],[X0 Y0],options);
figure
xlabel('Time')
ylabel('Concentration')
plot(T,Y(:,1),'r',T,Y(:,2),'g')
%hold
%figure
%xlabel('Time')
%ylabel('Concentration')
%plot(T,Y(:,2),'g')
result=[T,Y];
```

```
function dy = massbal(t,y,k1,k2,k3,k4,k5)
global k1 k2 k3 k4 k5
%function that provides the system of ODEs
dy=zeros(2,1); % a column vector
dy(1)=-k1*y(1)+k2*y(2);
dy(2)=k3*y(1)-k4*y(2)+k5;
```

APPENDIX B

RESIDENCE TIME DISTRIBUTION FUNCTIONS

In Chapter 3, moisture was used as tracer to study the Residence Time Distribution (RTD) functions of packed and fluidized beds of agglomerates of nanoparticles (Aerosil R974). This Appendix shows the RTD function ($E(t)$) and the function for finding its standard deviation (σ) for each of the different cases studied. The concentration of the moisture used for the plots shown was about 10 mbar of partial pressure of water.

B.1 Empty Column

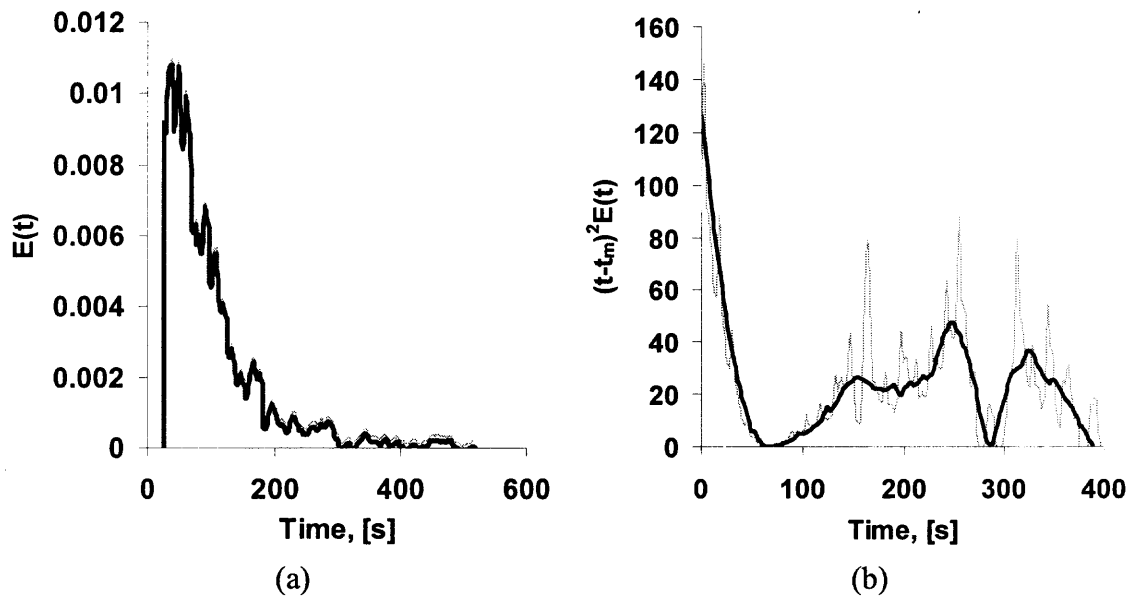


Figure B.1 Responses of the empty column: (a) RTD function, (b) Function for finding the variance (area under the curve). Gas velocity of about 2.2 cm/s

B.2 Packed Bed of Large Agglomerates of Aerosil R974

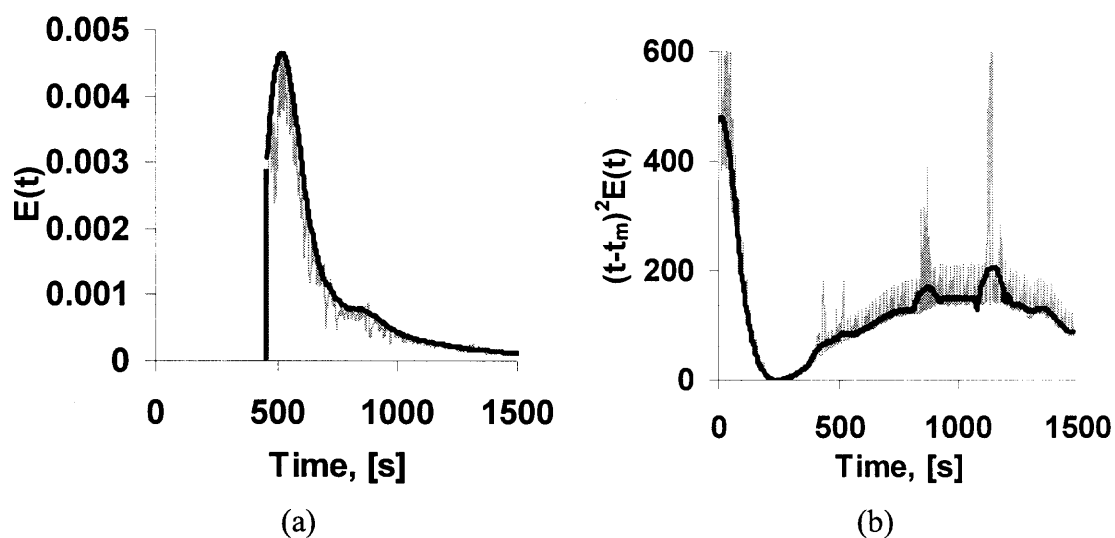


Figure B.2 Responses of the packed bed of large agglomerates of Aerosil R974 (41 in): (a) RTD function, (b) Function for finding the variance (area under the curve). Gas velocity of 2.2 cm/s.

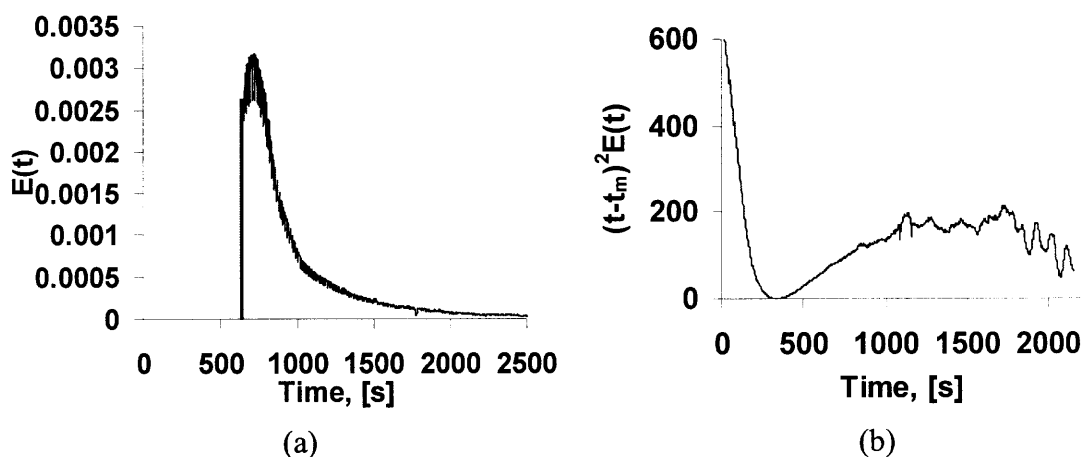


Figure B.3 Responses of the packed bed of large agglomerates of Aerosil R974 (41 in): (a) RTD function, (b) Function for finding the variance (area under the curve). Gas velocity of 1.5 cm/s.

B.3 Packed Bed of Glass Beads

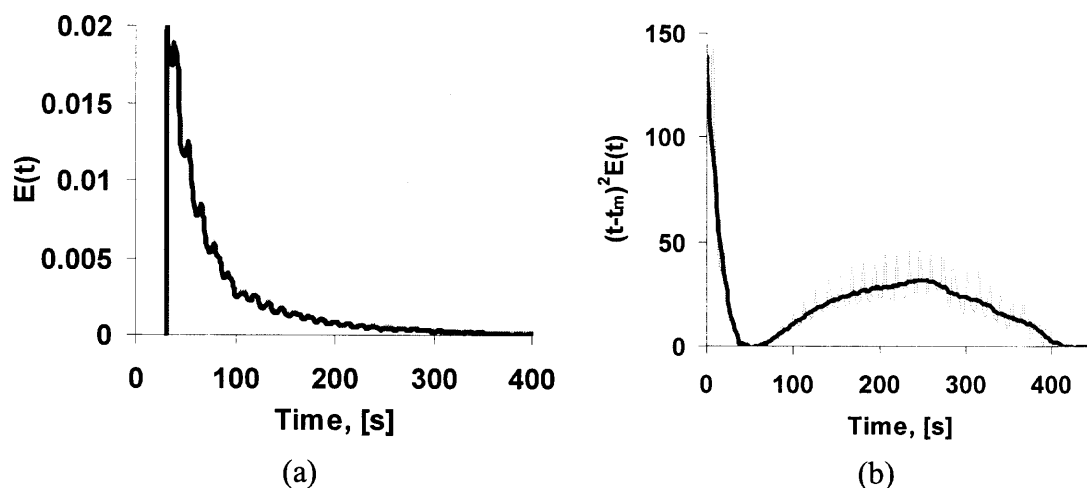


Figure B.4 Responses of the packed bed of glass beads (21 in): (a) RTD function, (b) Function for finding the variance (area under the curve). Gas velocity of 2.2 cm/s.

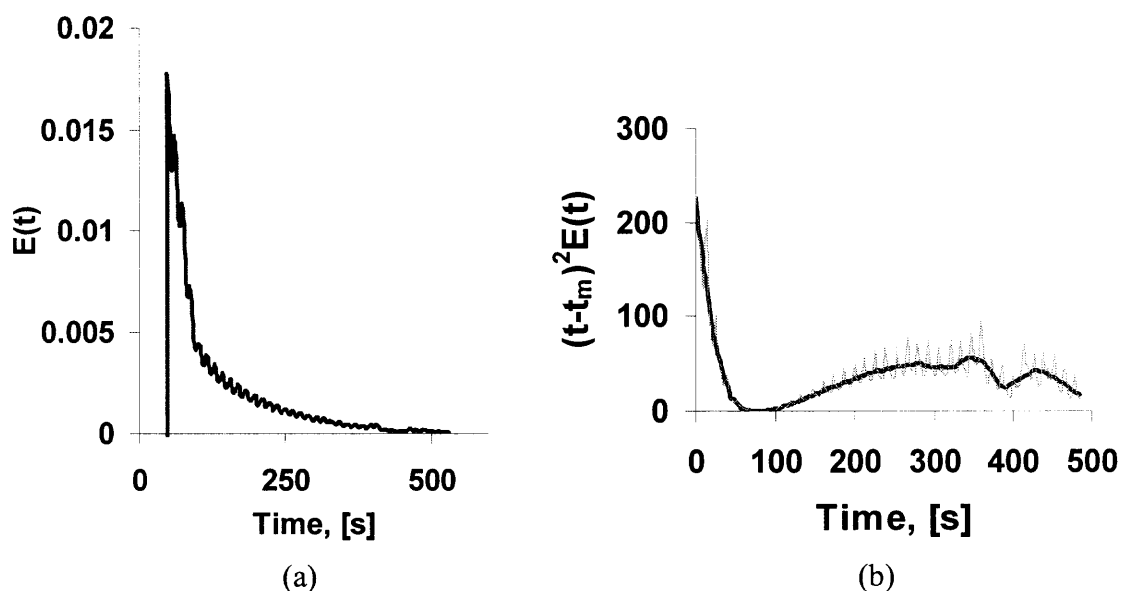


Figure B.5 Responses of the packed bed of glass beads (21 in): (a) RTD function, (b) Function for finding the variance (area under the curve). Gas velocity of 1.5 cm/s.

B.4 Fluidized Bed of Sieved Agglomerates of Aerosil R974

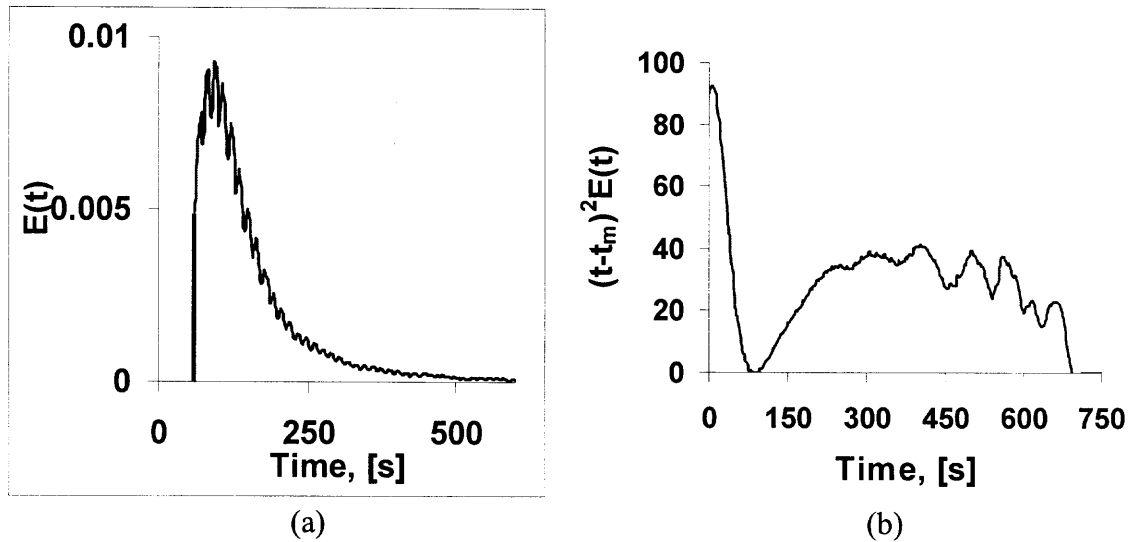


Figure B.6 Responses of the fluidized beds of sieved agglomerates of Aerosil R974 (21 in): (a) RTD function, (b) Function for finding the variance (area under the curve). Gas velocity of 2.2 cm/s.

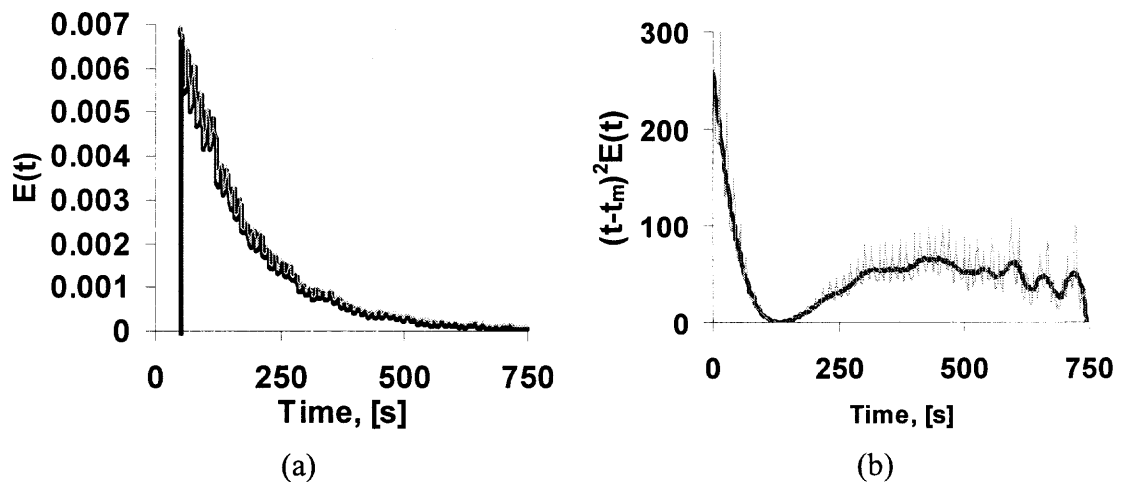


Figure B.7 Responses of the fluidized beds of sieved agglomerates of Aerosil R974 (42 in): (a) RTD function, (b) Function for finding the variance (area under the curve). Gas velocity of 2.2 cm/s.

B.5 Fluidized Bed of Jet Processed Agglomerates of Aerosil R974

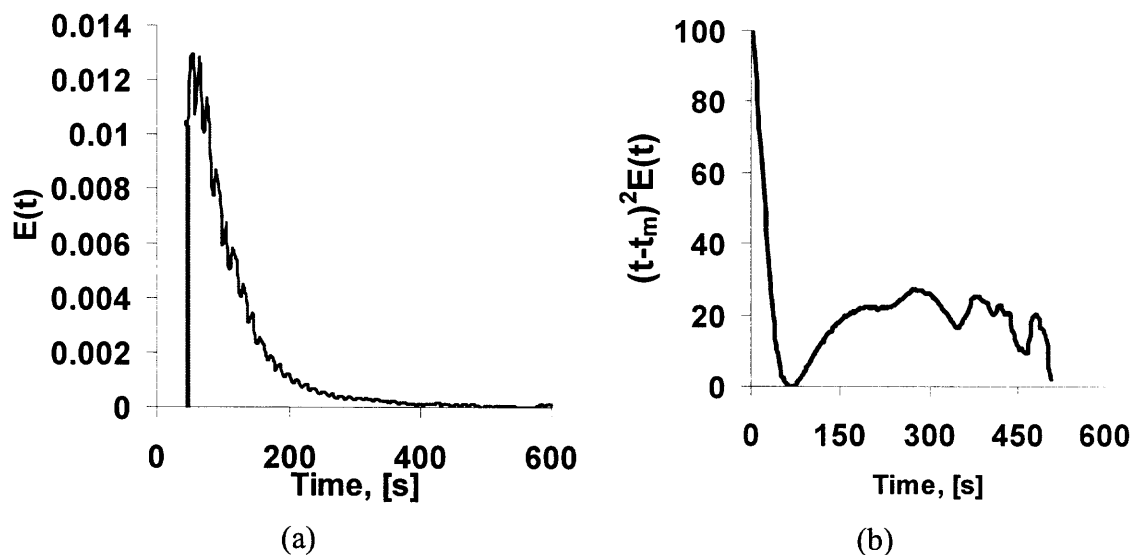


Figure B.8 Responses of the fluidized bed of jet processed agglomerates of Aerosil R974 (21 in): (a) RTD function, (b) Function for finding the variance (area under the curve). Gas velocity of 2.2 cm/s.

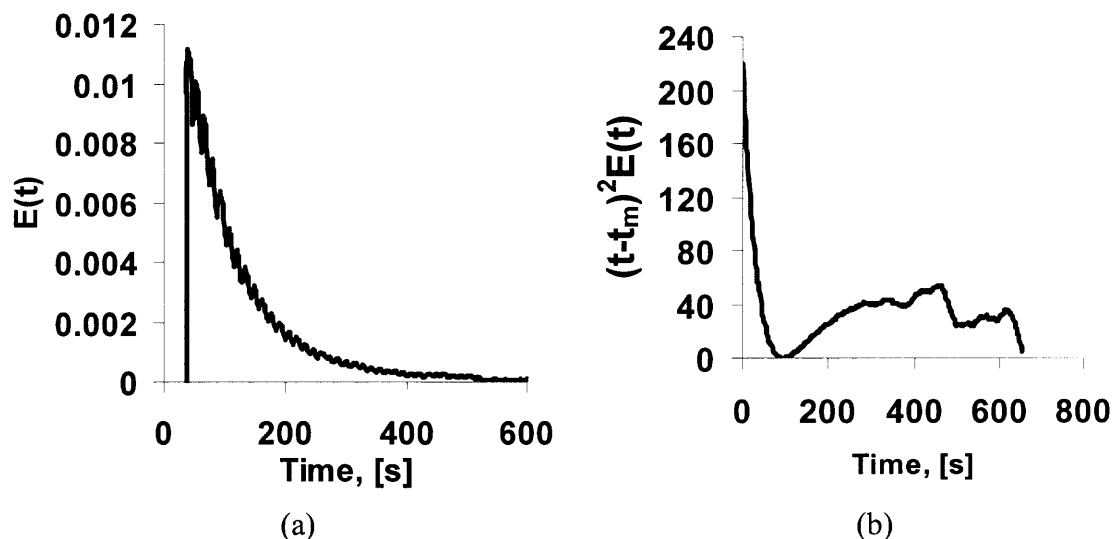


Figure B.9 Responses of the fluidized bed of jet processed agglomerates of Aerosil R974 (42 in): (a) RTD function, (b) Function for finding the variance (area under the curve). Gas velocity of 2.2 cm/s.

APPENDIX C

SEM IMAGES OF GRANULAR FILTRATION MEDIA

In Chapter 5, it has been shown that granular packed bed filter media composed of porous granules have collection efficiencies equivalent to HEPA fiber-based filters and larger filtration capacity due to the deep bed filtration mode. This appendix show SEM images of some of the granular filter media studied.

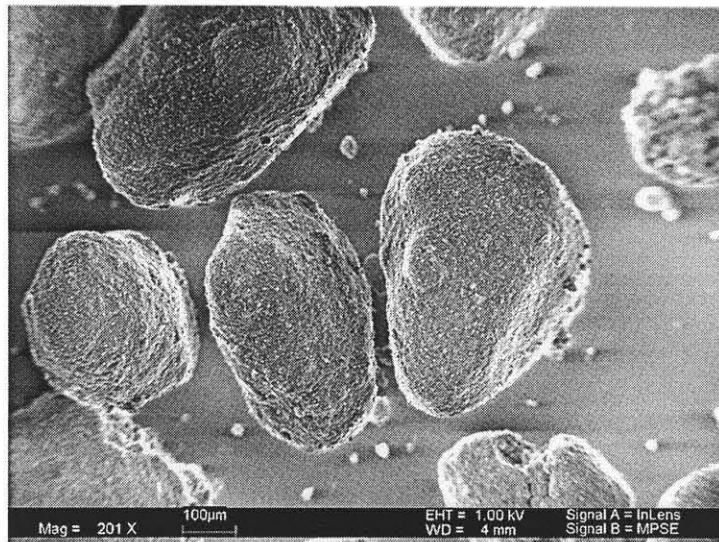


Figure C.1 Agglomerates of Aerosil 300 used as granular filter media.

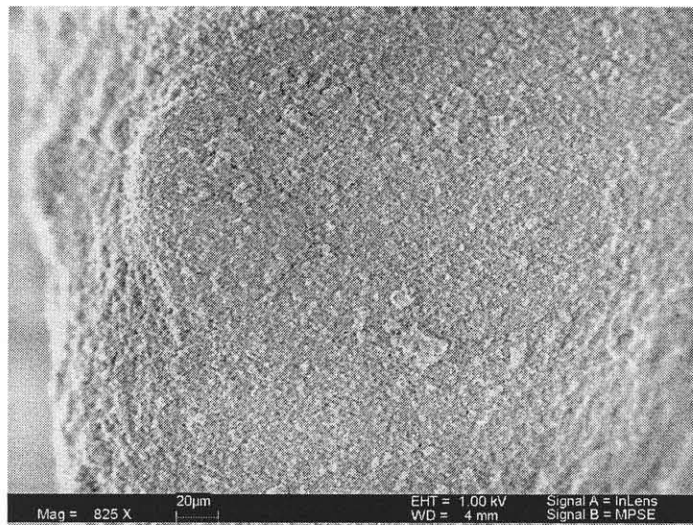


Figure C.2 Close-up of the surface of the agglomerate of Aerosil 300.

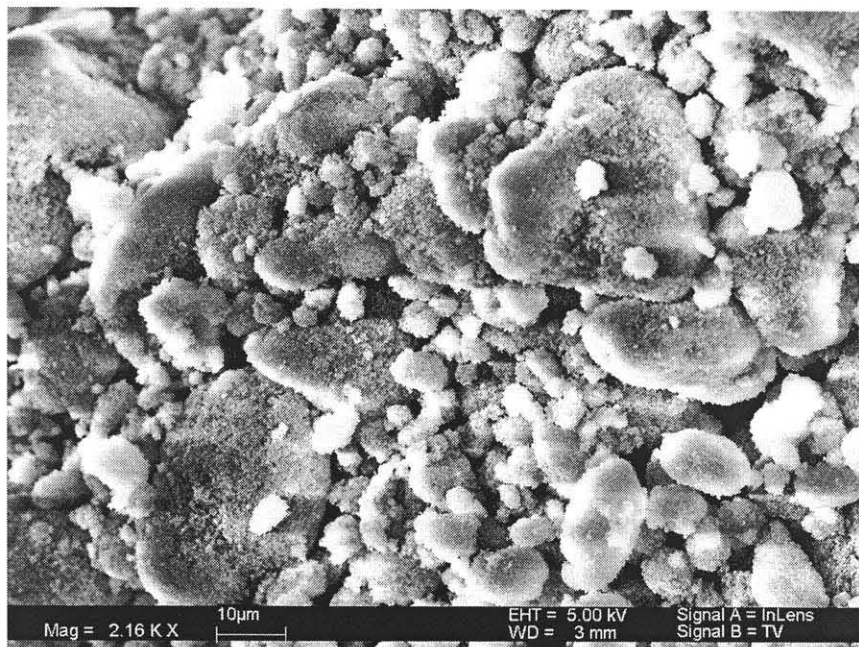


Figure C.12 Close-up of the surface of the agglomerate of Aerosil 300.

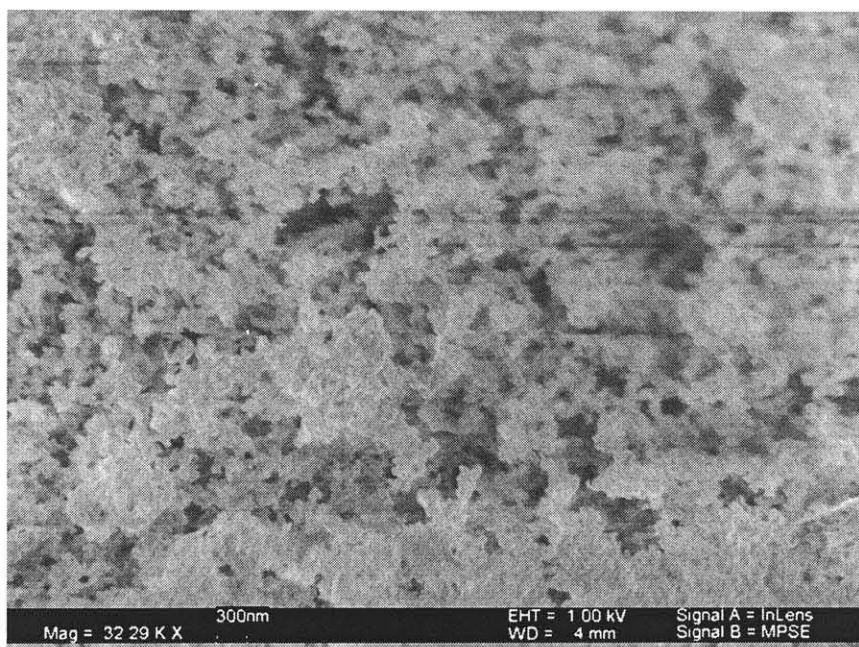


Figure C.13 Close-up of the surface of the agglomerate of Aerosil 300.

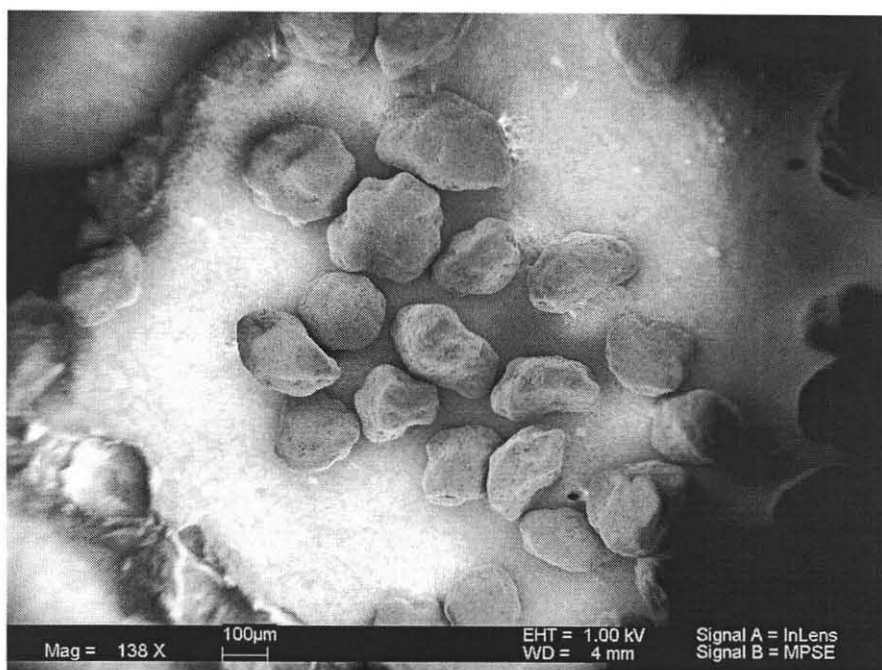


Figure C.14 Clean carbon black granules of Regal 660 A69.

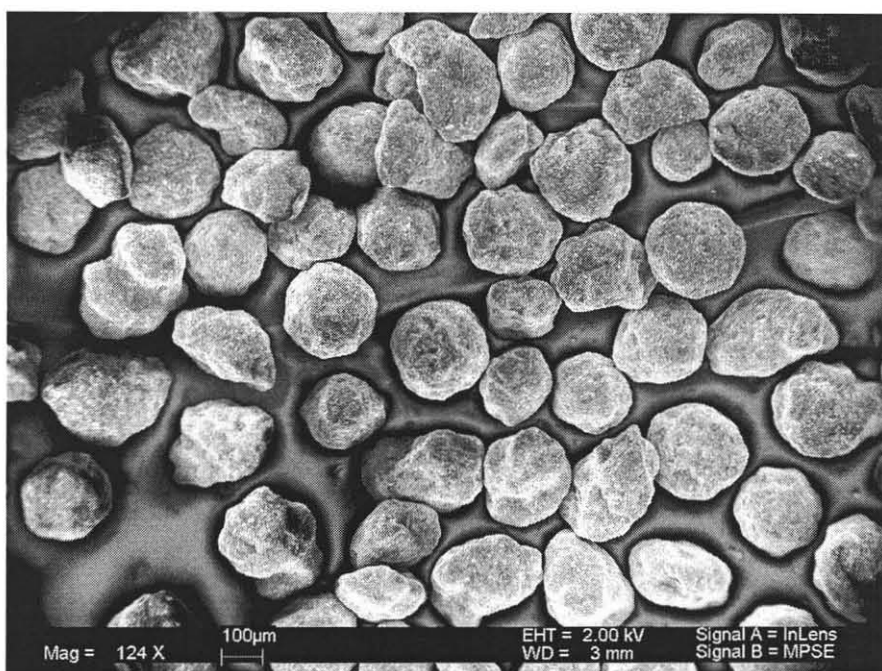


Figure C.15 Carbon black granules of Regal 660 A69 after being used as filter media for capturing SiC particles (bright dots).

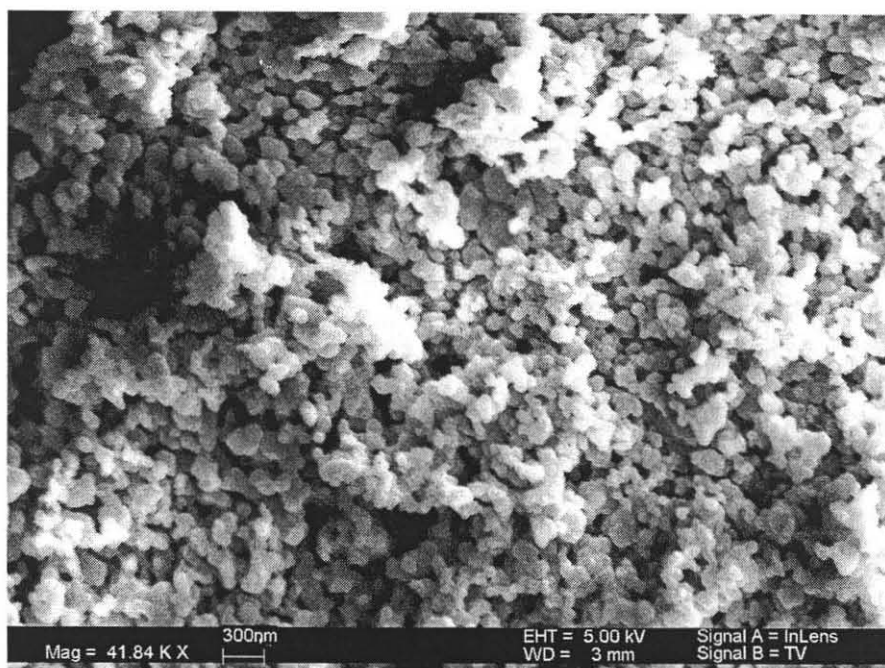


Figure C.16 Close-up of the surface of Carbon black granules of Black Pearl 120.

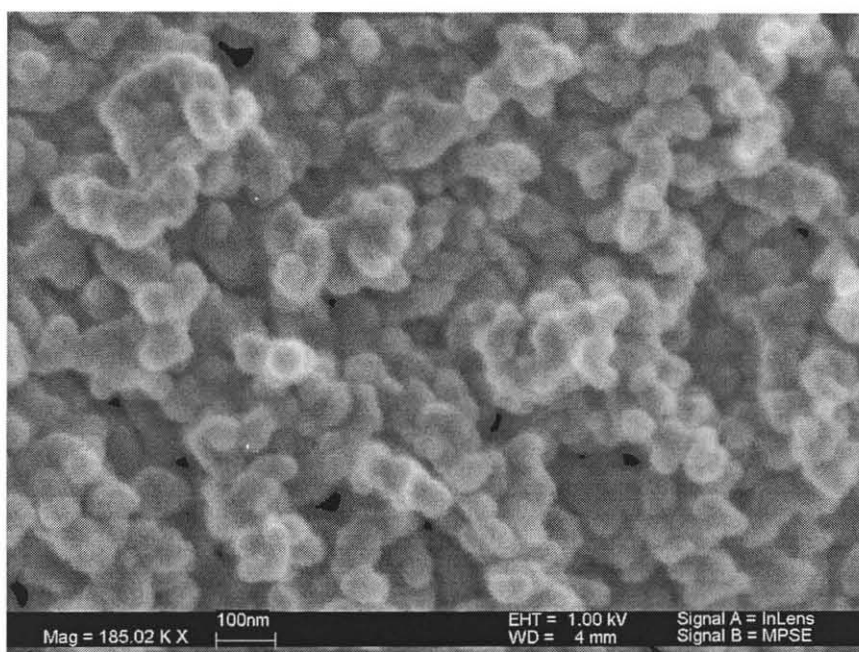


Figure C.17 Close-up of the surface of carbon black granules of Regal 660 A69.

REFERENCES

1. Wang Y, Gu G, Wei F, Wu J. Fluidization and agglomerate structure of SiO₂ Nanoparticles. *Powder Technology*, 2002; 124: 152.
2. Zhu C, Liu G, Yu Q, Dave R, Pfeffer R, Nam C. Sound assisted fluidization of nanoparticle agglomerates. *Powder Technology*. 2004; 141, 119-123.
3. Guo Q, Liu H, Shen W, Yan X, Jia R. Influence of sound wave characteristics on fluidization behaviors of ultrafine particles. *Chemical Engineering Journal*. 2006; 119: 1-9.
4. Guo Q, Li Y, Wang M, Shen W, Yang C. Fluidization characteristics of SiO₂ nanoparticles in an acoustic fluidized bed. *Chem. Eng. Technol.* 2006; 29 (1): 78-86.
5. Nam C, Pfeffer R, Dave R, Sundaresan S. Aerated vibrofluidization of silica nanoparticles. *AIChE Journal*. 2004; 50: 1776-1785.
6. Levy E., Celeste B. Combined effects of mechanical and acoustic vibrations on fluidization of cohesive powders. *Powder Technology*. 2006; 163: 41-50.
7. Zhu C, Yu Q, Pfeffer R, Dave R. Gas fluidization characteristics of nanoparticle agglomerates. *AIChE Journal*. 2005; 51-2: 426-439.
8. Yu Q, Dave R, Zhu C, Quevedo J, Pfeffer R. Enhanced fluidization of nanoparticles in an oscillating magnetic field. *AIChE Journal*. 2005; 51: 1971-1979.
9. Hakim LF, Portman JL, Casper MD, Weimer AW. Aggregation behavior of nanoparticles in fluidized beds. *Powder Technology*, 2005; 160: 149-160.
10. Yu H, Zhang Q, Gu G, Wang Y, Luo G, Wei F. Hydrodynamics and gas mixing in a carbon nanotube agglomerate fluidized bed. *AIChE Journal*. 2006; 52 (12): 4110 - 4123.
11. Wang XS, Palero V, Soria J, Rhodes MJ. Laser-based planar imaging of nanoparticle fluidization: Part I – determination of aggregate size and shape. *Chemical Engineering Science*. 2006; 61: 5476-5486.
12. Quevedo J, Pfeffer R, Shen Y, Dave R, Nakamura H and Watano S. Fluidization of Nanoagglomerates in a Rotating Fluidized Bed. *AIChE Journal*. 2006; 52 (7): 2401-2412.

13. Hakim LF, Blackson J, George SM, Weimer AW. Nanocoating individual silica nanoparticles by atomic layer deposition in a fluidized bed reactor. *Chem. Vap. Deposition*. 2005; 11: 420 – 425.
14. Park A-H, Bi HT, Grace J. Reduction of electrostatic charges in gas- solid fluidized beds. *Chemical Engineering Science*. 2002; 57: 153-162.
15. Mehrani P, Bi HT, Grace J. Electrostatic charge generation in gas-solid fluidized beds. *Journal of Electrostatics*. 2005; 63: 165-173.
16. Rowe PN, MacGillivray HJ, Cheesman DJ. Gas discharge from an orifice into a gas fluidized bed. *Trans. IChemE*. 1979; 57: 194-199.
17. Behie LA, Bergougnou MA, Baker CGJ, Bulani W. Jet momentum dissipation at a grid of large gas fluidized bed. *The Canadian Journal of Chemical Engineering*. 1970; 48: 158-161.
18. Clift R, Filla M, Massimilla L. Gas and particle motion in jets in fluidized beds. *Int. J. Multiphase Flow*. 1976; 2: 549-561.
19. Zhong W, Zhang M. Jet penetration depth in a two-dimensional spout-fluid bed. *Chemical Engineering Science*. 2005; 60: 315-327.
20. Richner D W, Minoura T, Princhet J W and Blake TR. Computer simulation of isothermal fluidization in large-scale laboratory rigs. *AIChE J*. 1990; 36(3):361-369.
21. Blake TR, Webb H, Sunderland PB. The non-dimensionalization of equations describing fluidization with application to the correlation of jet penetration height. *Chem. Eng. Sci*. 1990; 45(2): 365-371.
22. Hong R, Li H, Wang Y. Studies on the inclined jet penetration length in a gas-solid fluidized bed. *Powder Technology*. 1997; 92:205-212.
23. Hong RY, Li HZ, Cheng MY, Zhang JY. Numerical simulation and verification of gas-solid jet fluidized bed. *Powder Technology*. 1996; 87(1): 73-81.
24. Hong RY, Guo QJ, Luo GH, Zhang JY, Ding J. On the jet penetration height in fluidized beds wit two vertical jets. *Powder Technology*. 2003; 133(1-3): 216-227.
25. Xuereb C, Laguerie C, Baron T. Etude du comportement de jets continus horizontaux ou inclines introduits dans un lit fluidise par un gaz. I: Morphologie des jets. *Powder Technology*. 1991; 67: 43-56.
26. Chyang CS, Chang CH, Chang JH. Gas discharge modes at a single horizontal nozzle in a two-dimensional fluidized bed. *Powder Technology*. 1997; 90: 71-77.

27. Vaccaro S. Analysis of the variables controlling gas jet expansion angles in fluidized beds. *Powder Technology*. 1997; 92: 213-222.
28. Yang WC. Comparison of jetting phenomena in 30-cm and 3-m diameter semicircular fluidized beds. *Powder Technology*. 1998; 100: 147-160.
29. Guo Q, Yue G, Zhang J, Liu Z. Hydrodynamic characteristic of a two-dimensional jetting fluidized bed with binary mixtures. *Chemical Engineering Science*. 2001; 56: 4685-4694.
30. Shen Z, Briens CL, Bergougnou MA. Study of a downward grid jet in a large two dimensional gas fluidized bed. *Powder Technology*, 1990; 62: 227-234.
31. Hong R, Ding J, Li H. Fluidization of fine powders in fluidized beds with an upward or a downward air jet. *China Particuology*. 2005; 3(3): 181-186.
32. Wether J, Xi W. Jet attrition of catalyst particles in gas fluidized beds. *Powder Technology*. 1993; 76: 39-46.
33. Tasirin SM, Geldart D. Experimental investigation on fluidized bed jet grinding. *Powder Technology*. 1999; 105: 337-341.
34. Wang XS, Palero V, Soria J, Rhodes MJ. Laser-based planar imaging of nanoparticle fluidization: Part II – Mechanistic analysis of nanoparticle aggregation. *Chemical Engineering Science*. Accepted.
35. Pons MN, Milferstedt K, Morgenroth E. Modeling of Chord Length distributions. *Chemical Engineering Science*. Vol. 2006; 61: 3962 – 3973.
36. De Clercq B., Lant PA, Vanrolleghem PA. On-line particle measurement in secondary classifiers. Department of Applied Mathematics, Ghent University, 2002.
37. Barrett P, Glennon B. in-line FBRM Monitoring of particle size in dilute agitated suspensions. *Particle & Particle System Characterization*. Vol. 16 (5), pp. 207 – 211, Nov. 1999.
38. Heath AR, Fawell PD, Bahri PA, Swift JD. Estimating average particle size by focused beam reflectance measurement (FBRM). Review. *Particle & Particle System Characterization*, Vol. 19 (2), pp. 84-95. May 2002.
39. Richardson JF, Zaki R. Sedimentation and fluidization: Part I. *Trans. Instn. Chem. Engrs*. 1954; 32: 35-53.
40. Valverde JM, Castellanos A. Fluidization of nanoparticles: A modified Richardson-Zaki law. *AIChE J., R&D Notes*. 2006; 52(2): 838-842.

41. Lettieri P, Newton D, Yates JG. Homogeneous bed expansion of FCC catalysts, influence of temperature on the parameters of the Richardson-Zaki equation. *Powder Technology*. 2002; 123: 221-231.
42. Tran-Cong S, Gay M, Michaelides EE. Drag coefficient of irregularly shaped particles. *Powder Technology*. 2004; 139: 21-32.
43. Binder C, Feichtinger C, Schmid H-J, Thurey N, Peukert W, Rude U. Simulation of the hydrodynamic drag of aggregated particles. *Journal of Colloid and Interface Science*. Article in Press. 2006.
44. Beetstra R, Van der Hoef MA, Kuipers JAM. A lattice-Boltzmann simulation study of the drag coefficient of clusters of spheres. *Computers & Fluids*. 2006; 35: 966-970.
45. Quevedo JA. Fluidization of agglomerates of nanoparticles under different force fields. NJIT Masters Thesis. New Jersey, 2004.
46. Pope SB. *Turbulent Flows: Free shear flows*. Cambridge University Press, Cambridge, 2000.
47. Yang W-C. *Handbook of fluidization and fluid-particle systems*. Marcel Dekker, Inc. New York, 2003.
48. Li, H, Lu X, Kwauk M. Particulation of gas-solids fluidization. *Powder Technology*. 2003; 137: 54 - 62.
49. Van Dijk J-J, Hoffmann AC, Cheesman D, Yates JG. The influence of horizontal internal baffles on the flow pattern on dense fluidized beds by X-ray investigation. *Powder Technology*. 1998; 98: 273 – 278.
50. Gibilaro L G. *Fluidization-dynamics: Single particle suspension*. Butterworth-Heinemann, Oxford, 2001.
51. Friedlander SK. *Smoke, dust and haze: Fundamentals of aerosol dynamics*. (2nd edition). Oxford university press, New York, 2000.
52. Valverde JM, Quintanilla MAS, Castellanos A, and Mills P. The settling of fine cohesive powders. *Europhysics Lett*. 2001; 54, 3, 329.
53. Pratsinis S, Wegner K. Gas-phase synthesis of nanoparticles: scale-up and design of flame reactors. *Powder Technology*. 2005; 150, 117-122.
54. Gutsch A, Kraemer M, Micheal G, Muohlenweg H, Pridohl M and Zimmermann G. Gas-phase production of nanoparticles. *KONA*. 2002; 20, 24 – 37.
55. Vemury S, Pratsinis S. Self-preserving size distributions of agglomerates. *J. Aerosol Science*. 1995; 26 (2), 175-185.

56. Arnaldos J, Casal J, Lucas A, Puigjamer L. Magnetically stabilized fluidization: modeling and application to mixtures. *Powder Technology*. 1985; 44, 57-62.
57. Ganzha VL, Saxena SC. Heat-transfer characteristics of magneto-fluidized beds of pure and admixtures of magnetic and nonmagnetic particles. *International Journal of Heat & Mass Transfer*. 1998; 41, 209-218.
58. Wu WY, Navada A, Saxena SC. Hydrodynamic characteristics of a magnetically stabilized air fluidized bed of an admixture of magnetic and non-magnetic particles. *Powder Technology*. 1997; 90, 39-46.
59. Lu X, Li H. Fluidization of CaCO_3 and Fe_2O_3 particle mixtures in a transverse rotating magnetic field. *Powder Technology*. 2000; 107, 66-78.
60. Bhandarkar M, Shelekhin AB, Dixon AG, Ma YHJ. Adsorption, permeation, and diffusion of gases in microporous membranes. I. Adsorption of gases on microporous glass membranes, *Journal of Membrane Science*. 1992; 75, 221.
61. Breger V, Gileadi E. *Electrochim. Acta*. 1971; 16, 177.
62. Rouquerol F, Rouquerol J, Sing K. In: *Adsorption by powders and porous solids*, Academic Press, London, 1999, Great Britain.
63. Hoebnik J, Rietema K. Drying granular solids in fluidized bed-I: Description on basis of mass and heat transfer coefficients. *Chemical Engineering Science*. 1980; 35, 2135-2140.
64. Hoebnik J, Rietema K. Drying granular solids in fluidized bed-II: The influence of diffusion limitation on the gas-solid contacting around bubbles. *Chemical Engineering Science*. 1980; 35, 2257-2265.
65. Chandran A, Subba Rao S, Varma Y. Fluidized bed drying of solids. *AIChE Journal*. 1990; 36 (1), 29-38.
66. Chen P, Pei D. A mathematical model of drying processes. *International Journal of Heat and Mass Transfer*. 1989; 32 (2), 297-310.
67. Davidson JF, Thorpe RB, Al-Mansoori O, Kwong H, Peck M, Williamson R. Evaporation of water from air-fluidized porous particles. *Chemical Engineering Science*. 2001; 56, 6089 – 6097.
68. Wang ZH, Chen G. Heat and mass transfer in batch fluidized-bed drying of porous particles. *Chemical Engineering Science*. 2000; 55, 1857 -1869.

69. Tatemoto Y, Bando Y, Yasuda K, Senda Y, Nakamura M. Effect of fluidizing particle on drying characteristics of porous material in fluidized bed. *Drying Technology*. 2001; 19(7), 1305-1318.
70. Tatemoto Y, Mawatari Y, Saito K, Noda K. Effect of motion of drying materials in fluidized bed on drying characteristics. *Journal of Chemical engineering of Japan*. 2002; 35 (8), 735-758.
71. Hajidavallo E, Hamdullahpur F. Thermal analysis of a fluidized bed drying process for crops. Part I: Mathematical modeling. *Int. J. Energy Res*. 2000; 24, 791-807.
72. Hajidavallo E, Hamdullahpur F. Thermal analysis of a fluidized bed drying process for crops. Part II: Experimental results and model verification. *Int. J. Energy Res*. 2000; 24, 809-820.
73. Mihoubi D, Bellagi A. Thermodynamic analysis of sorption isotherms of bentonite. *J. Chem. Thermodynamics*. 2006, In Press.
74. Ng KC, Chua HT, Chung CY, Loke CH, Kashiwagi T, Akisawa A, Saha BB. Experimental investigation of the silica gel-water adsorption isotherm characteristics. *Applied Thermal Engineering*. 2001; 21, 1631-1642.
75. Roessler A. Loss on drying 2 hours at 105°C. Degussa Corporation. 1999; ISO787-2.
76. Padfield T. (1996). Equations describing the physical properties of moist air. Retrieved October 10, 2004, from <http://www.natmus.dk/cons/tp/atmcalc/atmoclc1.htm>
77. Bolton D. The computation of equivalent potential temperature. *Monthly Weather Review*. 1980; 108, 1046-1053.
78. De Levrie R. *Advanced Excel for scientific data analysis*. Oxford University Press, New York, 2004.
79. Flesch J. Untersuchungen zu den Gleichgewichten und zur Reaktionskinetic bei der Entsäuerung pyrogener Kieselsäuren in der Wirbelschichtan. Dissertation, 2005; Universität Karlsruhe (TH), Germany.
80. Schlichting H, Gersten K. (1999). 1. Some features of viscous flow. *Boundary layer theory*. Bochum, p. 24.
81. Bird RB, Stewart WE and Lightfoot EN, 2002. Chapter 22: Interphase Transport in Nonisothermal Mixtures. *Transport Phenomena*, second edition, New York, pp. 676-677.

82. Fuller EN, Shettler PD, and Giddings JC. *Industrial Engineering Chemistry*. 1966; 58, No. 5, 19-27.
83. Reid RC, (1987). "The properties of gases and liquids," Fourth Edition McGraw-Hill Book Company.
84. Fogler SH, (2002). *Models for Nonideal Reactors*, in: *Elements of Chemical Reaction Engineering*. Prentice Hall, Third Edition, New Jersey, p.871.
85. Watano S, Imada Y, Hamada K, Wakamatsu Y, Tanabe Y, Dave R, Pfeffer R. Microgranulation of fine powders by a novel rotating fluidized bed granulator. *Powder Technology*. 2003; 131: 250-255.
86. Watano S, Nakamura H, Hamada K, Wakamatsu Y, Tanabe Y, Dave R, Pfeffer R. Fine particle coating by a novel rotating fluidized bed coater. *Powder Technology*. 2004; 141: 172-176.
87. Qian G, Bagyi I, Burdick I, Pfeffer R, Shaw H, Stevens J. Gas-solid fluidization in a centrifugal field. *AIChE Journal*. 2001; 47:1022-1033.
88. Wang Y, Wei F, Jin Y, Luo T. Agglomerate particulate fluidization and e-particles. *Proceedings of CUChE-3*. Tsinghua University Press 2000.
89. Kroger DG, Levy EK, Chen JC. Flow characteristics in packed and fluidized rotating beds. *Powder Technology*. 1979; 24: 9-18.
90. Kao J, Pfeffer R, Tardos GI. On partial fluidization in rotating fluidized beds. *AIChE Journal*. 1987; 33: 858-861.
91. Chen YM. Fundamentals of a centrifugal fluidized bed. *AIChE Journal*. 1987; 33: 722-728.
92. Arman B. Fluid mechanics of flow through rotating cylinders with and without packed media. Bethlehem: Doctoral Dissertation, Chemical Engineering at Lehigh University, 1989.
93. Saunders JH. Particle entrainment from rotating fluidized beds. *Powder Technology*. 1986; 47: 211-217.
94. Matsuda S, Hatano H, Muramoto T, Tsutsumi A. Modeling for size reduction of agglomerates in nanoparticle fluidization. *AIChE Journal*. 2004; 50: 2763-2771.
95. Wen CY, Yu YH. A generalized method for predicting the minimum fluidization velocity. *AIChE Journal*. 1966; 12: 610.
96. Vanyo JP. *Rotating Fluids in Engineering and Science*. New York: Dover Publications, 2001.

97. Zhu C, Lin CH, Qian GH, Pfeffer R. Modeling of the pressure drop and flow field in a rotating fluidized bed. 6th World Congress of Chemical Engineering, Melbourne 2001.
98. Bennetts DA, Jackson DN. Source-sink flows in a rotating annulus: a combined laboratory and numerical study. *J. Fluid Mechanics*. 1974; 66: 689-705.
99. Kunii D, Levenspiel O. *Fluidization engineering*. New York: John Wiley & Sons, 1969.
100. Zhao Y, Wei L. Rheology of gas-solid fluidized bed. *Fuel Processing Technology*. 2000; 68: 153-160.
101. Poletto M, Joseph D. The effective density and viscosity of a suspension. *J. Rheology*. 1995; 39(2): 323-343.
102. Fabbro LD, Laborde JC, Merlin P, Ricciardi L. Air flows and pressure drop modeling for different pleated industrial filters. *Filtration and Separation*. 2002; 35-40.
103. Schroth T. New HEPA/ULPA filters for clean-room technology. *Filtration and Separation*. 1996; 245-250.
104. EPA-CICA, Air Pollution Technology Fact Sheet: High Efficiency Particle Air (HEPA) and Ultra Low Penetration Air (ULPA) Filter. U.S. EPA, Clean Air Technology Center. 2003, EPA-452/F-03-023.
105. Wepfer R. Characterization of HEPA and ULPA filters by proposed new European test methods. *Filtration and Separation*. 1995; 545-550.
106. Podgorski A, Zhou Y, Bibo H, Marijnissen J. Theoretical and experimental study of fibrous aerosol particles deposition in a granular bed. *J. Aerosol Sci*. 1996; 27: S479-S480.
107. Japuntich DA, Stenhouse JIT, Liu BYH. Effective pore diameter and monodisperse particle clogging of fibrous filters. *J. Aerosol Sci*. 1997; 28: 147-158.
108. Thomas D, Contal P, Renaudin V, Penicot P, Leclerc D, Vendel J. Modeling pressure drop in HEPA filters during dynamic filtration. *J. Aerosol Sci*. 1999; 30: 235-246.
109. Penicot P, Thomas D, Contal P, Leclerc D, Vendel J. Clogging of HEPA fibrous filters by solid and liquid aerosol particles: An experimental study. *Filtration and Separation*. 1999; 59-64.
110. Raynor PC, Leith D. The influence of accumulated liquid on fibrous filter performance. *J. Aerosol Sci*. 2000; 31: 19-34.

111. Frising T, Thomas D, Bemmerl D, Contal P. Clogging of fibrous filters by liquid aerosol particles: Experimental and phenomenological modeling study. *Chemical Engineering Science*. 2005; 60: 2751-2762.
112. Balazy A, Podgorski A, Gradon L. Filtration of nanosized aerosol particles in fibrous filters. I-Experimental results. Abstracts of the European Aerosol Conference. 2004; S967-S974.
113. Podgorski A. Effect of the fiber skewness on the collection efficiency of mechanical fibrous filters for the convective inertial range. *J. Aerosol Sci*. 2000; 31: S460-S461.
114. Guise MT, Hosticka B, Earp BC, Norris PM. An experimental investigation of aerosol collection utilizing packed beds of silica aerogel microspheres. *J. Non-Crystalline Solids*. 2001; 285: 317-322.
115. Otani Y, Kanaoka C, Emi H. Experimental study of aerosol filtration by the granular bed over a wide range of Reynolds numbers. *Aerosol Science and Technology*. 1989; 10: 463-474.
116. Marre S, Palmeri J. Theoretical study of aerosol filtration by nucleopore filters: The intermediate crossover regime of Brownian diffusion and direct interception. *J. Colloid Interface Sci*. 2001; 237: 230-238.
117. Marre S, Palmeri J, Larbot A, Bertrand M. Modeling of submicrometer aerosol penetration through sintered granular membrane filters. *J. Colloid Interface Sci*. 2004; 274: 167-182.
118. Wu X, Tien C. Polydispersed aerosol filtration in granular media. *Separations Technology*. 1995; 5: 63-75.
119. Bai R, Tien C. Transient behavior of particle deposition in granular media under various surface interactions. *Colloids and Surfaces*. 2000; 165: 95-114.
120. Bai R, Tien C. Particle deposition under unfavorable surface interactions. *J. Colloid Interface Sci*. 1999; 218: 488-499.
121. Leibold H, Wilhelm J.G. Investigations into the penetration and pressure drop of HEPA filter media during loading with submicron particle aerosols at high concentrations. *J. Aerosol Sci*. 1991; 22: S773-S776.
122. Kim HT, Kwon SB, Park YO, Lee KW. Diffusional filtration of polydispersed aerosol particles by fibrous and packed-bed filters. *Filtration and Separation*. 2000; 37-42.
123. Mortimer DP, Lpotts, Frost TH. Comparison of classical and contemporary methods for prediction of fibrous filter efficiency using computational fluid dynamics. *J. Aerosol Sci*. 1996; 27: S625-S626.

124. Mei JS, Yue PC, Halow JS. Granular filtration in fluidized-bed. U.S. Department of Energy. Morgantown Energy Technology Center. 13th International Conference on Fluidized Bed Combustion, Kissimmee, FL (1995).
125. Jankowska E. Determination of filtration efficiency with OPC and CPC counters. Abstracts of the European Aerosol Conference. 2004; S975-S980.
126. Chen D-R, Pui DYH, Hummes D, Fissan H, Quant FR, and Sem GJ. Design and Evaluation of a Nanometer Aerosol Differential Mobility Analyzer (Nano-DMA), *J. Aerosol Sci.* 1998; **29**(5):497-509.
127. Caldow RC, Palmer MR, and Quant FR. Performance of the TSI Model 3010 Condensation Particle Counter, paper presented at the American Association for Aerosol Research Eleventh Annual Meeting; San Francisco, California, USA; October 1992.
128. Bird RB, Stewart WE, Lightfoot EN. Chapter 6: Interphase transport in isothermal systems. Friction factors for packed columns, pp. 188 -192. 2nd Edition New York, 2002.
129. Tardos GI, Abuaf N, and Gutfinger CJ. *Air Pollut. Control Assoc.* 1978; 28:354.
130. Johnson RF, Manjrekar TG, Halligan HR. Removal of oil from water surfaces by sorption on unstructured fibers. *Environmental Science and technology.* 1973; 7: 439-443.
131. Paterson JW. *Industrial wastewater treatment technology.* Stoneham, MA: Butterworth Publishers, Inc. 1985. 2nd. Edition.
132. Quemeneur M, Marty Y. Fatty acids and sterols in domestic wastewaters. *Water Research.* 1994; 28: 1217-1226.
133. *Manual on Disposal of Refining Wastes.* American Petroleum Institute. 1969; 5: 5-15.
134. Manning F, Snider EH. Assessment data base for petroleum refining wastewater and residues. Washington: U.S. department of Commerce, NTIS. 1983; 94-101.
135. Churchill R. Air flotation techniques for oil water treatment. Engineering Science, Inc. April 1974.
136. Gaaseidnes K, Turbeville J. Separation of oil and water in oil spill recovery operations. *Pure Appl. Chem.* 1999; 71(1): 95-101.
137. Goldsmith R, Hossian S. Ultrafiltration concept for separating oil from water. Washington: U.S. Coast Guard, January 1973.

138. Cambiella A, Ortega E, Rios G, Benito JM, Pazos C, Coca J. Treatment of oil-in-water emulsions: Performance of a sawdust bed filter. *J. Hazardous Materials*. 2006; B131: 195-199.
139. Mathavan GN, Viraraghavan T. Use of peat in the treatment of oily waters. *Water, Air, Soil Pollut.* 1989; 45:17-26.
140. Mysore D, Viraraghavan T, Jin YC. Vermiculite Filtration for Removal of Oil from Water. *Practice Periodical of Hazardous, Toxic, and Radioactive Waste Management*. 2006; 156-161.
141. Pasila A. A biological oil adsorption filter. *Marine Pollution Bulletin*. 2004; 49: 1006-1012.
142. Ribeiro TH, Rubio J, Smith RW. A dried hydrophobic aquaphyte as an oil filter for oil/water emulsions. *Spill Science & Technology Bulletin*. 2003; 8(5-6): 483-489.
143. EPA US. Sorbent Materials in Storm Water Applications. <http://epa.gov/owm/mtb/mtbfact.htm>. Accessed July 2006.
144. Stenstrom MK, Lau S-L. Oil and grease removal by floating sorbent in a CDS device. CDS Technologies. 1998.
145. Alsaigh R, Boerma J, Ploof A, Regenmorter L. Evaluation of on-line media filters in the Rouge river watershed. Rouge river national wet weather demonstration project. 1999. Nonpoint work plan No.URBSW5, Task No.3.
146. Hrubesh et al. Method for removing organic liquids from aqueous solutions and mixtures. U.S. Patent 6709600 B2. March 23, 2004.
147. Ayres M, Hunt A. Silica aerogels. (<http://eetd.lbl.gov/ECS/aerogels/satoc.htm>) Ernest Orlando Lawrence Berkeley National Laboratory. Environmental Energy Technologies Division (EETD). Last updated April 2004.
148. Aerogel/Granulated Activated Carbon composites for adsorption of contaminants in water. Industrial Partnership and Commercialization (IPAC). January 2002. Website accessed on December 2006: (<http://www.llnl.gov/IPandC/technology/profile/aerogel/GACComposites/index.php>).
149. Fan LS, Muroyama K, Chern SH. Hydrodynamic Characteristics of inverse fluidization in liquid-solid and gas-liquid-solid systems. *The Chemical Engineering Journal*. 1982; 24:143-150.

150. Nikov I, Karamanev D. Liquid-solid Mass transfer in inverse fluidized bed. *AIChE Journal*. 1991; 37(5):781-784.
151. Karamanev DG, Nikolov LN. Bed expansion of liquid-solid inverse fluidization. *AIChE Journal*. 1992; 38(12):1916-1922.
152. Ibrahim YAA, Briens CL, Margaritis A, Bergongnou MA. Hydrodynamic characteristics of a three-phase inverse fluidized-bed column. *AIChE Journal*. 1996; 42(7):1889-1900.
153. Garcia-Calderon D, Buffiere P, Moletta R, Elmaleh S. Influence of Biomass Accumulation on Bed Expansion Characteristics of a Down-Flow Anaerobic Fluidized-Bed Reactor. *Biotechnology and Bioengineering*. 1998; 57(2):136-144.
154. Femin Benedict RJ, Kumaresan G, Velan M. Bed expansion and pressure drop studies in a liquid-solid inverse-fluidised bed reactor. *Bioprocess Engineering*. 1998; 19:137-142.
155. Lee DH, Epstein N, Grace JR. Hydrodynamic transition from fixed to fully fluidized beds for three-phase inverse fluidization. *Korean J. Chem. Eng.* 2000; 17(6): 684-690.
156. Cho YJ, Park HY, Kim SW, Kang Y, Kim SD. Heat Transfer and Hydrodynamics in Two-and Three-Phase Inverse Fluidized Beds. *Ind Eng Chem Res.* 2002; 41:2058-2063.
157. Renganathan T, Krishnaiah K. Prediction of minimum fluidization velocity in two and three phase inverse fluidized beds. *The Canadian Journal of Chemical Engineering*. 2003; 81:853-860.
158. Renganathan T, Krishnaiah K. Liquid phase mixing in 2-phase liquid-solid inverse fluidized bed. *Chemical Engineering Journal*. 2004; 98:213-218
159. Renganathan T, Krishnaiah K. Stochastic simulation of hydrodynamics of a liquid-solid inverse fluidized bed. *Ind Eng Chem Res.* 2004; 43:4405-4412.
160. Renganathan T, Krishnaiah K. Voidage characteristics and prediction of bed expansion in liquid-solid inverse fluidized bed. *Chemical Engineering Science*. 2005; 60:2545-2555
161. Jirka AM, Carter MJ. Reactor digestion method for COD analysis. *Analytical Chemistry*. 1975; 47(8):1397.

162. Hach Co. Method 8000: Reactor digestion method USEPA approved for oxygen chemical demand wastewater analysis. DR/890 Datalogging Colorimeter Handbook. 2004: 427-436.
163. Sakiadis BC. Fluid and particle mechanics. Perry's chemical engineer's handbook. 1984
164. Wen CY, Yu YH. Mechanics of fluidization. Chem. Eng. Prog. Symp. Ser. 1966; 62 (2): 100.